Synthesizing, Purifying, and Characterizing Molten Chloride Salts

A Dissertation Presented for the

Doctor of Philosophy

Degree

University of Tennessee, Knoxville

Phillip William Halstenberg

May 2023

Abstract

Molten chloride salts have vast potential as heat transfer fluids with both nuclear and concentrated solar power applications. For application in energy systems, the characteristics that govern these systems must be well understood. This work focuses on inorganic molten chloride salts with a special emphasis on the experimental aspect of chemical research. **Chapter 2** covers the synthetic approaches for the formation of molten chloride mixtures. Many salts can be purchased from industrial suppliers, but most must be purified therefore, **Chapter 3** evaluates various methodology developed for removal of impurities in salt mixtures. Once the salt of proper content and purity is obtained it can be characterized. **Chapter 4** reviews the characterization of various salts utilizing many analytical approaches. The remaining chapters focus on fluid property optimization needed for the industrial use of molten chlorides as heat transfer fluid. A novel mechanochemical synthetic route for the formation of $MgCl_2$:KCl carnallite was instituted and is reviewed in **Chapter 5**. **Chapter 6** reviews a novel apparatus designed to supercool chloride salts while still in the amorphous state. Magnetic nanoparticles are utilized in **Chapter 7** to demonstrate the efficacy and first-time formation of an ultra-high temperature ferrofluid.

Table of Contents

List of Tables

List of Figures

Chapter 1. Introduction

1.1 Molten Salt Background

Salt is defined in a general chemistry sense as a molecule that is held together by an ionic bond. This occurs in elements with differing electronegativities resulting in electrostatic attraction between oppositely charged species. If one of the atoms has low enough ionization energy, then electrons will be transferred between atoms to a more stable electron configuration.[1] The physical result of these ionic bonds is a relatively high melting point, lower vapor pressure, and polar solvent solubility. When a pure salt is above the melting point it is referred to as molten. Thus, molten salt is synonymous with liquid salt.

The phrase molten salt encompasses an innumerable number of different compounds. Two broad distinctions exist for the classification of molten salts. The first is known as room temperature molten salt or more recently, ionic liquid. Ionic liquids are defined as mixtures of ionic substances that contain a melting point less than 100 ^{o}C.[2] While these can consist of inorganic materials, ionic liquids are generally composed of organic cations and anions.[3] The salts that melt above a temperature of 100 ^{o}C are what is generally referred to as molten salt. While there are some organic salts that fall into this category, molten salts are usually composed of inorganic materials.[4] The subject of this dissertation is focused on materials that fall into the latter of the broad distinctions of molten salt.

A variety of metal cations can be utilized as the cationic component of a molten salt system. There are two general categories of anions that are relevant to molten salt research consisting of monoatomic halides such F^-, Cl^-, Br^-, and I^-.[5] The second anion category is polyatomic anions such as NO_3^-, SO_4^{2-}, and PO_4^{3-}.[6] One of the differences in physical characteristics that separates molten salts containing metal-halide anion and molten salts containing metal-polyatomic anion is the melting point.[7] The higher melting points are associated with metal halide melts.[8] The higher temperature melting points and other physical properties of metal halide molten salts make them ideal for application in next generation reactor systems.[9, 10] As outlined in later sections, metal-chloride based molten salts have some of the lowest cost of production for materials related to high-temperature molten salt applications. There is a knowledge gap pertaining to the fundamental characteristics of molten salt mixtures that must be filled prior to application. The research herein

is motivated by the advancement in understanding of molten chloride salt chemistry related to synthesis, analysis, and material interactions. For this reason, the material focus and use of the phrase molten salt as pertaining to this document is related to metal chloride-based mixtures. Therefore, because this dissertation focuses on metal-chloride based molten salt mixtures specifically, the phrases molten salt, molten chloride, molten metal chloride, and molten metal chloride salts are used interchangeably henceforth.

Much of the molten salt research in America is a direct result of the Molten Salt Reactor Experiment (MSRE) carried out at Oak Ridge National Laboratory (ORNL).[11, 12] Research into the physical characteristics of molten salt began in the 1940's after it was proposed for use in nuclear reactor systems by Raymond Briant and Alvin Weinberg in 1957.[10] This culminated into a molten salt test reactor that was operational at ORNL throughout the 1960's.[13] The majority of the research carried out during this time was centered around fluoride based salt mixtures.[14] Fluoride salts are optimized in reactor systems that are driven by thermal neutrons due to the fluoride ion's relatively large neutronic cross-section and ability to work as a neutron moderator.[15] At the operational conclusion of ORNL's experimental fluoride based reactor, much of the research into molten salt came to a stand-still and was not re-initiated for many years.[16]

In 1952 a reactor system utilizing a chloride-based salt system was first proposed by Goodman et al.[17] Subsequent reviews of a chloride based reactor systems determined feasibility of use. Further inquiry revealed that ^{37}Cl is an attractive isotope for application as it contains sufficiently small neutronic cross-section to be utilized in a fast neutron breeder reactor system.[18] In a fast breeder reactor, ^{238}U can be exploited as the major fuel component.[19] This makes fast spectrum neutron reactor systems advantageous because use of the ^{238}U isotope can help to remedy some of the current depleted uranium storage sites. It is estimated in the United States, there is a 1.2 million ton stockpile of ^{238}U remaining from various enrichment processes and is growing by approximately 50,000 tons annually.[20]

The potential application of molten chloride fast reactors in the electricity grid has resulted in a resurgence in research interest related to these systems recently. The research and development initiatives from the United States Department of Energy (DOE) related to molten salt reactor research is centered around chloride-based systems. The systems currently under study are related to alkali and alkaline earth chloride-based salts as solvents for both fuel and coolant matrices

within the nuclear reactor systems. In addition to nuclear reactor systems molten chloride salts are also being studied for application in concentrated solar systems.[21] The largest collaborative network working as part of the DOE initiative to understand the underlying fundamental mechanisms that govern these systems is the Energy Frontier Research Center: Molten Salt in Extreme Environments. The center utilizes a myriad of techniques to measure and quantify numerous chemical characteristics of these mixtures in the molten state. The experimental techniques developed and presented in Chapter 2 and Chapter 3 supported subsequent experiments conducted across institutions and are summarized in Chapter 4. The work of Energy Frontier Research Center is a culmination of much of the collaborative effort presented in this dissertation.

1.2 Applications of Molten Salts

Application of molten salts are largely related to their extensive liquidous range making them ideal for use as high-temperature heat transfer fluids (HTF).[22] The thermal energy storage applications of molten salts that are most important for the DOE and this dissertation are directly related to concentrated solar power (CSP), nuclear energy (NE), and grid level energy storage. Grid level energy storage must be available for renewable energy such as wind and solar to contribute dependably to energy production.[23] Without storage solutions, utility companies must rely on other, carbon intensive, resources to provide electricity during times of peak consumption or unfavorable weather.[24] Some matrices of molten salts are being examined for use as grid-level energy storage.[25] The higher the temperature a solution can be heated, the more thermal energy can be contained.[26] The characteristic low vapor pressures of many salts allow for them to be heated to high temperature without a substantial pressure increase.[27]

In a similar manner as molten salt for a grid-level battery, it can also be used to transduce solar energy into electricity in CSP plants. This works by using a series of mirrors that concentrate the solar radiation on a singular point.[28] The heated molten salt is then used in a loop to boil water and turn turbines, creating electricity.[29] A large advantage that CSP has relative to traditional photovoltaic harnessing of solar energy is excess energy created during peak production can be stored as thermal energy in the salt. This means that CSP has the potential produce electricity from solar power through the night and during unfavorable weather.[30] Therefore, CSP can more

continuously contribute to the base-load electricity production mitigating some of the need for grid-level batteries.

Molten salt's first potential nuclear energy application is used as a novel heat transfer fluid in a similar manner to the two previous HTF applications. Molten salt can carry the heat energy created by the fission process where thermal energy can be transduced to electrical energy. In addition, coolant salt is also tasked with maintaining proper temperature of the fission reaction.[31] Due to the low vapor pressure at high temperatures, the coolant salt can stably maintain the fission reaction at a higher temperature than classical coolants such as water.[32]

The second potential application of molten salt in nuclear energy is as a novel solvent for the fissile and fissionable materials used to maintain the fission cascade.[33] Indeed, there are many salt matrices that will allow a large concentration of actinide species to freely dissolve within the liquid creating a homogeneous liquid containing the nuclear fuel.[34] The homogeneity of the solution will allow for a more even distribution of the fission cascade as opposed to the current solid actinide oxide pellets used in reactors.[35] This allows the liquid fuel to more efficiently consume a higher percentage of fissile material that can result in a drastic reduction in nuclear waste produced.[36] Molten salt reactors can also be designed with on-line refueling and waste removal yielding a less materials intensive fission cascade. Allowing for larger diversity of fissile material utilization, such as thorium, that can increase economic competitiveness of energy production.[37]

The most advantageous feature of utilizing molten salt as fuel is many mixtures have the characteristics that as temperature of the solution increases, the density of the solution decreases.[38] For a fission cascade to propagate, a neutron must strike close enough to the nucleus of another fissile atom. As the temperature of the liquid fuel increases, the density will also increase resulting in the fission propagation to slow. The physical manifestation of this is using liquid fuel prevents runaway fission reactions that have resulted in disasters that have turned the public's opinion away from nuclear power over the last century. Meaning molten salt reactors are inherently safe.[39]

Alkali and Alkaline based chloride salts exhibit properties that are suited well for implementation as heat transfer fluids.[40] The first advantage these systems have over typical molecular solvents is the melting point of the mixture can be tuned according to the cationic composition of the mixture. An example of this is a typical binary mixture, $MgCl_2$ and KCl, when

melted together has very different melting points over a wide temperature range. Melting temperature variation's dependence on concentration is present in most metal chloride mixtures that are fused together in the liquid state. The melting temperature can be further manipulated when more components are added. Resulting in the ability to tune melting point to a very specific range depending on applicable need.

This trend extends to many different aspects of the thermophysical properties of liquid salt mixtures. Another property that makes these metal chloride salt mixtures attractive is their relatively moderate viscosity as a liquid. Many molten chlorides contain similar viscosity to water.[41] This is advantageous when designing systems utilizing molten salt as the fluid flow dynamics and engineering of systems based on water have been extensively interrogated. In the same way as the melting point, the viscosity can be tuned by additives to the mixture. This can allow for very fine tuning of designer high-temperature solvents.

Due to the ionic bonding present in molten chloride solutions, many mixtures have been observed to have negligible vapor pressure over a massive temperature range.[42] Most industrial processes require temperatures well exceeding the boiling point of water. This requires extensive engineering techniques to reinforce systems containment for safe continuous operation at elevated pressures. This extra engineering directly translates to an increased input cost for the process. Additionally, water cooled reactor cores are susceptible to critical heat flux which insulates the reactor core from the coolant resulting in runaway fission.[43] This potential safety hazard is circumvented in liquid fuel molten salt reactor systems due to the ultra-high boiling point of molten chloride salt mixtures.

The real-world consequence of the difference between the melting point of the two mixtures is the obvious one. Heat transfer applications that utilize water as coolant have a working window of approximately 100^{o}C where the system vapor pressure remains negligible. Whereas a solution of $MgCl_2$:KCl can maintain negligible vapor pressure over a working window greater than 1000^{o}C.[44] There is the potential for additives in water coolants that will change the melting point and boiling point slightly through various means. There is no water-based coolant that can maintain negligible vapor pressure over a 1000^{o}C temperature range above the melting point. This is important when determining the total cost of operating a nuclear reactor system. If the system overheats it will lead to an over pressurization of the system and the potential for a reactor

meltdown. The mitigation of this safety hazard requires the building of extremely costly containment vessels that are meant to act as failsafe during a reactor core meltdown. In a nuclear reactor system where a molten chloride salt is used as the coolant the most expensive component of the reactor construction is unneeded.

In addition to the potential these metal chloride mixtures have in application to the coolant component of a nuclear reactor they also exhibit novel properties for the fuel component of the nuclear reactor system. The reason for this is that the use of molten chlorides also allows for a liquidous fuel system as most actinide chlorides are soluble in alkali and alkaline earth chloride solutions. All current reactor systems use a solid fuel component as the energy source of the reactor. The fissionable materials in the current state-of-the-art pellets are spatially hindered from furthering the daughter products to near the end of the decay chain. This means, in the current disc-fuel approach, there is an unnecessarily high amount of fuel discarded as waste. If the actinide chlorides are solubilized and able to flow freely throughout the solution, the fissile material can be allowed to decay to much easier to handle radioactive products.

1.3 Motivation

There is a great need for a secure, consistent, and green base-load power source to meet the world's growing need for electricity without sacrificing societal prosperity.[45] This has rejuvenated the interest in nuclear power sources to once again be utilized as larger percentages of electrical generation.[46] The leading candidates to be employed commercially in the coming decade are the generation IV molten salt reactors (MSR).[47] These reactor systems are expected to utilize simple inorganic chloride and fluoride base salts for both the fuel solvent and system coolant. This has initiated vast amounts of scientific effort to systematically evaluate the efficacy of these systems. To do this, an evaluation of the characteristics from a fundamental chemistry perspective must first be developed. The work of this dissertation focuses on the experimental aspect of synthesizing, purifying, and characterizing these systems.

Information needed to foster the application of molten salt necessitates a vast variety of chemical research approaches. Requiring collaboration between many different scientists with a wide range of expertise. This dissertation and the facilities at Oak Ridge National

Laboratory and the University of Tennessee Knoxville have been a cornerstone of a substantial portion of these efforts. The approach of the work related to this dissertation is motivated to further the development of advanced synthesis and purification pathways for salt production as outlined in section 1.3.1. The requirement of maintaining salt at high temperatures during analytical experiments has been a hindrance to advanced characterization techniques. This motivated work outlined in section 1.3.2 to create amorphous salt mixtures that allow for a room-temperature snapshot of the chemical structure of the solution state. Specific heat capacity is directly proportional to efficiency of heat transfer fluid in application. The potential influence of magnetic nanoparticles on specific heat capacity of molten salts motivated the formation of the magnetic nanofluids outline in section 1.3.3.

1.3.1 Mechanochemistry Motivation

Scaled synthesis and purification techniques are one of the challenges associated with application molten chloride salt on an industrial scale. The purity requirements of the salt mixtures vary depending on application but all current and intended uses for molten chloride salts require a low oxygen content. Oxygen content remains a central challenge due to the insolubility of the metal oxide form of the cations utilized for the molten salt matrix. In application, solid particles will disturb fluid flow dynamics resulting in improper flow calculations and potentially inaccurate engineering controls. At higher concentrations the particles can also agglomerate inside pipes or pumps, potentially damaging components of heat transfer systems. Previous literature has also shown that increased metal oxide content within metal chloride melts increases corrosion to metallic containment materials.[48] The insolubility of the metal oxide within the melt is the central problem if the salt is not in the presence of other forms of oxygen. If the chloride salt contains the hydrated form of any of the metal chloride components, then the metal chloride will react forming the oxide form. The byproducts of this reaction produce various types of hazardous chlorinated gases. Off gassing creates over pressurization concerns and can be detrimental to applications that are closed systems.

There are three methodologies that are currently used for salt purification. The first method is distillation and is examined in more detail in section 3.5 of this document. This methodology produces the highest purity salt, but there is much waste from this methodology, and requires the

salt to be anhydrous prior to the heating for distillation. Industrial applications do not require the ultra-trace purity of salt produced during distillation and is therefore not the economically efficient purification route for scaled applications. The next route for production of high purity, low oxide salts is via gaseous chlorination utilizing chlorinating agents such as CCl_4, Cl_2, $COCl_2$, among others. While this method can produce chloride salt matrices in a more cost-effective way than distillation there is still substantial increase in cost associated with waste streams. The third and final route for purification of salt is known as the carnallite method and is often used as a precursor purification step prior to the final chlorination. This method involves creating a new crystal structure that hydrolyzes at a lower rate than the pure hydrated salt upon dehydration.

The carnallite method has previously involved addition of ammonium chloride to magnesium chloride. The two have previously been combined by either dissolving in the same solution followed by dehydration or by heating together. Upon heating, the NH_4Cl reacts with the salt to create the crystal structure of the carnallite mineral. The formation of this structure involves intercalation of an extra Cl^- from KCl into the coordination sphere of the hydrated $MgCl_2$. This reduces the likelihood of hydrolysis of the Mg^{2+} cation as the water molecules is driven off at high temperatures. This results in anhydrous salt matrix that can subsequently undergo further purification via chlorination. The carnallite method is used as a pre-treatment method to produce anhydrous salt in previous purification methodologies. Using NH_4Cl for this purpose produces waste of similar corrosivity and hazard to gaseous chlorination methods.

For molten chloride salts to be cost competitive with other solvents in industrial applications an atom efficient, low-cost synthetic route is required. This motivated work outlined in Chapter 5 to examine a mechanochemical synthetic process for producing high purity, low oxide $MgCl_2$ and KCl mixtures by creating the carnallite crystal structure. The mechanochemistry carnallite method research is motivated by the potential reduction of waste generated compared to the previous NH_4Cl carnallite method. This can also negate the need to maintain the reaction to form the carnallite at high temperatures for extended periods as is the case for NH_4Cl. Furthermore, the mechanochemical carnallite method can create multiple component salt mixtures such as KCl:$MgCl_2$ directly. Whereas to make a salt mixture such as KCl:$MgCl_2$ with the previous carnallite method involves first drying $MgCl_2 \cdot 6H_2O$ with NH_4Cl followed by a second step that requires the anhydrous $MgCl_2$ to be mixed and melted together with appropriate amounts of KCl.[49]

1.3.2 Salt Glass Machine Motivation

The most prevalent challenge to characterizing chloride salt using nearly every analytical technique is the elevated temperature required to maintain the salt in the liquid state. Conducting experiments at elevated temperatures increases the costs, safety, and radiological contamination considerations for each experiment. This problem is compounded by the requirement that the salt must not contact atmospheric gases at any point during experiment. The practical result of this is that many current methodologies involving molten chloride salts require sealing the sample under high vacuum in various types of containment. If there are any impurities within the salt that result in gaseous products, then the likelihood of containment vessel failure can occur during experiment. A large portion of time required per experiment is devoted to method development of the high-temperature requirement. While it is important to have methodologies for high temperature experimentation, experimental progress could be substantially expedited if the experiments can be conducted at room temperature. To conduct experiments related to the liquid structure at room temperature, the salt would need to be vitrified in a glass or amorphous state.

Experiments cannot be conducted related to the solution structure of molten salt at room temperature as under normal conditions metal chloride salts are crystalline. A glass contrasts a crystal in that it is considered a solution whose viscosity approaches infinity and retains the chemical arrangement of the liquid state.[50] Therefore, if molten chloride salt can be supercooled and retain the chemical arrangement of the solution, then analytical experiments can be conducted at room temperature. The ability to conduct analytical experiments related to the solution state of molten salts at room temperature would greatly benefit the field molten salt research. This potential benefit to the field is the overarching motivation to create a methodology for the vitrification of metal chloride salts.

There are commercial apparats currently available to fast quench materials to maintain solution structure. The state of the art within the field is known as a splat quench apparatus. Once example of a commercially available instrument is the Splat Quencher/Ultra Rapid Quenching Machine produced by Edmund-Buhler. This apparatus, and most commercially available, is used to rapidly quench single metals and alloys in from a high temperature to create bulk metallic glass.[51] Sample processing begins with levitation melting to a maximum temperature of 2500 ^{o}C. After the sample has reached the appropriate temperature, the rf generator turns off allowing the

molten sample to fall. Two metal plates rapidly close together and catch the molten sample that "splats" between the two plates. This creates a thin layer of rapidly cooled material with a thickness of 20 – 100 μm and width/length of 10 – 30 mm.

The techniques utilized in commercial splat quench apparats cannot be used to rapidly quench molten chloride salts for a few reasons. The first is that using commercially available systems with levitation cannot be used with chloride salts as the salt cannot be levitated using a magnetic field. The second consideration is the time between the heating and quenching. Molten chloride salts contain a relatively low heat capacity and therefore quickly lose thermal energy to the environment. The drop is not temperature controlled during the fall in commercial splat quenching apparats. This can be detrimental to the rapid quenching as the sample will have already slowly cooled while falling. Lastly, there is little potential for alterations of the physical characteristics or dimensions of the quenched sample as the metal plates are designed to splat the sample in the same manner consistently. This would disallow custom sizes and shapes of chloride salt glass to be produced based on subsequent experiment needs for the salt sample. The motivation of this work is to invent a machine that is compatible with chloride salts to consistently produce amorphous products with varying sample sizes and compositions.

1.3.3 Molten Ferrofluid Motivation

In nuclear reactor systems the heat transfer fluid's ability to remove heat from the fission reaction is central to the design of every part of the system. One of the drawbacks for molten chloride salts in application as heat transfer fluids is their relatively low specific heat capacity. For reference, most of the nuclear reactor systems in operation today depend on water as a coolant.[52] The measured specific heat capacity of water is 4184 $J \cdot kg^{-1} \cdot K^{-1}$ while the measured specific heat capacity for molten alkali and alkaline earth chlorides ranges from ~1000 – 1200 $J \cdot kg^{-1} \cdot K^{-1}$.[53] Alkali and alkaline earth halide molten salts all contain approximately the same heat capacity regardless of ratio of salts used and the pure salt mixtures have been examined extensively.[54, 55] Therefore, a reactor system that utilizes molten alkali and alkaline earth chlorides would require more volume of coolant and therefore a larger facility than water.

To increase the efficiency and thus attractiveness of molten salt for implementation as a heat transfer fluid, the addition of nanoparticles have been assessed.[56-60] Previous research has demonstrated that when nanoparticles are added to molten salt matrix it results in large increases in the specific heat capacity of the entire solution due to the creation of a nanofluid. A nanofluid is a stable suspension that contains nanometer size particles that are inseparable from the bulk of the solution.[61] Recent literature has shown the formation of molten salt nanofluids using various types of nanoparticles.[62, 63] Prior literature has largely focused on the addition of silica nanoparticles, but more recently, the addition carbon nanotubes to melts have been evaluated.[64] Forming nanofluids within molten salt allows for fine tuning of specific parameters of the fluid, which can be advantageous for implementation as a coolant in nuclear systems.

In recent years there has been increased academic interest in the physical properties of ferrofluids. A ferrofluid is a nanofluid that contains nanoparticles that interact with an external magnetic field resulting in the entire fluid containing magnetic susceptibility.[65] There have been studies demonstrating that an external magnetic field can alter the specific heat capacity of the ferrofluid. .[66-76] If the same control of specific heat capacity and other parameters are present in molten chloride ferrofluids, then the result could be advantageous in heat transfer applications. A review of literature revealed there has been no investigation into the change of specific heat capacity in a molten chloride ferrofluid using an external magnetic field. In fact, there is no literature available on the creation of a magnetic molten chloride salt solution in any capacity. The lack of research into physical characteristics of a molten chloride ferrofluid and the potential benefits in application as a heat transfer fluid are the motivation to create and study this material for the first time.

1.4 Research Objectives

The overarching research goals of this work are to further the field in synthesizing, purifying, and characterizing molten chloride salts. The application focus of this work is related to the use of molten chloride salts as a heat transfer fluid or high temperature solvent in energy systems. The experimental techniques related to the production of salts through synthesis and purification are demonstrated in Chapter 2 and Chapter 3. The objective of this work was to create

the methodology to conduct molten salt experimental chemistry outside of the inert atmosphere glovebox environment. These two chapters culminated in the collaboration work that is presented in Chapter 4 summarizing the characterization related to the research objectives of understanding the bulk and interfacial chemistry of molten chloride solutions. Advancement in synthesis and purification via mechanochemistry is outlined in section 1.4.1 and Chapter 5. The approach to vitrification is outlined in Chapter 6 and section 1.4.2. The contribution of this work to the formation of the first molten chloride ferrofluid is described in Chapter 7 and the objectives outlined in section 1.4.3.

1.4.1 Mechanochemistry Research Objectives

The central research objective of Chapter 5 is to determine if direct mechanochemical synthesis of carnallite structure utilizing KCl and $MgCl_2 \cdot 6H_2O$ followed by a stepwise heating process to dehydrate the salt produces comparable MgO content to previous carnallite dehydration methods. This will be accomplished by first treating the salt with a centrifugal ball mill to ensure change of phase induced by mechanochemistry. The resulting mixture is then validated by X-ray diffraction to validate alteration in crystal structure between the treated and untreated salt mixtures. Answering the research question of: can mechanochemical treatment create the carnallite crystal structure of hydrated alkali and alkaline earth chlorides? After this, the mechanically treated salt is dried in a stepwise fashion based on the thermodynamic basis of for dehydration. The characteristics of the resulting mixture will enable examination of the second research objective of understanding the influence of a stepwise heating procedure on the MgO content formed via titration.

1.4.2 Salt Glass Machine Research Objectives

The overarching research objective for Chapter 6 is to create a methodology to reliably vitrify chloride salts in an amorphous state. This is first accomplished through the design of a novel super-cooling apparatus that is compatible with the experimental requirements of chloride salts. The design will improve the current state of the field in two key areas. The first optimization will

create a more controlled temperature environment prior to the moment of supercooling. Current splat quench apparats heat material and allow it to drop with no control over temperature during the time the material is falling. Whereas this work will drop material through a path that is surrounded by heating elements for the duration of the fall. This finer control of temperature should enable the formation of amorphous chloride glass. The second improvement is the use of two metallic wheels rotating toward each other as opposed to the metallic arms of the splat quench machine. The distance and rotation speed of the wheels allows for more control of the product's physical characteristics. Additionally, the quenching wheels within the glass machine are cooled to a temperature of -196 ^{o}C creating a larger temperature gradient during material quenching. Analytical evaluation of the resulting material determines the success of the improvements in apparatus design. Completing the research objective of creating a solid metal chloride material with less crystallinity when examined by X-ray diffraction and Raman spectroscopy.

1.4.3 Molten Ferrofluid Research Objectives

The predominant research objective of Chapter 7 is to create a ferrofluid utilizing molten chloride salt as the liquid matrix for magnetic nanoparticle suspension. The approach to evaluating this research objective will involve three subtasks to determine if synthesis of a molten chloride based ferrofluid is successful. The first subtask is to determine if the particles remain suspended in the molten salt at elevated temperatures. Immediate phase separation indicates phase immiscibility between the particles and liquid. To evaluate the suspension, a laser is used to visually demonstrate light scattering due to presence of particles within the solution. The second research subtask is the determination of chemical stability of the suspended particles in solution at elevated temperatures. The last research subtask required to evaluate the research objective is to determine if the particles maintain susceptibility to an external magnetic field at elevated temperatures. A novel experimental methodology is developed to address the latter two research subtasks. The experiment uses changes in mass due to presence of an external magnetic field and transduces the information to magnetic susceptibility as a function of temperature. The presence of magnetic susceptibility at increased temperatures indicates the particles remain chemically stable enough to retain magnetic properties.

1.5 Organization of Dissertation

The experimental approach required for handling high temperature molten salt solutions outside of the inert atmosphere glovebox is outlined in Chapter 2. Once a salt species is formed it almost always requires further purification. Additionally, it is demonstrated throughout this work that most commercially available chloride salt requires further purification. The different pathways applied for the purification of salts related to this work are discussed in Chapter 3. Chapter 4 emphasizes the collaboration enabled because of advancements in experimental handling of molten salt during this work. Chapter 5 reviews a novel mechanochemical synthetic pathway developed to produce low oxide binary chloride salt matrix. The contents of Chapter 6 are related to the design and operation of a quenching apparatus that freezes chloride salt in an amorphous state. Chapter 7 examines the first-time formation of an ultra-high temperature magnetic solution or molten ferrofluid.

Chapter 2. Synthesis

2.1 Development of Air Free Methodology

To increase the ease of handling and the variety of experimentation that can be performed using molten chloride salts, air free techniques needed to be developed. Due to the absorption of atmospheric water and subsequent hydrolysis upon melting, covered in subsequent chapters, all handling of anhydrous metal chloride salts must be done in the absence of atmospheric air. This requirement results in most current lab scale handling to be done inside an inert atmosphere glovebox, slowing experimental progress. This chapter seeks to present high-temperature apparats used during this work to successfully handle metal chloride salts outside an inert atmosphere glovebox.

The first step in the development of air free methodology involves the building of the inert gas lines needed to support a continuous flow during experiments. The inert gas used for all high temperature experimentation was argon gas, although any noble gas can be used.[77] Once proper inert gas lines have been established, a Schlenk type apparatus should be built with a vacuum capable of achieving 1.0×10^{-3} Torr atmosphere or better.[78] This will allow proper degassing and evacuation of the apparatus that will contain the molten chloride salt solution. Great care must be taken to ensure there is minimal leakage throughout the vacuum/gas manifold. Nearly all types of inorganic chloride salts are very reactive to both H_2O and O_2 at elevated temperatures.[49]

The methodological advancement of this chapter is handling of salts in the molten state outside of the inert atmosphere glovebox. All room temperature storage of prepared salt samples should be maintained in an inert atmosphere glovebox while inside a sealed container. The container should only be opened when salt is being taken for further experimentation. Bulk, crystalline, room temperature salts are extremely susceptible to many different types of contamination in addition to typical oxygen containing species. Another large source of bulk salt contamination can be attributed to carbon species which, under an inert atmosphere, will not be burned away. The carbon will morph into various, insoluble, species and remain semi-elevated in solution due to an elevated turbulent flow with increased temperature but can be removed via oxygen sparge shown in section 3.3.

Most inorganic chloride species in the molten state are only negligibly reactive with silica which makes fused silica an ideal ceramic material for molten chloride salt handling.[79] This, in addition to the material's transparency, makes fused silica advantageous over other ceramic materials such as aluminum oxide (alumina). Most of the apparatus designs used during this work utilized silica tubes as the cornerstone of the rest of the experimental methodology. The least costly and widest available geometry of fused silica is in the form of circular tubing. There are many vendors of fused silica tubing throughout both the United States and the world. The circular tubing can be cut into varying sizes, depending on liquid volume of experiment, and then closed on one end to resemble a classical test tube. The measured diameter of the opening of the silica test tube should match the size of associated fitting.

The silica test tube can be used for a vast number of experimental needs related to the formation of various mixtures. The best method for choosing the tubing diameter and length relates not only to the volume of salt, but also to the temperature needed. The ideal length and width of silica tubing would allow for 100% of the liquid salt total encapsulation of the heating source. Such that the average temperature of the entire mixture is semi-uniform within the furnace's hot zone at an equivalent thermocouple reading. The height of the tube should be directly related to the softening temperature of the O-ring in the compression fitting. The length of tubing above the heating zone should be sufficient so that no critical temperature of the fitting is possible. The temperature above the furnace can be controlled utilizing ceramic fiber insulation or a flow of air to ensure no overheating. Additionally, volatility of the molten salt and temperatures of experiment should be considered when determining length of cold zone before fitting connection.

For the open end of the silica tube, a compression fitting should be used. The two types of fittings used for this experiment to connect liquid vessels to gas/vacuum are the Swagelok glass and corrosion resistant stainless steel ultra-Torr fittings. Both connections can be secured on top of a tube with the appropriate diameter and tightened to create a reliable seal. Once the appropriate containment tube connection is chosen, the vessel can be connected to a vacuum valve. For simple solutions of a volume of >10 mL the fitting can be connected to the vacuum valve directly. A schematic representation of the connection can be seen in Figure 2.1.1.

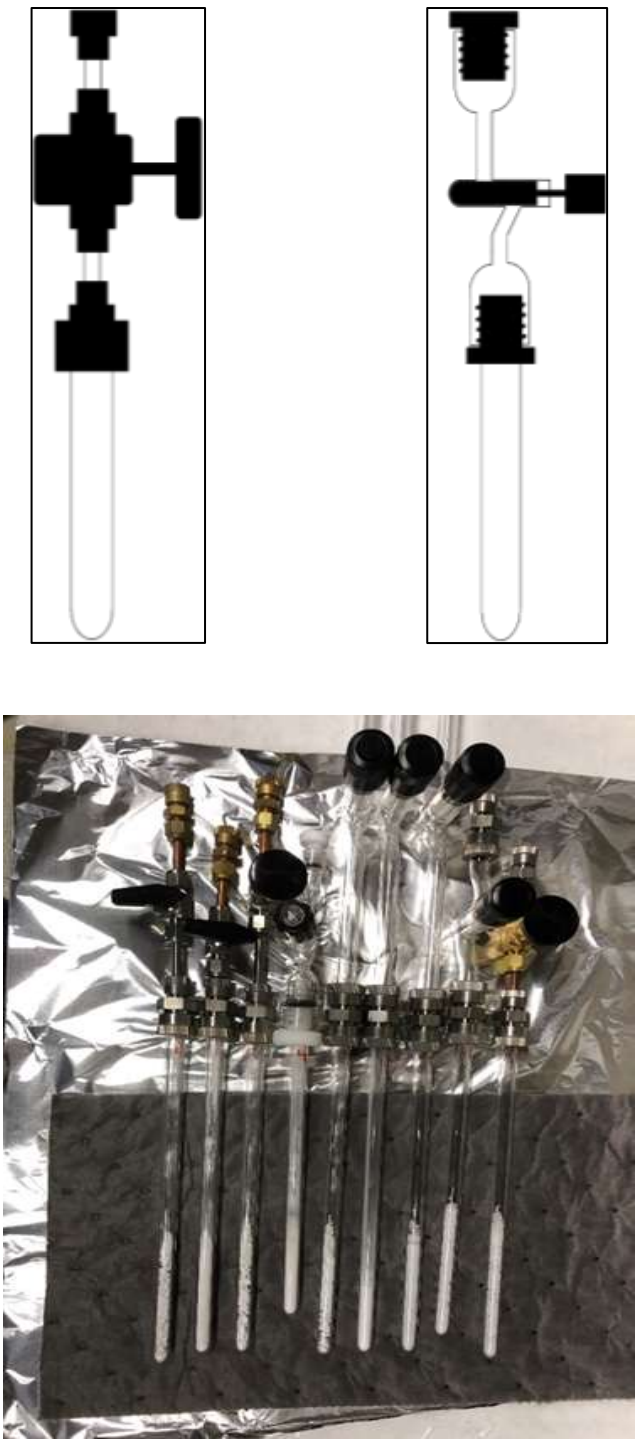

Figure 2.1.1 Schematic representation of vacuum valve connection to small diameter silica tube (top). Pictorial representation of vacuum valve connection to small diameter silica tube (bottom).

Larger diameter tubes require glass compression fittings such as Ace-Threds. This is largely for two reasons. First being the potentially large number of gaseous by-products produced during heating of large amounts of chloride salts. The corrosive nature of many of these gases is prohibitive for the use of metallic connections at the apex of the containment vessel. In some instances, corrosion products of metallic connections have contaminated the liquid salt solutions. In most instances, upon experiment conclusion, metallic connections must be maintained under an inert atmosphere or thoroughly cleaned. Proper care is not taken to remove corrosive products or atmospheric conditions will catalyze degradation and render metallic connections useless. The second advantage of using a glass compression fitting for larger liquid vessels is the variety of design availability. Some examples of custom glass compression fittings.

Larger diameter experimental vessels are often utilized for extended experimentation which allows for a myriad of different experiments requiring different probes and sensors. The same principle as mentioned earlier applies to the need for gaseous dead space in the tubing of the silica vessel. The temperature of the tubing at the location of the compression fitting O-ring, should not exceed any critical temperatures of the O-ring's material. One important note in experimental apparats requiring larger diameter tubing, liquid amount, and temperature can increase heat dissipation complexity. While the area on the exterior of the liquid containment vessel above the furnace can be well insulated, the interior of the vessel cannot. After a period at an elevated temperature, large amounts of heat can interiorly propagate through the vessel and overheat the compression fitting. This can result in loss of containment's integrity with catastrophic consequences.

In addition to the potential need for a heat sink at the top of the containment tube, it should be noted that potential layers of containment are required for larger liquid volumes. Silica test tubes holding a volume of <250 mL of liquid salt can be handled directly in the tube. For larger salt volumes >250 mL the tube should be used as a secondary containment and the liquid salt volume should be contained in a crucible made from appropriate materials. It should also be noted that a bottom heating element should be shielded or absent altogether from the furnace. During failure of the structural integrity of the liquid vessel, the liquid salt will fall through to the bottom of the furnace. Once there, the salt will react vigorously with the much hotter furnace elements and atmosphere, potentially ending in potentially disastrous results.

Once the appropriate test tube diameter, length, fitting, vacuum valve, and tubing connection has been fit, the room temperature salt can be loaded to the tube inside the inert atmosphere glovebox. The innovation outlined in the designs in this, and the next chapter is the ability to do molten salt experiments using Schlenk technique. High-temperature molten salt experiments can be conducted inside an inert atmosphere glovebox if it is maintained at an ultra-high purity. Although, if commercially purchased salt is used without being first purified and melted at an elevated temperature then melting open inside the glovebox will release many reactive chloride species. In addition to contamination of other materials present in the glovebox, the gases released will damage the box components over the long term. For this reason, unless salt history and contamination levels are known, Schlenk technique would be required for experiments conducted inside an inert atmosphere glovebox. The methodology described in this work results in safer, cleaner, and more productive experimental molten salt research.

2.2 Simple Melting

Once the proper components for apparats have been built, formation of a simple chloride melt can be performed. This requires the proper connections, valve, silica tube, vacuum line, and a furnace. The valve, connections, and tube should be transferred into an inert atmosphere glovebox where the salt of interest, analytical balance, weighing materials, and clamps are located. It should be noted that certain chloride species will expand during the initial melting phase and/or at higher temperatures so the density change should be considered during experimental preparation. Once the proper materials have been transferred, a stand for the tube should be made in a way that the silica tube can be positioned upright and balanced on the analytical balance. From there, the salt should be directly added to the tube until the desired mass of salt has been reached. This can be seen in Figure 2.2.1 which also shows small and large volumes of melted salt. The compression fitting should then be connected to the top of the tube and tightened well. The other end of the fitting should then be attached to a closed vacuum valve. Once the connections are secure, the vessel can be transferred outside of the inert atmosphere glovebox.

The Schlenk apparatus should be evacuated prior to removing the salt from the glovebox. Immediately after removing the vessel, the open end of the vacuum valve should be connected to tubing of the Schlenk apparatus. While there are many types of soft laboratory specific tubing, this

work has determined the most appropriate is polytetrafluorethylene (PTFE) or Teflon tubing. Due to its chemical resistance to the corrosive off gassing of high temperature chlorine chemistry and moderate physical strength allowing reuse. While non-fluorinated hard plastics can be used temporarily, they will degrade after continued use. Tubing made of soft plastic should not be used for molten chloride work due to reactiveness to chlorinated vapor.[80] Soft tubing will degrade too quickly to use safely for most molten chloride experiments.

Upon removal of salt containing vessel from the glovebox, it should be immediately connected to the vacuum line and proper valves opened so that the salt in continuously under dynamic vacuum. Using proper supports, the tube should be placed inside the hot zone of a furnace with proper distance of valve and insulation. A representation of the salt vessel inside a furnace with proper connections and insultation can be seen in Figure 2.2.2. A scaled version with multiple connections for gases can be seen in Figure 2.2.3. It has been found that a heating ramp rate of approximately 10 ^{o}C per minute is the most appropriate heating rate for most of the molten chloride experiments. This heating rate also discourages excess gaseous flow from the salt that is melting. Off-gassing from the salt during initial heating is very common among many species. This can be due to surface adsorbed water molecules, organic molecules, or many other contaminates. If the heating rate is large enough when these molecules are volatilized, it can create a large gaseous flow into the vacuum system. This can potentially contaminate the salt mixture or remove it from the tube and into the vacuum system itself. Hence, it is of vital importance that the vessel is maintained under dynamic vacuum.

Anhydrous metal chloride salts are extremely susceptible to absorption of water. Experience of this work and literature available (section 4.2) has shown that even commercially available metal chlorides labeled “anhydrous” still contain some level of hydration. Therefore, prior to use in experiments or formation of salt mixtures, all metal chloride should be melted under a dynamic vacuum and resolidified for storage. This approach allows for complete hydrolysis of any metal hydrates present reducing the gaseous HCl release during subsequent experiments. The formation of a single solid salt plug after solidification reduces the surface area of the solid salt compared to powder salt. This reduces the magnitude of water absorption during storage and also increases the ease of handling for subsequent experiments.

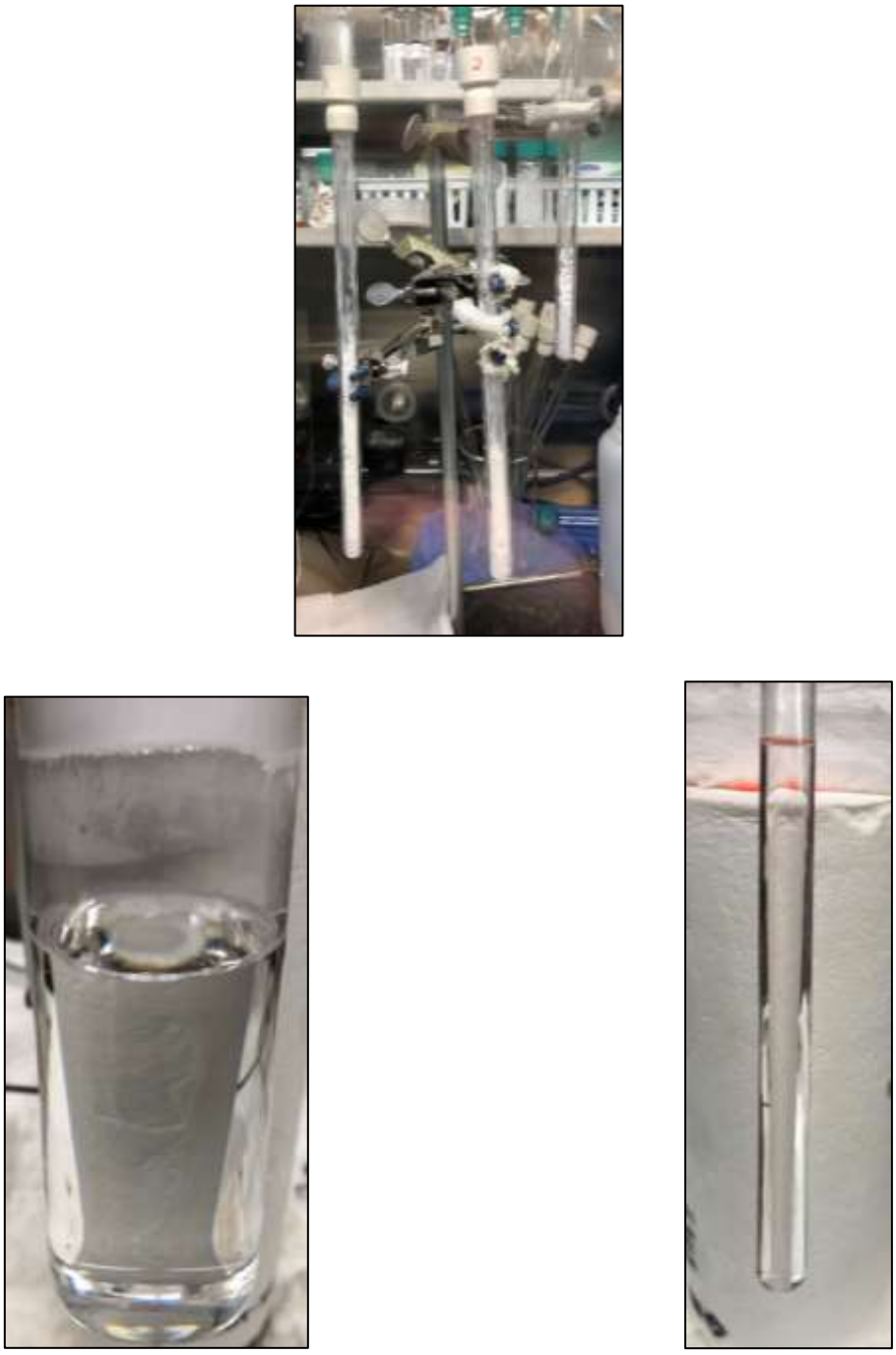

Figure 2.2.1 Solid KCl/$MgCl_2$ mixtures loaded in silica tubes inside glovebox (top). Molten distilled MgCl2 at 800ºC, 150 grams (bottom left). Molten distilled $MgCl_2$ at 800ºC, 10 grams (bottom right).

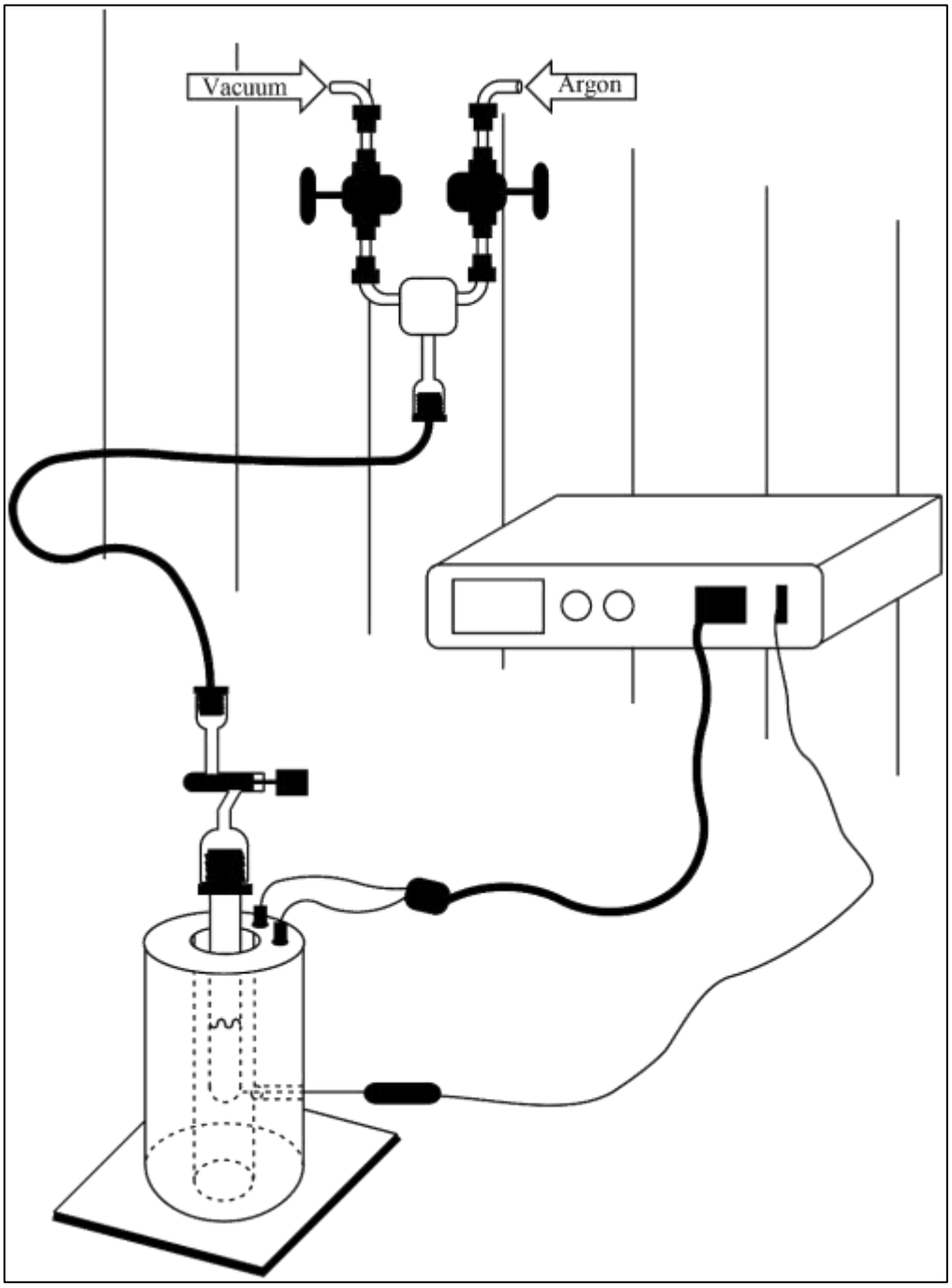

Figure 2.2.2. Schematic representation of the salt melting apparatus.

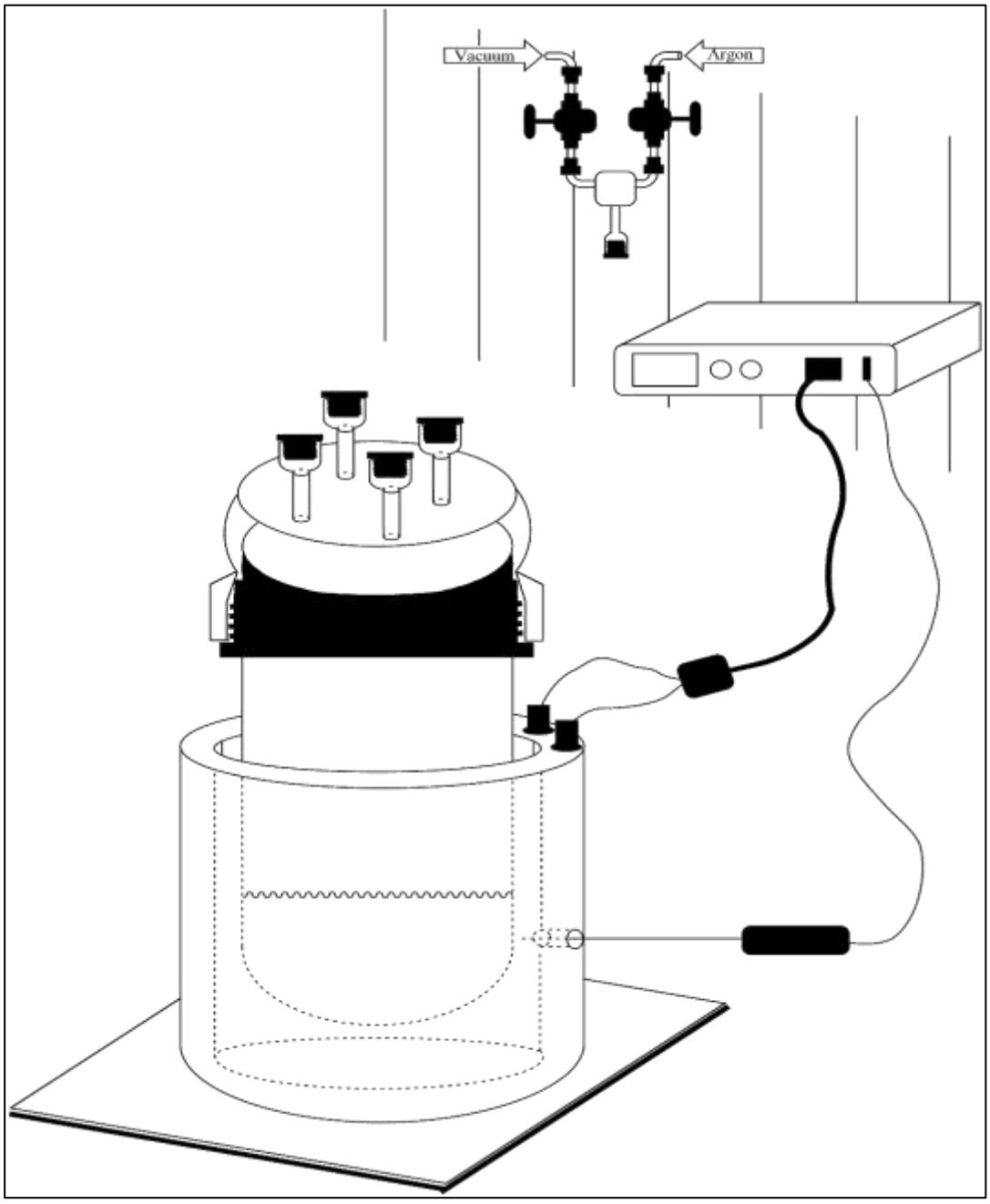

Figure 2.2.3. Schematic representation of the scaled salt melting apparatus.

As the salt is heated, the vacuum gauge measurement output can give an approximate qualitative estimate of the salt's purity and water content. When there are many impurities or water, the system pressure will increase by a substantial amount throughout the duration of the heating. When the salt is completely anhydrous, there should be negligible pressure change observed during salt melting. If the thermophysical properties differ from what is expected, then there is most likely contamination. The main sources of contamination during these experiments are the presence of floating particles. Throughout this work, there were two major sources of repeated contamination that could be identified visually. First, presence of some type of metal-oxide or metal-oxychloride species was likely when the solution appeared cloudy and white particles can be observed.

The second common type of contamination present in molten chloride systems that can be identified visually appears as dark particles. This work has found that in most cases, the presence of black particles in the solution is a result of carbon-based contamination. There is a multitude of sources that the presence of these particles can be attributed to. Some chloride-based salts are packaged in a plastic container which includes a desiccant pad with some carbon components. The desiccant pad present in the salt and the plastic from the container itself can shed small carbon particulates into the salt mixture. It is advisable not to use crystalline salt directly from a plastic container unless first purified. It is believed that other sources of carbon-based contamination include organic solvent residue on glassware and dust. A pictorial representation of molten chloride salt with carbon contamination present can be seen in Figure 2.2.4.

In most cases, when there is carbon contamination present in the chloride salt mixture, the salt must be in the liquid state to visualize the contamination. Once the salt recrystallizes in the solid state, the appearance would resemble non-contaminated salt as shown in Figure 2.2.5. Further laboratory scale purification can be performed to remove any contamination such as oxide or carbon-based particles. Oxygen based contamination present during this work was removed by reaction or separation covered in subsequent sections. Carbon-based contamination was removed during this work through sparging the molten salt solution at elevated temperature using dry air, covered in detail in section 3.3. The first step of simple melting is the most important preparatory step for any metal chloride molten salt experiment as it enables visual confirmation of contamination and ensures the salt is completely anhydrous.

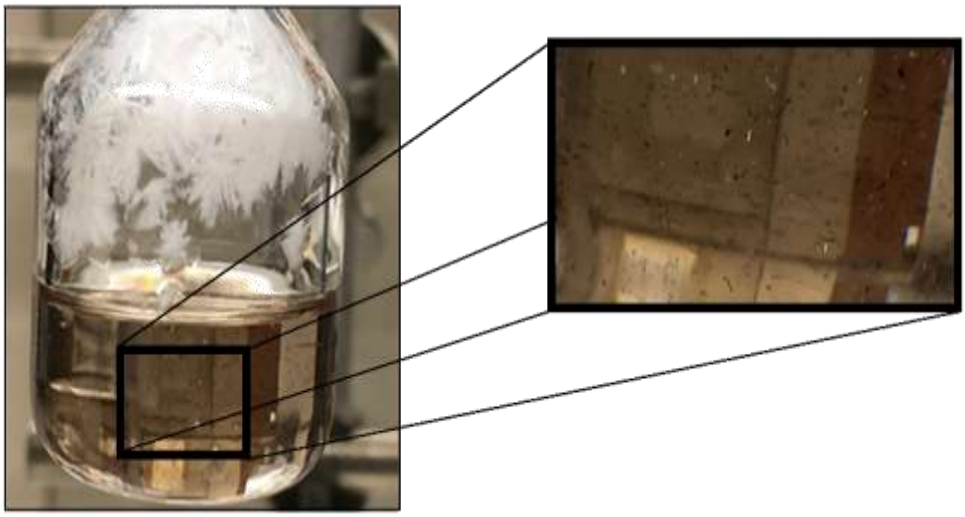

Figure 2.2.4. Pictorial representation of molten $MgCl_2$ with carbon-based contamination present.

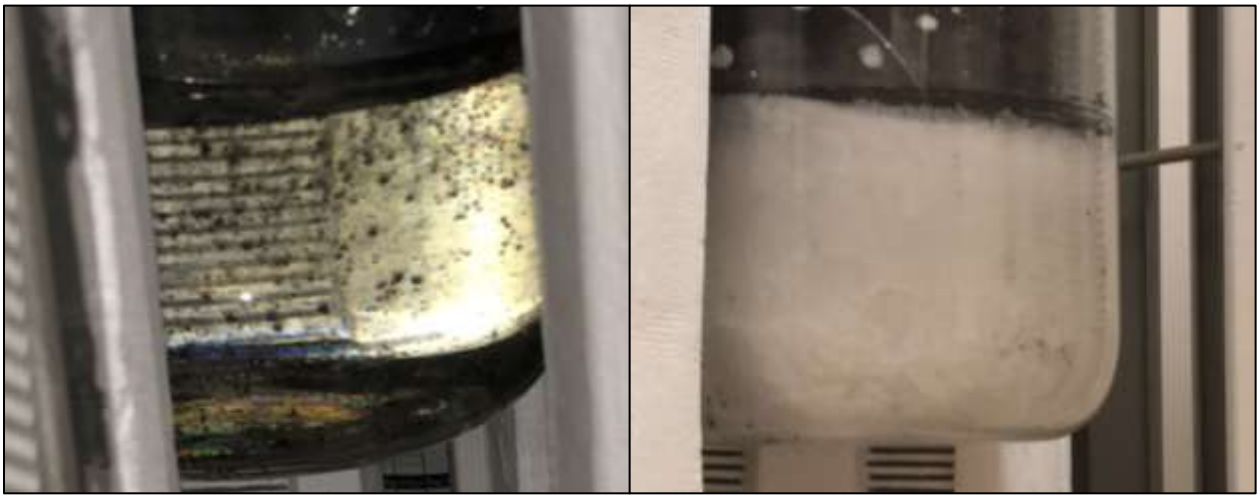

Figure 2.2.5. Molten $MgCl_2$ containing carbon contamination at 800^oC (left) and the same $MgCl_2$ cooled to room temperature (right).

2.3 Formation of Liquid Salt Mixtures

The composition of cations present in the molten salt solution can greatly influence the physical and chemical properties of the solution.[81] Thermophysical properties can be altered through mixing of cations and can depress the melting point to well below the melting point of any individual component.[82] An example of this would be the eutectic point of $MgCl_2$ and KCl. The individual melting points of $MgCl_2$ and KCl are 714 ^oC and 770 ^oC, respectively. When the pair is melted together in a 32/68 mole % ratio, the melting point of the resulting eutectic compound is 420 ^oC.[38] This allows for a much larger liquidous window and analytical experiments to be carried out at much lower temperatures. Depending on the ratio of individual components unique compounds can be formed such as $KMgCl_3$, K_2MgCl_4, and $K_3Mg_2Cl_7$ that have structures and properties that differ from individual KCl and $MgCl_2$ components, as detailed in Chapter 6.

The methodology behind the formation of fused chloride mixtures is much the same as the simple melting section. A singular silica tube should be transferred into an inert atmosphere glovebox along with associated fittings and valve. The mass of the crystalline salt should be obtained directly in the silica tube. An important note is that the salt with the lower melting point should be placed in the silica tube first and the higher melting salt should be placed on top. If there are more than two types of solid salts being added to the same mixtures, then they should be placed inside the tube from lowest melting salt to highest melting salt. While heating above all melting points will fuse the components into one after some time, ensuring the ordering is correct will reduce preparation time.

Once the components of the mixture are added to the tube, the fitting containing the vacuum valve should be added, closed, removed, and attached to the outside vacuum line. Once a dynamic vacuum has been established, the salt should be heated under dynamic vacuum at 10 ^oC per minute until visually homogeneous. It is important to heat the mixture to a temperature above the melting point of the individual components. For most molten chloride mixtures, the turbulent flow within the liquids from increased temperature will be enough to induce mixing of the two solutions. Mixing of solutions incurs increased difficulty when forming a suspension with solid particles. Methods developed for the mixing of molten chloride solutions will be detailed in the subsequent section.

2.4 Methods of Solution Mixing

Molten chloride based nanofluids have properties that could be advantageous to thermal energy storage applications, as described in more detail in Chapter 7. The influence of nanostructures on the properties of molten salt is not fully understood. The lack of experimental research in the literature results in a research need to develop the methodology of synthesizing molten chloride colloids. For proper polydispersity of particles, systems were required to be mixed to equilibrium prior to any analytical experimentation. Multiple different mixing apparats were designed and used to disperse nanoparticles and other various solutes during this work.

The first apparatus designed to mix the salt involves rotational force along the vertical axis of a silica tube. This methodology dispersed analytes in molten salt by connecting a sealed vacuum valve to a rotational motor. The tube connected to the valve was then heated by a furnace secured to a lab jack. A schematic diagram of the experimental apparatus that enabled this type of mixing can be seen in Figure 2.4.1. This method is advantageous for especially volatile or reactive molten chloride-based solutions because it allowed for solution mixing in the same vessel the salt was initially melted in. The design also allows for a slower mixing of contents relative to the other two methods developed for this work. Over pressurization can be avoided by increasing the length of the fused silica tubing containing the salt allowing for a cold zone above the furnace.

The next method involves introducing stir-bars to the molten chloride solutions and using a magnetic stir plate like room temperature solution mixing. This method has the advantage of introduction of internal mixing of the solution while the other two methods that only mix via external movement of the solution. To accomplish this, a cylindrical metallic iron rod was obtained for use as magnetic part of stir bar. This iron rod matched the internal diameter of a cylindrical silica tube with 1.0 mm of free space. The iron is then flame sealed inside of the fused silica to create a magnetically susceptible stir bar that does not introduce metal contamination to the salt matrix. Once the stir bar is totally encapsulated with silica tubing, the stir bar will maintain inertness to the molten salt solution. If the metallic iron is placed directly in the molten chloride solution, the solution will become contaminated with iron chloride. To use the stir bar, silica test tubes should be used in the same way described in the simple melting section except the stir bar should be added to the test tube first. The solution should be melted inside of a furnace with insulation and a stir plate placed below. A schematic depiction of this can be seen in Figure 2.4.2.

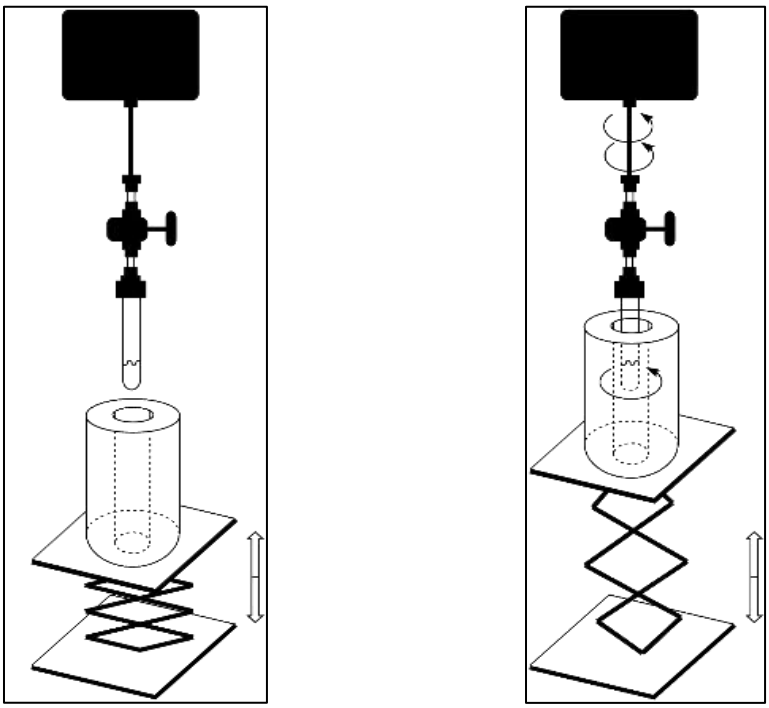

Figure 2.4.1. Schematic diagram representing silica tube based centrifugal solution mixing.

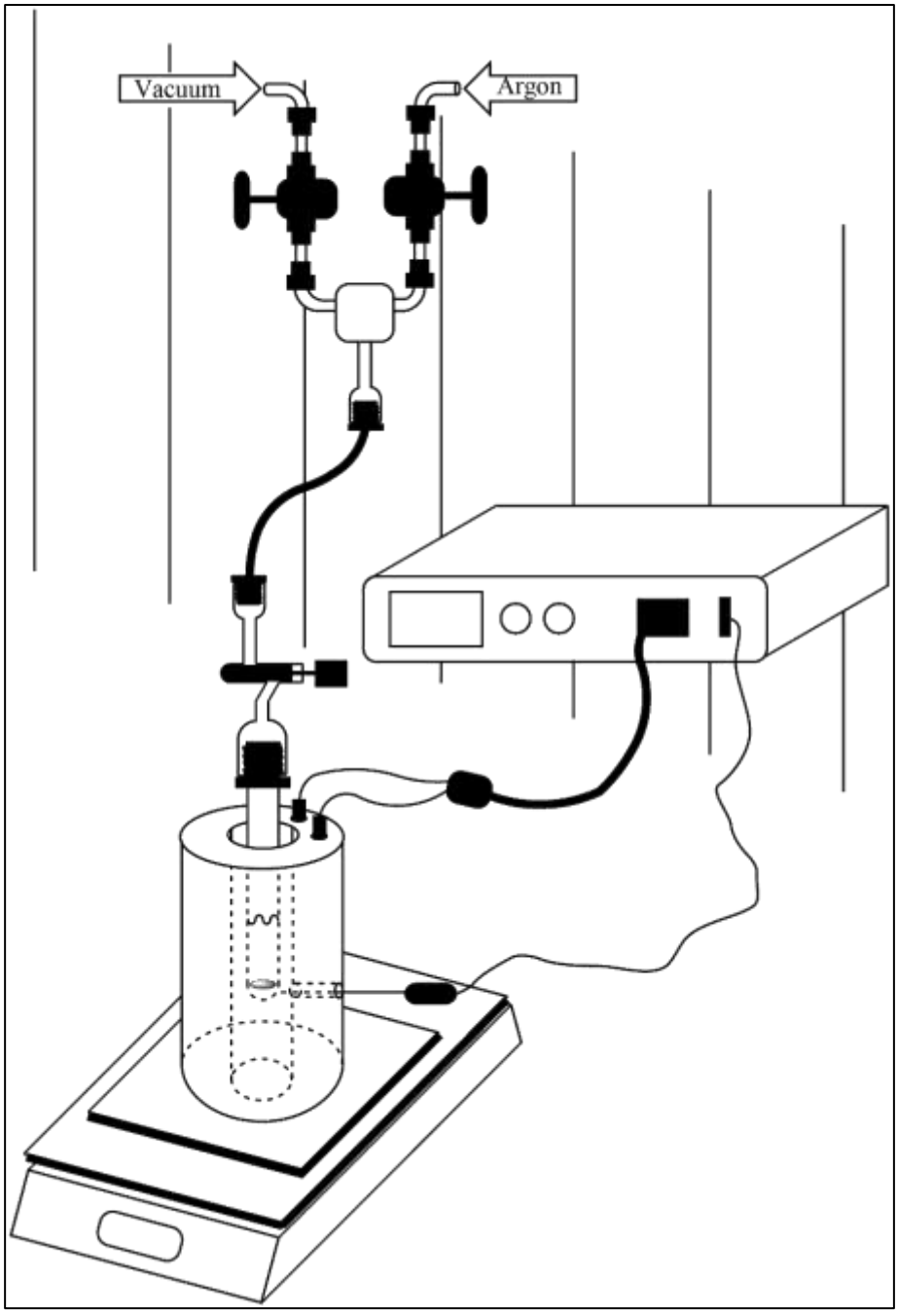

Figure 2.4.2. Schematic depiction of stir bar mixing method in molten chloride salts.

The drawback of this solution mixing methodology is the temperature limit for the magnetic properties of the iron stir bar. At approximately 600ºC the iron will undergo a phase change and lose magnetic properties, as detailed in Chapter 7. Therefore, this methodology cannot be applied to mix solutions above 600ºC. For molten salt solutions that can be mixed in the molten state the stir bar methodology is the most effective method of the three presented. The mixing can be completed directly in the same tube the salt was melted in and does not require a closed system for mixing like the other two methods.

The third methodology for solution mixing, shown in Figure 2.4.3, that was developed during this work utilizes a shaker plate, furnace, and silica tube. The contents of the solution are first melted together under dynamic vacuum in a silica tube as described in sections 2.2 and 2.3. Ensuring that the contents are fused together and degassed. The tube is then flame sealed into an ampule under vacuum. The ampule containing the salt is placed inside a horizontal furnace, in the horizontal position. The furnace is then heated above the melting point of the salt and maintained at that temperature while the shaker plate rotates the furnace containing the salt. This method is the most effective at fusing types of salt as well as forming colloidally stable solutions for experiments that require mixing above 600 ºC.

2.5 Flame Sealing Salt in Silica Ampules

High energy X-Ray or neutron scattering experiments were completed as a part of this work, outlined in more detail in Chapter 4. The methodology to use these analytical techniques to measure molten salts during was developed and are outlined in this and the following sections. Sample containment utilized thin-walled cylindrical capillaries with an internal diameter of 1.0 mm – 2.0 mm and a wall thickness of 10.0 µm. The silica X-ray capillaries used were commercially purchased from Charles-Supper. In a classic air free scattering experiment, the capillary is loaded with the sample material inside of an inert atmosphere glovebox and the opening is sealed using epoxy sealant. Once the sealant sets, the capillary can be removed from the inert atmosphere environment without exposing the contents to atmospheric gases. The epoxy sealing methodology for inert atmosphere samples can be utilized only to a temperature between 250 ºC – 300 ºC. Above this temperature, the epoxy sealant begins to decompose.[83]

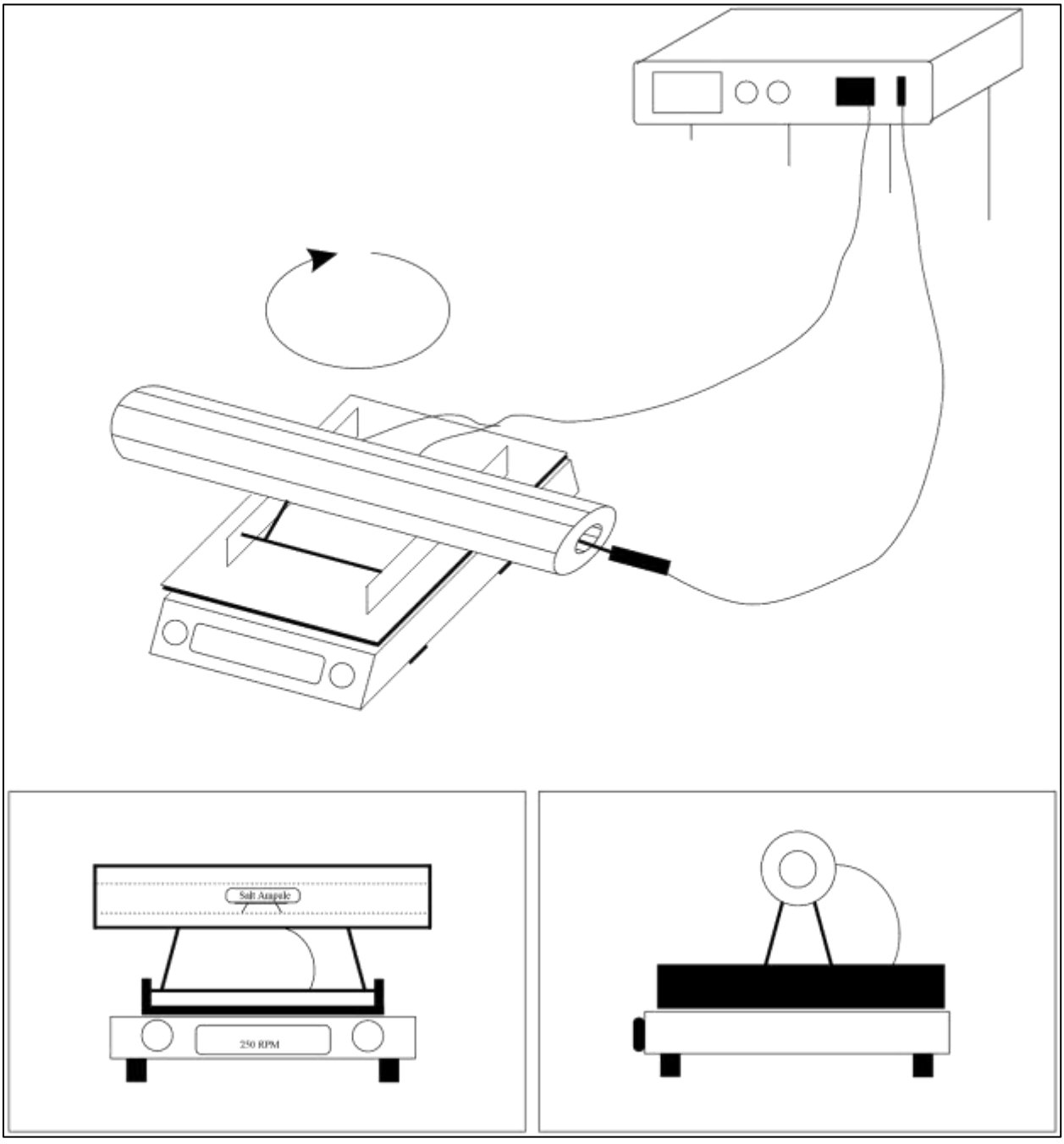

Figure 2.4.3. Schematic depiction of shaker-plate mixing method in molten chloride salts.

Measuring molten chloride salts in the liquid state requires temperatures well above degradation temperature for any epoxide-based adhesive. Therefore, the capillary must be flame sealed so that the sample containment can reach the necessary temperatures above the chloride salt's melting point and not expose the salt to atmospheric gas. The material composition for commercially available X-Ray capillaries is most commonly high purity fused silica or borosilicate type glass. The borosilicate type capillaries begin to lose integrity as the temperature reaches approximately 500^{o}C, borosilicate will soften. Above temperatures of approximately 800^{o}C, borosilicate glass will lose all integrity and liquify. Fused silica will not begin to lose integrity until it reaches a temperature more than 1500^{o}C allowing fused silica to withstand the temperature needed to melt all the alkali and alkali earth chloride salts and most other metal chlorides.[84]

The X-ray capillary options available for purchase vary slightly in wall thickness, length, and internal diameter. The additional tubing added to the commercially purchased capillary provides enough wall thickness for a natural gas/oxygen flame to successfully enclose the sample. This methodology has been attempted using salt loaded into capillaries under an inert atmosphere and vacuum. Attempts to seal chloride salts inside the capillary at atmospheric pressure have a substantially higher likelihood of structural failure while the salt is heated compared to samples sealed under vacuum. The increased chance of containment failure of this type is due to the expansion of gas sealed inside the capillary couple with off-gassing of salt that potentially contains some degree of hydration. Some chloride salt matrices have a relatively high rate of density decrease upon heating, further contributing to the over pressurization of the vessel. Therefore, all flame sealed capillary samples produced as a part of this work were sealed under vacuum.

Commercially purchased X-ray capillaries can be directly flame sealed although this method results in a higher rate of structural failure when heating salt containing sealed X-ray capillary samples. If the wall of the capillary softens exactly across the surface of the cylindrical capillary, then the resulting seal will be thin and easily ruptured. Coupled with the unevenness of the seal due to the heat distribution surrounding the flame, capillaries sealed using the capillary wall will over pressurize and rupture during measurements at an increased frequency.

To mitigate this problem, additions of 5.0 mm I.D. x 7.0 mm O.D. fused silica tubes were sealed to the open end of the capillary. Additions of 4.0 mm I.D. x 6.0 mm O.D were also used with no noticeable change in rate of rupture during experiment between the two sizes. This

additional tubing allowed for a more secure attachment of a vacuum compression fitting enabling achievement of lower pressures of around $1.0x10^{-3}$ Torr inside the capillary during sealing. Additionally, this extra tubing prevented over thinning of capillary wall during sealing. The addition of tubing also increases ease of handling and loading of salt within the glovebox. An X-Ray capillary used during this work with attached extension is shown in Figure 2.5.1.

After salt is added to the capillary, it can be attached to a vacuum fitting in the same way as described in Chapter 2 and the capillary can be removed from the glovebox. The capillary was then transferred outside of the glovebox and attached to a vacuum. A torch utilizing natural gas and oxygen was then used to seal the capillaries under vacuum. This involved first evacuating the capillary until a stable pressure is achieved at room temperature. Then, while the capillary is maintained under dynamic vacuum, the torch is used with negligible oxygen supply to quickly heat the surface of the capillary to remove any gasses that may have adsorbed to the surfaces during sample preparation, shown in Figure 2.5.2. This process was repeated until vacuum pressure remains unchanged with the introduction of heat to the capillary surface. While the capillary remains under dynamic vacuum, the oxygen flow was increased resulting in a flame with a higher temperature. The torch is then used to seal the capillary with the apex of the flame centering approximately 15.0 mm above the solid salt and top of original capillary opening. This allows for enough heat to be imparted on the tubing so that the fused silica will soften, and the salt remains within the capillary ampule. The process of flame sealing X-ray capillaries is demonstrated in Figure 2.5.3.

Great care was taken to ensure there is enough distance between the heat from the flame and the salt. If the salt has an especially low melting point coupled with increased volatility, this can damage the seal. During the sealing, various salts can intercalate in the soft silica matrix. This can change the physical properties of the area where the salt is introduced, creating a weak spot where stress cracks can propagate upon subsequent heating. This can also result in immediate loss of structural integrity as shown in Figure 2.5.4. This rupturing can also occur if salt remains present on the surface of the tube from initially adding it in the glovebox. A representation of the final capillary samples is shown in Figure 2.5.5.

Figure 2.5.1. Pictorial representation of 2.0 mm X-ray capillary purchased from Charles-Supper with added extension loaded with $MgCl_2$.

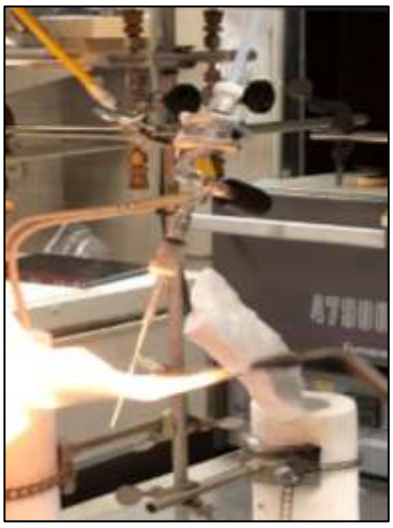

Figure 2.5.2. Pictorial representation of removing surface adsorbed gasses from capillary during initial sealing.

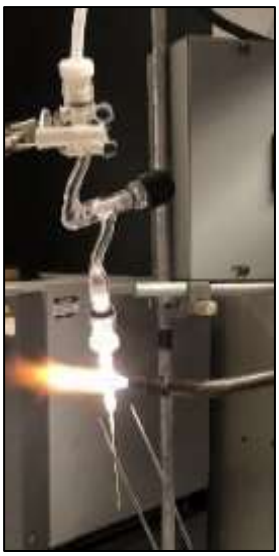

Figure 2.5.3. Pictorial representation of process of sealing chloride salt in quartz capillary ampule.

Figure 2.5.4. Silica capillaries ruptured during flame sealing due to salt intercalation.

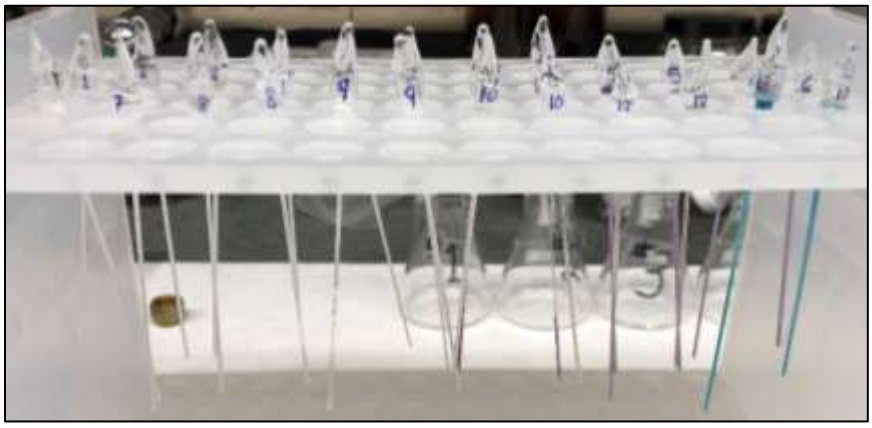

Figure 2.5.5. Various chloride salt samples sealed in silica capillaries.

2.6 Flame Sealing of Larger Diameter Tubes

Due to the air sensitive nature of most of the chloride salts, it can be convenient to seal ampules containing larger volumes for storage or experiment. During this work, commercially purchased high purity fused silica nuclear magnetic resonance (NMR) sample tubes were adapted for neutron scattering experiments. The experiments were conducted at the Nanoscale-Ordered Materials Diffractometer (NOMAD) beam from the spallation neutron source (SNS) located at ORNL. These experiments represent the first time this neutron scattering technique has been applied to uranium chloride containing samples in the molten state utilizing this technique. First, the UCl_3 and UCl_4 materials were chlorinated from a uranyl nitrate starting material, as described in section 3.4. Samples were then sealed flame sealed into a fused silica 5.0 mm NMR tube as shown in Figure 2.6.1.

The NOMAD experiment required the use of a furnace composed of vanadium metal to heat the salt to the molten state. For the furnace to function at a high temperature without risking oxidation of the materials, the entire system must remain under vacuum. The large pressure gradient that would be present between the molten salt inside the ampule and the vacuum outside the ampule caused concern of structural integrity of the sealed fused silica ampule. To mitigate the concerns, each of the samples measured were tested at temperatures above the expected temperatures of the beamline experiments. Liquid salt at that temperature can be seen in Figure 2.6.2.

The containment of all samples tested withstood the pressure differential, temperature gradient, and material interaction. From here the samples were sent to SNS where each was again heated under an external vacuum while neutron scatting measurements were collected. This resulted in the first successful neutron scattering measurements collected by an actinide containing chloride salt at SNS. The results of these experiments are not outlined in the collaboration work presented in Chapter 4 but will be published later pending complementary experimental results. The impact of the methodology development presented in this section is the creation of an accepted procedure for measuring radioactive molten salt solutions. This procedure can be used by future facility users to gain further insight into chemical details of actinide containing molten salts via neutron scattering experiments.

Figure 2.6.1. Pure UCl_3 (top) and 50/50 mole % KCl/UCl_3 (bottom)flame sealed inside fused silica tube for NOMAD scattering experiment.

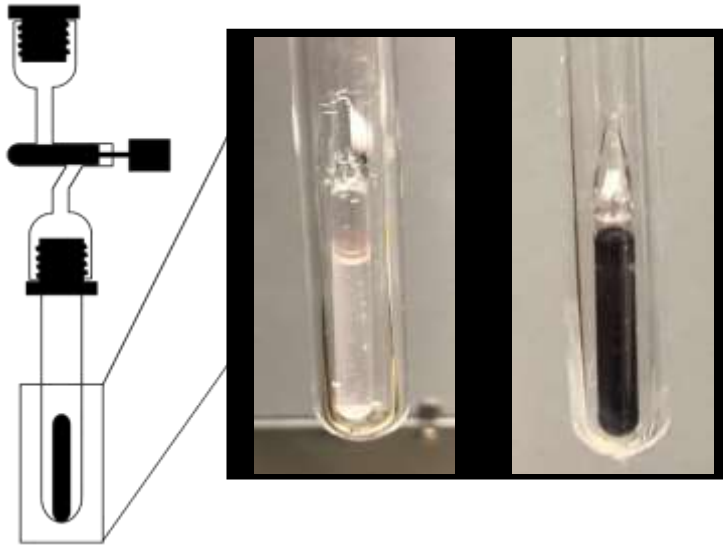

Figure 2.6.2. Solutions of 100% KCl (left) and 100% UCl_4 (right) during sample containment integrity testing.

Chapter 3. Purification

3.1 Introduction

Throughout the course of this work and previous works the need for further purification of metal chloride salts upon receipt from an industrial supplier has been demonstrated. The most prevalent impurity in molten chlorides is the metal oxide species. Most metal chlorides are hygroscopic. Upon heating, most metal centers relevant to molten chloride salt research will undergo partial hydrolysis and release HCl gas as shown in Equation 3.1.1.

$$MgCl_2 \cdot 2H_2O \rightarrow MgOHCl + HCl_{(g)} + H_2O_{(g)} \quad (3.1.1)$$

Upon further temperature increase the magnesium oxide species will form from the decomposition of MgOHCl, evolving HCl gas, as shown in equation 3.1.2.[85, 86]

$$MgOHCl \rightarrow MgO + HCl \quad (3.1.2)$$

The hydrolysis reaction demonstrated in Equations 3.1.1 and 3.1.2 for magnesium occurs in many of the cations of interest for molten salt research. Previous research has shown that MgO has little solubility in molten $MgCl_2$.[87]

Insoluble material present during analytical measurements can skew results and prohibit accurate spectroscopy. In addition to this, it has been shown that oxide species present in chloride melts may catalyze the corrosion process.[49] Substantial effort was devoted to the scaling of the fractional distillation methodology throughout the course of this work. During this work, distillation proved most effective in removing moderate metal oxide impurities from already dehydrated, low oxide salt mixtures. In addition to the oxide impurity, other impurities are present in molten chloride mixtures. The second most prevalent impurity from industrially procured salt is carbon. There are a variety of sources from which these impurities could be traced.

The problem of impurities in commercially provided chloride salts arises from the high likelihood for the salts to absorb water during packaging or in transit from manufacturer. This work has found that chloride salts packaged in plastic are especially susceptible to contamination. Once the salt becomes hydrated, the innermost waters in the hydration sphere will readily undergo hydrolysis upon heating. This will evolve HCl gas and cause the metal center to become a high melting metal oxide with low solubility in most chloride melts.[88-92] In the case of thorium chloride, hydrolysis occurs as shown in Equation 3.1.3.

$$ThCl_4\ (s) + 2\ H_2O\ (l) \rightarrow ThO_2\ (s) + 4\ HCl\ (g) \qquad (3.1.3)$$

Most of the chloride salts are labeled and sold as the anhydrous form, while still containing residual waters of hydration. Trace water presence presents an unacceptable level of contamination during molten salt experiments. These commercial mixtures containing this residual water are unsuitable for high temperature chemistry. The Gibbs Free Energy (ΔG) can be found if enthalpy (ΔH), temperature (T), and free entropy (ΔS) are known.[93] These values are useful for calculating the thermodynamics of reactions as shown in Equation 3.1.4.

$$\Delta G = \Delta H - T\Delta S \qquad (3.1.4)$$

The more negative the value obtained for ΔG in Equation 3.1.4, the more likely the reaction in Equation 3.1.3 is to occur. This also causes the reaction equilibrium constant, K, to become more positive, indicating a higher likelihood for Equation 3.1.3 to proceed. Where K is defined in relation to ΔG as:

$$K = e^{-\Delta G/RT} \qquad (3.1.5)$$

Where R is the ideal gas constant (8.314 J mol^{-1} K^{-1}) and T is temperature in Kelvin. The values of Equation 3.1.4 and Equation 3.1.5 relate to Equation 3.1.3 at various temperatures can be seen in Table 3.1.1.

Table 3.1.1. Values of Gibbs Function (Eq. (3.4)) for the formation, K, (Eq. (3.5)) of ThO_2 shown in Eq. (3.3) calculated using Enthalpy, Entropy, and Heat Capacity (HSC Chemistry 6 v. 6.00) software.

Temperature (°C)	ΔH (kcal/mol)	ΔS (cal/mol*K)	ΔG (kcal/mol)	Log(K)
0.0	42	128	7	-6
100	37	110	-4	2
200	35	105	-15	7
300	32	99	-25	9
400	28	93	-34	11
500	23	85	-43	12
600	18	80	-51	12
700	14	76	-59	13
800	-5	57	-66	13
900	-9	53	-72	13
1000	-14	50	-77	13

Table 3.1.1 demonstrates that hydrated thorium chloride salts are unsuitable to be used in molten chloride experiments without purification. The data shown in Table 3.1.1 can be expanded to most chloride salts. This includes alkali and alkaline chloride salts of interest for application in reactor coolant and the actinide chloride salts to be used as part of liquidous reactor fuel matrix. After conversion to the metal oxide species, a high temperature chlorination is the most useful way to convert the metals back to the chloride salt.[94] To mitigate the effect of hydrolysis on the experimental results, a distillation method has been developed. This method involves the fractional sublimation and condensation of chloride salts based on their high vapor pressure relative to the oxide contaminates that form upon melting.[95-97]

This problem of impurities within the salt matrices is not a new problem and has plagued molten salt chemists since before the operational reactor at ORNL. During the MSRE project with fluoride-based salts during the 1960's, the major impurities present in the salts were carbon, water, oxide species, sulfur species, and transition metal species.[14, 98, 99] To remove the sulfur, water, and subsequent oxide species the fluoride salts were sparged with F_2 or HF gas. To remove the structural (transition) metal impurities, the mixtures were sparged with H_2 gas.[100] The impurities present in the salt melt can have many different adverse effects on the operation and structural containment of the reactor system. Additionally, impurities hinder the ability to understand the fundamental chemical interactions during experimental measurements due to error introduced by the insoluble metal oxide species. To fully understand the underlying mechanisms through which these systems will operate, analysis must be carried out with ultra-high purity salt.

For alkali, alkaline earth, and transition metal halide salts there are numerous previously established techniques for synthesis and purification. Previously established techniques have been used in conjunction with newly established protocol to provide the Energy Frontier Research Center: Molten Salts in Extreme Environments (EFRC:MSEE). The MSEE research center was the central point of collaborative work presented in Chapter 4. The focus of the work completed by MSEE has been exclusive to chloride-based salt mixtures. Therefore, the focus of purification techniques has been centered around methodology related to chloride melts, specifically mixtures using alkali halides and alkaline earth halides. The techniques utilized during this work to form salt mixtures that meet the purity requirements of all experiments are presented in the subsequent sections of this chapter. Section 3.2 reviews filtration of high temperature molten chloride salts

coupled with dehydration under an atmosphere of HCl. Section 3.3 reviews the technique developed to utilize atmospheric air as a source of O_2 gas needed for removal of carbon impurities. Section 3.4 outlines the carbochlorination methodology utilized. The last section, 3.5, details the scaled distillation methodology that currently produces metal chloride salts with the lowest known metal oxide contamination.

3.2 Filtration

Filtration can be used as an initial step to remove oxide contaminants when they are present at concentrations above the solubility limit for that oxide species within the melt. This approach can be utilized to reduce the amount of chlorination gas required to remove the metal oxide contaminant. This approach can also be useful for removal of other solid contaminants. During this work, a fused silica filtering apparatus was first designed to filter ThO_2 from $ThCl_4$. A schematic diagram of the filtering device can be seen in Figure 3.2.1.

The procedure for filtration began with commercially produced 'anhydrous' 99.999% $ThCl_4$ purchased from an industrial supplier. To ensure proper dehydration of any surface adsorbed water contained in the thorium chloride, the salt was purged with gaseous HCl. The HCl gas was generated via the dropwise addition of H_2SO_4 to NaCl, shown in Equation 3.2.1.

$$H_2SO_4\ (l) + 2\ NaCl\ (s) \rightarrow Na_2SO_4\ (s) + 2\ HCl\ (g) \qquad (3.2.1)$$

The generated HCl gas was then passed through Teflon tubing and bubbled through a solution of pure H_2SO_4 to filter out any contaminates generated. From the bubbler, the HCl gas passes to the filtration chamber, and through the quartz filter. From there, the HCl gas passes through another solution of H_2SO_4 and absorbed in water and neutralized using NaOH. The production of HCl gas was maintained at a positive pressure so that a continuous flow of HCl gas over the salt is maintained during dehydration.

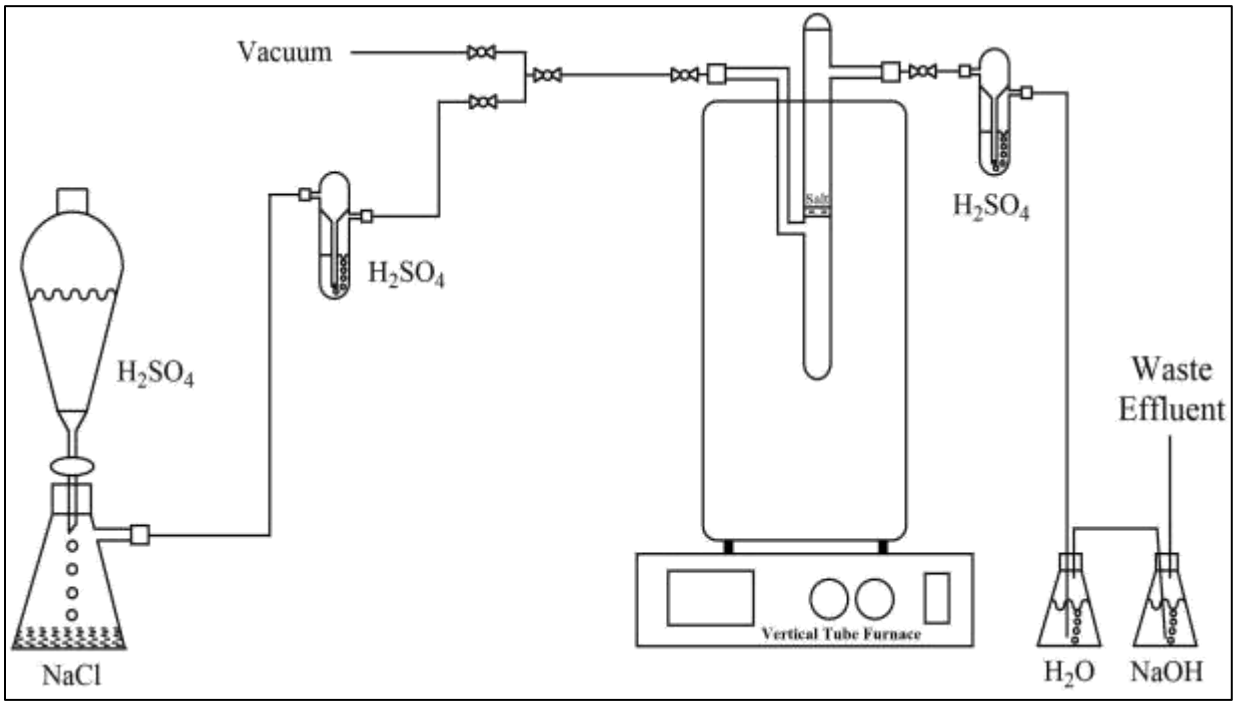

Figure 3.2.1. Schematic diagram of quartz filtering apparatus.

During the continuous flow of HCl gas, the furnace heated the salt above the melting point at a rate of 10°C per minute. After the salt solution is fully liquid, the HCl gas stream is halted by closing the valve connecting the gas production chamber to the filtration apparatus. The valve connected to the outlet of the filtration apparatus is also closed, enclosing the system. Immediately after, the valve connected to the inlet of the filtration chamber is opened, pulling the liquid through the filter to the bottom of the tube. The furnace is then cooled to ambient temperature while remaining under dynamic vacuum. $ThCl_4$ was converted to unusable $ThOCl_2$ or ThO_2. This conversion took place under a dynamic flow of 100% anhydrous HCl gas. After heating 200°C above the melting point (770°C) of $ThCl_4$ there was no phase change, but there was a large evolution of water. The drying apparatus, evolved water, and solid $ThOCl_2$ and ThO_2 can be seen in Figure 3.2.3. While the filtration apparatus was used for 3.0 grams of thorium chloride, the method can be scaled based on need as shown in Figure 3.2.3. This work demonstrated that the as purchased "anhydrous" $ThCl_4$ contains too much water for use without further purification. For a scaled filtration, an inert gas such as argon can be used in place of a chlorinated gaseous species. The experimental setup for the scaled filtration can be seen in Figure 3.2.3 and in the furnace in Figure 3.2.4.

3.3 Oxygenation

Bubbling of oxygen containing gas through the molten chloride solution prior to further purification can remove carbon impurities by reacting in solution to form removable products.[101, 102] This method is a beneficial precursor to fractional distillation as the bubbling of a dry oxygen containing gas through the liquid converts the various trace metal impurities in the salt to the oxide form in addition to removing carbon. In most cases, the vapor pressure of the metal oxide is much lower than the chloride form at equivalent temperature. This allows for much more efficient separation when fractional distillation is being performed, regardless of scale. In addition, the dry gas sparge will remove any adsorbed water which will be removed in the waste effluent as opposed to being pulled into the vacuum pump during distillation. If proper care is taken when the salt is initially melted, then the atmosphere above the salt solution should always remain inert. In metal chloride melts the carbon species will not dissolve nor will it burn. This creates the need for research into a reliable methodology to cost effectively remove carbon impurities present.

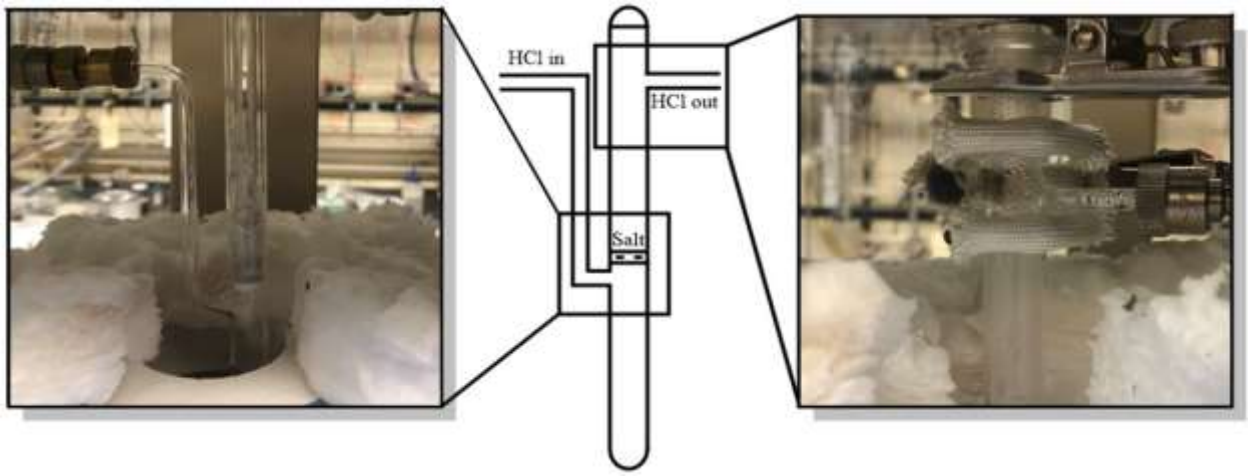

Figure 3.2.2. Schematic diagram of quartz drying apparatus (middle) loaded with 2.5 grams of thorium oxide, and thorium oxychloride (left) and water evolved upon heating to 450^{o}C (Right).

Figure 3.2.3. Scaled silica filtration apparatus containing approximately 100 grams of $MgCl_2$.

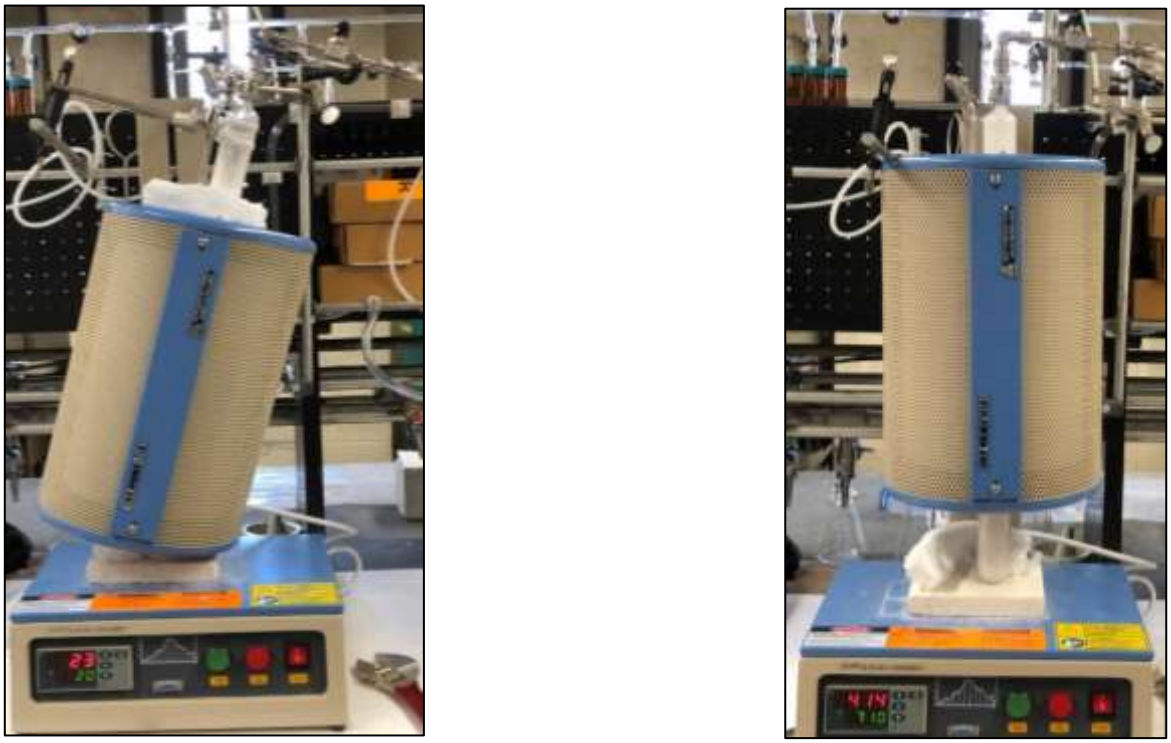

Figure 3.2.4. Scaled filtration apparatus filtering approximately 100 grams of $MgCl_2$.

Removal of carbon species was accomplished in this work through sparging dried air through molten chloride mixtures. This was accomplished by using a flow of pressurized atmospheric air through a series of desiccants and purifiers then bubbled through molten salt. A schematic of this can be seen in Figure 3.3.1. The desiccant system successfully removed H_2O and trace contaminant gases from the inlet stream to the sparging system. Above 600^oC, any carbon species contained in the salt will react and is removed from the system in some type of carbon containing oxide species (CO, CO_2, etcetera). The system continues sparging until all contamination was removed. Once the solution is carbon free, the oxygen flow will begin to convert the bulk salt solution and any dissolved transition metal chloride species to the metal oxide form. This can be advantageous if the salt is fractionally distilled after bubbling oxygen due to the much lower vapor pressure of metal oxides compared to their chloride forms. If the solution is bubbled with oxygen for too long then much of the chloride salt can be converted to the oxide form, disallowing distillation. To convert between the metal oxide form and metal chloride form, chlorination can be carried out.

3.4 Chlorination

Chlorination is an invaluable technique for preparation of chloride salts that will be melted.[103] A chlorination of arbitrary metal center, denoted M, is shown in the Equation 3.4.1.

$$M\text{-}X + Y\text{-}Cl \rightarrow M\text{-}Cl + Y\text{-}X \qquad (3.4.1)$$

Where the metal center, denoted M, can be coordinated to any ligand, denoted X, and reacts with a chlorinating agent denoted Y-Cl. The chlorination can be carried out in the molten state by bubbling a chlorinating gas through the liquid in a similar manner as described with oxygen in section 3.3. The chlorination can also be carried while the metal center is in the solid phase by maintaining a laminar flow of a chlorinating gas over the solid while it is heated. The chlorinating agents used for this work included HCl, CCl_4, and C_3Cl_6. A schematic representation of the process to chlorinate ThO_2 can be seen in Figure 3.4.1.

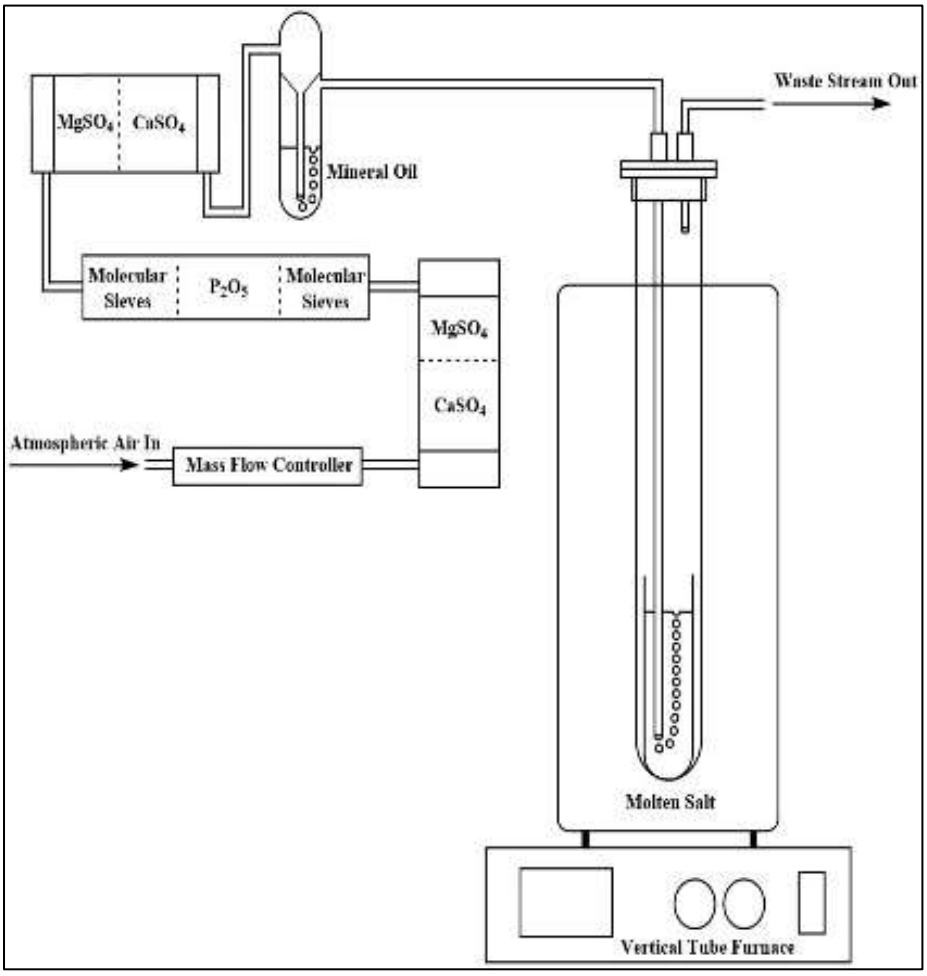

Figure 3.3.1. Schematic representation of atmospheric air drying and purifying process.

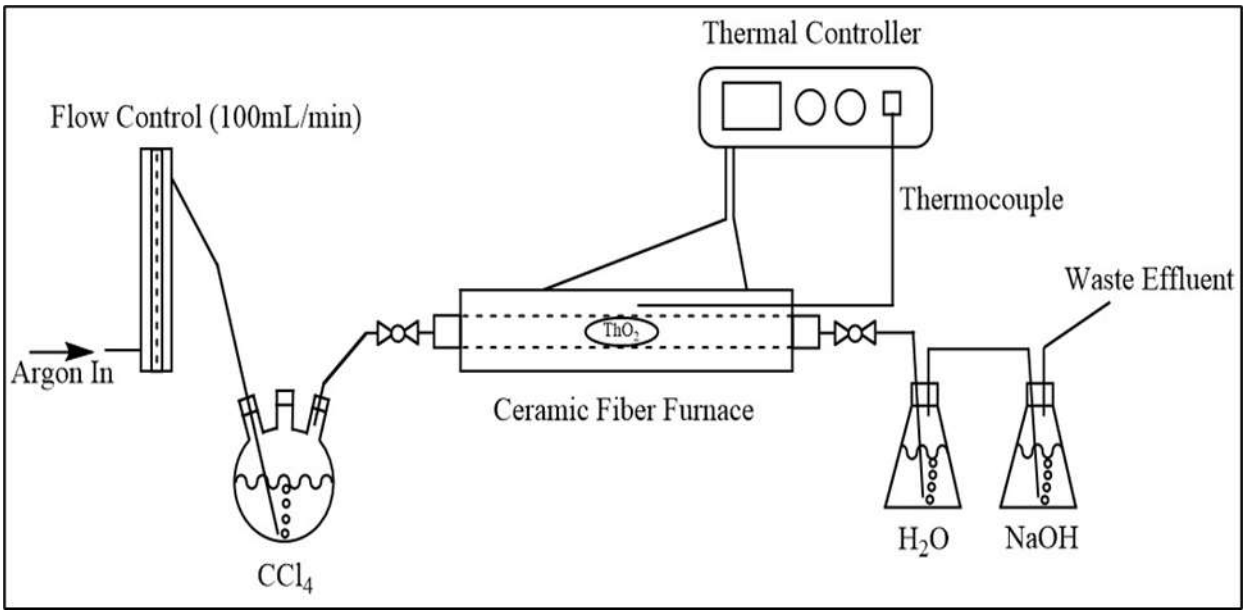

Figure 3.4.1. Schematic representation of chlorination of thorium oxide species using carbon tetrachloride as the chlorinating agent.

3.5 Distillation

The largest challenge to obtaining accurate and reproducible experimental results of molten chloride salts is the maintenance of the purity throughout all experimental preparations. When a salt composition is used as a solvent, the effects of impurities can be amplified massively. For most experiments, even the highest purity available in most cases, 99.999% trace metals grade is not acceptable for the solvent. This is amplified by the potential for water contamination that results in the oxide formation. The previous methodology for distillation of salt involved a two-chamber fused silica apparatus open to vacuum on one side, as shown in Figure 3.5.1.[104] The previous design for the distillation apparatus shown in Figure 3.5.1 resulted in the distillation apparatus being a single use device. As the bottom of the column is heated under dynamic vacuum, the vapor is pulled into the condensation zone at the top of the distillation column. Upon cooling, the salt vapor quickly deposits in cold zone located above the furnace. After enough salt has migrated, the column is taken into an inert atmosphere glovebox and broken so the distilled salt can be recovered. This created the research need for a distillation apparatus with more cost and time effectiveness than the current state of the field.

To meet this research need, the fused silica distillation column was redesigned with the goal of producing more distilled salt per use and creating a reusable apparatus. The design for the scaled version of the distillation column was centered around a three-inch tube furnace as shown in Figure 3.5.2. The column was designed so that the starting material can be loaded into the close ended compartment labeled distillation chamber in Figure 3.8. On the opposing end of the apparatus, there was an opening that was fit with a #18 ace thread vacuum fitting. This allowed the column to be removed from the furnace and evacuated without exposing the salt to atmospheric gases. While the salt was being evacuated the distillation column would be placed inside a tube furnace and heated at a rate of 10^{o}C per minute.

Many of the initial scaled distillation attempts using this design of column worked without any problems. Though some of the distillation attempts resulted in the buildup of solid salt deposition inside the tube that transferred from the hot zone to the cold zone. Figure 3.5.2 is an example of the stopping of distillation due to formation of salt plug. This resulted in the need for a large elevation in temperature at which the distillation must be performed. When the temperature increase was still not enough the plug that formed in the column can cause elevated pressure inside

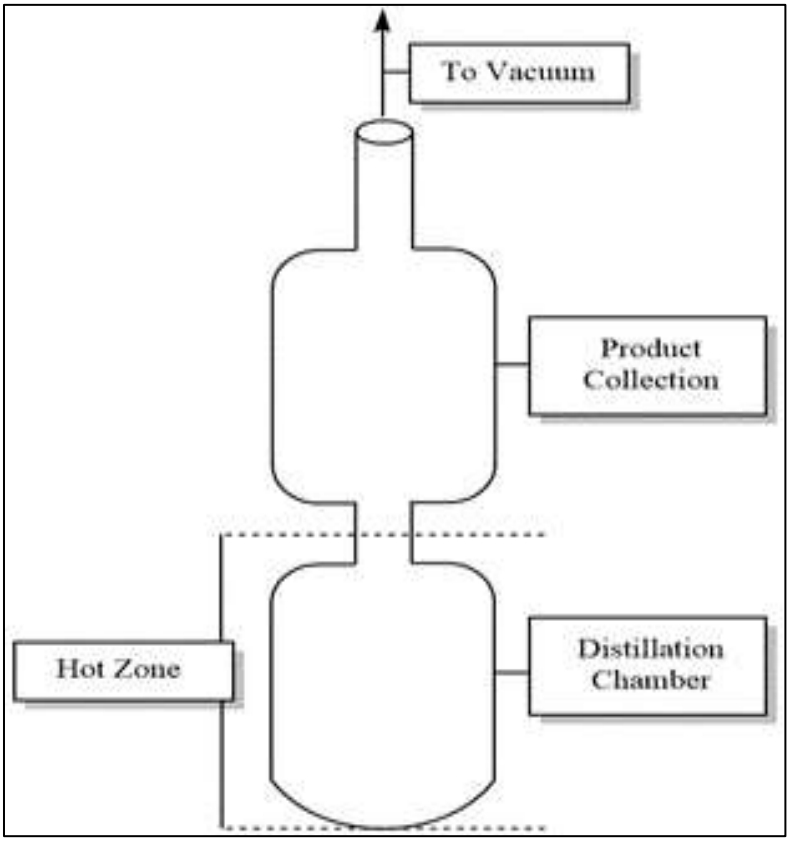

Figure 3.5.1. Schematic representation of previous chloride salt distillation apparatus.

the hot zone. This can lead to rupturing of the column and release of liquid salt into the furnace. In addition, the recovery of salt from the collection chamber was exceedingly difficult in this design. The salt would often crystallize inside the collection chamber and need to be broken into smaller pieces to fit through the collection chamber opening. In most cases this resulted in unrepairable damage to the structural integrity of the column, limiting the number of uses.

The scaled distillation column design was altered by removing the connecting tube between the hot and cold zones. This allowed the temperature required for the materials to be greatly decreased. In addition to the removal of the tube, the collection chamber of the distillation column was also altered. The end of the collection chamber was fitted with an 80 mm O-ring compression connection as shown in Figure 3.5.3. A cap was used that also contained an 80 mm O-ring compression fitting. The new design allowed for the salt to be loaded inside the glove box, end fit with an O-ring, and then sealed with a cap to a vacuum valve connection. The newly designed column loaded with $MgCl_2$ prior to distillation can also be seen in Figure 3.5.3. The implementation of the end cap and removal of hot/cold zone connection tube increased efficiency of distillation substantially. The impact on the field of this methodology development resulted in the ability to provide ultra-purified salt to collaborators at a myriad of different research institutions. This column design can be used many times before structural integrity fails. A visualization of the entire distillation process can be seen in Figure 3.5.4.

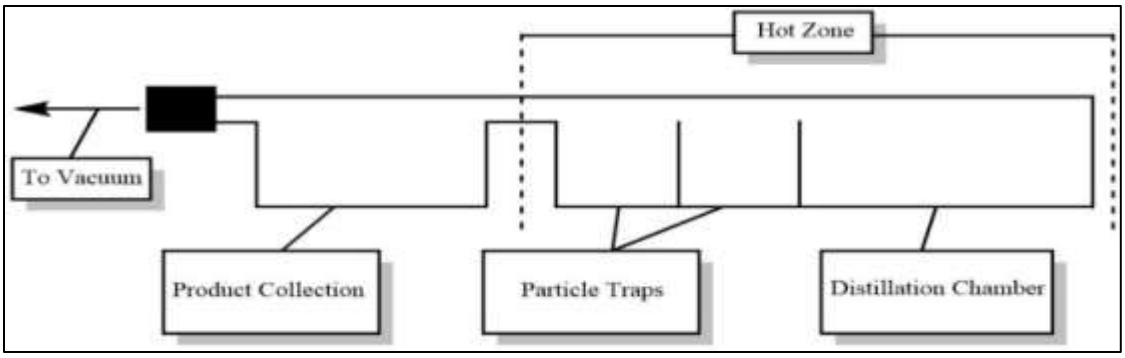

Figure 3.5.2. Schematic drawing of fused silica high temperature distillation column (top). Pictorial representation of initial bulk salt distillation column inside 3” tube furnace (bottom).

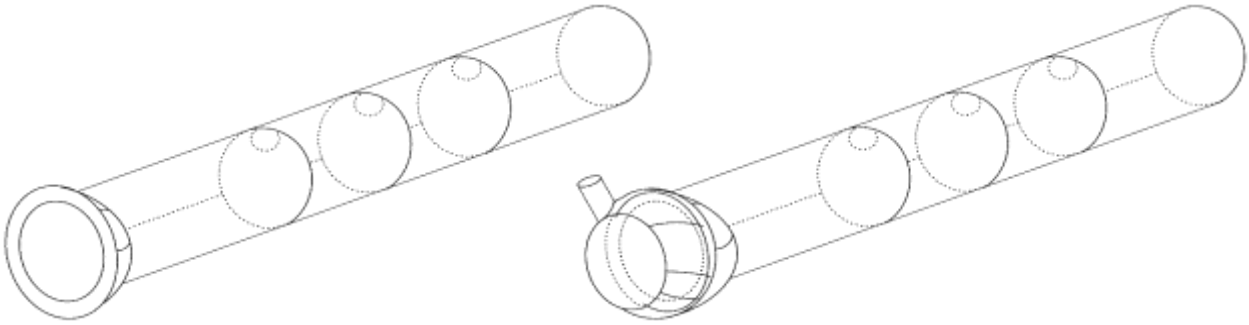

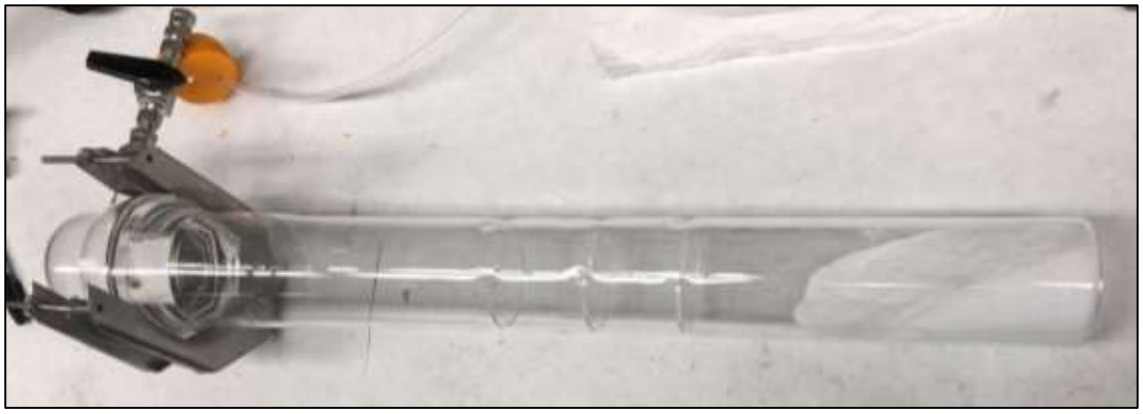

Figure 3.5.3. Schematic representation of scaled distillation column with end cap (top). Pictorial representation of scaled distillation column with commercially purchased $MgCl_2$ prior to distillation (bottom).

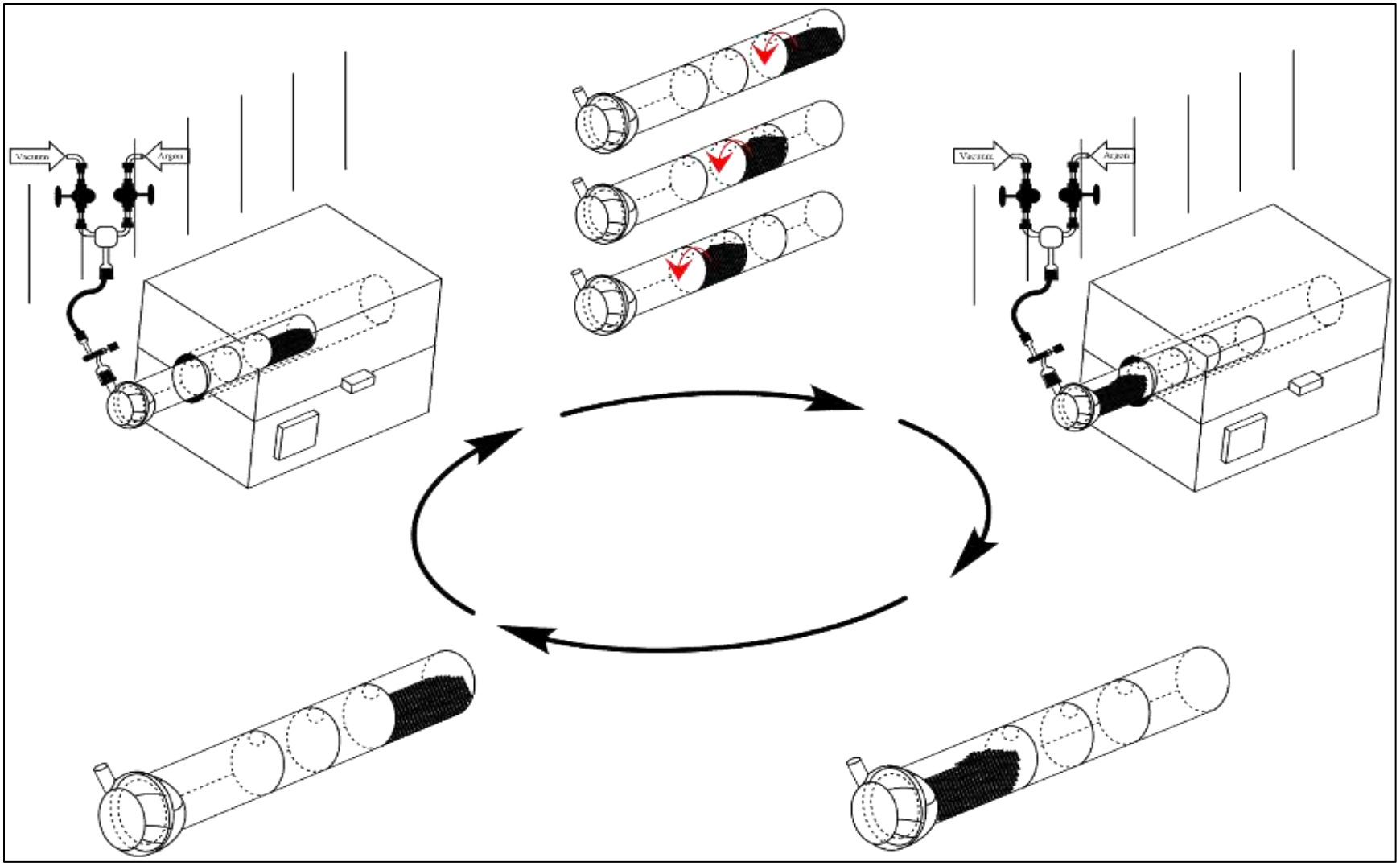

Figure 3.5.4. Schematic drawing of the distillation process.

Chapter 4. Characterization

4.1 Introduction

To properly understand the physical properties of solutions of metal chloride salts the fundamental chemical interactions must be understood. The contents of Chapter 2 and Chapter 3 established the ability to complete most of the experimental handling of salts outside of the inert atmosphere environment of the glovebox. The establishment of experimental capability resulting in supporting many different experimental approaches spanning many institutions. The current advancements in fundamental chemical understanding are related to two very broad categories. The first is the chemical interactions within the molten solvent matrix including interactions between the solution itself and between the solution and solute. The second area of current fundamental chemical research is the interactions between the molten salt solution material in a solid interface.

Chapter 4 is organized into three sections covering a broad range of analytical approaches that have been utilized to probe the chemistry of the molten chloride systems. Metal oxide contamination is a constant problem in chemical experiments related to molten chloride salt systems and applications. Various methodologies during this work and in previous literature have been used for purification by reduction of metal oxide concentrations. To understand the relative effectiveness of the methods and subsequent purification standards, section 4.2 reviews results of MgO reduction in $MgCl_2$ containing salt mixtures using the techniques. In section 4.3, the results of analyzing the materials related to molten metal chloride salt are the central theme. This section focuses on analytical approaches to understand materials that are synthesized within the molten salt or present as an impurity. The following section, 4.4, reviews the various approaches for analyzing the interaction between a molten metal chloride salt and various interfaces. This is accomplished through scattering, microscopy, electrochemistry, and reflectometry. Section 4.5 explores the solution structure and interactions within molten chloride systems. Focusing on spectroscopic approaches to analyze both solvent – solvent interactions in addition to solvent – solute interactions.

The materials reviewed in the subsequent sections of this chapter are the result of many extensive collaborations and would not have been possible without the hard work of many people.

The section titles are very loosely based categories with many instances of subject matter overlap. Due to the scale of the collaboration and availability of the published work, this chapter is to outline the accomplishment and provide a brief synopsis of the work. The support for this dissertation was provided by the Department of Energy through the establishment of the Energy Frontier Research Center: Molten Salts in Extreme Environments in addition to nuclear energy and concentrated solar related projects.

4.2 Oxide Quantification

Due to the difference in the vapor pressure of the potential contaminants present in the recovered distillate, it can be assumed that their contribution to aqueous solution acidity or basicity is negligible. Meaning the only source of contamination is attributed to absorption of water in the time between distillation and subsequent experimentation. Meaning that upon melting, the metal oxide will again form and remain present after the salt has been cooled. If this salt is added to an aqueous solution, then the largest contribution of solution pH originates from the metal oxide acting as a weak base in solution.[105-107] The thorium chloride to thorium oxide example used in Eq. (1) is reversible and applicable to most metal oxides in aqueous solution such that.

$$HCl\ (g) + X(Y)O_{(Y/2)}\ (s) \rightarrow X(Y)Cl_{(Y)}\ (s) + H_2O\ (l) \qquad 4.1.3$$

Where X is the metal center and Y is the oxidation state of the metal center and the equivalent chloride required for the reaction to proceed. Adding the recovered already melted and cooled, purified salt to a standard volume of H_2O and titrating in an equivalent amount of HCl will force Eq. (4) to proceed. This allows for a simple and reliable methodology to quantify the amount of oxide impurities present in most metal chloride systems.[49]

The most utilized methodologies to reduce the metal oxide content in previously hydrated metal chloride salts is through the “carnallite method”, chlorination, and distillation. All three methodologies were used to produce ultra-high purity salts used for experimentation. Data is available in the literature of the measured MgO content utilizing the various purification methods

in $MgCl_2$, therefore, it will be used to compare the methodologies. This work has found that the MgO content in purchased $MgCl_2 \cdot 6H_2O$ can be as high as 43.6% weight when heated above melting point. Previous research found that as purchased anhydrous salt can contain an MgO content ranging from 10,000 – 30,000 $\mu mol \cdot kg^{-1}$ when directly heated above the melting temperature.[49] The same work demonstrated that by carbochlorination through the use of CCl_4, the detected MgO content in the $MgCl_2$ salt matrix is reduced to a concentration of 42 $\mu mol \cdot kg^{-1}$. The carnallite method reduces the MgO content formed upon heating by first reacting $MgCl_2 \cdot 6H_2O$ with KCl or NH_4Cl at elevated temperature to form of the carnallite crystal structure. The intercalation of the chloride ions into the Mg^{2+} octahedra reduces the thermodynamic probability of MgO formation up heating.[108] The carnallite methodology has been shown in previous work to reduce the MgO content in the $MgCl_2$ salt after heating above the melting point to between 4.3% – 0.02 % weight.[109] In the same work, the authors found that commercially purchased $MgCl_2 \cdot 6H_2O$ contained approximately 31% weight MgO content upon direct melting. Chapter 5 of this work demonstrates the same carnallite method can successfully reduce the oxide content in salt through mechanochemical synthesis of the carnallite instead of through heating. The results showed that utilization of the mechanochemical carnallite methodology the MgO present in the KCl – $MgCl_2$ mixture after melting can be reduced to 4.1% – 0.98%. Verification of salt purity through titration has revealed that the distillation process shown in Figure 3.5.4 and used during this work yields the lowest MgO content anhydrous $MgCl_2$. After subsequent remelting and titration, the distilled salt contains MgO content of 1.0 – 50.0 $\mu mol \cdot kg^{-1}$.

4.3 Materials Interactions

Synthesis and purification are important for the accuracy of analytical measurements of solutions of molten chloride salts. The first work published during this dissertation titled, *Enabling Chloride Salts for Thermal Energy Storage: Implications of Salt Purity*, was related to the implications of impurities present in salt mixtures.[49] During this work, a novel titration methodology was developed to quantify the oxygen content present in molten chloride mixtures. The titration was used to examine the efficacy of a variety of chlorinating agents utilized to remove the oxygen impurities from the salt. Corrosion experiments demonstrated that the higher purity salt mixtures were less corrosive than mixtures with higher oxygen content examined through

gravimetric and microscopic analysis. The titration methodology related to oxygen quantification was also used to quantify the oxygen content for the work outlined in Chapter 5. The titration methodology has also been adopted by institutions for a quality assurance measure related to commercially purchased alkali and alkali earth chloride salt. The method has been used regularly for the duration of the experimental work outlined in the document to ensure the highest salt purity for analytical measurements.

Nanoparticle formation was observed in the work titled, *Radiation-Assisted Formation of Metal Nanoparticles in Molten Salts*.[110] Synchrotron X-rays from the National Synchrotron Light Source II at Brookhaven National Laboratory were utilized to provide a source of solvated electrons for reducing Ni^{2+} ions in a molten $ZnCl_2$ solution. The X-rays were also used as a probe for atomic level interaction and the formation of metallic nickel nanoparticles. Analysis of extended X-ray absorption fine structure analysis with near edge structure modeling provided the average size and structure of nanoparticles formed. A mechanism for the formation resulted from the measurements along with the observation that the yield of nanoparticles formed is dependent on the concentration of $NiCl_2$ in the initial sample and the magnitude of the irradiation dose.

In addition to nanoparticles, graphite can also be formed in a molten salt solution via the transformation of amorphous carbon. This graphitization has been demonstrated in the work titled, *Low-Cost Transformation of Biomass-Derived Carbon to High-Performing Nano-Graphite via Low-Temperature Electrochemical Graphitization*.[111] Biomass that originated from coconuts was added to a molten salt mixture at 850^{o}C followed by an electrocatalytic transformation. The resulting product was then analyzed by X-ray diffraction, Raman spectroscopy, scanning electron microscopy, and Transmission electron microscopy. The produced graphite demonstrated high purity, high crystallinity, and a highly graphitized and ordered nanosheet architecture.

4.4 Solution Interface Interactions

The interaction between a solution of metal chloride salts and solid surfaces they are contacted with is not well understood. Interactions were experimentally probed using X-ray nano-tomography and electron microscopy in *Revealing 3D Morphological and Chemical Evolution Mechanisms of Metals in Molten Salt by Multimodal Microscopy*.[112] The focus of this work was

to understand two model systems. The first system contained pure nickel metal and the second system contained a nickel alloyed with 20% chromium. Both systems were submerged in a 50-50 mole percentage mixture of molten KCl:$MgCl_2$ maintained at 800 ^oC. Analysis of the product revealed shell-like structures forming on the surface of the metal in both systems. A bicontinuous porous structure was formed during the corrosion of the nickel chromium alloy sample. The first-time observation of this structure formed through the dealloying process provides a better mechanistic understanding of interactions between salt and potential industrial containment materials.

To gain further insight into this interaction real-time in situ synchrotron three-dimensional X-ray nano-tomography was utilized to further understand the molten salt dealloying process in *Formation of Three-Dimensional Bicontinuous Structures via Molten Salt Dealloying Studied in Real-Time by in situ Synchrotron X-ray Nano-Tomography*.[113] This work determined that the molten salt dealloying process prevents surface oxidation of the metal. This was found by contacting metallic nickel and chromium alloys with KCl:$MgCl_2$ molten salt mixtures analyzing metallic surfaces with X-ray absorption near edge structure spectroscopy. Resulting in this work determining the dealloying mechanism to be primarily diffusion controlled. A mechanism Rayleigh instability leads to ligament pinch-off making isolated bubbles was observed in real time, validating the results of the first Ni/Cr surface metal study.

The corrosive effects of molten salt on metallic nickel and chromium were further studied in molten $ZnCl_2$ in the work *Electrochemical Noise Studies on Localized Corrosion of Ni and Ni-20Cr in Molten $ZnCl_2$*.[114] The electrochemical noise technique was employed to quantify the corrosion of both pure nickel and a nickel alloy containing 20% (mole percent) chromium. Accomplished by measuring transients in current and open-circuit potential from two nominally identical Ni – Ni and Ni20Cr – Ni20Cr electrodes. The results allowed for further insight into the fundamental chemical interactions resulting in the localized corrosion first observed by microscopy.

Electron energy loss spectroscopy can analyze the oxidation state of materials. This technique analyzed metallic substrates corroded by molten salts in *Determining Oxidation States of Transition Metals in Molten Salt Corrosion using Electron Energy Loss Spectroscopy*.[115] This work examined three corrosion environments. These included a nickel alloyed with 20%

chromium exposed to molten $ZnCl_2$, pure nickel exposed to molten $ZnCl_2$, and pure nickel exposed to molten KCl:$MgCl_2$ (68:32 molar ratio). Three different methods of analyzing changes in the $L_{2,3}$ edges were utilized including chemical shift investigation, L_3/L_2 integrated intensity ratios, and multiple linear least squares regression. The L_3/L_2 integrated intensity ratio in conjunction with multiple linear least squares regression successfully identified the presence of Cr^0 and Ni^0 in the metal region and Cr^{3+} and Ni^{2+} in the salt region of the corroded molten salt structure. The developed technique will enable future research to develop the mapping of molten salt corrosion damage using oxidation state maps.

Neutron reflectometry is a powerful analytical measurement tool for helping to understand the interaction between a solid surface and a liquid contacting that surface. In the case of molten chloride salts, in situ neutron reflectometry could substantially increase the mechanistic understanding of corrosion mechanisms. The first experimental apparatus to make this measurement was design, assembled, and utilized in *A High Temperature Cell for Investigating Interfacial Structure on the Molecular Scale in Molten Salt/Alloy Systems*.[116] A 68 – 32 molar ratio mixture of KCl – $MgCl_2$ was measured via in situ neutron reflectometry on a single crystal sapphire substrate at 450 ^oC. The analysis of the measurement results revealed the presence of a 60 Å layer with a scattering length density of 1.72×10^{-6} $Å^{-2}$ between the sapphire substrate and the bulk salt solution. While this layer was most likely formed due to contamination present on the surface of the sapphire substrate, these measurements represent the first successful neutron reflectometry experiment with these materials.

4.5 Solution Structure and Interactions

Atomistic and molecular level behavior of pure salts and salt mixtures must be understood for thermodynamic models to be accurate. To describe the molten $MgCl_2$ and KCl structures X-ray scattering experiments are coupled with molecular dynamics simulations in *Elucidating Ionic Correlations Beyond Simple Charge Alterations in Molten $MgCl_2$-KCl Mixtures*.[117] The results of these analysis demonstrated simple charge alteration in the pure KCl system. When larger percentages of $MgCl_2$ are mixed with KCl, more complex coordination occurs. Intermediate-range ordering and the formation of Cl^- decorated Mg^{2+} chains were observed. The findings of a pre-

peak in the X-ray scattering structure function S(q) measurements indicated molten mixtures of $MgCl_2$ and KCl forming local structures around Mg^{2+} is dependent on the mole fraction of $MgCl_2$ in the solution.

The observations of these interactions demonstrated a non-Debye–Waller temperature behavior in molten $MgCl_2$:KCl mixtures. The results of *Temperature Dependence on Short and Intermediate Range Order in Molten MgCl2 and its Mixture with KCl* addresses this behavior utilizing molecular dynamics and X-ray scattering.[118] Putting the results in context of controversies extending back at least forty years and demonstrating the liquid $MgCl_2$:KCl mixture is characterized by two structural motifs. The first motif is related to molecular chains of alternating positive and negative charges. The second structural motif is responsible for the pre-peak present in the structure function is related to the interaction of Cl^- and Mg^{2+} that do not belong to the same charge alteration chain but are still interacting. This work provided a quantitative explanation for the increase of pre-peak intensity and the relation this peak has to temperature in opposition to other peaks that follow normal Debye – Waller behavior. Additionally demonstrating that temperature affects the peaks related to the two different structural motifs in an opposite manner.

The long-standing concerns and controversies about the local structure of molten $MgCl_2$ is fully resolved in the work titled Unraveling Local Structure of Molten Salts via X-ray Scattering, Raman Spectroscopy, and Ab Initio Molecular Dynamics.[119] This is accomplished through a multimodal approach that involved synchrotron X-ray scattering and Raman spectroscopy experiments coupled with theoretical modeling based on ab initio molecular dynamics utilizing five different density functional theory methods. Simulations agree with experimentally collected data for pure $MgCl_2$, 50/50 molar ratio of $MgCl_2$/KCl, and $ZnCl_2$ in the molten state. The results of this work demonstrate that magnesium is once melted, MgCl2 transitions from octahedral coordination structure to a structure of distorted square pyramidal. The square pyramidal structures are connected to each other by the corners and, to a lesser extent, the edges. The results of $MgCl_2$ contrast those measured for $ZnCl_2$, in which no differences in the tetrahedral coordination are observed upon melting. Resulting in a successful resolution to previous experiments that demonstrated observations that were seen to be contradictory.

After the observation of these ionic clusters present between solvent molecules in molten chloride salt, the next logical angle of exploration is potential clustering of dissolved solutes in

molten chloride solutions. To accomplish this, the behavior of Cr^{3+} dissolved in a solution of molten KCl – $MgCl_2$ is studied in *X-ray Scattering Reveals Ion Clustering of Dilute Chromium Species in Molten Chloride Medium*.[120] The behavior was investigated utilizing integrated synchrotron X-ray scattering experiments in conjunction with *ab initio* molecular dynamics and rater theory concepts. Analysis of results was assisted by a hybrid transition state-Marcus theory model revealing clustering of dilute chromium species, which was unexpected. This clustering led to the formation of octahedral Cr–Cr dimers that persisted in the high-temperature, low Cr^{3+} concentration KCl – $MgCl_2$ solution. These unexpected findings suggest that the charge density of constituent ions is the primary governing factor of dynamical processes in molten salt systems. Due to the low statistical likelihood of dilute species aggregation at high temperatures, the findings of this work challenge many assumptions of ion interactions and ion transport in molten chloride systems.

Macroscopic properties of molten salt mixtures can ultimately be described by the ion dynamics and structure at the atomic level. An approach for understanding these atomic level interactions in monovalent cations was developed in *Structure and Dynamics of the Molten Alkali-Chloride Salts from and X-ray, Simulation and Rate Theory Perspective*.[121] This approach utilizes high-energy X-ray scattering experiments in addition to classical and ab initio molecular dynamic simulations. Resulting in the determination that the anion exchange process occurs on the picosecond timescale and the rate order increases in the order of KCl < NaCl < LiCl. The results found during this work conflict with ion pair dissociation trends in aqueous solutions although is consistent for observations related to conductivity, cation mass, and cation size.

Spectroscopic techniques are again utilized to understand solution structure in *Connections Between the Speciation and Solubility of Ni(II) and Co(II) in Molten $ZnCl_2$*.[122] In this work, X-ray and optical absorption spectroscopy is used with molecular dynamics calculations to investigate the coordination environment of $NiCl_2$ and $CoCl_2$ in a solution of molten $ZnCl_2$. The nickel ion when dissolved in a $ZnCl_2$ matrix prefers tetrahedral coordination as opposed to the octahedral coordination typically found in the solid state. In contrast to this, the Co^{2+} prefers the tetrahedral coordination in totality when dissolved in molten $ZnCl_2$. These results help to explain the fundamental reason behind the reduced solubility of Ni^{2+} compared to Co^{2+} is due to the mixture

of tetracoordinate and pentacoordinate creating bond disorder due to the coordination heterogeneity.

4.6 Conclusion

This chapter demonstrates the vastness of collaboration that is currently ongoing to study the fundamental chemical characteristics of molten chloride salts. While the subject areas related to the materials aspect of the salts covers a broad range in this chapter, it is a small portion of the research work needed. This dissertation re-establishes the framework of methodologies needed to properly prepare and handle chloride salts in both the solid and molten state. These large networks of collaborations were made possible by providing the highest purity salt matrices possible and understanding the physical parameters that govern the sample containment. Working to accelerate the timeline of real-world application of molten chloride salt mixtures in nuclear, concentrated solar, and heat transfer applications based on a fundamental understanding of the underlying chemical processes.

Chapter 5. Mechanochemical Synthesis of High-Purity Anhydrous Binary Alkali and Alkaline Earth Chloride Mixtures

5.1 Publication Statement Chapter 5

A version of this chapter was originally published by Phillip Halstenberg, Dmitry Maltsev, Dianna Nguyen, Ellie Kim, and Sheng Dai in the Journal of Industrial and Engineering Chemistry Research.

Halstenberg, P. W.; Maltsev, D.; Nguyen, D.; Kim, E.; Dai, S., Mechanochemical Synthesis of High-Purity Anhydrous Binary Alkali and Alkaline Earth Chloride Mixtures. *Industrial & Engineering Chemistry Research* **2020,** *59* (45), 19884-19889.

5.2 State of the Field

The study of purification of inorganic compounds has existed since the birth of the field. There exists a myriad of potential pathways through which metal chloride salts can be purified of oxygen impurities, some demonstrated in previous chapters of this document. The technological need in the field is for a scalable, cost-effective route to produce metal chloride salt compositions at the purity levels required for individual applications. The most likely scenario for the industrial scale ultra-purification of metal chloride salts is one that employs different methodologies of purification depending on the level of hydration in the starting material. Previous work has shown that $MgCl_2 \cdot 6H_2O$ dehydration using the carnallite (NH_4Cl) method followed by carbochlorination to remove trace MgO contamination is a viable methodology for production of salt at required purities for some applications.[49] The reduction of MgO content upon initial dehydration is critical to the effectiveness of the carbochlorination.

Previous work has found that if the carnallite crystal structure is not formed prior to melting $MgCl_2 \cdot 6H_2O$ then >30% weight of the original salt will react to form MgO.[109] Previous methodologies have reacted the $MgCl_2 \cdot 6H_2O$ with either KCl or NH_4Cl by mixing them together and heating until the carnallite structure is formed, followed by dehydration and melting. The by-products produced by reacting NH_4Cl increase the total cost of production and reduces efficacy of

methodology on an industrial scale. Additionally, forming the carnallite crystal structure previously required maintaining the mixture at an elevated temperature for an extended period, also potentially increasing the cost of production.

Cost would be lowered if a synthetic route was developed that formed the carnallite crystal structure directly without heating or excess by-products. Therefore, this work advances the state of the field by utilizing mechanochemistry to form the carnallite crystal structure and then dehydrating the salt. Through the mechanochemical carnallite method the cost of hazardous gases produced, and prolonged heating can be replaced with ball milling. The process of forming the carnallite salt directly between $MgCl_2 \cdot 6H_2O$ and KCl also reduces the number of steps required prior to the final carbochlorination route. Application of this methodology in place of the current state of the field will further decrease the cost of production by reducing the amount of CCl_4 needed to reach the purity standard required for application.

5.3 Introduction

The demand for heat transfer fluids with applications in industrial processes, energy production and energy storage are rapidly increasing. For a heat transfer fluid (HTF) to be utilized on a large scale, it must have the characteristics of high heat capacity, low vapor pressure at increased temperature, and tunable thermophysical properties.[123-125] Recently, more attention and research effort has been paid to mixtures composed of alkali and alkaline earth chloride salt mixtures. These mixtures are currently being considered for potentially large roles in the production and storage of energy in both concentrated solar energy plants and Generation IV molten salt nuclear reactors.[126]

The binary salt mixture that has been selected for development and extensive scientific evaluation includes varying ratios of $MgCl_2$ and KCl.[127] The $MgCl_2$:KCl mixture has reasonable fluid flow dynamics, melting point, a large temperature range for the liquid state, and low vapor pressure.[128] In addition to favorable thermophysical characteristics, the chloride salts of magnesium and potassium are relatively cheap, accessible, and abundant. The carnallite ($KMgCl_3 \cdot 6H_2O$) double salt is available as a raw material that can be found naturally at moderately high purities.[129] The largest challenge remaining for industrial scale implementation of $MgCl_2$:KCl

mixtures as HTFs is related to the hygroscopic and oxyphilic nature of the salt. The salt mixtures so readily absorb atmospheric water that they are deliquescent. Once the hydration sphere is formed around $MgCl_2$, it will readily undergo hydrolysis upon temperature increase, forming MgO and evolving HCl gas.[49, 130] It has been shown in the literature that the presence of the oxide within the chloride melt increases corrosion to unsuitable levels for long-term industrial application.[131-134]

Currently, there are only two viable routes for the ultra-purification of $MgCl_2$: both involving a two-step process. The first step in either route is thermal decomposition, which involves the initial formation of a carnallite salt through the reaction of a mixture of $MgCl_2 \cdot 6H_2O$ and NH_4Cl and its subsequent decomposition at high temperature.[135] This first step is then followed by carbochlorination or fractional distillation. Carbochlorination involves the sparging of various types of chlorinated gases such as HCl, Cl_2, $COCl_2$, and CCl_4 through the molten salt mixture.[49] Fractional distillation involves heating the salt to a temperature where there is an increased vapor pressure under dynamic vacuum, causing migration that separates ultra- high purity salt.[118]

Both carbochlorination and distillation are feasible on a lab scale but fall short of the cost-competitive requirements of industrial scale. Each approach requires specialized alloys to mitigate corrosion effects and to operate. In addition, for large-scale distillation or carbochlorination there is a significant volume of waste effluent in the form of various chlorinated gases resulting from impurity removal; further increasing cost. For both distillation and carbochlorination techniques, the individual salt components that form the binary salt mixtures must be manually mixed and fused by melting together to form the desired binary ratios. Fusing the salt components at high temperature is a time and energy intensive process.

This work proposes a third synthetic route for direct synthesis of a high-purity anhydrous $MgCl_2$:KCl mixtures. Accomplished through mechanochemical treatment of KCl and $MgCl_2 \cdot 6H_2O$ components to form the carnallite ($KMgCl_3 \cdot 6H_2O$). This process fuses the binary salt in the hydrated phase, resulting in the direct formation of the binary salt without melting. Once the carnallite phase has been formed during the mechanochemical treatment, the new phase is dehydrated using via a stepwise heating profile.

Mechanochemistry is the use of mechanical energy to drive chemical reactions.[136, 137] Most commonly, mechanochemical syntheses involve the use of a reagents, a milling machine, and

metallic or ceramic milling media. The chemical transformation occurs when the reagent species experience the mechanical force between the milling media during machine operation. This interaction between the milling media and the reagents results in an enormous amount of heat energy imparted from the media to the reagents. This can, in many cases, overcome the reaction energy barrier, propagating new species formation. Mechanochemistry has the potential for replacement of many classical synthetic pathways. The direct synthetic route can substantially reduce the time of reaction, solvent volume, and amounts of byproducts produced. Lastly, industrial milling systems are already commonplace in some industries, thus reducing the difficulty of process scaling from the lab to industrial level.

This technique has recently been the subject of numerous fields of chemical research such as the synthesis of catalysts and highly porous materials.[138, 139] Mechanochemical synthesis can also be used when reactions are discouraged by strongly coordinating solvents. This approach can lead to the formation of high-energy, non-stoichiometric products as was shown in recent work utilizing mechanochemistry to synthesize a neutral allyl complex.[140] The advantage of solvent free synthesis causes mechanochemistry to be an attractive pathway not limited to inorganic and organometallic materials. This approach has also been implemented recently to synthesize biomolecules, polymers, and gaseous materials.[141-143]

Ball milling mechanically forms the carnallite structure under ambient atmospheric conditions. The salt is then dehydrated by heating under an inert laminar gas flow resulting in a decreased total MgO content upon melting. Potentially decreasing production cost for the anhydrous binary salt. This will mitigate the need to employ specialized superalloys during anhydrous salt production and minimize chlorinated waste stream effluents relative to other synthetic and purification methods. Lastly, unlike the distillation and carbochlorination methods, the chemically formed double salt can be maintained in the hydrated phase until the drying procedure is performed.

The dehydration of bischofite ($MgCl_2 \cdot 6H_2O$) at elevated temperatures has been shown to be a stepwise dehydration as shown in Equations 5.5.1 – 5.5.4.[129]

$$MgCl_2 \cdot 6H_2O \rightarrow MgCl_2 \cdot 4H_2O + 2H_2O_{(g)} \quad (117\ ^oC) \qquad (5.5.1)$$

$$MgCl_2 \cdot 4H_2O \rightarrow MgCl_2 \cdot 2H_2O + 2H_2O_{(g)} \quad (185\ ^oC) \qquad (5.5.2)$$

$$MgCl_2 \cdot 2H_2O \rightarrow MgCl_2 \cdot H_2O + H_2O_{(g)} \quad (242\ ^oC) \qquad (5.5.3)$$

$$MgCl_2 \cdot H_2O \rightarrow MgCl_2 + H_2O_{(g)} \quad (304\ ^oC) \qquad (5.5.4)$$

When dehydrating $MgCl_2 \cdot 6H_2O$ through simple heating, partial hydrolysis begins at 185 ^oC as shown in Equation 5.5.5.

$$MgCl_2 \cdot 2H_2O \rightarrow MgOHCl + HCl_{(g)} + H_2O_{(g)} \quad (185\ ^oC) \qquad (5.5.5)$$

After the partial hydrolysis shown in the above equation, the MgOHCl species present in the salt will undergo complete hydrolysis via decomposition of MgOHCl prior to the melting point of $MgCl_2$.[144] As shown in section 4.2, water present in pure $MgCl_2$ salt will result in a large percentage of MgO present in the molten salt. The carnallite double salt follows a similar stepwise dehydration to the pure $MgCl_2$ as shown in Equations 5.5.6 – 5.5.8.

$$KMgCl_3 \cdot 6H_2O \rightarrow KMgCl_3 \cdot 4.2H_2O + 1.8\ H_2O_{(g)} \quad (185\ ^oC) \qquad (5.5.6)$$

$$KMgCl_3 \cdot 4.2H_2O \rightarrow KMgCl_3 \cdot 2H_2O + 2.2\ H_2O_{(g)} \quad (240\ ^oC) \qquad (5.5.7)$$

$$KMgCl_3 \cdot 2H_2O \rightarrow KMg(OH)_{0.14}Cl_{2.86} \cdot 0.15H_2O + 1.85\ H_2O_{(g)} \quad (265\ ^oC) \qquad (5.5.8)$$

According to calculations using Enthalpy, Entropy, and Heat Capacity Software (HSC Chemistry 6 v.6.00), complete hydrolysis occurs at 354 ^{o}C as shown in Equation 5.5.9.

$$MgCl_2 + H_2O \rightarrow MgO + 2HCl_{(g)} \quad (354\ ^{o}C) \qquad (5.5.9)$$

Therefore, the heating profile used for dehydration of the carnallite structure during this work holds the salt at the temperature of each step of dehydration then above the temperature of full hydrolysis of hydrated $MgCl_2$.[145]

5.4 Experimental Section

$MgCl_2 \cdot 6H_2O$ was purchased from Sigma-Aldrich at 99.99% purity. Anhydrous KCl was also purchased from Sigma-Aldrich, trace metals grade, 99.999% purity. All titrations were completed using 18.2 MΩ-cm^{-1} water purified by a Millipore filtration unit.

The mechanochemical synthesis was carried out by first weighing out appropriate amounts of $MgCl_2 \cdot 6H_2O$ and anhydrous KCl for the desired Mg:K molar ratio. The salts were combined in a vial and mixed until visibly uniform particle distribution was obtained. The mixture was then transferred from the vial to a zirconium oxide ball mill container (Retsch PM100 Planetary milling machine). Spherical zirconium oxide milling media (6.35 mm diameter, 10 pieces) was added to the container and the salt was milled at 500 RPM for one hour under atmospheric conditions. The milled salt was then recovered and transferred to a sealed vial, under ambient air, until the drying profile was performed.

After milling, the salt mixture was loaded into a fused silica evaporation dish that was placed in a fused silica tube furnace. All mixtures were heated stepwise following the thermodynamic dehydration steps demonstrated by Emons et. al.[146] Each ramp and dwell in the heating profile corresponded with a loss of approximately two waters from the $MgCl_2$:$KCl \cdot 6H_2O$ hydration sphere. The heating was maintained under a laminar flow of argon gas at 80 mL/min.

Once the heating program had concluded and the sample cooled to room temperature, the tube endcap corresponding with the argon gas inlet was removed from the tube. The dish

containing the salt was pushed into a cavity in the endcap while the argon gas flow was maintained. The endcap was then removed from the tube and a smaller tube with a valve was sealed into the endcap compression fitting, maintaining the sample under an argon atmosphere. The sealed endcap containing the sample was then transferred into an inert atmosphere glovebox. Then samples were then melted by heating to 800 °C under dynamic vacuum for 15 minutes. A summary of the heating profile used for all samples in this work can be seen in Figure 5.4.1.

X-ray diffraction measurements were carried out using a Panalytical Empyrean X-ray diffractometer scanning from 5-90°, 2Θ.

Quantification of oxide content was accomplished via strong acid, weak base titration described by Kurley et al.[49] It is assumed that the basicity contribution of any species other than MgO during the titration is negligible. Therefore, all oxide concentrations presented are assumed a function of MgO magnitude relative to KCl:$MgCl_2$ magnitude.

5.5 Results and Discussion

To evaluate the effect of milling on the structure of the $MgCl_2$-KCl mixtures, the powder X-ray diffraction patterns of the individual components $MgCl_2 \cdot 6H_2O$ and KCl were measured. The resulting diffraction patterns were then compared to the $MgCl_2$-KCl mixture before and after the mechanochemical treatment. The diffraction pattern of the pre-milled KCl-$MgCl_2 \cdot 6H_2O$ mixture seen in Figure 5.5.1 is the combination of the individual components of the mixture. Prior to the mechanochemical treatment of the two salts there is nearly complete overlap of the diffraction patterns of the salt mixture with the individual KCl and $MgCl_2 \cdot 6H_2O$ components.

In contrast to this, the diffraction pattern of the mixture after the milling treatment was also measured. Demonstrating a clear change in the structure of the salt components relative to the pure $MgCl_2$ hexahydrate and KCl. After milling (Figure 5.5.2), the diffraction peaks associated with the individual $MgCl_2 \cdot 6H_2O$ and KCl components are no longer seen. Suggesting the formation of a new phase resembling the octahedral $KMgCl_3 \cdot 6H_2O$ structure associated with the carnallite double salt. The resulting $KMgCl_3 \cdot 6H_2O$ structure formed after mechanochemical treatment of the mixture relative to the individual KCl and $MgCl_2 \cdot 6H_2O$ diffraction patterns can be seen in Figure 5.5.2.

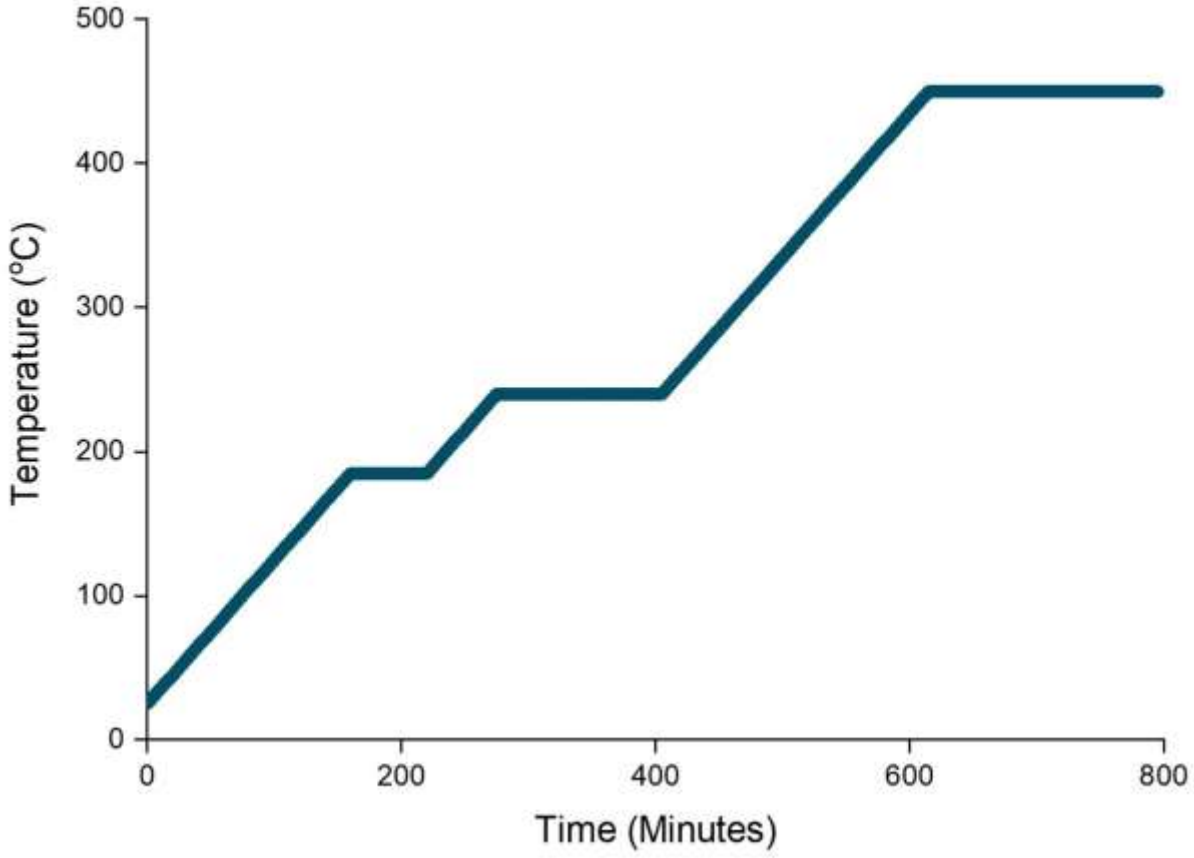

Figure 5.4.1. Heating profile used for $MgCl_2$:$KCl \cdot 6H_2O$ dehydration.

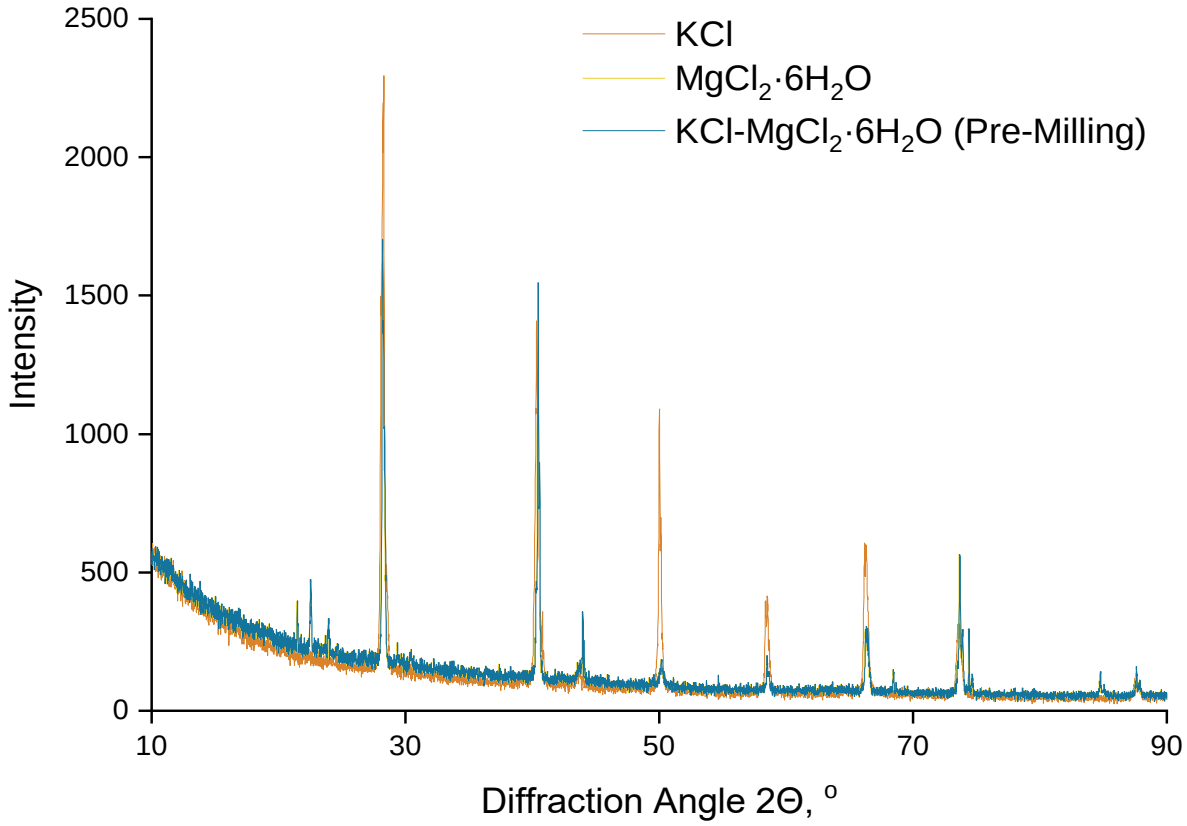

Figure 5.5.1. X-ray diffraction pattern of $MgCl_2 \cdot 6H_2O$, KCl, and $MgCl_2$-KCl mixture (1:1 mol%) before milling treatment.

The new phases that form after the mechanochemical synthesis have peak positions that share the positions of the literature values of the carnallite salt diffraction pattern. However, comparing the diffraction patterns of the mechanochemical synthesis product and the literature diffraction pattern of carnallite reveals discrepancies, as seen in Figure 5.5.3. These can be attributed to the formation of (to varying degrees) hydrated $KMgCl_3$, K_2MgCl_4, and K_3MgCl_7 structures. Phase change was quantitatively confirmed by matching the peaks in the X-ray diffraction results to the literature values for potential species responsible for detected peak. The values for the peaks associated with the crystal structure of KCl, $MgCl_2$, $KMgCl_3$, K_2MgCl_4, and $K_3Mg_2Cl_7$ are labeled in Figure 5.5.3. Each of the species responsible for the diffraction pattern is labeled for the Miller index hkl value of the associated Bravais lattice plane. The identity of species potentially responsible for the measured X-ray diffraction pattern of the post milled products and associated hkl values for 15.4 – 50.4º, 2Θ are shown in in Table 5.5.1 and values for 51.4 – 73.7º, 2Θ are shown in Table 5.5.2. The results demonstrate clear formation of new , $KMgCl_3$, K_2MgCl_4, and $K_3Mg_2Cl_7$ species after the mechanochemical treatment.

After structural change induced via ball milling was confirmed using pXRD, MgO content present after melting the mixture was evaluated via strong acid-weak base titrations. Three samples containing the $MgCl_2 \cdot 6H_2O$ and KCl components were formed containing molar ratios ($MgCl_2$:KCl) of (2:1), (1:1), and (1:2), respectively. Each of these ratios were then evaluated for total MgO content after milling and heating procedures. The results of titrations can be seen in Figure 5.5.4.

Mechanochemical treatment with a subsequent heating profile decreased the oxide content for all ratios of $MgCl_2$:KCl examined during this work. The largest reduction in MgO content, demonstrated in Figure 5.5.5, was present in the 33:66 and 50:50 mole (%) $MgCl_2$:KCl. The $MgCl_2$:KCl ratio dependency experiments demonstrated that the ratio 33:66 (mol%) $MgCl_2$:KCl resulted in the lowest overall oxide content. For this reason, the effect of milling and heating were examined using the 33:66 mol% $MgCl_2$:KCl ratio. It is an important note that the ratio giving the lowest oxide in this work is nearly identical to the eutectic 32:68 (mol%) $MgCl_2$:KCl that is being examined for HTF application.[126] The results of these experiments show a clear correlation between the degree of hydrolysis and milling/heating procedure. The results of which can be seen in Figure 5.5.6.

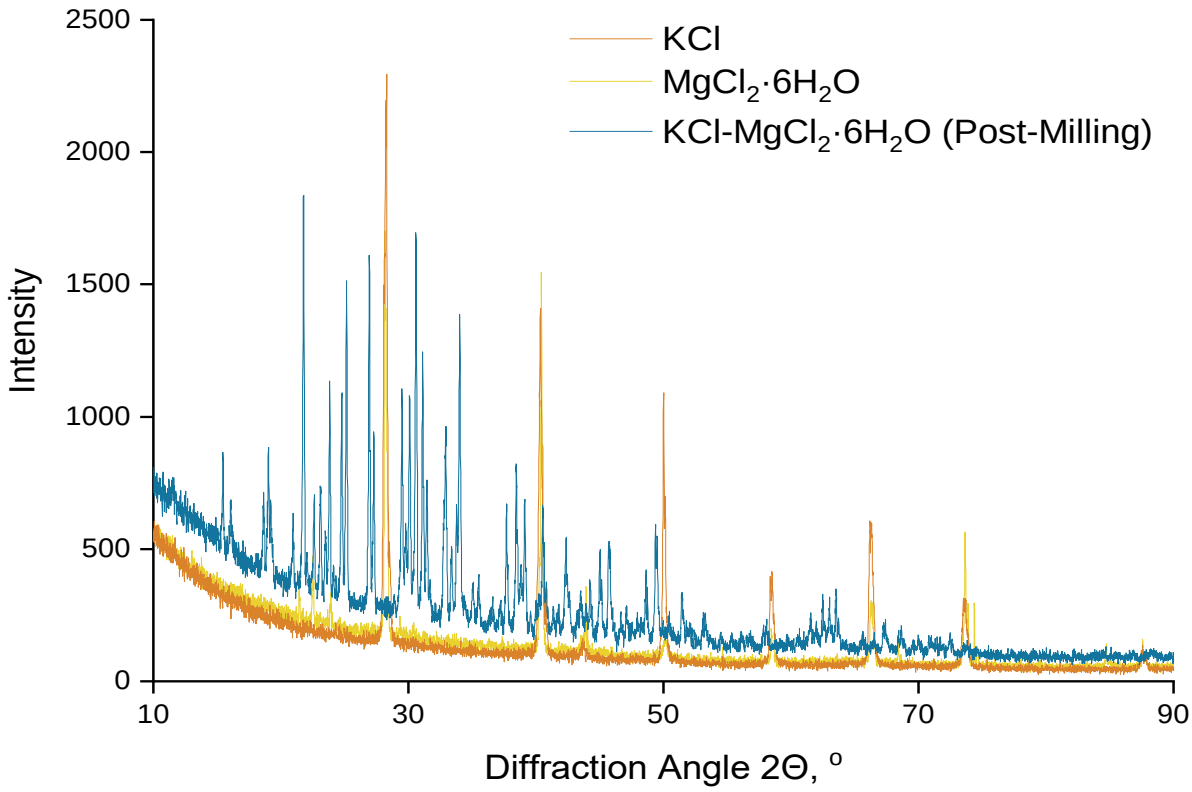

Figure 5.5.2. X-ray diffraction pattern of $MgCl_2 \cdot 6H_2O$, KCl, and $MgCl_2$-$KCl \cdot 6H_2O$ mixture after milling treatment.

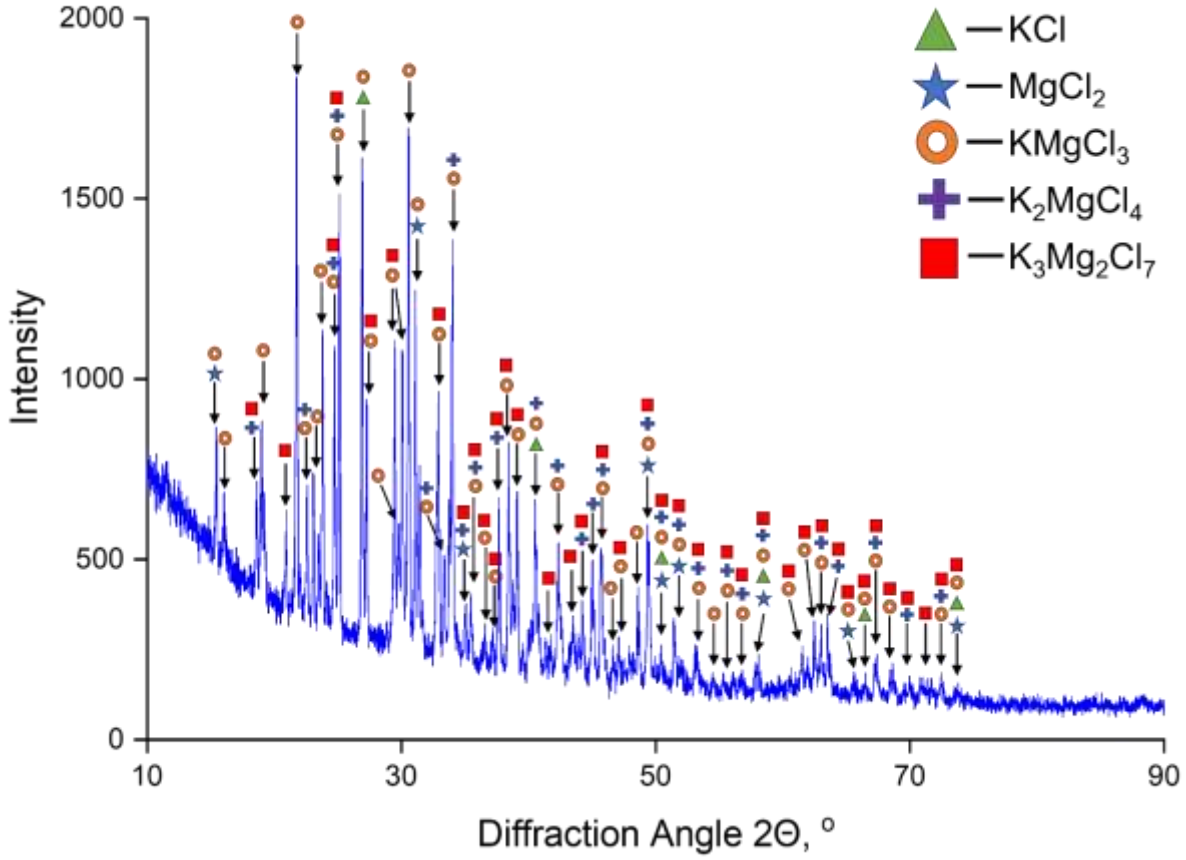

Figure 5.5.3. X-ray diffraction pattern of newly formed $KMgCl_3 \cdot 6H_2O$ phase after ball milling compared to literature carnallite peaks.[147]

Table 5.5.1. Identified peaks in X-ray diffraction measurements (15.4 – 50.4°, 2Θ) for treated 68.0% KCl – 32.0% $MgCl_2$ (mole) and matching literature peaks for KCl, $MgCl_2$, $KMgCl_3$, K_2MgCl_4, and $K_3Mg_2Cl_7$. No matching values are indicated by (-) while matching values are indicated by their associated Miller index lattice planes (hkl).

Salt Matrix	Identified Peak (2Θ, °)	KCl	$MgCl_2$	$KMgCl_3$	K_2MgCl_4	$K_3Mg_2Cl_7$
68.0% KCl – 32.0% $MgCl_2$	15.4	-	003	002	-	-
	16.0	-	-	110	-	-
	18.6	-	-	-	101	101
	19.0	-	-	111	-	-
	20.9	-	-	-	-	006
	21.7	-	-	130	-	-
	22.6	-	-	222	004	-
	24.7	-	-	112	103	105
	25.1	-	-	112	110	110
	26.9	200	-	200	-	-
	27.2	-	-	120	-	008
	29.4	-	-	103	-	114
	29.7	-	-	121	-	-
	30.1	-	-	211	-	107
	30.6	-	-	022	-	-
	31.1	-	1010	202	-	-
	32.9	-	-	113	-	116
	33.4	-	-	122	105	-
	34.0	-	-	212	114	-
	35.0	-	004	-	006	0010
	35.5	-	-	004	200	200
	36.5	-	-	220	-	109
	37.2	-	-	221	-	202
	37.7	-	-	-	202	118
	38.4	-	-	213	-	204
	39.0	-	-	301	-	211
	40.5	220	-	130	211	-
	41.6	-	-	-	-	206
	42.3	-	-	311	006	-
	43.5	-	-	-	-	110
	44.2	-	-	-	107	215
	45.0	-	-	-	213	-
	45.7	-	-	312	008	208
	46.6	-	-	320	-	-
	47.0	-	-	105	-	217
	48.6	-	-	133	-	-
	49.4	-	2-1-10	313	215	1112
	50.4	222	110	322	206	2010

Table 5.5.2. Identified peaks in X-ray diffraction measurements (51.4 – 73.7°, 2Θ) for treated 68.0% KCl – 32.0% $MgCl_2$ (mole) and matching literature peaks for KCl, $MgCl_2$, $KMgCl_3$, K_2MgCl_4, and $K_3Mg_2Cl_7$. No matching values are indicated by (-) while matching values are indicated by their associated Miller index lattice planes (hkl).

Salt Matrix	Identified Peak (2Θ, °)	KCl	$MgCl_2$	$KMgCl_3$	K_2MgCl_4	$K_3Mg_2Cl_7$
68.0% KCl – 32.0% $MgCl_2$	51.4	-	2-1-11	224	220	219
	53.2	-	-	140	118	224
	54.4	-	-	323	-	-
	55.4	-	-	134	109	301
	56.8	-	-	142	224	2012
	58.1	400	2-1-12	412	217	310
	61.5	-	-	242	-	307
	62.4	-	-	333	-	316
	63.0	-	-	216	305	1116
	63.5	-	-	-	226	2210
	65.6	-	10-14	144	-	318
	66.5	420	-	107	110	-
	67.3	-	-	151	219	321
	68.6	-	-	342	-	2212
	70.0	-	-	-	316	325
	71.2	-	-	-	-	1019
	72.5	-	-	127	228	327
	73.7	422	0005	153	-	0020

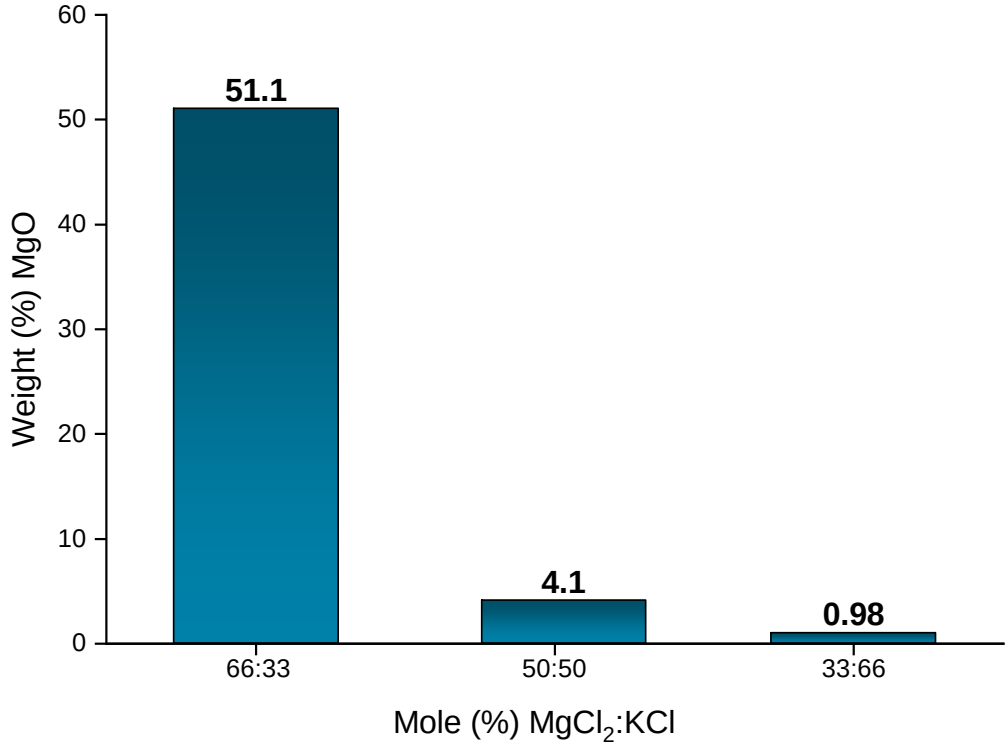

Figure 5.5.4. Weight (%) MgO in salt after mechanochemical treatment of $MgCl_2$:KCl mixtures containing 33%, 50%, and 66% (mol%) $MgCl_2$.

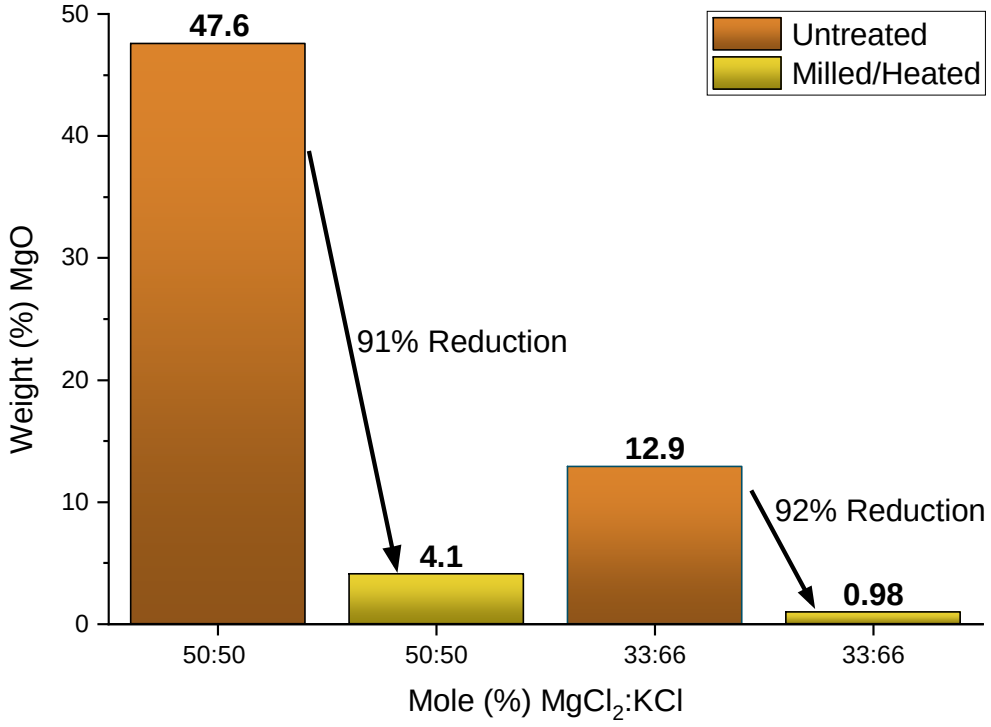

Figure 5.5.5. Weight (%) MgO measured in untreated (blue) and mechano-treated (yellow) $MgCl_2$-:KCl.

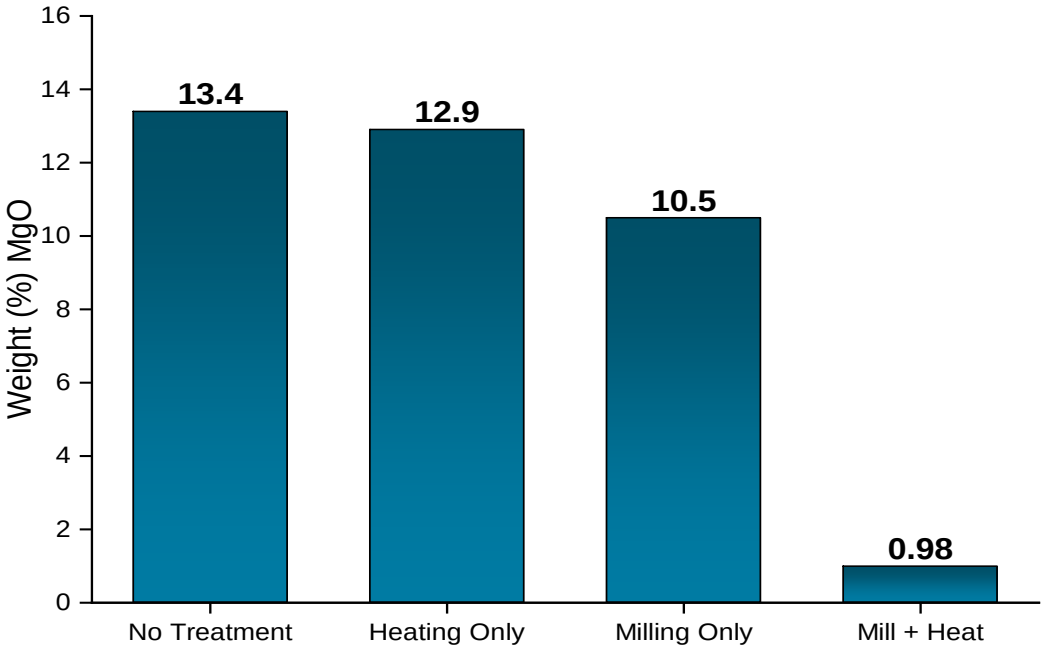

Figure 5.5.6. Weight (%) MgO in $MgCl_2$:KCl after each synthetic step related to the 1:2 $MgCl_2$:KCl ratio.

While the stepwise heating and milling independently reduces the total MgO content of the melt, the reduction is minimal when the two are not combined. When the mechanochemical formation of the double and triple salts is followed by subsequent stepwise heating shown in Figure 5.4.1, the largest reduction in the MgO present after melting is observed.

The reduction of oxide content can be traced to the formation of the carnallite double salt during the synthetic milling step. Mechanochemical treatment causes the intercalation of KCl and $MgCl_2$ coordination spheres and the distortion of the octahedra of KCl and $MgCl_2$. The effective atomic radius ratio once repeating octahedra are formed allows for twelve chlorine atoms to be coordinated around the Mg^{2+} ion. Double the normal coordination of six Cl^- atoms around the regular Mg-Cl octahedra. This causes the Mg-H_2O (0.2045 nm) distance to shorten relative to the usual Mg-O (0.208 nm) distance.[148]

The K-Cl structure present in carnallite is a repeating series of two non-equivalent octahedra. These repeating octahedra share 2/3rd of their faces and therefore have three corners in common. The spaces between the K-Cl octahedra are large enough so that one Mg-H_2O octahedron can fit between them. This results in the coordination around the chlorine atom to also be octahedral, consisting of two potassium and four water molecules, allowing for distribution of the magnesium charge between these octahedra. Each chlorine receives 2/6th positive charge from potassium and 4/6th positive charge from magnesium, all transmitted through the water molecules, balancing the -1 valency of the chlorine atom. A depiction of this can be seen in Figure 5.5.7. The interaction between the coordination spheres of K^+ and Mg^{2+} is believed to allow for the reduction in overall amount of MgO generated during dehydration. Milling allows for the formation of these octahedra without total dehydration that is required to form anhydrous $KMgCl_3$ via fusing through melting together and subsequent recrystallization.

These experiments allow for a new synthetic pathway for mixtures of $MgCl_2$ and KCl relevant for industrial HTF applications. Mechanochemical synthesis has the advantages of being free of harsh solvents needed for carbochlorination and decomposition with species containing NH_3. Scaling the mechanochemical synthesis to the industrial level should present a more attractive alternative for construction and operation of previously studied alkali and alkaline earth chloride synthetic and purification techniques.

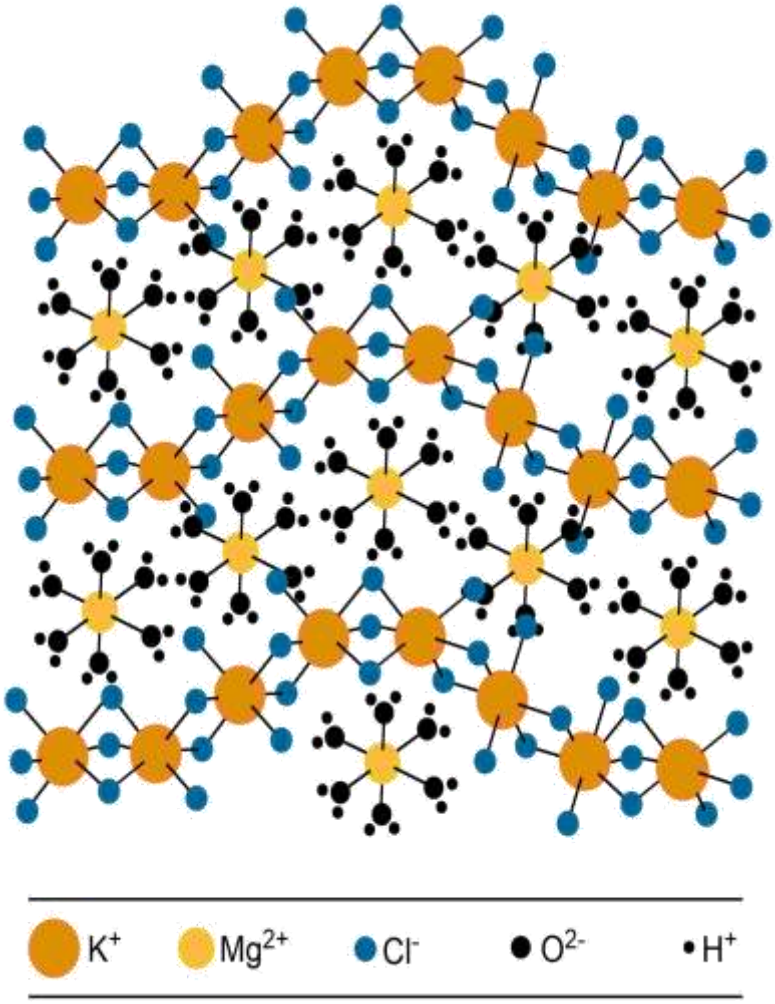

Figure 5.5.7. Depiction of the $KMgCl_3 \cdot 6H_2O$ carnallite structure.[25]

5.6 Impact of Research Progression

In the work that preceded this chapter, a purification route was utilized to create low oxide KCl:$MgCl_2$ mixtures starting from hydrated $MgCl_2$ and KCl.[49] The first step in this process utilizes the carnallite method that was previously described.[149, 150] This was to dehydrate the $MgCl_2$ by heating in the presence of NH_4Cl to produce anhydrous $MgCl_2$ with moderate MgO content. In the second step, the $MgCl_2$ was transferred to a new container and sparged with CCl_4 to further reduce the MgO content in the salt before being transferred to an inert atmosphere glovebox. In the third step, the KCl was dried and chlorinated with CCl_4 before being transferred to an inert atmosphere glovebox. The fourth step consisted of manually mixing the anhydrous $MgCl_2$ and KCl inside of an inert atmosphere glovebox at desired cationic ratios and then melting together under a flow of argon gas. Once fused together, the fifth step further purified the KCl:$MgCl_2$ mixtures via chlorination with a CCl_4 sparge for up to 55 hours to produce the salt mixture containing trace oxide amounts. The research objective of creating a methodology for synthesis of carnallite crystal structure and dehydration of KCl – $MgCl_2 \cdot 6H_2O$ was completed successfully via mechanochemical treatment followed by stepwise dehydration. This advances the field by reducing the number of steps and materials required for purification. Mechanochemically forming the carnallite structure and then heating in a stepwise manner negates the need to dry $MgCl_2$ with NH_4Cl, chlorinate the $MgCl_2$ and KCl separately, and fuse together prior to final purification.

This reduces the number of steps for purification and results in a more energy and atom efficient route to obtain low oxide, fused KCl:$MgCl_2$. Additionally, the mechanochemical synthetic route circumvents the difficulties associated with maintaining the $MgCl_2$ and KCl in a completely anhydrous environment up to the point of fusing and final purification. Maintenance of an inert atmosphere during the mechanochemical synthesis is only required between the heating profile and the final purification step. The streamlining of the purification process via mechanochemistry has the potential to impact the industrial scale costs of producing a low oxide, high purity fused KCl:$MgCl_2$ salt. The carnallite method utilizing NH_4Cl produces hazardous waste streams that will increase the costs of production in addition to the initial materials cost of NH_4Cl. There are also the costs associated with input materials and waste stream of initial CCl_4 purification of individual $MgCl_2$ and KCl. The mechanochemical synthetic route demonstrated in this work will require less materials, fewer facility requirements, and less energy to produce low

oxide KCl:$MgCl_2$ resulting in the potential for industrial production that is more energy efficient, environmentally friendly, and cost-effective than current standards.

5.7 Future Directions

To further optimize the mechanochemical synthetic route described in this work there should be two main areas of focus requiring further study. The first would be the optimization of the mechanochemical synthesis. The correlation between the formation of the carnallite crystal structure and the reduction in thermodynamic likelihood of MgO formation is described previously and in section 5.4 of this document. It is believed that the presence of the Cl^- within the crystal structure of $MgCl_2 \cdot 6H_2O$, originating from the added KCl, reduces the likelihood of MgO formation. The next steps toward optimization would require study of additional materials added during milling to further displace the H_2O coordinated around the Mg^{2+} cation. Studies are needed to determine the impact on MgO formation of mixing alkali chlorides other than KCl with $MgCl_2 \cdot 6H_2O$ and following the procedure outlined in this work. Additionally, adding multiple alkali cations may also reduce the oxide in the final product. For example, in this work KCl was utilized due to previously established interest for the application of the KCl:$MgCl_2$ mixtures as heat transfer fluid due to advantageous thermal properties. If small amounts of less electronegative alkali chloride salts such as RbCl or CsCl can potentially further reduce the thermodynamic potential of hydrolysis upon drying while allowing the salt mixture to retain favorable thermophysical properties. This is one example of a potential improvement; much work can still be done to further optimize the mechanochemical synthesis.

The second area of focus for future research related to this process is the stepwise drying profile under a laminar flow of inert gas. This work demonstrates that utilizing the established thermodynamic data for stepwise drying allows for a controlled dehydration that reduces the formation of the MgO. While the stepwise drying slightly reduces the concentration of MgO present after melting, the major reduction requires intercalation of the KCl into the hydrated $MgCl_2$ crystal lattice. Further research is needed into potential additives that can be included to help suppress hydrolysis during dehydration. This can be carried out by adding material directly to the salt matrix after the ball milling step such as NH_4Cl whose decomposition during the stepwise

heating process would produce HCl. This Cl^- rich environment could help further discourage hydrolysis during dehydration. Similarly, stepwise dehydration can be further optimized by utilizing a laminar flow of chlorinating gas in place of the inert gas used during this work. Creating a more streamlined, easily scalable methodology to produce chloride salts with low oxide content.

5.8 Conclusion

Generation IV reactors based on molten salts are an attractive option to meet our current and future energy requirements. One of the main obstacles in implementation of chloride-based systems is the ability to synthesize salt that meets the purity requirements. This work provides a cost-effective route for synthesis of double and triple $MgCl_2$ – KCl containing salts. These salts can be formed while still hydrated via mechanochemical treatment to form the carnallite crystal structure. This conclusion was made based on the results of X-ray diffraction measurements confirming the presence of KCl, $MgCl_2$, $KMgCl_3$, K_2MgCl_4, and $K_3Mg_2Cl_7$ in the post milled sample. The X-ray diffraction results confirm completion of the research objective of forming the carnallite crystal structure from KCl and $MgCl_2 \cdot 6H_2O$ starting materials via mechanochemistry. The mechanochemical treatment followed by subsequent stepwise heating and melting can directly produce low-oxide containing $MgCl_2$ – KCl eutectic, relevant to both molten salt reactors and concentrated solar power plants. The mechanochemical synthetic route has advantages over all current methodologies to produce anhydrous, high purity alkali and alkaline earth chloride salt.

Chapter 6. Salt Glass Machine

6.1 State of the Field

A recurring theme of the studies summarized in Chapter 4 is that measurements relating to the properties of the salt while in a molten state required the measurements to be made while the salt is liquid. While this provides direct insight into the solution structure and properties it substantially increases experimental difficulty, time, and cost. There is currently no possibility to conduct experiments related to the details of the liquid state of chloride salts while the material is solid. This is due to the crystallization of the salt upon cooling, rearranging to the crystal structure instead of the amorphous, liquid state of interest.

In a similar manner, the crystallization of water disallows study of the amorphous structure in the solid state and can damage biological samples due to crystal formation.[151] It has been shown that water can be supercooled and retain chemical structure of the amorphous, liquid, state.[152] The interesting properties of the solid amorphous water and implications of potential experiments will impact the physical chemistry understanding of the chemical interactions in liquid water.[153] There are two main experimental routes to create amorphous water. The first is condensing water molecules from the gaseous state in such a way that prevents crystallization.[154] The second route is supercooling, or vitrification, of liquid water molecules at a rate of $> 10^6$ $K^{-1}s^{-1}$ that freezes the molecules in the amorphous state before crystallization can occur.[155] While there are other additional pathways in the literature, vitrification is the most common.[156]

Metal chloride salts are difficult to vitrify and current commercially available machines for bulk metallic glass are not compatible with or capable of forming metal chloride glasses as detailed in sections 1.3.2, 1.4.2, and 6.2. Literature is very limited related to the vitrification of metal chloride salts resulting in little option to study the amorphous state at room temperature. Therefore, the work of this chapter advances the state of the field by creating a vitrification apparatus compatible with the requirements of metal chloride salts. The ability to study the amorphous state of chloride salts at room temperature has the potential to revolutionize the experimental approach to molten salt solution structure experiments. Reducing the difficulty, time, and costs associated

with high-temperature, molten state experiments will result in streamlining the property screening process and shortening the research time required for application.

6.2 Introduction

A glass is a material that is at a temperature where the material is solid while still retaining a structure like the liquid. This means that the material retains amorphous character and lacks crystallinity.[157] Glass is usually made by cooling a liquid substance from a very high temperature and depends on preventing crystallization during cooling.[158] Glass formation is related to the viscosity temperature relation of the substance in the liquid state. Therefore, the likelihood that a material forms a glass in the solid state depends on controlling the rate of cooling to in turn control the viscosity. A higher viscosity indicates that the material would have an increased difficulty rearranging atoms in response to mechanical stress. Indeed, a higher viscosity in the liquid state would indicate a higher likelihood the material will form glass. This relationship can be described by the Vogel-Tammann-Fulcher equation.[159] Previous work has found that rates of nucleation and crystal growth peak at a certain temperature and decrease at lower temperatures. In addition, nucleation occurs more rapidly than crystal growth at low temperatures. The physical manifestation of this is that a fast enough colling rate can completely prevent crystal growth.[160] This is because at high temperature when crystal growth is rapid there are few nuclei and at lower temperature when nucleation growth occurs there is a negligible rate of crystal growth.[161]

The ability to create metal chloride glasses would streamline many of the current analytical techniques. Due to the relatively low viscosity of molten metal chloride salts, it is difficult to adequately prevent crystallization. Most glasses are more viscous than molten salts and rapidly increase in viscosity as the temperature falls.[159] This same physical characteristic is true for many metal chloride systems such as the KCl:$MgCl_2$ system examined during this work. The viscosities of KCl, $MgCl_2$, and 32% KCl – 62% $MgCl_2$ at temperatures near the melting point is shown in Table 6.2.1, demonstrating the importance of fine temperature control during experiment. Previous research into vitrifying metal chloride salts focused on eutectic mixtures for two reasons. The first is the eutectic point remains liquid at a lower temperature allowing for less excess thermal energy during cooling. The second reason the eutectic point is chosen is because it requires the most atomic rearrangement within the melt to form the crystalline structure.[162]

Table 6.2.1. Viscosity (η) of KCl, $MgCl_2$, and eutectic KCl:$MgCl_2$ mixture in units of poise.[163]

Temperature (K)	KCl	$MgCl_2$	32% $MgCl_2$:68% KCl
940	-	-	1.71
960	-	-	1.65
980	-	-	1.58
1000	-	2.14	1.52
1020	-	2.04	1.45
1040	-	1.94	1.37
1060	-	1.86	1.29
1080	0.996	1.78	-
1100	0.950	1.70	-
1120	0.907	1.63	-
1140	0.868	1.57	-
1160	0.832	-	-

Molten salt mixtures containing $MgCl_2$ – KCl and $ZnCl_2$ – KCl have recently started to receive interest as potential candidates for next generation heat transfer fluids. A large portion of the difficulty in performing analytical measurements to elucidate atomic level structure of chloride salts in the amorphous state is the temperatures needed to maintain a molten state. Elevated temperatures cause increased signal noise in many spectroscopic measurement techniques. The reactivity of the liquid salt at high temperatures increases the difficulty of sample containment and the likelihood of the salt will react with the container material. The large temperature and types of materials needed also results in a substantially higher experiment cost, prohibitively so in some cases. If chloride salt mixtures can be cooled from the molten state fast enough, then amorphous chloride salt glass can be performed. Chloride salts studied at room temperature while in the amorphous state would greatly expedite progress.

The first attempt of producing amorphous material during this work utilized pouring the molten salt mixture directly into a bath of LN2. While these experiments were very exciting, they did not produce a product that contained differences in the x-ray diffraction patterns compared to untreated salt. After this, metallic ingots were cooled to LN2 temperatures and then the molten salt was added dropwise to the LN2 cooled metal. The product formed using the metallic ingot was also measured by x-ray diffraction and showed no change compared to the untreated salt. In these methods, the molten salt was heated inside of a fused silica test tube above the melting point and then poured directly or drawn inside a quartz tube and added dropwise to the cooling media. A conclusion was drawn that adding salt in ambient conditions creates an environment where a large amount of thermal energy is slowly lost from the salt while falling through atmospheric air. Additionally, during the direct addition of salt to LN2, vigorous boiling occurred and could have reduced the rate of cooling of the salt. For the cooled metal ingot, the rate of cooling would depend on the distance from metal to the top of the droplet. The more forced the droplet strikes the metal surface with a thinner film of solid salt will result and the distance between the metallic surface and top of salt will be reduced. The only way to increase the force of the droplet striking the metallic surface was increasing the distance between cooling media and drop height. This introduces more cooling during the time the droplet is falling. While it is possible a thin film of amorphous material was produced on the bottom of the salt droplet in the latter methodology, it was negligible to the bulk material. Both experimental methods also had the

problem of hydration of the salt product since the experiments were carried out in ambient atmospheric conditions.

To fill that gap and overcome the problems of the initial experiments, a fast quench machine was designed and tested during this work, referred to henceforth as the glass machine. The glass machine was designed to cool liquid salt at the fastest rate possible. This would be accomplished by heating droplets of chloride salts through a furnace while in free-fall until reaching liquid nitrogen filled rollers. The concept behind this design is to create a system where thermal energy from the cooling element is transferred to the molten salt as fast as possible. An alumina tube was utilized as the heating element inside the furnace and extends from the top to two centimeters away from the rollers. This design ensures the salt droplet remains at elevated temperature and in the molten state until it reaches the rollers. This work represents the first time a design utilizing two, LN2 cooled, inward rotating metallic rollers have been experimentally examined for the formation of glass and amorphous materials.

6.3 Experimental Methods

The design of the salt glass machine can be seen in Figures 6.3.1 – 6.3.4 . The attachments in the front of the machine connect Teflon bushings to stainless steel attachment arms where liquid nitrogen enters the roller system. The stainless-steel tubing traverses the glass machine where they are connected in the back via Teflon tubing. This system allows liquid nitrogen to be pumped in one roller and out through the adjacent roller. In the middle of each stainless-steel attachment arm is a copper section with larger diameter than the steel located directly under the furnace opening. In the back of the machine, both stainless steel arms are also connected to a motor that powers rotation inward. This Design allows for a piece of solid chloride salt measuring 1.0 mm – 5.0 mm in diameter to be dropped through the furnace, where it is heated to a temperature above the melting point and liquifies. Immediately after falling through the hot zone of the furnace, the droplet of molten salt strikes the copper rollers cooled to liquid nitrogen temperatures. The droplet instantly solidifies and is caught in the removable tray below. A cover for the glass machine was added as a safety precaution against any splattering of molten salt that would occur during the experiment. The cover also allowed for an inert environment to be introduced to the glass formation chamber and the furnace tube.

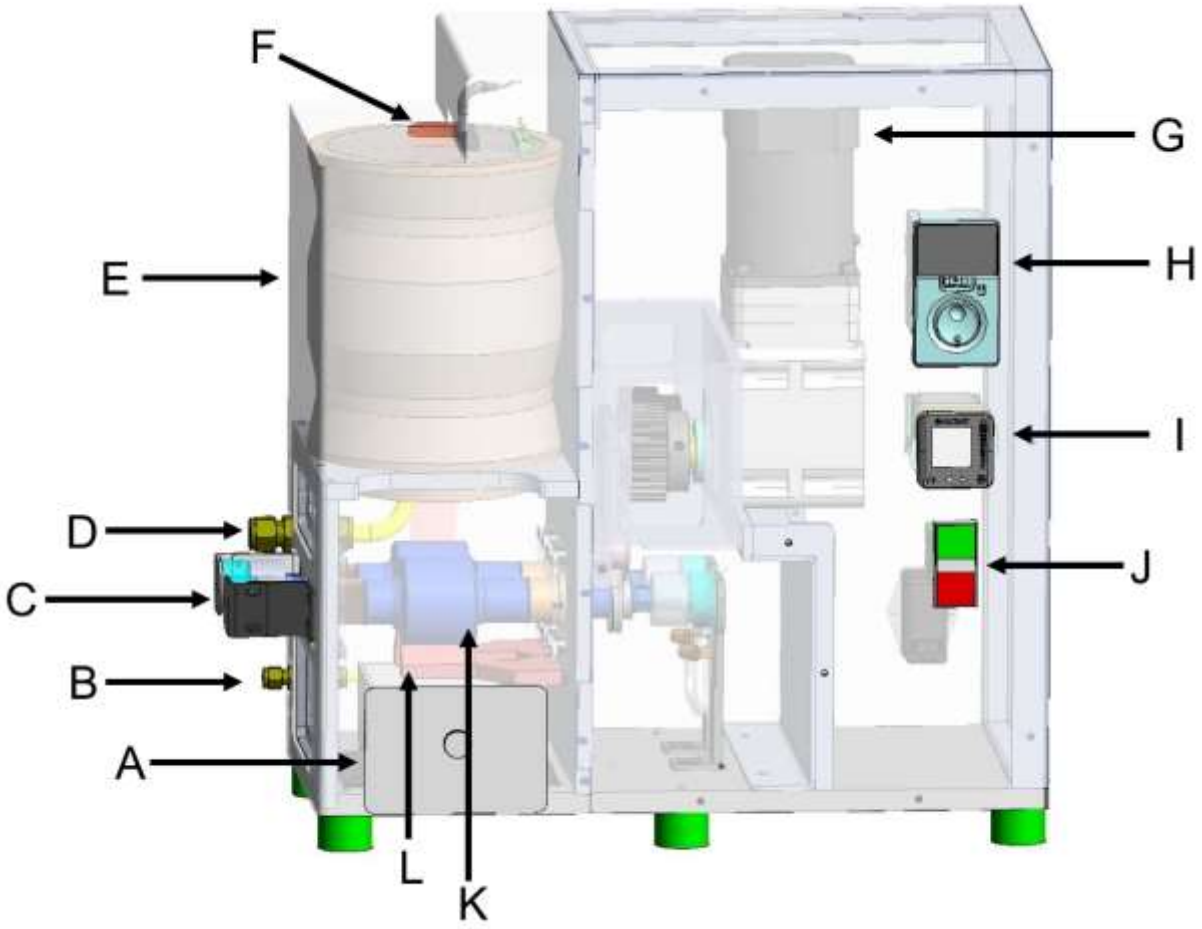

Figure 6.3.1. Schematic diagram of salt glass machine where A is the product collection tray, B is the inert gas inlet, C is the liquid nitrogen connections, D is the inert gas outlet, E is the furnace, F is the drop tube, G is the roller motor, H is motor controller, I is the thermal controller, J is the start/stop button, K is the salt contacting portion of rollers, and L are the roller blades.

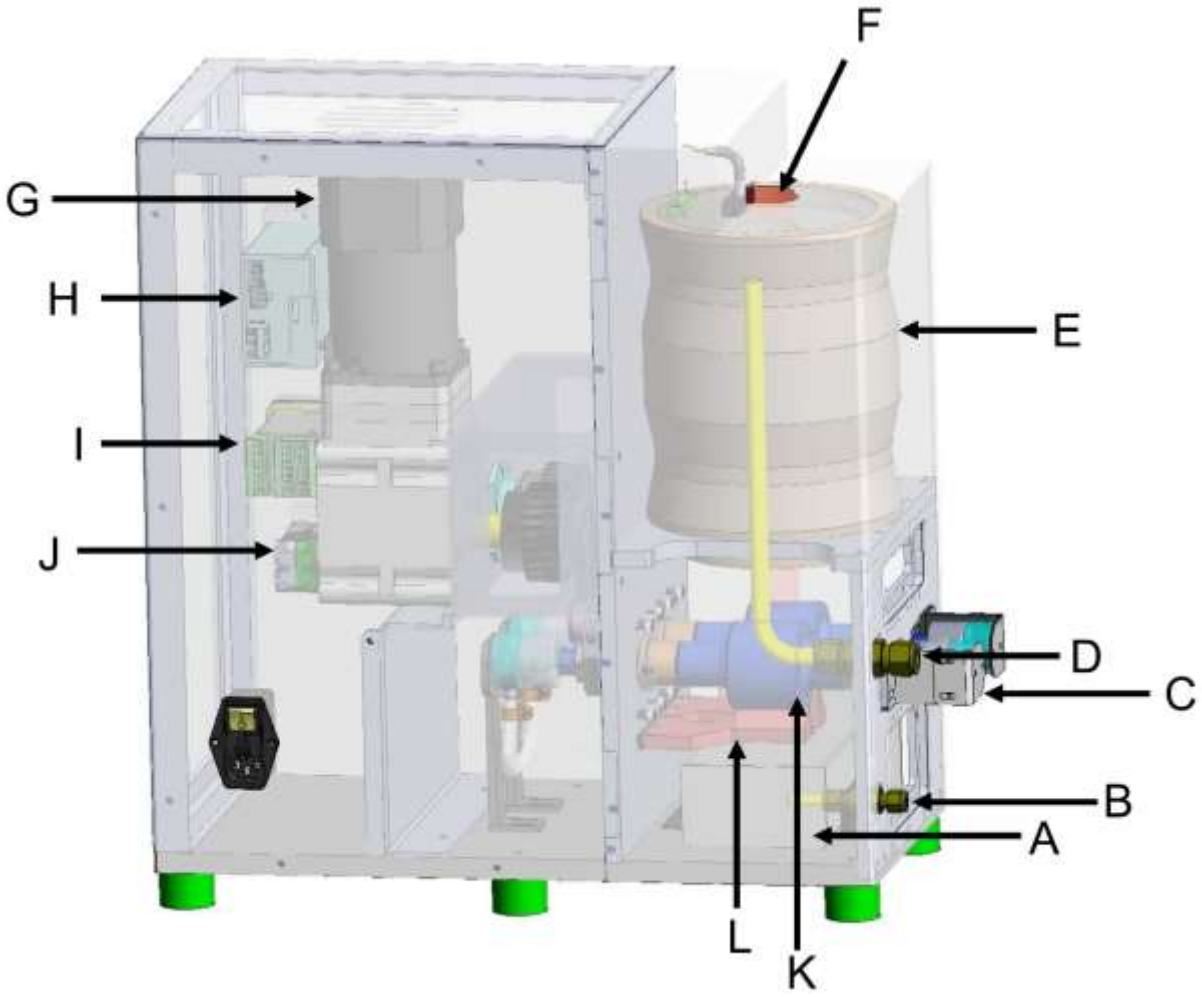

Figure 6.3.2. Schematic diagram of salt glass machine where A is the product collection tray, B is the inert gas inlet, C is the liquid nitrogen connections, D is the inert gas outlet, E is the furnace, F is the drop tube, G is the roller motor, H is motor controller, I is the thermal controller, J is the start/stop button, K is the salt contacting portion of rollers, and L are the roller blades.

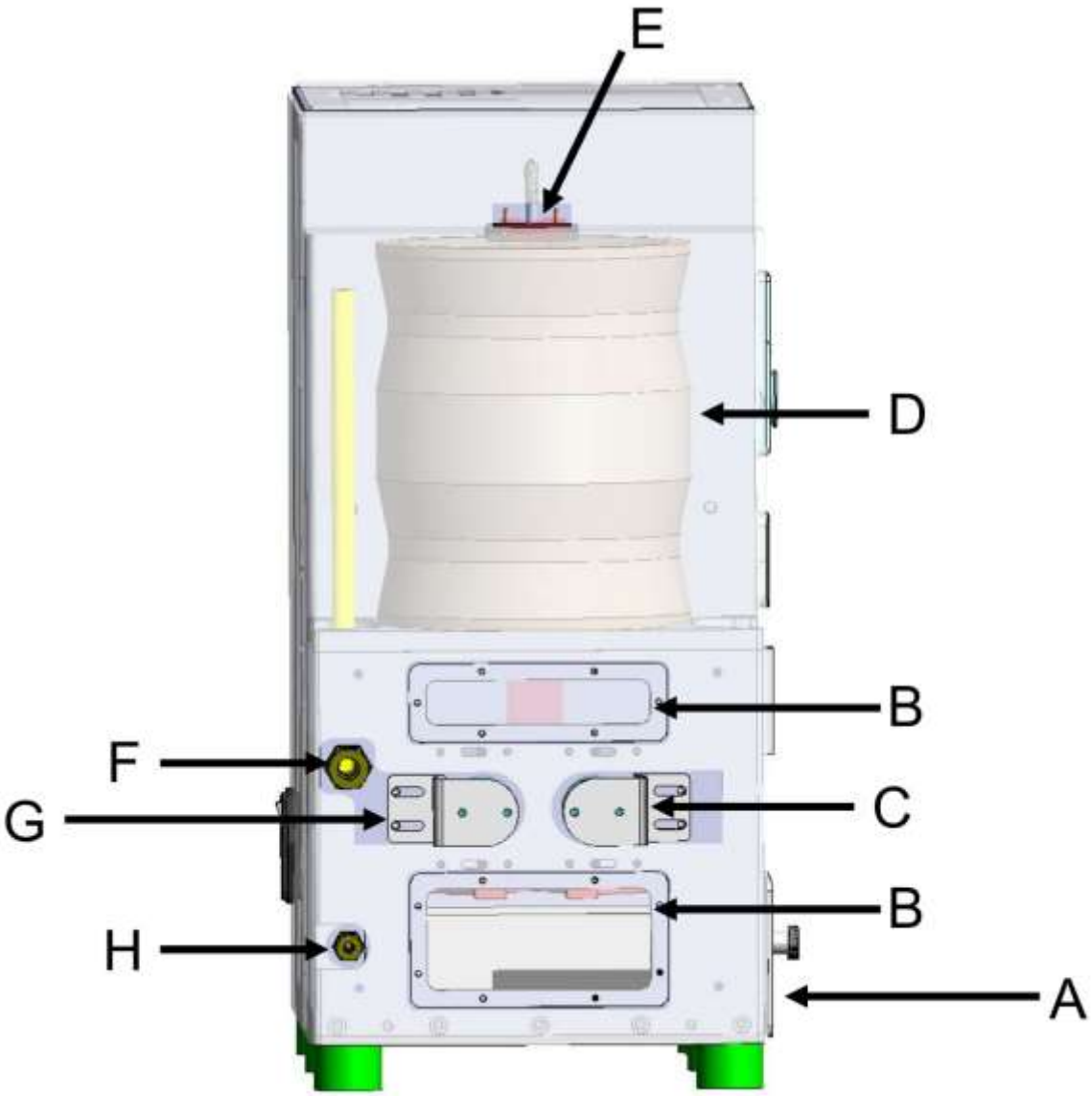

Figure 6.3.3. Schematic diagram of salt glass machine where A is the sample collection tray, B are viewing windows, C is LN2 inlet, D is the furnace, E is the drop tube, F is the inert gas outlet, G is the LN2 outlet, and H is the inert gas inlet.

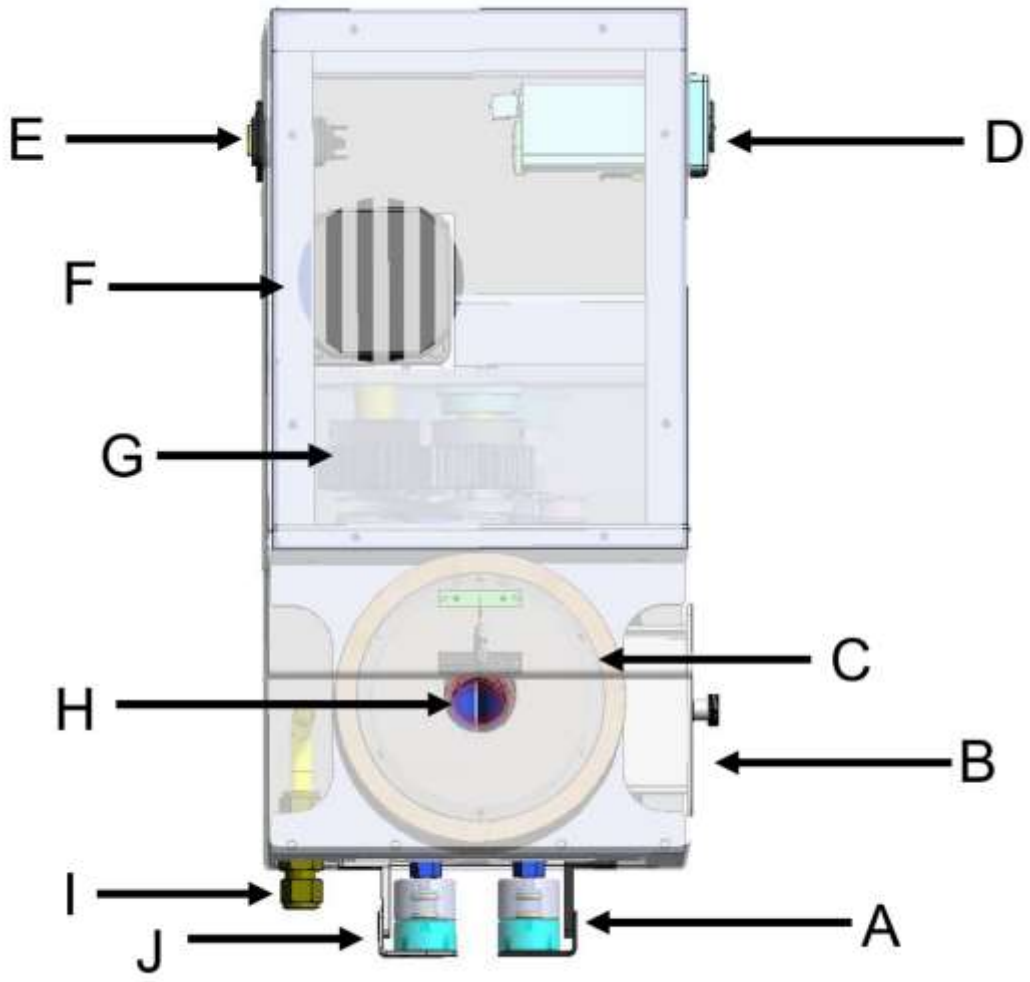

Figure 6.3.4. Schematic diagram of salt glass machine where A is the LN2 inlet, B is the sample collection tray, C is the furnace, D is the control units, E is the electrical inlet, F is the roller motor, G is gears for rollers, H is the salt drop tube, I is the gas connections, and J is the LN2 outlet.

Glass Machine Operation

The constructed salt glass machine can be seen in figure 6.3.5. The nylon bushings shown in Figure 6.3.5 D were replaced with Teflon bushings as shown in Figure 6.3.5 C. This is due to differences in contraction with temperature creating too much friction between the parts, stopping the rollers from spinning at LN2 temperatures. The flow of dry argon gas through the machine stopped the condensation of H_2O on the outside of the rollers. The argon also prevented hydration and subsequent oxide formation of the chloride salt as it was being transformed to glass.

The glass machine built as shown in Figure 6.3.5 was fitted with a hollowed high temperature insulation fire brick. Inside the hollowed fire brick, an open-ended alumina tube was placed and secured in places using Watlow high temperature ceramic fiber binder. A smaller diameter open-ended fused silica tube was placed inside and centered in the middle using soft ceramic fiber insulation. The top end of the fused silica tube was held in place using a clamp. The additional insulation reduced the temperature of the area above the furnace. A fan was added beside the injection area so that all parts above the quartz tube were approximately room temperature. A flow of nitrogen gas was passed through a desiccant trap and then utilized to remove atmospheric air from the inside of the machine. The flow of dry nitrogen gas was maintained at a flow of 100 mL/min for the duration of experiments and lowered to a flow of 10 mL/min when the machine was not in use. Pressurized LN2 was passed in through the hollow rollers through the bottom of the first and exited out of the top of the second. A depiction of the glass machine as used is shown in Figure 6.3.8.

Liquid nitrogen was stored in a Worthington 10 LDB Liquid Nitrogen Storage Dewar. A LN2 cryogenic pumping system was attached to the top of the Dewar and sealed. One hose was connected between the Dewar and a pressurized nitrogen valve, and a second hose connected the Dewar to the roller of the glass machine. Both tubes were Teflon lined high pressure Swagelok Tubing. A pressure of 10 PSI was maintained for the nitrogen gas used to pressurize the LN2. During experimentation, A needle valve was opened slowly until a pressure within the Dewar was 0.04 MPa, which was empirically determined to enable flow of LN2 through the entirety of the glass machine. Once proper pressure was achieved, the roller motor started to slow ice formation on the external portion of the rollers. The connection of the cryogenic pumping system is shown in Figure 6.3.9.

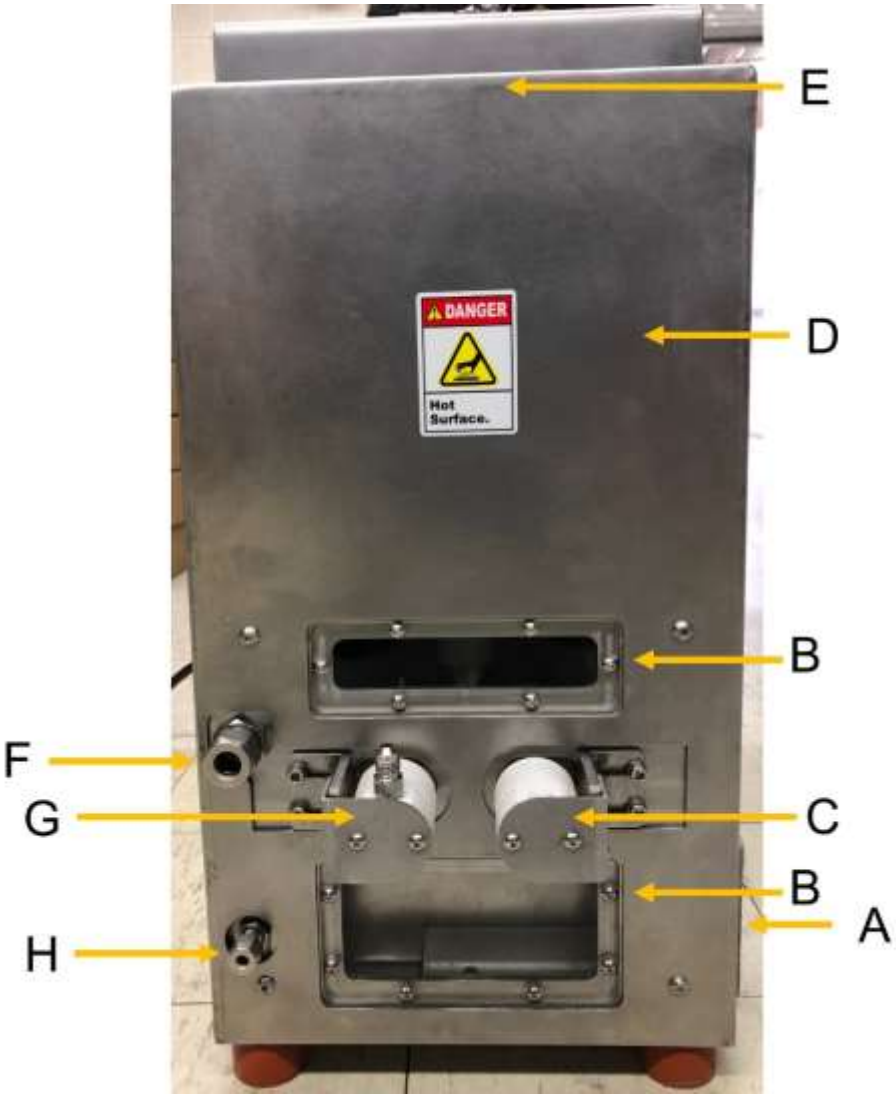

Figure 6.3.5. Pictorial representation of assembled of salt glass machine where A is the sample collection tray, B are viewing windows, C is LN2 inlet, D is the furnace, E is the drop tube, F is the inert gas outlet, G is the LN2 outlet, and H is the inert gas inlet.

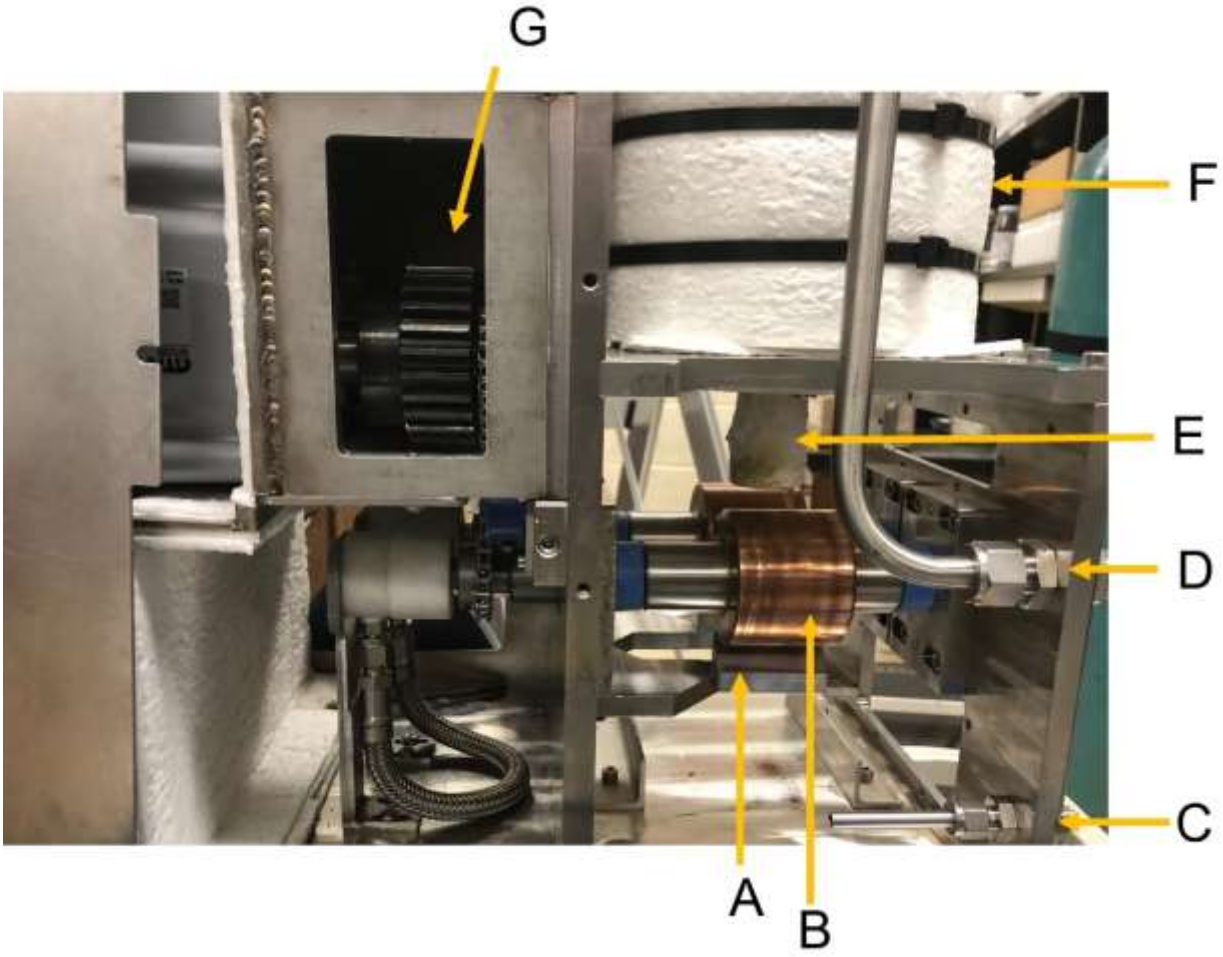

Figure 6.3.6. Pictorial representation of assembled of salt glass machine with cover removed where A is the roller blades, B is the copper portion of the roller, C is the inert gas inlet, D is the inert gas outlet, E is the drop tube, F is the furnace, and G is the gearbox for the rollers.

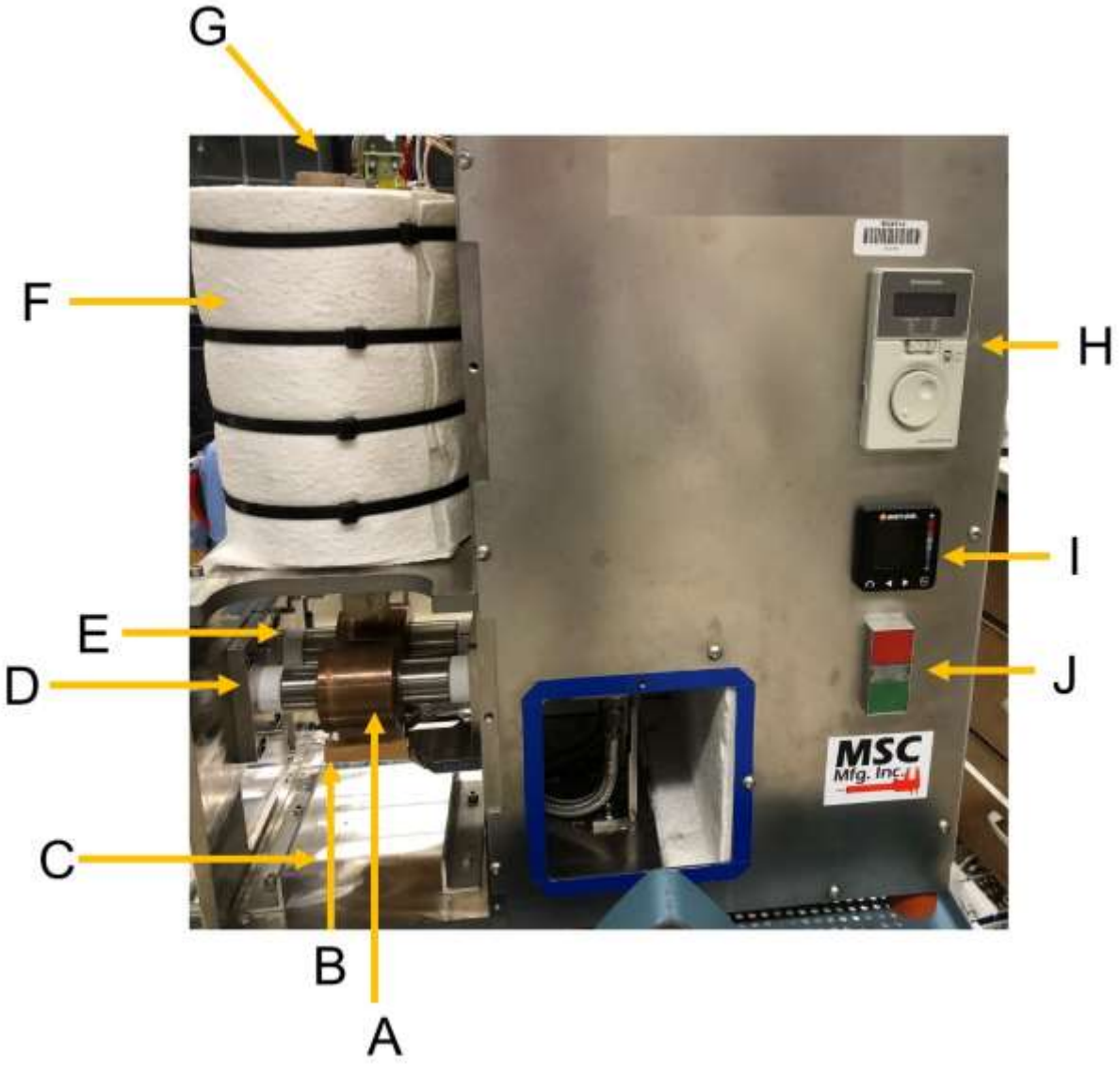

Figure 6.3.7. Pictorial representation of assembled of salt glass machine with the cover removed where A is the copper portion of the rollers, B is the roller blades, C is the location of the collection tray, D is the LN2 entrance, E is the LN2 exit, F is the furnace, G is the drop tube, H is the motor controller, I is the thermal controller, and J is the start/stop button.

Figure 6.3.8. Salt glass machine as used during experiments.

Figure 6.3.9. Depiction of pressurized LN2 delivery system used with salt glass machine.

Procedure for Salt Treatment and Analysis

Four different mixtures of three types of chloride-based salts were examined for amorphous character due to glass machine treatment. The salts tested were 45.6% KCl – 54.4% $ZnCl_2$, 51.5% KCl – 48.5% $ZnCl_2$, 70.0% KCl – 30.0% $ZnCl_2$, and 68.0% KCl – 32.0% $MgCl_2$ (given in mole %). Approximately 5.0 grams of each salt was heated under vacuum as described in Chapter 2 to a temperature of 100^{o}C above the mixtures melting point. After the salt was initially melted under dynamic vacuum, the vacuum was removed, and argon introduced to the tube's atmosphere until equalizing with ambient pressure. While remaining 100^{o}C above the mixture's melting point, the Ace Thread valve was removed. A syringe connected to a bevel tipped fused silica tube was quickly used to draw molten salt approximately 5.0 cm into the silica tube and removed from bulk solution and heat. Once removed from heat, the drawn salt solidified within approximately 10 seconds. The syringe with drawn salt can be seen in Figure 6.3.10.

The temperature of the glass machine furnace was maintained at a working temperature of 700^{o}C for all experiments. The syringe containing the drawn salt mixture was immediately transferred into the fused silica quartz tube at the top of the glass machine. The syringe was clamped in place so that the syringe was centered above the rollers. Additionally, the syringe was positioned so that all drawn salt was within the hot zone of the glass machine's furnace or approximately 2.0 cm below the top of the furnace. The rollers rotation speed was then increased to 1000 RPM, rotating inward. After approximately two minutes the drawn salt would transition into a liquid state. Pressure would then be applied to the top of the syringe so that molten salt would fall dropwise between the rollers. Two glass Mason jars were placed inside the metal drawer as the bottom of the glass machine to collect the product. The treated salt samples were then transferred to an inert atmosphere glovebox for analysis.

The x-ray diffraction measurements were carried out using a Panalytical Empyrean X-ray diffractometer scanning from 20-70°, 2Θ. All samples were loaded into the x-ray diffractometer stage inside an inert atmosphere glovebox equipped with an airtight dome so that no sample was exposed to atmosphere during measurement. In addition, Raman spectroscopy measurements were taken between 100 cm^{-1} – 400 cm^{-1} using a Horiba T64000 spectrometer. A 100-mW diode laser of 532 nm was focused through a 50x objective of a microscope to collect Raman spectra.

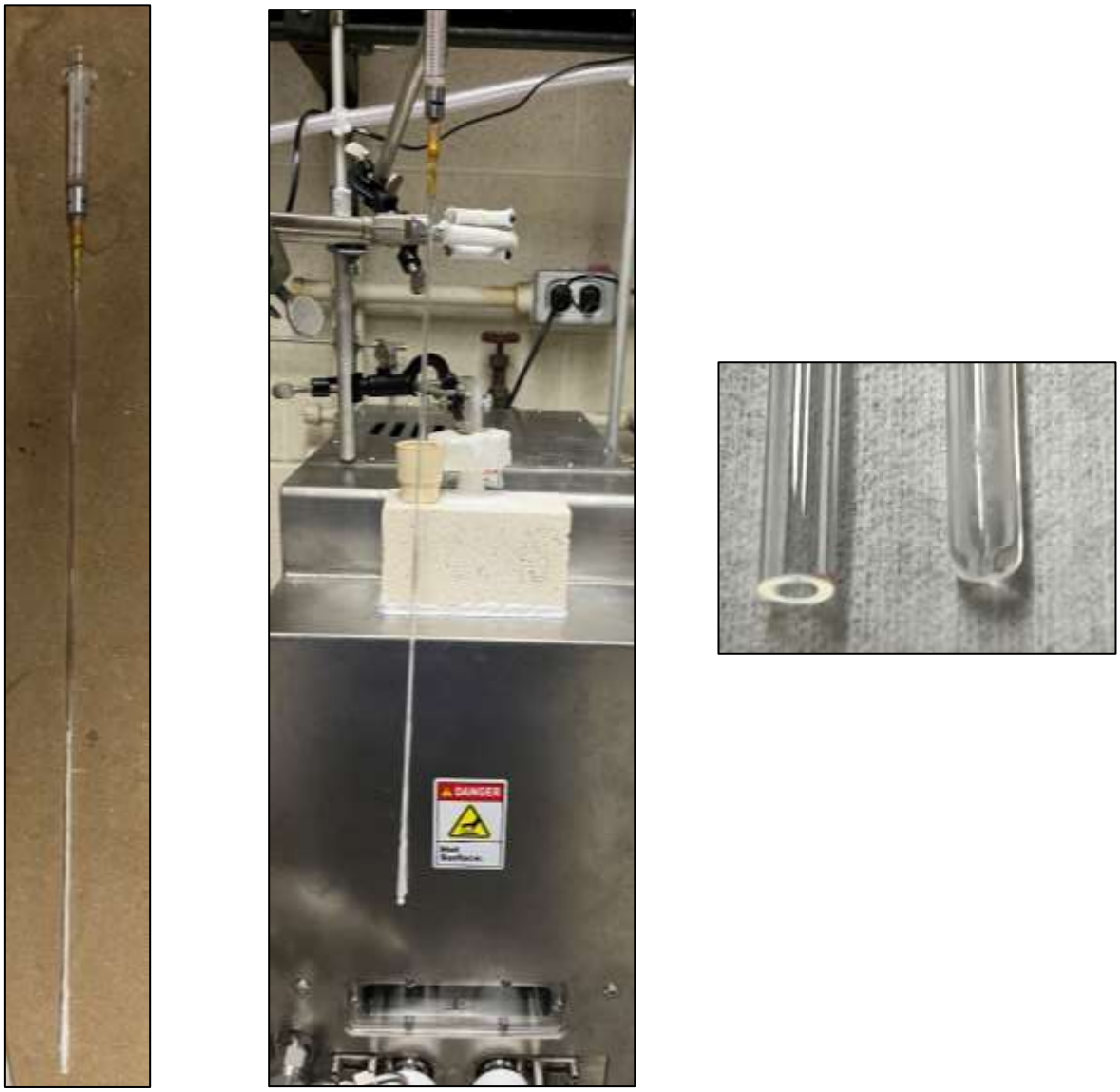

Figure 6.3.10. Depiction of syringe/fused silica tube injector for salt glass machine (left), comparison of syringe/fused silica tube injector to the glass machine (middle), beveled tip of fused silica tube that reduced drop size and early injection.

6.4 Results and Discussion

Treated products were semitransparent and in some cases, fully transparent, indicating more homogeneity in ionic distribution compared to non-transparent polycrystalline materials.[164] The product for all four different salt mixtures tested was markedly more brittle than the untreated salt from the same batch which can indicate glass formation.[165] There was large variation in the shape and length of each different product collected. In all samples collected, the width of the product was no wider than the spacing between the rollers. Indicating that the salt was still in the molten state upon passing through the LN2 cooled copper rollers. The KCl – $ZnCl_2$ mixtures were all shaped as flat, elongated pieces indicating that they were immediately passed through the roller and solidified. The glass machine treated product of the eutectic KCl – $MgCl_2$ mixture also contained mostly flat, elongated pieces. Additionally, the KCl – $MgCl_2$ product contained round spherical pieces with a diameter approximately the size of the space between the rollers. The spherical product could indicate that some of the KCl – $MgCl_2$ product was not immediately pulled through the rollers to the collection jar. The spherical products were likely formed by the motion of the rollers by solidifying and then being passed through the rollers. Spherical products could also have been formed if the drop of molten KCl – $MgCl_2$ mixture solidified while falling between the quartz syringe tube and the rollers. Images of the treated 45.6% KCl – 54.4% $ZnCl_2$, 51.5% KCl – 48.5% $ZnCl_2$, 70.0% KCl – 30.0% $ZnCl_2$ and 68.0% KCl – 32.0% $MgCl_2$ can be seen in Figure 6.4.1.

Verification of crystal structure alteration was initially completed by x-ray diffraction. The salt that was used in the experiment for the salt machine was compared to salt from the same initial synthetic batch. The analytical measurements were conducted on the treated salts as collected from the glass machine and not crushed further as mechanical forces can induce crystal formation as demonstrated in Chapter 5. Pieces of the untreated salt used for analytical measurements were chosen to be approximately the same dimensions of the treated salt used so that background signal is comparable. All results of x-ray diffraction measurements demonstrate an alteration of crystal structure between salt treated by the glass machine and identical, untreated salt. Results of analytical measurements can be identified utilizing the phase diagrams shown in Figures 6.4.2 and 6.4.3 to analyze potential chemical species present in each measured sample.

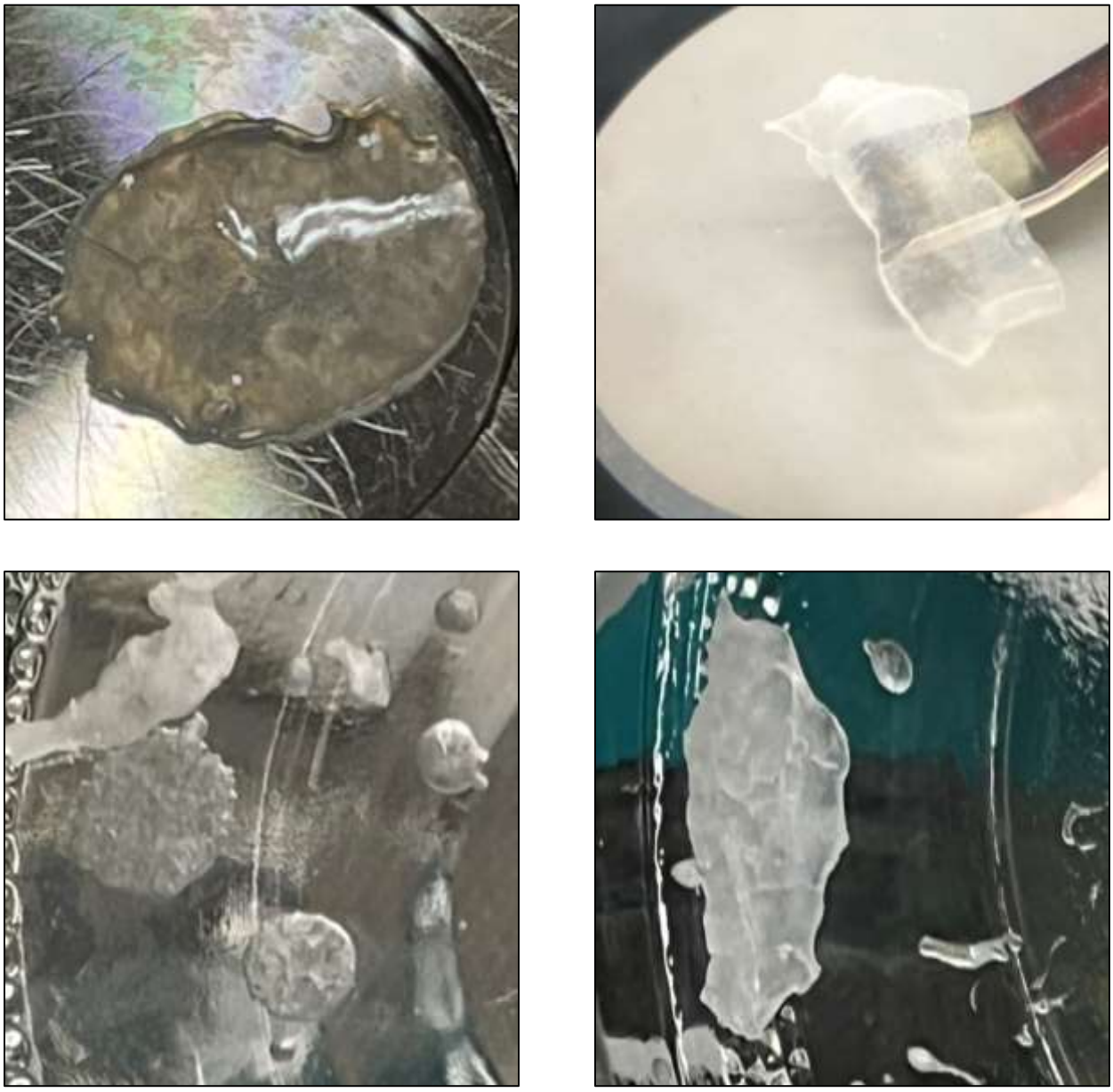

Figure 6.4.1. Salt after treatment with salt glass machine. 45.6% KCl – 54.4% $ZnCl_2$ (top left), 51.5% KCl – 48.5% $ZnCl_2$ (top right), 70.0% KCl – 30.0% $ZnCl_2$ (bottom left) and 68.0% KCl – 32.0% $MgCl_2$ (bottom right).

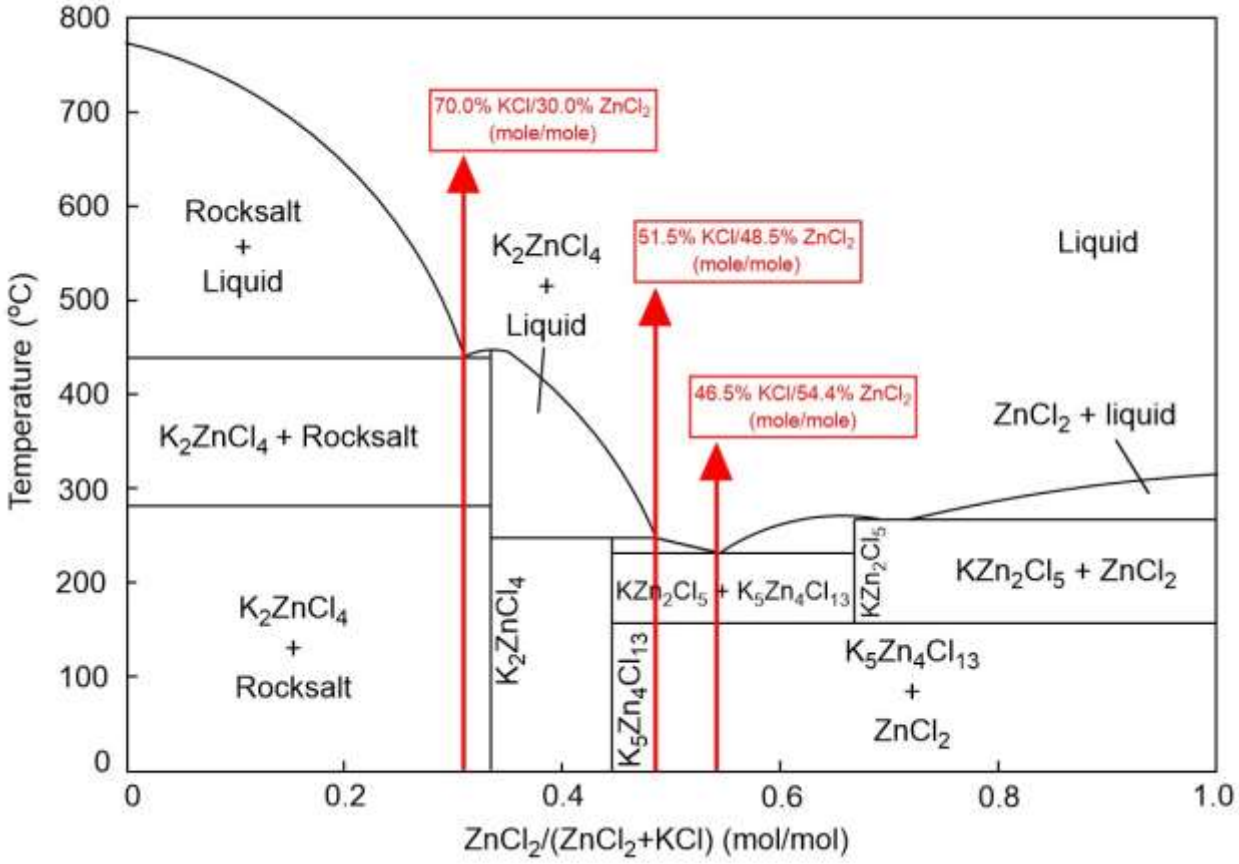

Figure 6.4.2. Phase diagram of KCl – $ZnCl_2$ mixture reproduced from FactSage thermodynamic properties database.[166]

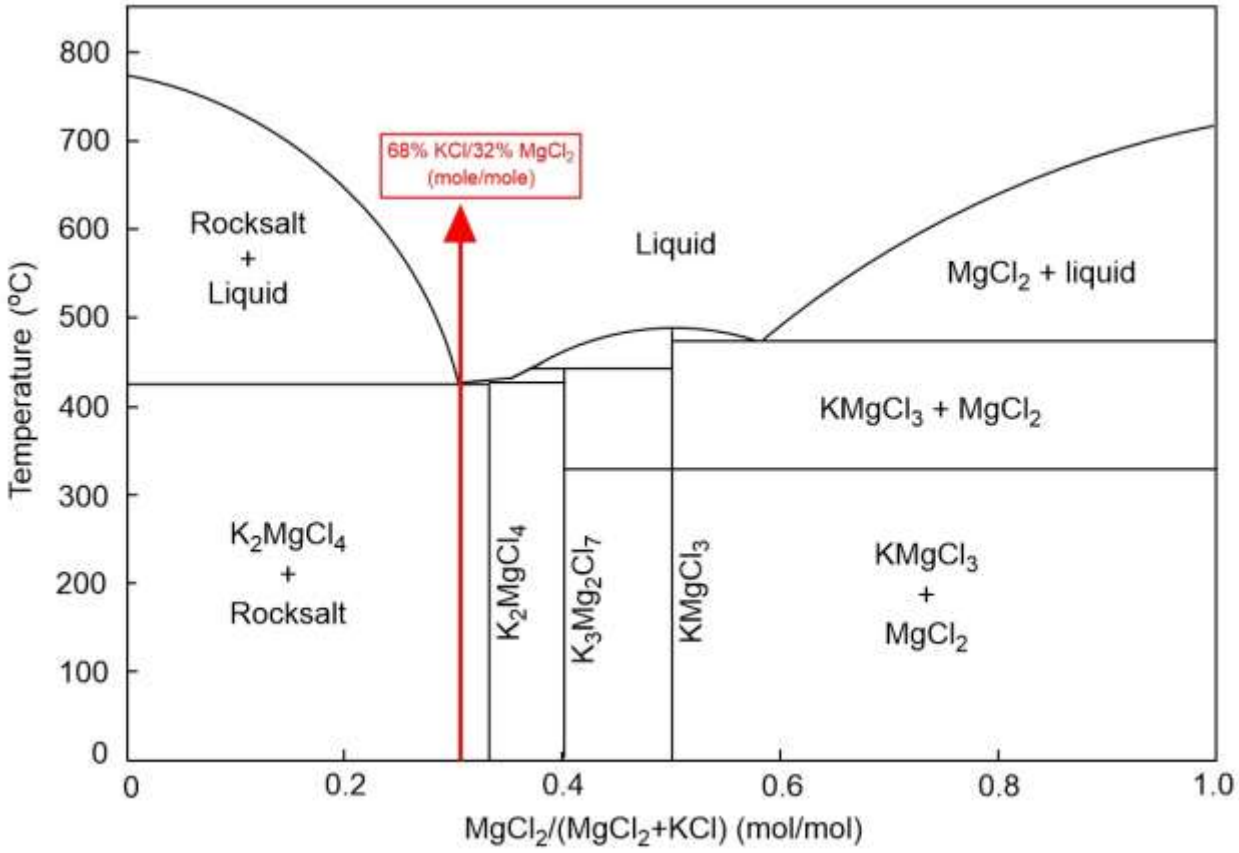

Figure 6.4.3. Phase diagram of KCl – $MgCl_2$ mixture reproduced from FactSage thermodynamic properties database.[166]

The phase diagrams for the KCl – $ZnCl_2$ and KCl – $MgCl_2$ help to determine the potential species present in analytical results, but due to incongruent transition, any listed species is potentially present in the solid.[167] Diffraction patterns for crystalline KCl, $MgCl_2$, $ZnCl_2$, K_2ZnCl_4, $KMgCl_3$, K_2MgCl_4, and $K_3Mg_2Cl_7$ are available in the literature.[168-174] The only species in the KCl – $ZnCl_2$ considered for peak matching is K_2ZnCl_4 as it is the species that is majorly observed experimentally between 0.33 – 0.66 mole % $ZnCl_2$.[175] The samples cooled to room temperature from molten under ambient conditions (untreated) were measured utilizing X-ray diffraction. The results are plotted for samples 45.6% KCl – 54.4% $ZnCl_2$, 51.5% KCl – 49.5% $ZnCl_2$, 70.0% KCl – 30.0% $ZnCl_2$, and 68.0% KCl – 32.0% $MgCl_2$ with identified peaks are shown in Figures 6.4.4, 6.4.6, 6.4.8, and 6.4.10, respectively. The samples supercooled to room temperatures via processing with the glass machine (glass machine treated) also were analyzed using X-ray diffraction and compared to literature. The results are plotted for samples 45.6% KCl – 54.4% $ZnCl_2$, 51.5% KCl – 49.5% $ZnCl_2$, 70.0% KCl – 30.0% $ZnCl_2$, and 68.0% KCl – 32.0% $MgCl_2$ with identified peaks are shown in Figures 6.4.5, 6.4.7, 6.4.9, and 6.4.11, respectively.

Although the results of the X-ray diffraction measurements cannot quantify the total extent of change in crystallinity of the measured samples, the difference in peaks can provide some insight. The untreated samples containing 45.6% KCl – 54.4% $ZnCl_2$, 51.5% KCl – 49.5% $ZnCl_2$, 70.0% KCl – 30.0% $ZnCl_2$, and 68.0% KCl – 32.0% $MgCl_2$ matched literature peaks that indicated the presence of 33, 25, 32, and 21 potential detected lattice planes, respectively. The identification of measured diffraction peaks and comparison to literature for potential Miller Index hkl values for untreated 45.6% KCl – 54.4% $ZnCl_2$, 51.5% KCl – 49.5% $ZnCl_2$, 70.0% KCl – 30.0% $ZnCl_2$, and 68.0% KCl – 32.0% $MgCl_2$ samples are shown in Tables 6.4.1, 6.4.3, 6.4.5, and 6.4.7, respectively. The equivalent sample compositions treated by the glass machine were also measured and compared to literature to determine total potential lattice planes detected. These measurements revealed the total potential lattice planes detected for the glass machine treated 45.6% KCl – 54.4% $ZnCl_2$, 51.5% KCl – 49.5% $ZnCl_2$, 70.0% KCl – 30.0% $ZnCl_2$, and 68.0% KCl – 32.0% $MgCl_2$ samples are 27, 6, 8, and 12, respectively. The identification of measured diffraction peaks and comparison to literature for potential Miller Index hkl values for glass machine treated 45.6% KCl – 54.4% $ZnCl_2$, 51.5% KCl – 49.5% $ZnCl_2$, 70.0% KCl – 30.0% $ZnCl_2$, and 68.0% KCl – 32.0% $MgCl_2$ samples are shown in Tables 6.4.2, 6.4.4, 6.4.6, and 6.4.8, respectively. An overlay of diffraction results for glass machine treated and untreated samples is shown in Figure 6.4.12.

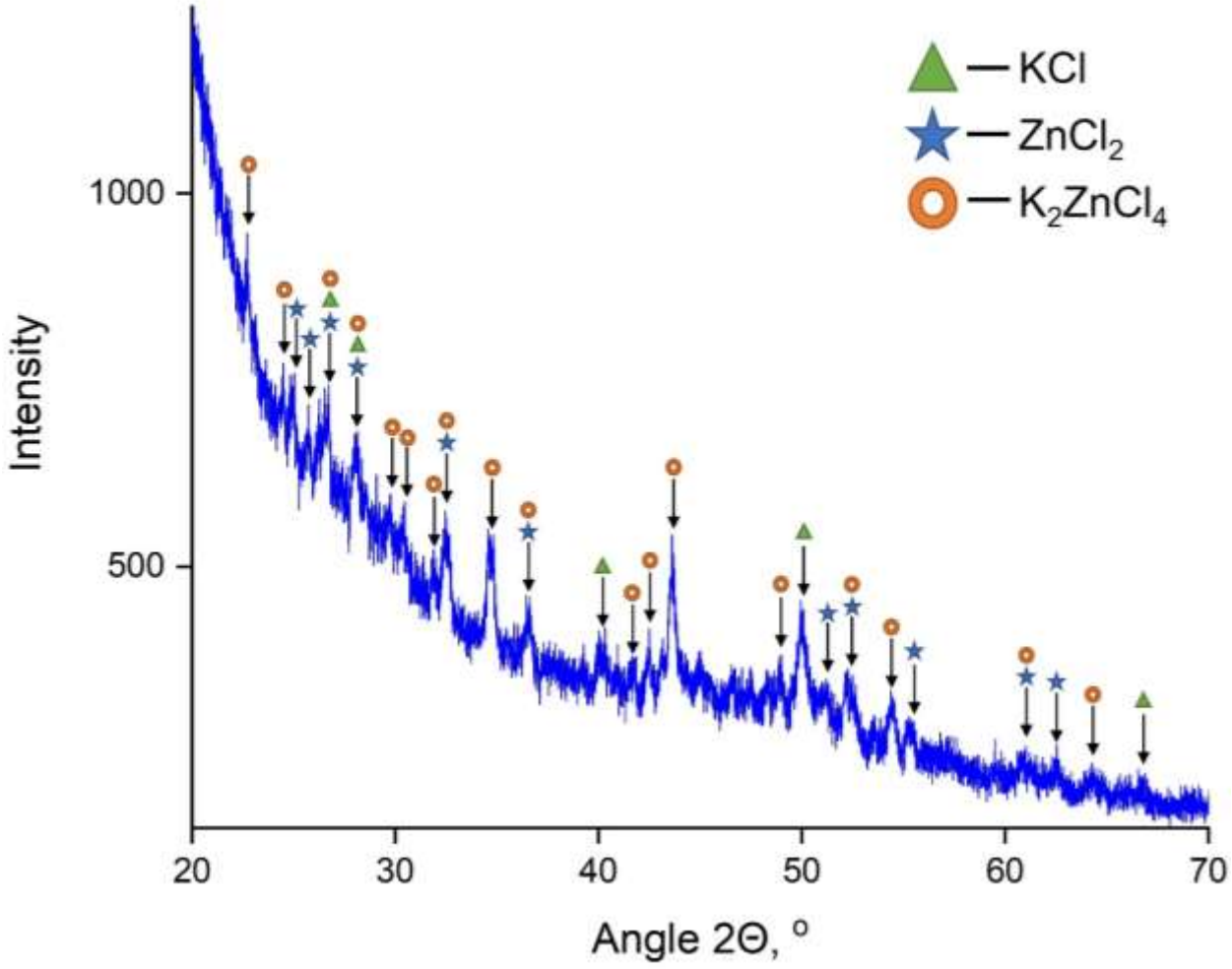

Figure 6.4.4. Results of x-ray diffraction measurements for the 45.6% KCl – 54.4% $ZnCl_2$ containing salt mixture cooled from molten under ambient conditions (untreated). Identified peaks compared to literature measurements for KCl, $ZnCl_2$, and K_2ZnCl_4 and matching positions are indicated.

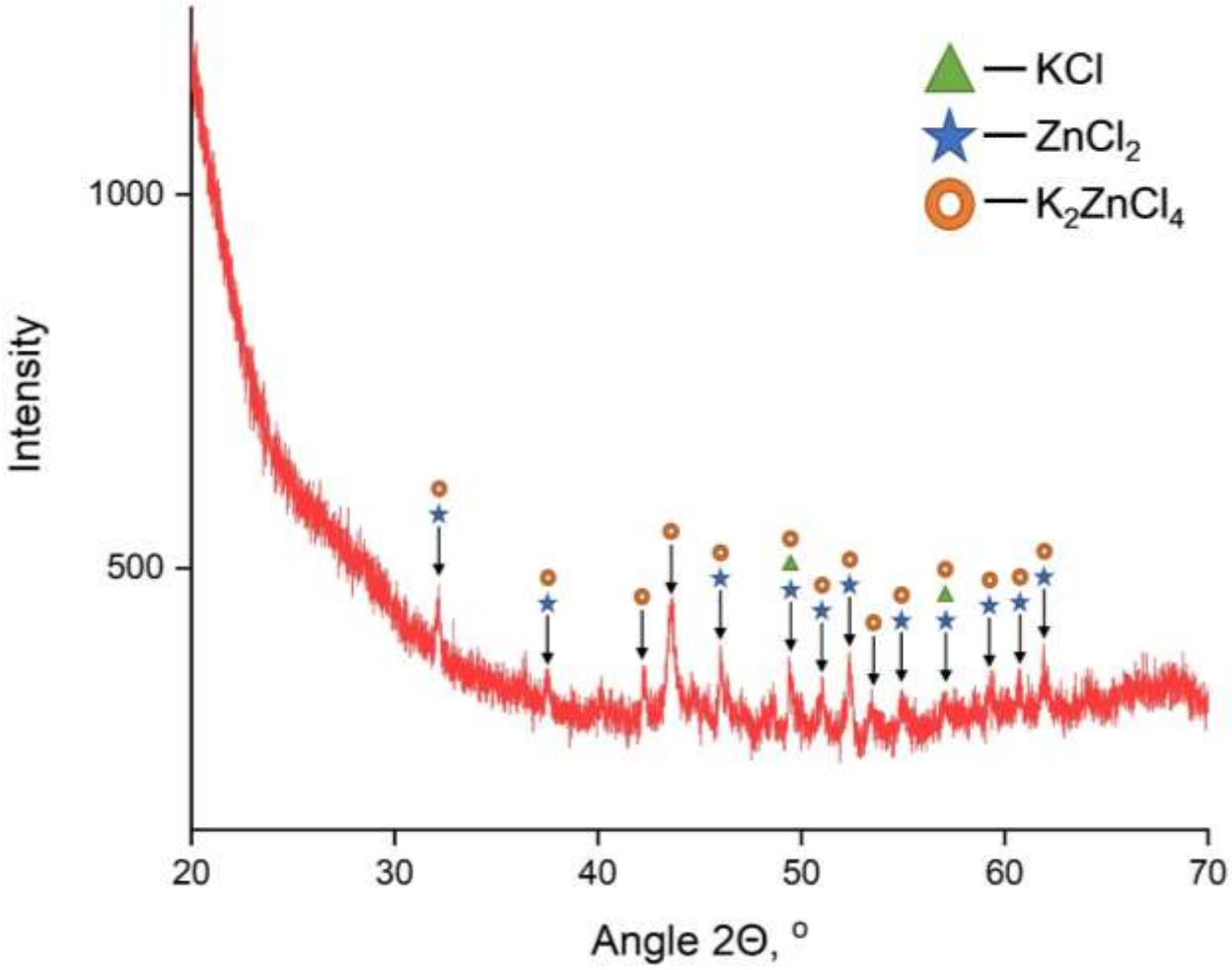

Figure 6.4.5. Results of x-ray diffraction measurements for the 45.6% KCl – 54.4% $ZnCl_2$ containing salt mixture processed using the glass machine (treated). Identified peaks compared to literature measurements for KCl, $ZnCl_2$, and K_2ZnCl_4 and matching positions are indicated.

Table 6.4.1. Identified peaks in X-ray diffraction measurements for untreated 45.6% KCl – 54.4% $ZnCl_2$ (mole) and matching literature peaks for KCl, $ZnCl_2$, and K_2ZnCl_4. No matching values are indicated by (-) while matching values are indicated by their associated Miller index lattice planes (hkl).

Salt Matrix	Identified Peak (2Θ, °)	KCl	$ZnCl_2$	K_2ZnCl_4
Untreated 45.6% KCl – 54.4% $ZnCl_2$	22.7	-	-	020
	24.4	-	-	103
	24.0	-	101	-
	25.8	-	004	-
	26.7	200	004	004
	28.1	200	004	004
	29.7	-	-	014
	30.3	-	-	031
	31.8	-	-	114
	32.4	-	103	032
	34.6	-	-	024
	36.7	-	112	015
	40.0	220	-	-
	41.6	-	-	140
	42.5	-	-	006
	43.6	-	-	215
	48.3	-	-	-
	50.0	222	-	-
	51.1	-	202	243
	52.5	-	106	226
	54.4	-	-	-
	55.4	-	211	-
	60.8	-	213	137
	62.5	-	008	-
	64.2	-	-	137
	66.7	420	-	-
Total Lattice Planes Detected:		5	11	17

Table 6.4.2. Identified peaks in X-ray diffraction measurements for glass machine treated 45.6% KCl – 54.4% $ZnCl_2$ (mole) and matching literature peaks for KCl, $ZnCl_2$, and K_2ZnCl_4. No matching values are indicated by (-) while matching values are indicated by their associated Miller index lattice planes (hkl).

Salt Matrix	Identified Peak (2Θ, °)	KCl	$ZnCl_2$	K_2ZnCl_4
Glass Machine Treated 45.6% KCl – 54.4% $ZnCl_2$	32.2	-	103	114
	37.5	-	112	223
	42.3	-	-	006
	43.6	-	-	215
	46.0	-	114	143
	49.4	222	200	206
	51.0	-	202	107
	52.3	-	106	243
	53.4	-	-	226
	55.1	-	211	325
	57.1	400	212	251
	59.3	-	107	431
	60.7	-	213	335
	61.9	-	008	061
Total Lattice Planes Detected:		2	11	14

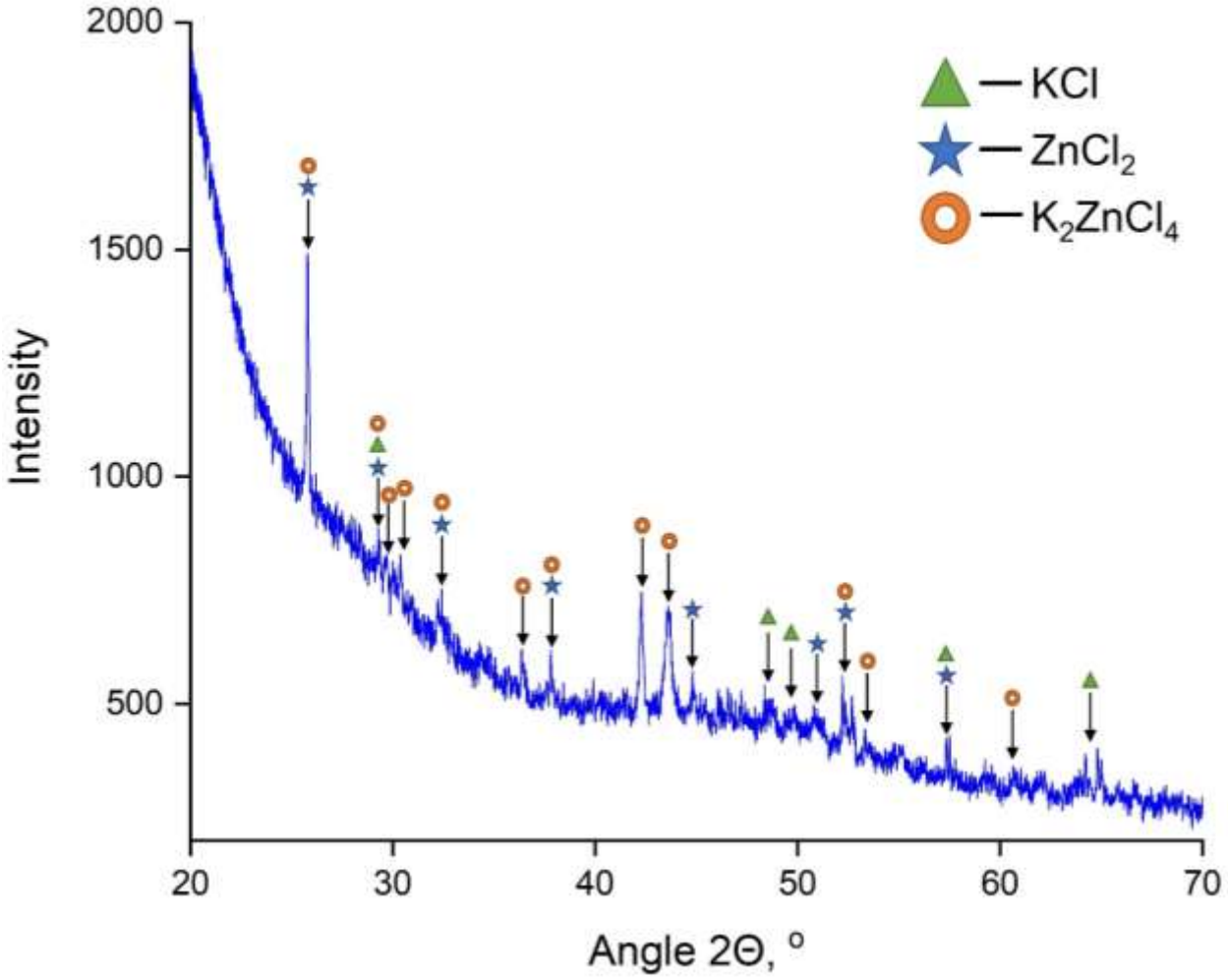

Figure 6.4.6. Results of x-ray diffraction measurements for the 51.5% KCl – 48.5% $ZnCl_2$ containing salt mixture cooled from molten under ambient conditions (untreated). Identified peaks compared to literature measurements for KCl, $ZnCl_2$, and K_2ZnCl_4 and matching positions are indicated.

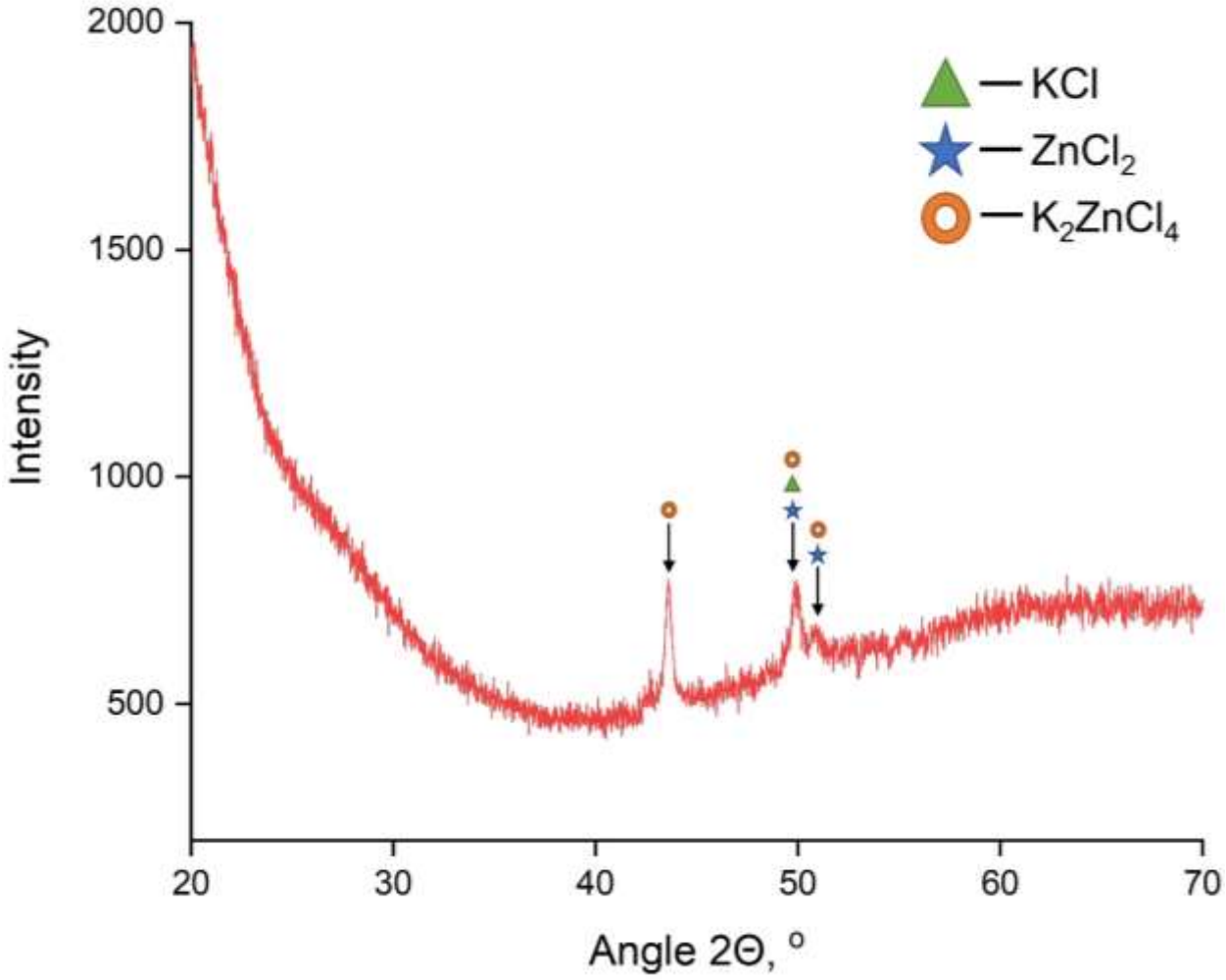

Figure 6.4.7. Results of x-ray diffraction measurements for the 51.5% KCl – 48.5% $ZnCl_2$ containing salt mixture processed using the glass machine (treated). Identified peaks compared to literature measurements for KCl, $ZnCl_2$, and K_2ZnCl_4 and matching positions are indicated.

Table 6.4.3. Identified peaks in X-ray diffraction measurements for untreated 51.5% KCl – 48.5% $ZnCl_2$ (mole) and matching literature peaks for KCl, $ZnCl_2$, and K_2ZnCl_4. No matching values are indicated by (-) while matching values are indicated by their associated Miller index lattice planes (hkl).

Salt Matrix	Identified Peak (2Θ, °)	KCl	$ZnCl_2$	K_2ZnCl_4
Untreated 51.5% KCl – 48.5% $ZnCl_2$	25.8	-	101	103
	29.2	200	102	004
	29.7	-	-	014
	30.3	-	-	031
	32.3	-	103	114
	36.4	-	-	124
	37.8	-	112	223
	42.2	-	-	140
	43.6	-	-	215
	44.8	-	105	-
	48.7	-	200	-
	49.8	222	-	-
	51.0	222	-	-
	52.2	-	106	243
	52.6	-	-	226
	57.4	400	212	-
	64.2	-	-	317
	64.8	420	-	-
Total Lattice Planes:		5	8	12

Table 6.4.4. Identified peaks in X-ray diffraction measurements for glass machine treated 51.5% KCl – 48.5% $ZnCl_2$ (mole)and matching literature peaks for KCl, $ZnCl_2$, and K_2ZnCl_4. No matching values are indicated by (-) while matching values are indicated by their associated Miller index lattice planes (hkl).

Salt Matrix	Identified Peak (2Θ, °)	KCl	$ZnCl_2$	K_2ZnCl_4
Glass Machine Treated 51.5% KCl – 48.5% $ZnCl_2$	43.6	-	-	215
	49.8	222	200	206
	50.9	-	202	107
Total Lattice Planes Detected:		1	2	3

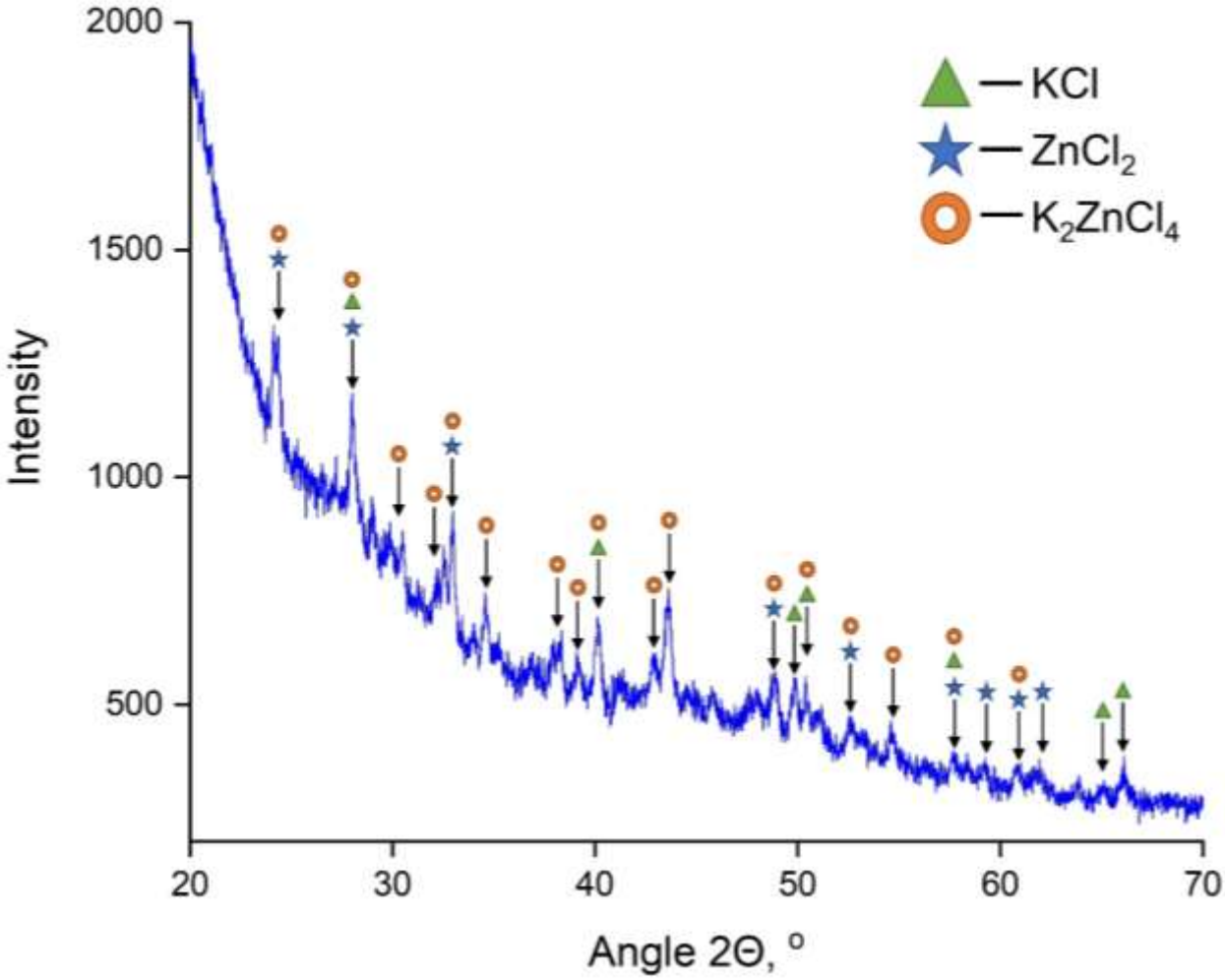

Figure 6.4.8. Results of x-ray diffraction measurements for the 70.0% KCl – 30.0% $ZnCl_2$ containing salt mixture cooled from molten under ambient conditions (untreated). Identified peaks compared to literature measurements for KCl, $ZnCl_2$, and K_2ZnCl_4 and matching positions are indicated.

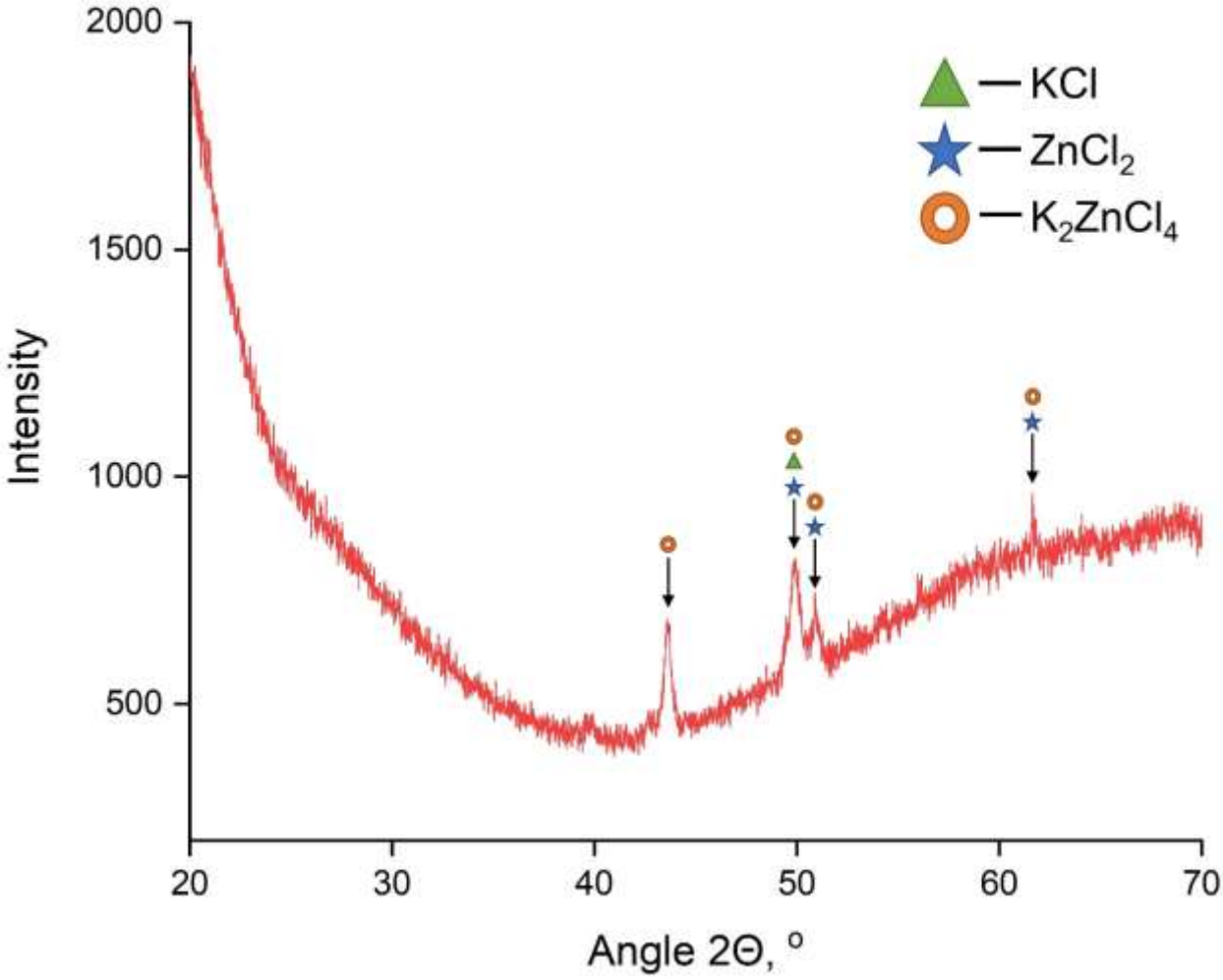

Figure 6.4.9. Results of x-ray diffraction measurements for the 70.0% KCl – 30.0% $ZnCl_2$ containing salt mixture processed using the glass machine (treated). Identified peaks compared to literature measurements for KCl, $ZnCl_2$, and K_2ZnCl_4 and matching positions are indicated.

Table 6.4.5. Identified peaks in X-ray diffraction measurements for untreated 70.0% KCl – 30.0% $ZnCl_2$ (mole) and matching literature peaks for KCl, $ZnCl_2$, and K_2ZnCl_4. No matching values are indicated by (-) while matching values are indicated by their associated Miller index lattice planes (hkl).

Salt Matrix	Identified Peak (2Θ, º)	KCl	$ZnCl_2$	K_2ZnCl_4
Untreated 70.0% KCl – 30.0% $ZnCl_2$	24.3	-	101	103
	28.0	200	102	004
	30.5	-	-	114
	32.5	-	-	032
	33.0	-	103	213
	34.5	-	-	024
	38.2	-	-	223
	39.1	-	-	231
	40.1	220	-	025
	42.9	-	-	006
	43.6	-	-	215
	48.8	-	200	331
	49.8	222	-	-
	50.4	222	-	206
	52.6	-	-	243
	54.6	-	-	226
	57.7	400	212	251
	59.2	-	107	-
	60.8	-	213	137
	61.9	-	008	-
	65.1	420	-	-
	66.0	420	-	-
Total Lattice Planes Detected:		7	8	17

Table 6.4.6. Identified peaks in X-ray diffraction measurements for glass machine treated 70.0% KCl – 30.0% $ZnCl_2$ (mole) and matching literature peaks for KCl, $ZnCl_2$, and K_2ZnCl_4. No matching values are indicated by (-) while matching values are indicated by their associated Miller index lattice planes (hkl).

Salt Matrix	Identified Peak (2Θ, º)	KCl	$ZnCl_2$	K_2ZnCl_4
Glass Machine Treated 70.0% KCl – 30.0% $ZnCl_2$	43.6	-	-	215
	49.8	222	200	206
	61.6	-	008	137
	50.9	-	202	107
Total Lattice Planes Detected:		1	3	4

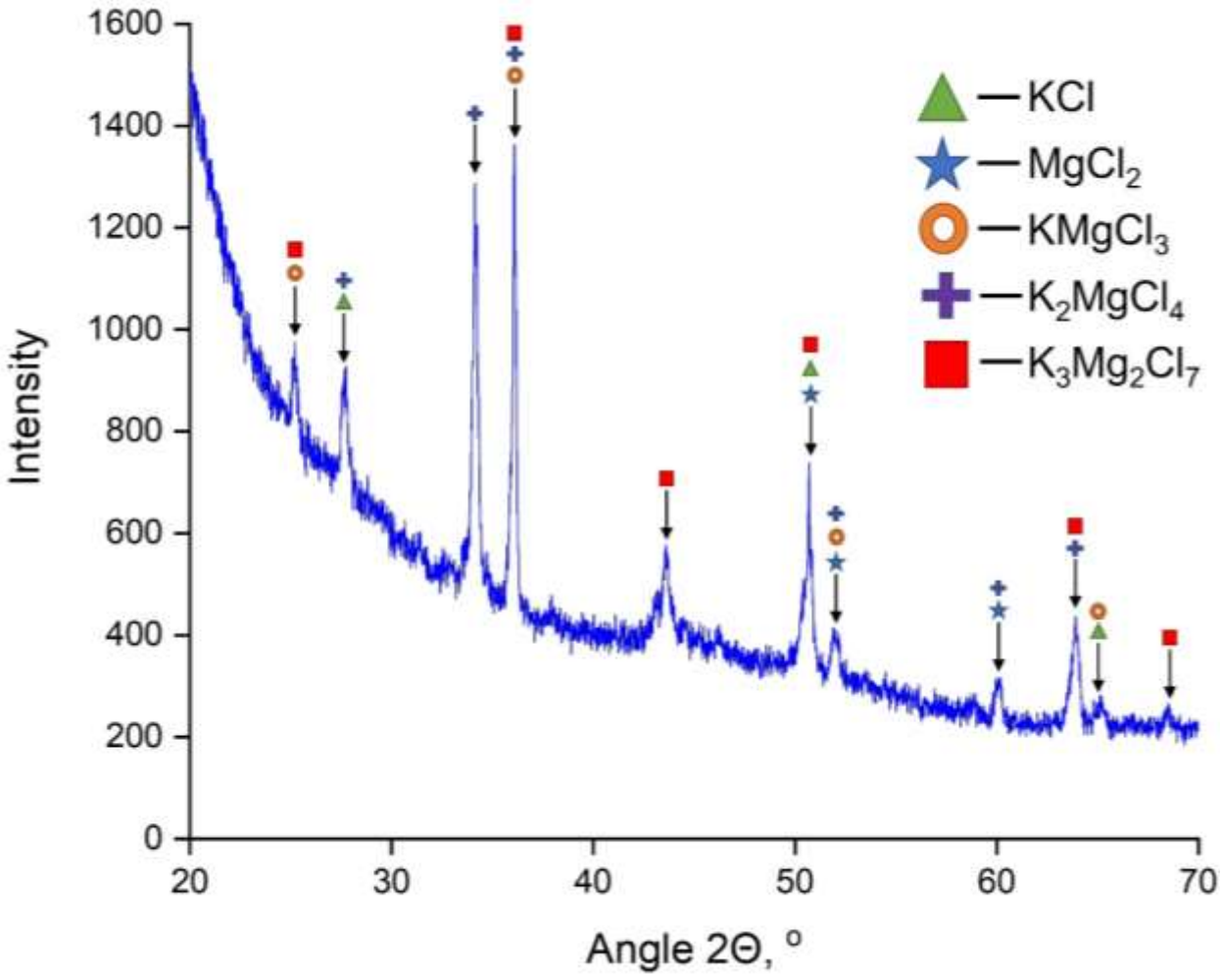

Figure 6.4.10. Results of x-ray diffraction measurements the 68.0% KCl – 32.0% $MgCl_2$ containing salt mixture cooled from molten under ambient conditions (untreated). Identified peaks compared to literature measurements for KCl, $MgCl_2$, $KMgCl_3$, K_2MgCl_4, and $K_3Mg_2Cl_7$ and matching positions are indicated.

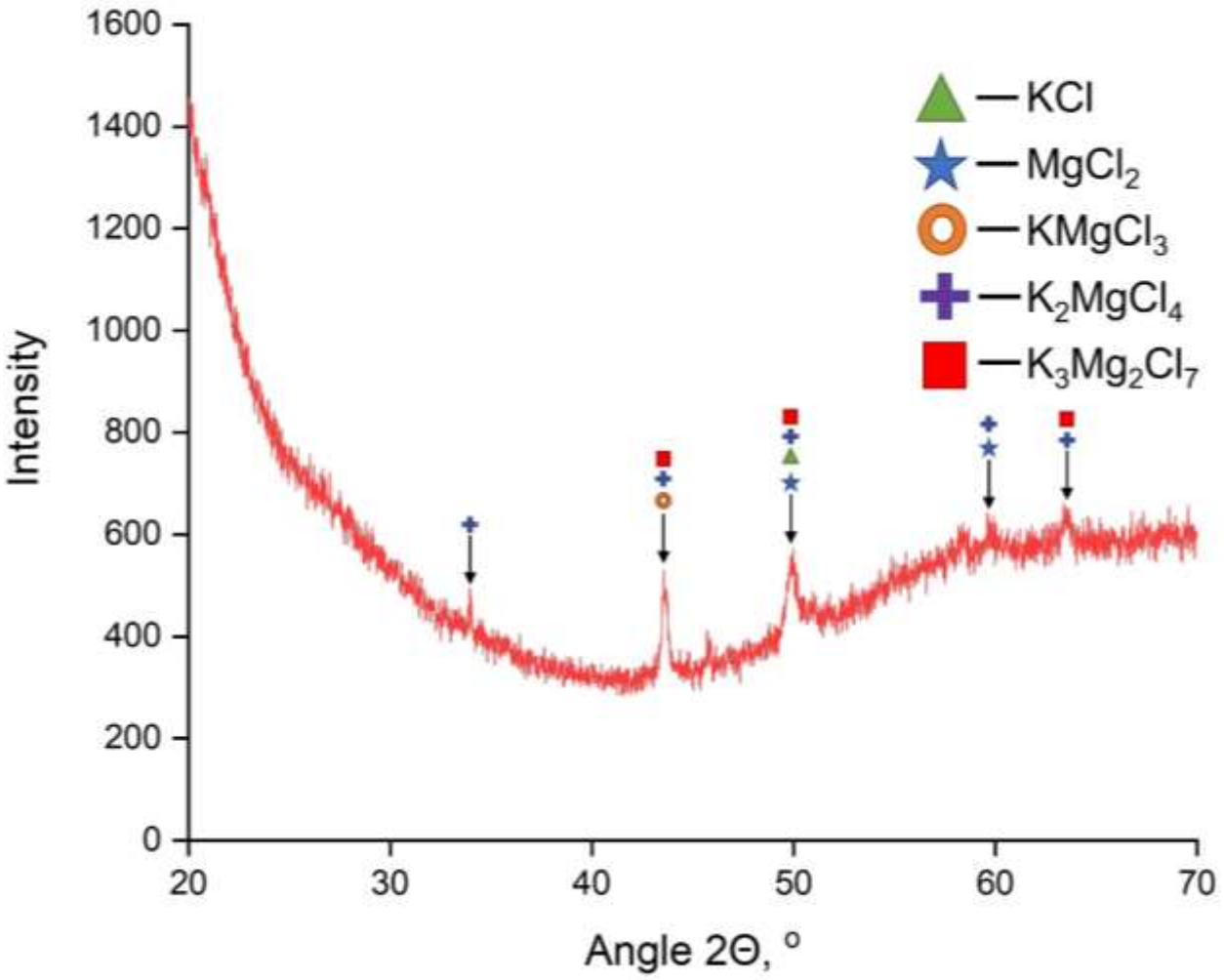

Figure 6.4.11. Results of x-ray diffraction measurements the 68.0% KCl – 32.0% $MgCl_2$ containing salt mixture processed using the glass machine (treated). Identified peaks compared to literature measurements for KCl, $MgCl_2$, $KMgCl_3$, K_2MgCl_4, and $K_3Mg_2Cl_7$ and matching positions are indicated.

Table 6.4.7. Identified peaks in X-ray diffraction measurements for untreated 68.0% KCl – 32.0% $MgCl_2$ (mole) and matching literature peaks for KCl, $MgCl_2$, $KMgCl_3$, K_2MgCl_4, and $K_3Mg_2Cl_7$. No matching values are indicated by (-) while matching values are indicated by their associated Miller index lattice planes (hkl).

Salt Matrix	Identified Peak (2Θ, °)	KCl	$MgCl_2$	$KMgCl_3$	K_2MgCl_4	$K_3Mg_2Cl_7$
Untreated 68.0% KCl – 32.0% $MgCl_2$	25.2	-	-	112	-	110
	27.7	200	-	-	112	-
	34.1	-	-	-	006	-
	36.1	-	-	220	200	200
	43.7	-	-	-	-	110
	50.7	222	110	-	-	2010
	52.0	-	2-1-11	224	220	-
	60.1	-	20-21	-	208	-
	63.9	-	-	-	208	2210
	65.2	420	-	044	-	-
	68.5	-	-	-	-	2212
Total Lattice Planes Detected:		3	3	4	6	5

Table 6.4.8. Identified peaks in X-ray diffraction measurements for glass machine treated 68.0% KCl – 32.0% $MgCl_2$ (mole) and matching literature peaks for KCl, $ZnCl_2$, and K_2ZnCl_4. No matching values are indicated by (-) while matching values are indicated by their associated Miller index lattice planes (hkl).

Salt Matrix	Identified Peak (2Θ, °)	KCl	$MgCl_2$	$KMgCl_3$	K_2MgCl_4	$K_3Mg_2Cl_7$
Untreated 68.0% KCl – 32.0% $MgCl_2$	43.6	-	-	312	116	1110
	49.8	222	110	-	206	2010
	59.6	-	20-21	-	208	-
	63.6	-	-	-	208	2210
	34.0	-	-	-	006	-
Total Lattice Planes Detected:		1	2	1	5	3

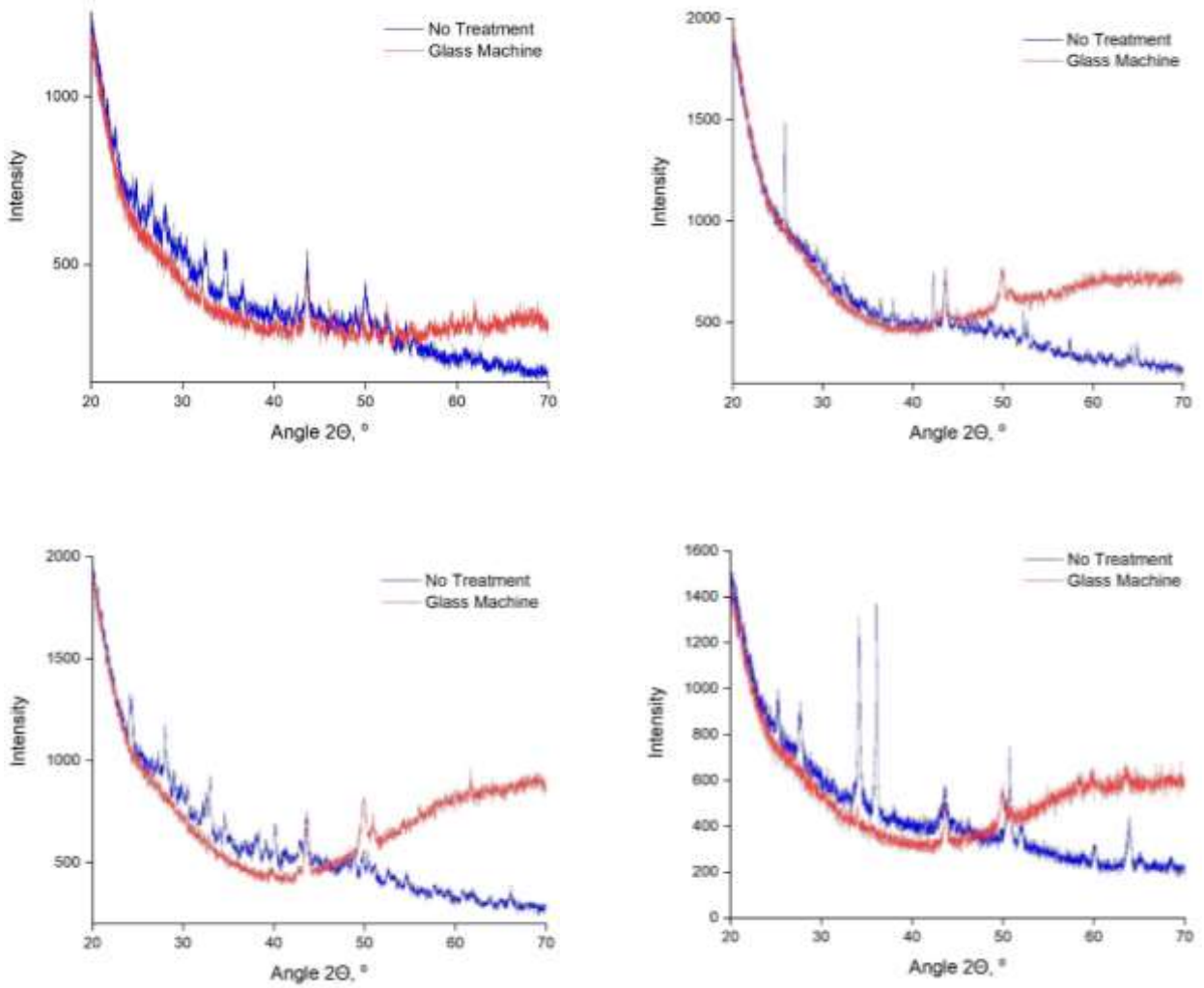

Figure 6.4.12. Results of x-ray diffraction measurements for the 45.6% KCl – 54.4% $ZnCl_2$ containing salt mixture (top left), 51.5% KCl – 48.5% $ZnCl_2$ containing salt mixture (top right), 70.0% KCl – 30.0% $ZnCl_2$ containing salt mixture (bottom left), and 68.0% KCl – 32.0% $MgCl_2$ containing salt mixture. Blue line indicates no treatment (cooled from molten under ambient conditions) and red line indicates glass machine treatment.

All samples treated with the glass machine demonstrated a reduction in total peaks detected by X-ray diffraction measurement. The untreated 45.6% KCl – 54.4% $ZnCl_2$, 51.5% KCl – 49.5% $ZnCl_2$, 70.0% KCl – 30.0% $ZnCl_2$, and 68.0% KCl – 32.0% $MgCl_2$ samples X-ray diffraction patterns contained 26, 18, 22, and 11 identified peaks, respectively. The glass machine treated 45.6% KCl – 54.4% $ZnCl_2$, 51.5% KCl – 49.5% $ZnCl_2$, 70.0% KCl – 30.0% $ZnCl_2$, and 68.0% KCl – 32.0% $MgCl_2$ samples X-ray diffraction patterns contained 14, 3, 4, and 5 identified peaks, respectively. A comparison of the total number of detected crystalline features (total number of identified peaks) reveals that glass machine treatment results in a peak reduction of 46%, 83%, 81%, and 54% for 45.6% KCl – 54.4% $ZnCl_2$, 51.5% KCl – 49.5% $ZnCl_2$, 70.0% KCl – 30.0% $ZnCl_2$, and 68.0% KCl – 32.0% $MgCl_2$ samples, respectively. More than one crystalline species can potentially contribute to the detected peak in the X-ray diffraction pattern. Therefore, it may be useful to compare total detected lattice planes from all potential species, as shown in Tables 6.4.1 – 6.4.8. This comparison reveals the reduction in detected lattice planes for all potential contributing species to be 18%, 76%, 75%, and 43% for 45.6% KCl – 54.4% $ZnCl_2$, 51.5% KCl – 49.5% $ZnCl_2$, 70.0% KCl – 30.0% $ZnCl_2$, and 68.0% KCl – 32.0% $MgCl_2$ samples, respectively.

All KCl – $ZnCl_2$ containing samples had peaks matching the literature reported values for crystalline KCl. The untreated 45.6% KCl – 54.4% $ZnCl_2$, 51.5% KCl – 49.5% $ZnCl_2$, and 70.0% KCl – 30.0% $ZnCl_2$ samples contained 5, 5, and 7 measured diffraction peaks that matched the literature values for KCl. The glass machine treated 45.6% KCl – 54.4% $ZnCl_2$, 51.5% KCl – 49.5% $ZnCl_2$, and 70.0% KCl – 30.0% $ZnCl_2$ samples had 2, 1, and 1 measured diffraction peaks that matched the literature values for KCl. Comparison reveals glass machine treatment reduces detected KCl crystalline features by 60%, 80%, and 85% for 45.6% KCl – 54.4% $ZnCl_2$, 51.5% KCl – 49.5% $ZnCl_2$, and 70.0% KCl – 30.0% $ZnCl_2$ samples, respectively. The reduction of the detected KCl diffraction peaks at increased KCl concentrations suggests a degree of success in the suppression of KCl crystallization.

All KCl – $ZnCl_2$ containing samples had peaks matching the literature reported values for crystalline $ZnCl_2$. The untreated 45.6% KCl – 54.4% $ZnCl_2$, 51.5% KCl – 49.5% $ZnCl_2$, and 70.0% KCl – 30.0% $ZnCl_2$ samples had 11, 8, and 8 measured diffraction peaks that matched the literature values for $ZnCl_2$. The glass machine treated 45.6% KCl – 54.4% $ZnCl_2$, 51.5% KCl – 49.5% $ZnCl_2$, and 70.0% KCl – 30.0% $ZnCl_2$ samples had 11, 2, and 3 measured diffraction peaks that

matched the literature values for $ZnCl_2$. Comparison reveals glass machine treatment reduces detected $ZnCl_2$ crystalline features by 0%, 75%, and 62% for 45.6% KCl – 54.4% $ZnCl_2$, 51.5% KCl – 49.5% $ZnCl_2$, and 70.0% KCl – 30.0% $ZnCl_2$ samples, respectively. Results of these measurements suggest successful reduction of the crystallization of $ZnCl_2$ for the samples containing 51.5% KCl – 49.5% $ZnCl_2$ and 70.0% KCl – 30.0% $ZnCl_2$. For the sample containing 45.6% KCl – 54.4% $ZnCl_2$ the diffraction results indicate no reduction in detected lattice planes as all peaks associated with $ZnCl_2$ are detected in both samples. Although, all diffraction peak positions associated with $ZnCl_2$ in the treated sample also match the literature reported locations for K_2ZnCl_4 peaks (Figure 6.4.5).

All KCl – $ZnCl_2$ containing samples had peaks matching the literature reported values for crystalline K_2ZnCl_4. The untreated 45.6% KCl – 54.4% $ZnCl_2$, 51.5% KCl – 49.5% $ZnCl_2$, and 70.0% KCl – 30.0% $ZnCl_2$ samples contained 17, 12, and 17 measured diffraction peaks that matched the literature values for $ZnCl_2$. The glass machine treated 45.6% KCl – 54.4% $ZnCl_2$, 51.5% KCl – 49.5% $ZnCl_2$, and 70.0% KCl – 30.0% $ZnCl_2$ samples had 14, 3, and 4 measured diffraction peaks that matched the literature values for K_2ZnCl_4. Comparison reveals glass machine treatment reduces detected K_2ZnCl_4 crystalline features by 17%, 75%, and 76% for 45.6% KCl – 54.4% $ZnCl_2$, 51.5% KCl – 49.5% $ZnCl_2$, and 70.0% KCl – 30.0% $ZnCl_2$ samples, respectively. Additionally, all KCl – $ZnCl_2$ containing samples had increased baseline signal compared to the X-ray diffraction results of the untreated samples. The increase in baseline signal could indicate a more non-homogeneous crystal structure compared to the untreated samples providing more evidence of amorphous character post treatment.[176]

Both the untreated and treated 68.0% KCl – 32.0% $MgCl_2$ sample had peaks in measured X-ray results matching the locations of KCl, $MgCl_2$, $KMgCl_3$, K_2MgCl_4, and $K_3Mg_2Cl_7$. The untreated 68.0% KCl – 32.0% $MgCl_2$ sample's X-ray diffraction peaks corresponded with 3, 3, 4, 6, and 5 detected lattice planes associated with KCl, $MgCl_2$, $KMgCl_3$, K_2MgCl_4, and $K_3Mg_2Cl_7$, respectively. The glass machine treated 68.0% KCl – 32.0% $MgCl_2$ sample's X-ray diffraction peaks corresponded with 1, 2, 1, 5, and 3 detected lattice planes associated with KCl, $MgCl_2$, $KMgCl_3$, K_2MgCl_4, and $K_3Mg_2Cl_7$, respectively. These results suggest a total reduction of crystalline character of 66%, 33%, 75%, 16%, and 40% for crystalline KCl, $MgCl_2$, $KMgCl_3$, K_2MgCl_4, and $K_3Mg_2Cl_7$, respectively. The measured X-ray diffraction pattern of the glass

machine treated 68.0% KCl – 32.0% $MgCl_2$ sample also had an increased baseline signal compared to the untreated sample, suggesting increased inhomogeneity in crystal structure.

All samples measured during this work demonstrated a phase change after being supercooled using the glass machine as measured by powder X-ray diffraction. Comparison of the potential phases that could contribute to the measured diffraction peaks yields insight into the degree of success in forming an amorphous metal chloride salt mixture. The X-ray diffraction results only qualitatively describe the degree of potential phase transformation through peak identification. Quantitative analysis of speciation based on measured X-ray diffraction results cannot be done due to the potential for multiple compounds to contribute to the same diffraction peak. While X-ray diffraction measurements show the reduction in number of detected peaks, broadening of detected peaks, and increase in baseline suggest increased amorphous character after glass machine treatment, a fully amorphous material should have no peaks in the measured range.

Comparing the measured X-ray diffraction patterns of the treated samples to literature shows that the species with the highest number of peaks matching measured values is K_2ZnCl_4, K_2ZnCl_4, K_2ZnCl_4, and K_2MgCl_4 for 45.6% KCl – 54.4% $ZnCl_2$, 51.5% KCl – 49.5% $ZnCl_2$, 70.0% KCl – 30.0% $ZnCl_2$, and 68.0% KCl – 32.0% $MgCl_2$ samples, respectively. Therefore, it is possible that the cooling rate during treatment was fast enough to hinder incongruent crystallization of varying crystal structures. This agrees well with the phase diagrams indicating the salt compositions of and KCl – $ZnCl_2$ and KCl – $MgCl_2$ used during this work that are shown in Figures 6.4.2 and 6.4.3. All three KCl – $ZnCl_2$ compositions pass through a phase of (K_2ZnCl_4 + liquid salt) prior to cooling and full solidification. Crystallization of K_2ZnCl_4 could have occurred first during supercooling with the glass machine resulting in the highest level of detection with X-ray diffraction measurements. The same explanation could be applied to the presence of the K_2MgCl_4 peaks in the treated 68.0% KCl – 32.0% $MgCl_2$ sample's X-ray diffraction pattern. X-ray diffraction measurements alone can only suggest a phase change but cannot quantitatively determine total amorphous character. Raman spectroscopy was utilized to further the analysis of phase change in the treated samples. Raman spectra for the untreated and treated samples was collected and overlayed for 45.6% KCl – 54.4% $ZnCl_2$, 51.5% KCl – 49.5% $ZnCl_2$, 70.0% KCl – 30.0% $ZnCl_2$, and 68.0% KCl – 32.0% $MgCl_2$ samples in Figures 6.4.13, 6.4.14, 6.4.15, and 6.4.16, respectively. Major peaks were identified and are shown in Tables 6.4.9 and 6.4.10.

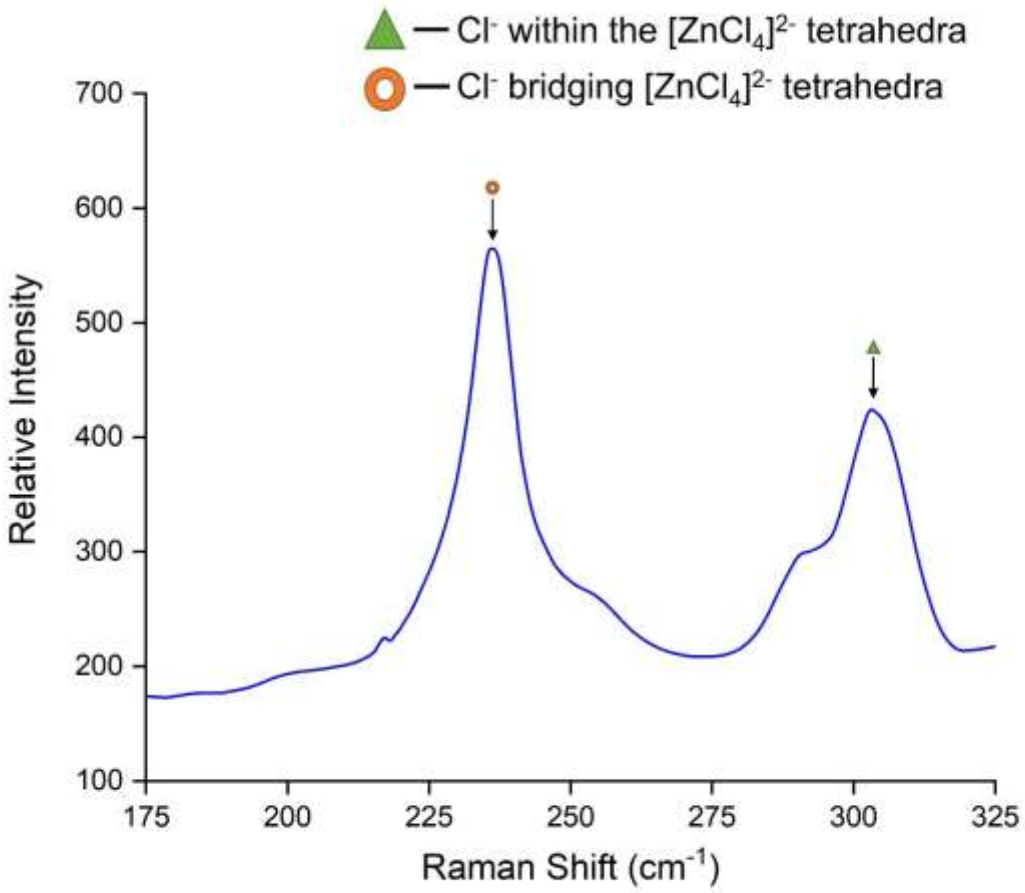

Figure 6.4.13 Results of Raman spectroscopy measurements for the 45.6% KCl – 54.4% $ZnCl_2$ salt mixture cooled from molten under ambient conditions.

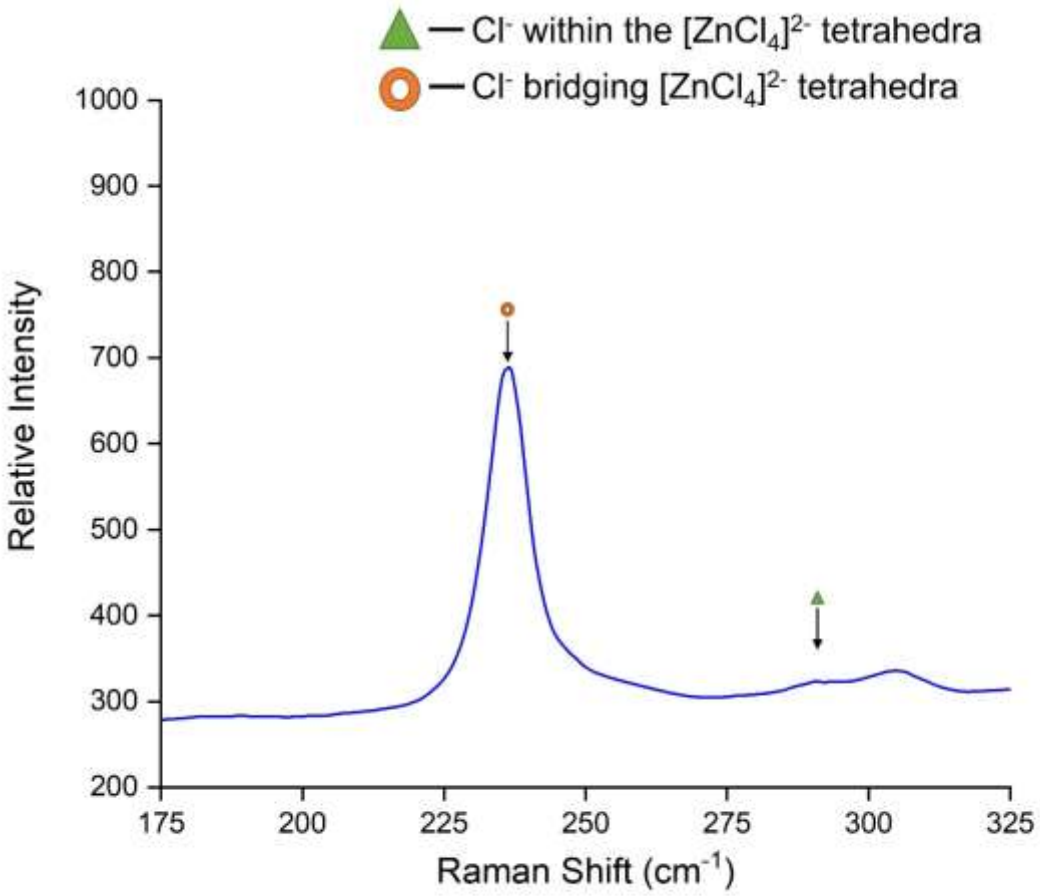

Figure 6.4.14. Results of Raman spectroscopy measurements for the 51.5% KCl – 49.5% $ZnCl_2$ salt mixture cooled from molten under ambient conditions.

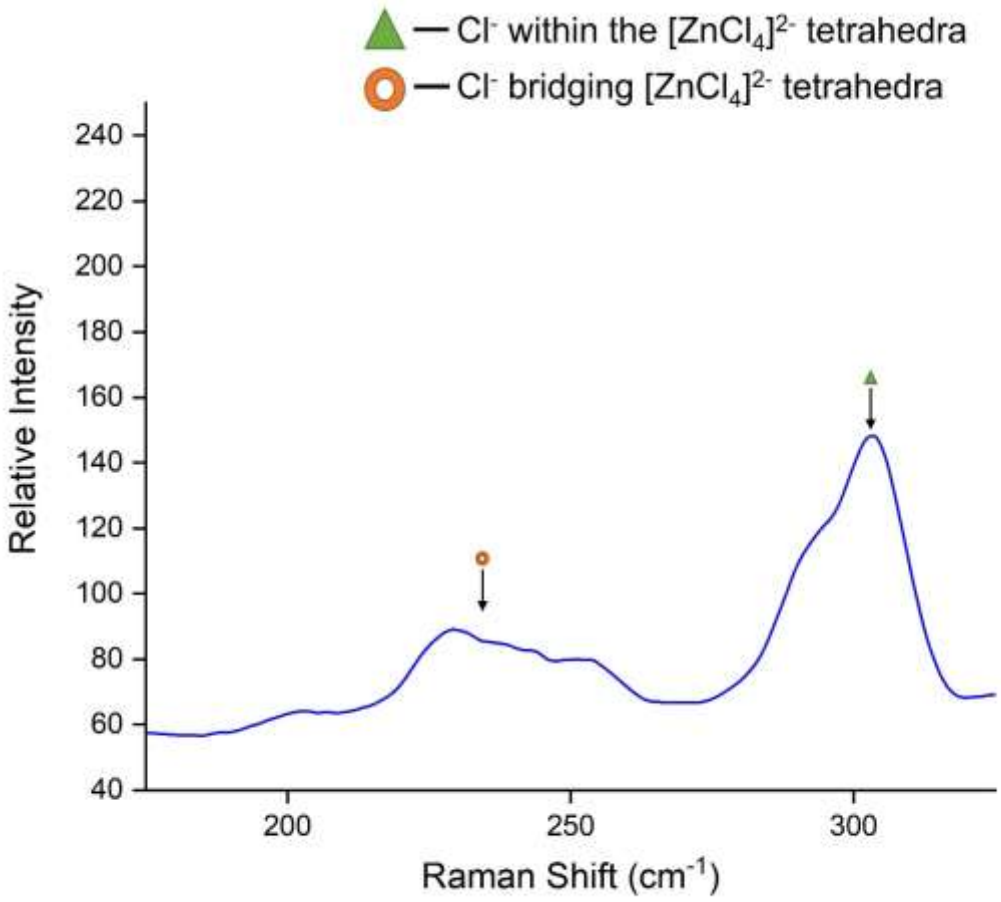

Figure 6.4.15. Results of Raman spectroscopy measurements for the 70.0% KCl – 30.0% $ZnCl_2$ salt mixture cooled from molten under ambient conditions.

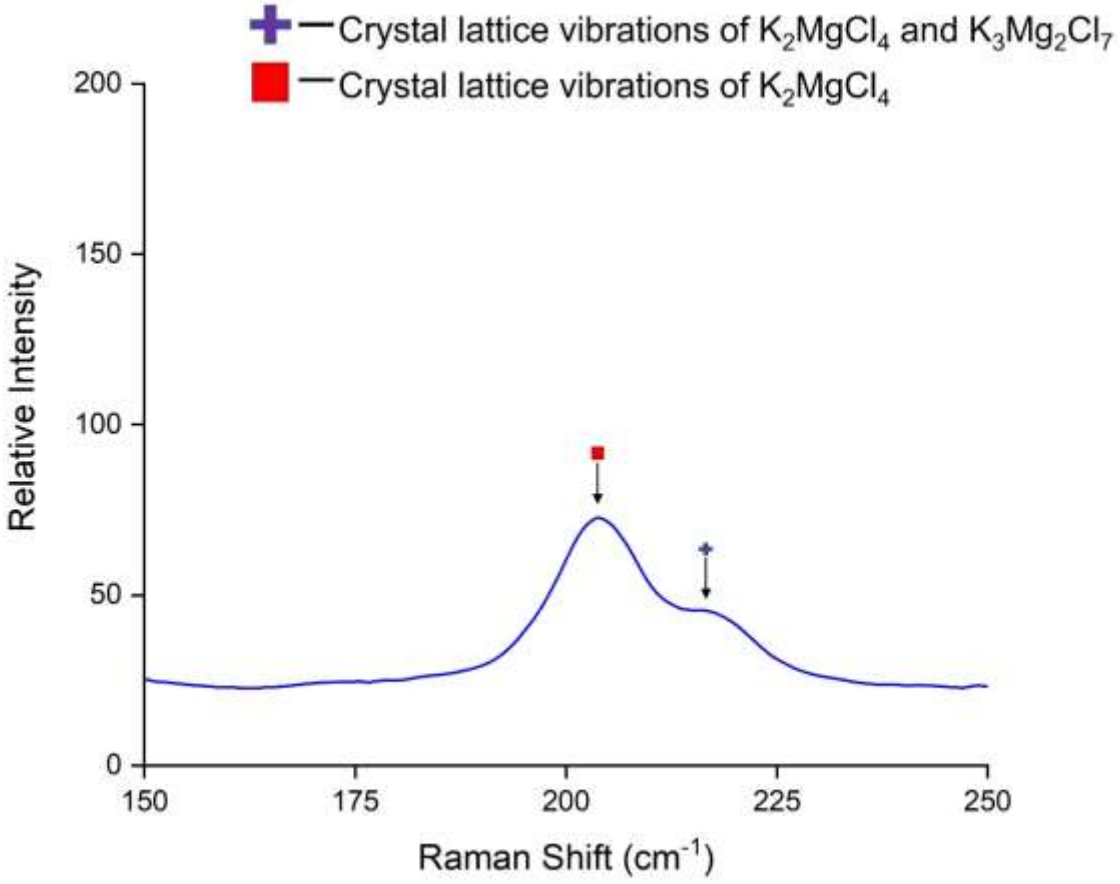

Figure 6.4.16. Results of Raman spectroscopy measurements for the 68.0% KCl – 32.0% $MgCl_2$ salt mixture cooled from molten under ambient conditions.

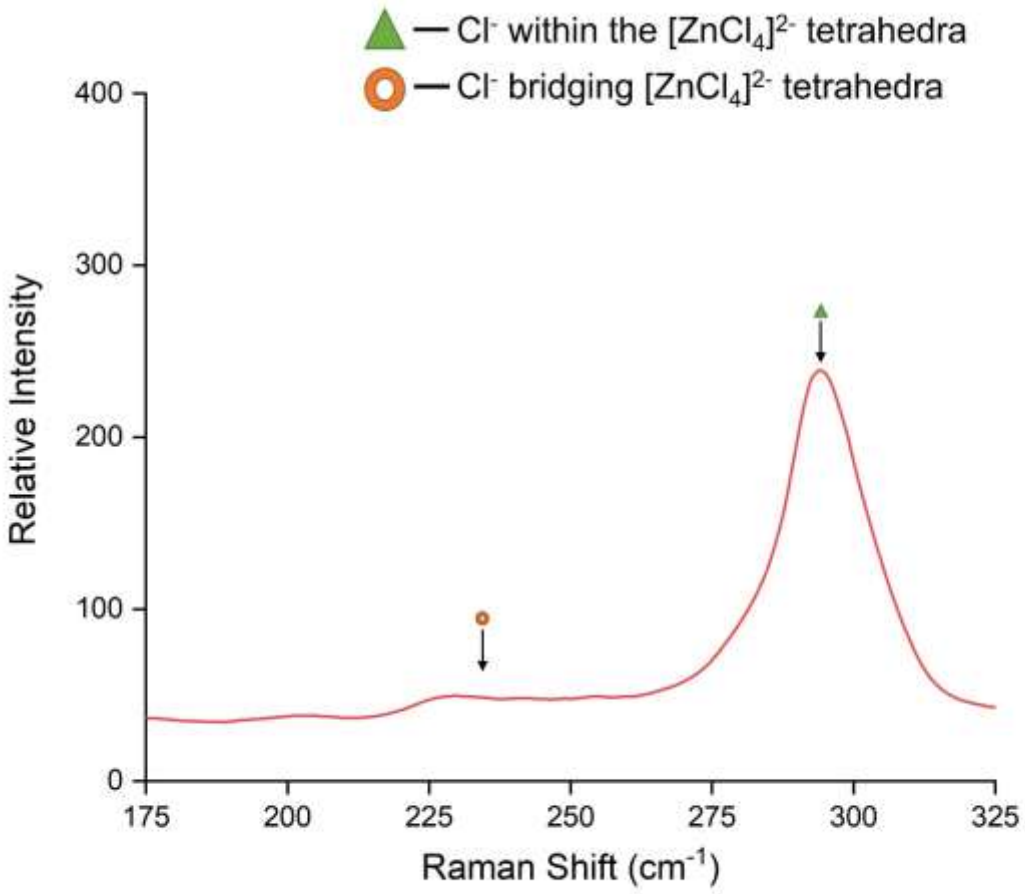

Figure 6.4.17. Results of Raman spectroscopy measurements for the 45.6% KCl – 54.4% $ZnCl_2$ salt mixture treated by the glass machine.

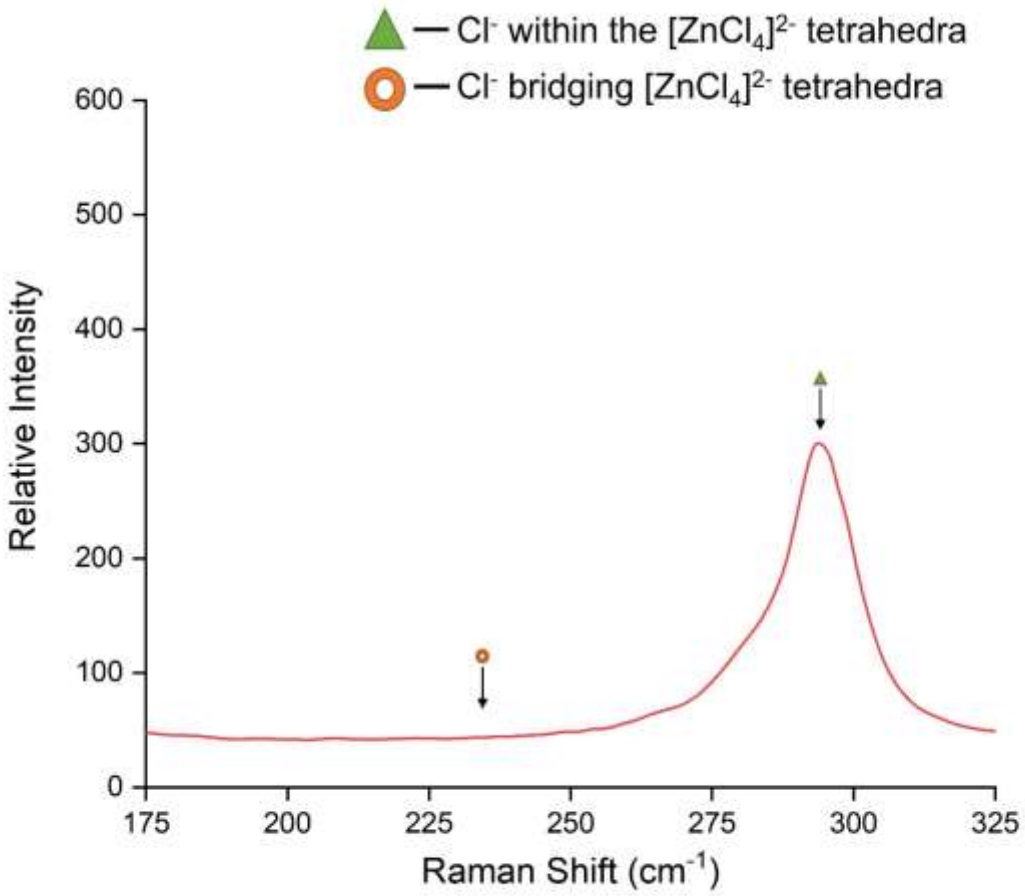

Figure 6.4.18. Results of Raman spectroscopy measurements for the 51.5% KCl – 49.5% $ZnCl_2$ salt mixture treated by the glass machine.

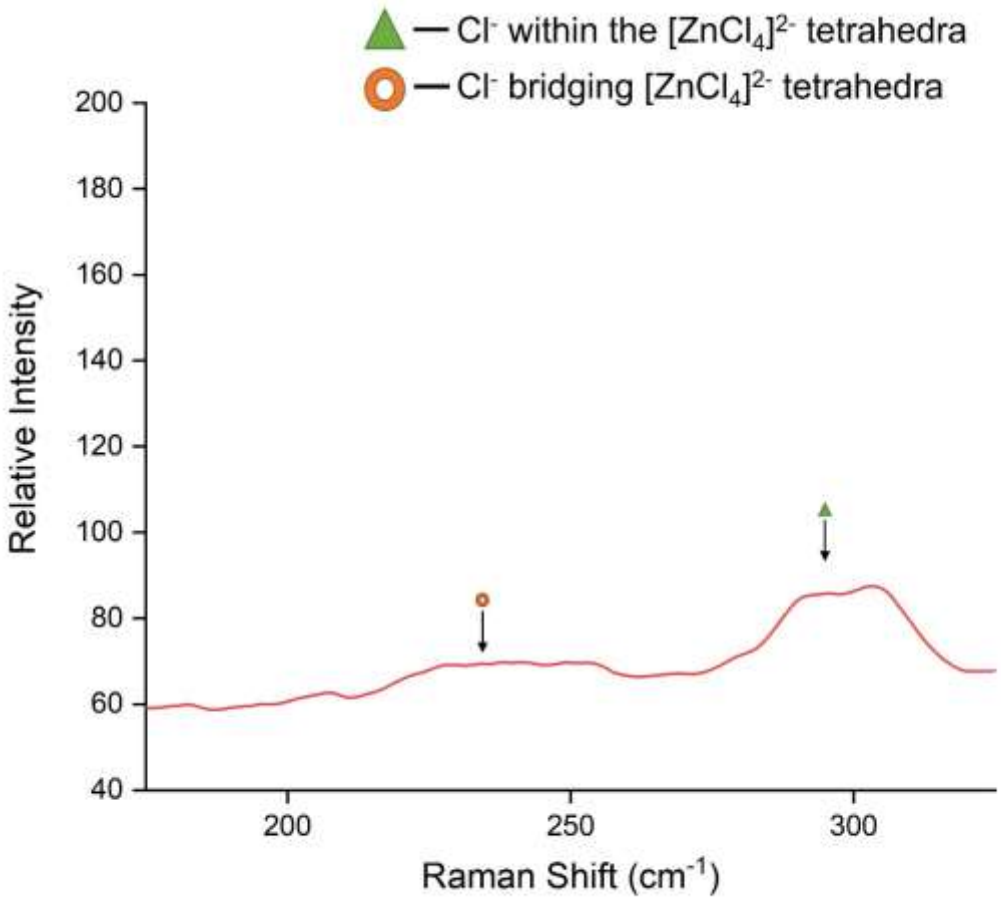

Figure 6.4.19. Results of Raman spectroscopy measurements for the 70.0% KCl – 30.0% $ZnCl_2$ salt mixture treated by the glass machine.

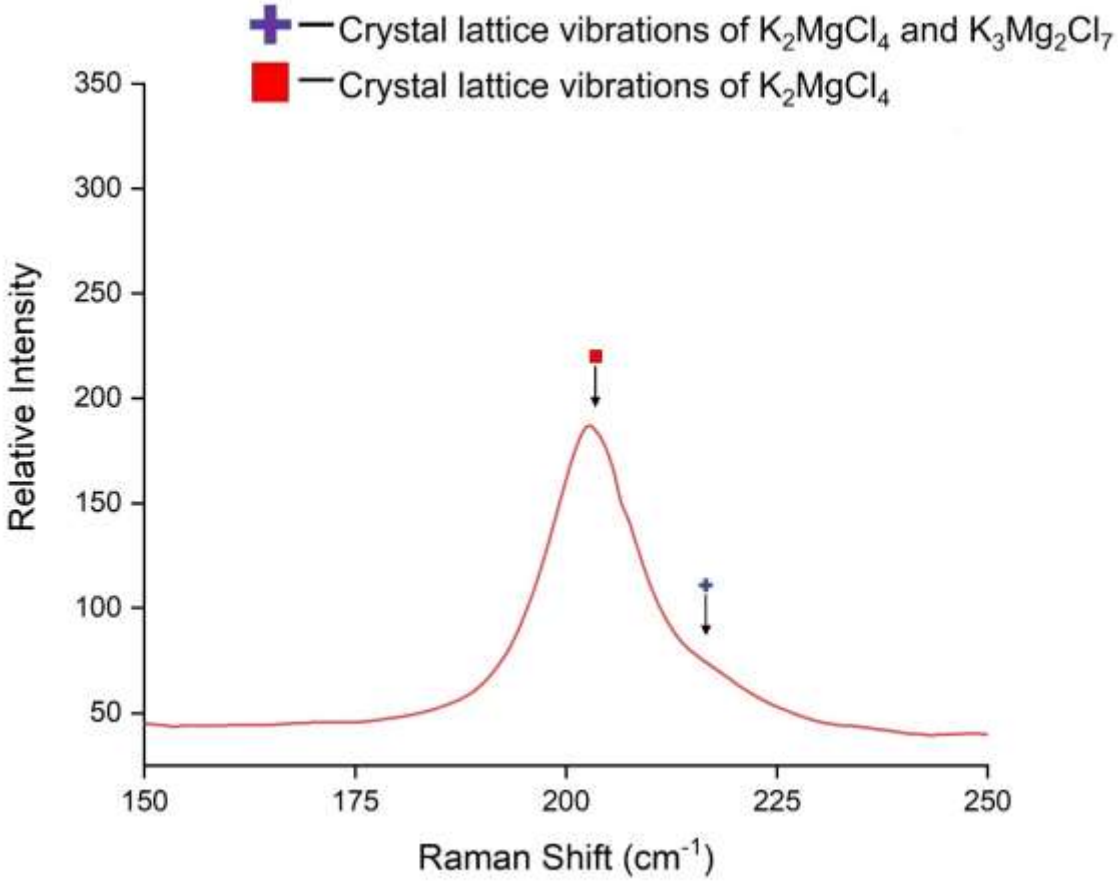

Figure 6.4.20. Results of Raman spectroscopy measurements for the 68.0% KCl – 32.0% $MgCl_2$ salt mixture treated by the glass machine.

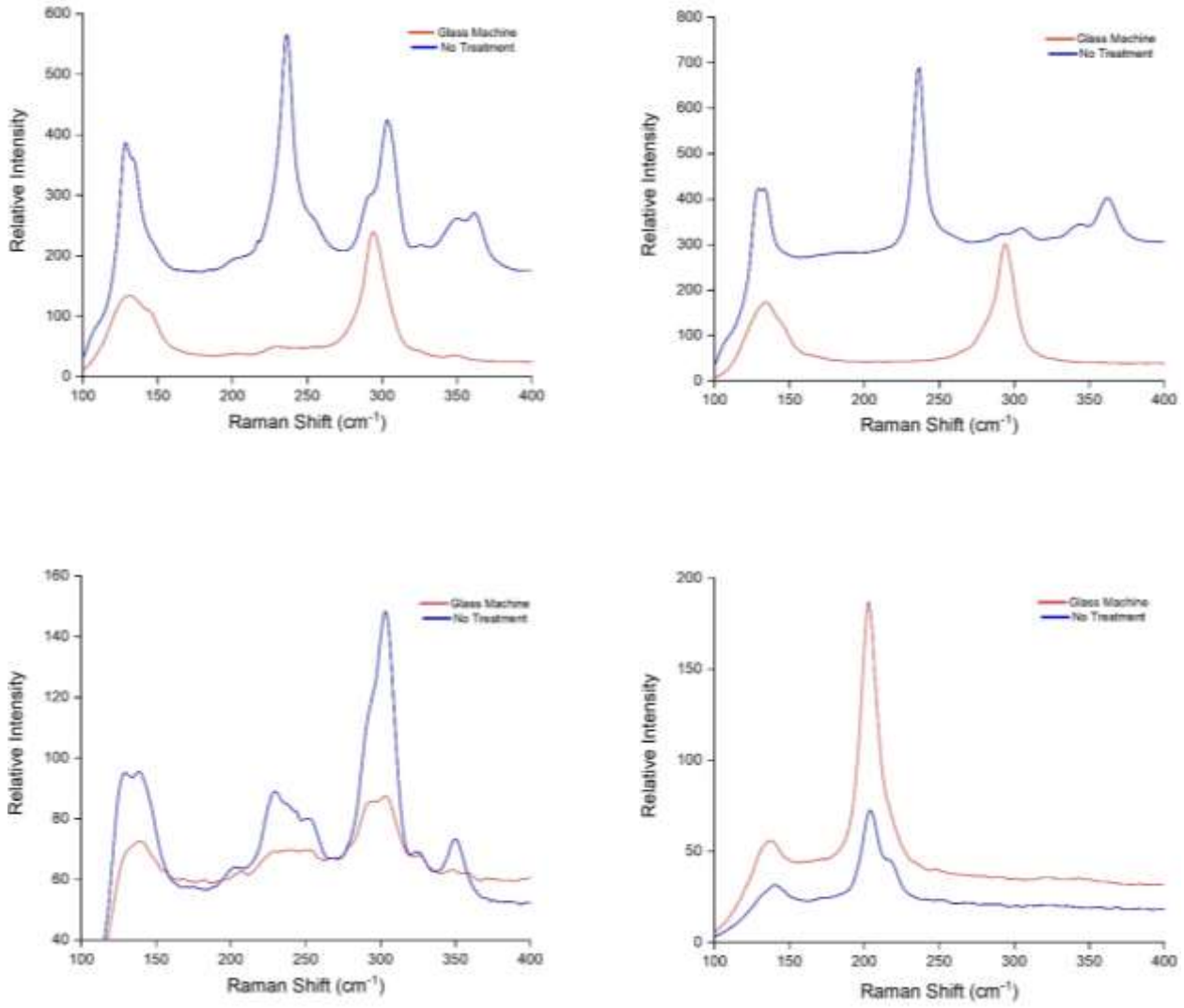

Figure 6.4.21. Results of Raman spectroscopy measurements for the 45.6% KCl – 54.4% $ZnCl_2$ containing salt mixture (top left), 51.5% KCl – 48.5% $ZnCl_2$ containing salt mixture (top right), 70.0% KCl – 30.0% $ZnCl_2$ containing salt mixture (bottom left), and 68.0% KCl – 32.0% $MgCl_2$ containing salt mixture. Blue line indicates no treatment (cooled from molten under ambient conditions) and red line indicates glass machine treatment.

Table 6.4.9. Identified peaks from Raman spectroscopy measurements for untreated 45.6% KCl – 54.4% $ZnCl_2$, 51.5% KCl – 49.5% $ZnCl_2$, 70.0% KCl – 30.0% $ZnCl_2$, and 68.0% KCl – 32.0% $MgCl_2$ (mole %) salt mixtures.

Salt Matrix	45.6% KCl 54.4% $ZnCl_2$	51.5% KCl 49.5% $ZnCl_2$	70.0% KCl 30.0% $ZnCl_2$	68.0% KCl 32.0% $MgCl_2$
Identified Raman Peaks (cm^{-1})	**236**	**236**	**229**	**204**
	302	**291**	**303**	**217**
	350	343	349	-
	362	362	-	-

Table 6.4.10. Identified peaks from Raman spectroscopy measurements for glass machine treated 45.6% KCl – 54.4% $ZnCl_2$, 51.5% KCl – 49.5% $ZnCl_2$, 70.0% KCl – 30.0% $ZnCl_2$, and 68.0% KCl – 32.0% $MgCl_2$ (mole %) salt mixtures.

Salt Matrix	45.6% KCl 54.4% $ZnCl_2$	51.5% KCl 49.5% $ZnCl_2$	70.0% KCl 30.0% $ZnCl_2$	68.0% KCl 32.0% $MgCl_2$
Identified Raman Peaks (cm^{-1})	293	294	240	202
	-	-	303	-

The untreated 68.0% KCl – 32.0% $MgCl_2$ sample contained peaks in measured Raman spectrum located at 204 cm^{-1} and 217 cm^{-1}. The peak that is located at 217 cm^{-1} is associated with incongruent melting of components and can be indicative of the presence of K_2MgCl_4, $K_3Mg_2Cl_7$, and KCl and can be matched to the lattice vibrations of the D_{2h} structure.[177] The peak at 204 cm^{-1} is associated with the out-of-plane rotary motion of the Cl^- in the crystalline sublattice and the presence of K_2MgCl_4. Consistent with the D_{4h} lattice vibrations of the $MgCl_6$ subunit oriented in a distorted octahedral arrangement.[178] The salt that was treated with the glass machine was also measured by Raman and contained only one relevant peak located at 202 cm^{-1}. The peak of the treated sample was more intense and broader than the untreated salt, but location of the peak maximum suggest it is a result of the lattice vibrations within the K_2MgCl_4 compound. This determination is supported by measured X-ray diffraction data (Figure 6.4.11) where all identified peaks match literature values of K_2MgCl_4.

The collected Raman spectra for the three KCl – $ZnCl_2$ mixtures contained peaks at approximately 230 cm^{-1}, 295 cm^{-1}, and 350 cm^{-1}. The samples containing 45.6% KCl – 54.4% $ZnCl_2$, 51.5% KCl – 49.5% $ZnCl_2$, had an additional peak located at 361 cm^{-1}. The peaks present at approximately 350 cm^{-1} and 361 cm^{-1} is potentially due to the crystal lattice vibrations of the $[ZnCl_3]^-$ species, but more likely due to hydrate contamination and background fluctuations or $ZnCl_2$ polymer.[179, 180] For this work, the two most important peaks are the two highly polarized bands occurring at approximately 230 cm^{-1} and 295 cm^{-1} present in all three measured KCl – $ZnCl_2$ mixtures. The lower frequency band occurring at approximately 230 cm^{-1} is attributed to the symmetric stretching mode of the tetrahedra containing mainly Zn-bridging Cl^- vibrations. The Cl^- bridges indicate a more extended crystalline network due to more connected tetrahedra, and therefore a higher degree of overall crystallinity. The higher frequency peak occurring at approximately 290 cm^{-1} is attributed to the non-bridging Cl- within the $[ZnCl_4]^{2-}$ tetrahedra.[181]

Measurements of 45.6% KCl – 54.4% $ZnCl_2$ and 51.5% KCl – 49.5% $ZnCl_2$ revealed one peak present in their Raman spectra with the apex located at 293 cm^{-1} and 294 cm^{-1}, respectively. The 70.0% KCl – 30.0% $ZnCl_2$ sample had two prevalent Raman peaks located at 240 cm^{-1} and 303 cm^{-1}. In the latter sample the signal for the peak located at 240 cm^{-1} is weak compared to the equivalent peak in the untreated sample. Therefore, the measured spectrum provides evidence of the presence of the symmetric lattice vibrations of the bridging Cl^- anions. The weaker signal

intensity at 240 cm^{-1} in the treated 70.0% KCl – 30.0% $ZnCl_2$ sample compared to untreated suggests that it is possible some reduction in bridging Cl^- atoms occurred, but the extent of the reduction cannot be quantified based on measurements. The signal located at approximately 240 cm^{-1} is reduced to background in the samples containing 45.6% KCl – 54.4% $ZnCl_2$ and 51.5% KCl – 49.5% $ZnCl_2$ can be indicative of amorphous character present in these two samples. The absence of detection for the bridging Cl^- atoms between the tetrahedra suggests reduction in size and connectivity of the crystalline subunits. The results of Raman spectroscopy measurements of the 45.6% KCl – 54.4% $ZnCl_2$ and 51.5% KCl – 49.5% $ZnCl_2$ samples and reduction of bridging Cl^- is in good agreement with the measured X-ray diffraction since those two samples demonstrated the largest reduction in diffraction peaks. The signal present in all three KCl – $ZnCl_2$ samples located at approximately 290 cm^{-1} does not provide insight into the extent of crystallinity change. This is because the detected vibration at this energy is related to the non-bridging Cl^- atom within the tetrahedra.

The results of the X-ray diffraction and Raman spectroscopy measurements indicate a change in crystallinity of the samples treated with the glass machine. The untreated salts in these two plots contain peaks that are within the range of the literature values for the crystalline KCl – $ZnCl_2$ system. For the glass machine treated salts, there is a distinct change in spectral peaks. The peaks for treated samples in 45.6% KCl – 54.4% $ZnCl_2$ and 51.5% KCl – 49.5% $ZnCl_2$ samples do coincide with the Raman spectra available in the literature for the salt in the molten state.[182, 183] The 68.0% KCl – 32.0% $MgCl_2$ sample shown in Figure 6.4.9 also confirms an alteration in the sample's crystallinity. The untreated sample contains the characteristic peak for mixed species of KCl and $MgCl_2$.[184] The comparison of the peak at approximately 210 cm^{-1} in the treated 68.0% KCl – 32.0% $MgCl_2$ sample shown in Figure 6.4.9 does correspond to the literature measured peak for the same 68.0% KCl – 32.0% $MgCl_2$ ratio in the molten state.[184] This indicates the likelihood of glass formation in the treated sample. Therefore, based on the measurements of x-ray diffraction coupled with Raman scattering, this work is the first-time formation of amorphous 68.0% KCl – 32.0% $MgCl_2$ glass. The results of this work and comparability to the Raman spectroscopy measurements available in the literature indicate similarities in structural features. Therefore, once the glass machine operation has been fully optimized and extent of crystallization after treatment quantitatively determined, then the processed materials can replace the high temperatures required for current experiments with room temperature glass containing a snapshot of the crystal structure.

The salt glass machine used in this work successfully created an amorphous structure of 45.6% KCl – 54.4% $ZnCl_2$, 51.5% KCl – 48.5% $ZnCl_2$, 70.0% KCl – 30.0% $ZnCl_2$ and 68.0% KCl – 32.0% $MgCl_2$. These results are the first time these compositions have successfully frozen in the amorphous state. The success of these experiments indicates that the glass machine can be extended to other compositions of chloride-based salts. More analytical tools are required to provide more in-depth insight into the extent of crystallinity reduction. Once confirmation of magnitude of phase change is complete, the utilization of this machine can result in room temperature measurements of salts containing the liquid structure. Allowing for the reduction of cost and complications associated with performing analytical experiments on chloride salts at high temperatures.

6.5 Impact of Research Progression

A vitrification apparatus was designed, built, and utilized to vitrify four different mixtures of metal-chloride salts. Analysis of products via X-ray diffraction and Raman spectroscopy confirmed successful completion of the research objective of building a device that can vitrify molten chloride salts. The impact of the creation of the vitrification apparatus presented in this work is the ability to create amorphous metal chloride at room temperature. The apparatus contains several advantages over the current commercially available quenching apparats. The first is the extent of temperature control via the furnace encasing an alumina tube. Current methodologies for glass forming heat material and it is dropped and quenched with no thermal control during the drop time. The apparatus developed during this work can more finely tune the materials temperature in the time before quenching. This provides a higher control on processing parameters. The next advantage is the supercooled rollers provide a higher thermal gradient during quenching. A larger thermal gradient will result in shorter time frame of cooling that leads to a smaller likelihood of crystal formation compared to current non-LN2 cooled apparats. Lastly, the adjustability of the rotation speed and width of the rollers allows for more control over the physical characteristics of the product than current splat quench apparats. The advantages of the apparatus designed during this work will impact the design of comparable machines currently commercially available. Additionally, this work could impact vitrification of other materials such as bulk metallic glasses.[185]

This work has the potential to substantially impact the field of experimental studies related to the solution state properties of molten chloride salts by allowing measurements at room temperature. As outlined earlier in this chapter, there are numerous complications related to high temperature experiments. Providing amorphous room temperature metal chloride salt samples will allow experimental examination of solution state chemistry. This will greatly improve the speed and safety of most experiments and reduce the handling difficulties of the materials. In addition, many molten chloride salts are corrosive in the molten state requiring experimental containment apparats to be single use. If the same experiments can be conducted with a room temperature solid then there will be no need for custom single-use containment vessels during each experiment, reducing experimental costs. Finally, due to the reactivity of salt with containment vessels and other sources of contamination, the salt is usually discarded after each experiment. Conducting the experiment with solid salt at room temperature will reduce the likelihood of contamination allowing the same sample to be used for more than a single analysis. The ability to reuse samples would be especially advantageous when using complementary analytical techniques that require a variety of measurements.

6.6 Future Directions

While the analysis of the treated product of this work demonstrated alteration in crystal structure based on X-ray diffraction and Raman spectroscopy measurements, the extent of crystallinity in the samples is not quantified. The next step to further the development of the salt glass machine methodology would be to examine the extent of crystallization in the treated samples in a more quantitative manner. Many computational approaches have been utilized to predict structure of amorphous solids such as reverse Monte Carlo modelling, molecular dynamics simulations, and density functional theory.[186-188] Experimental techniques have also been utilized to examine structure of amorphous materials including X-ray diffraction, neutron diffraction, X-ray absorption fine structure, angstrom/nano beam electron diffraction, high resolution transmission electron microscopy, and fluctuation electron microscopy.[189-193] Each of the above techniques provide further insight into the local atomic structuring in amorphous solids, but none provide a comprehensive view of the full three dimensional picture. The past approaches have only

been qualitative and have impeded the full understanding of crystal-amorphous and glass transition and the full three-dimensional structure.[194]

According to Yang et al, the extent only available experimental methodology that can directly determine the full three dimensional atomic positions in glass samples is atomic electron tomography.[195] Atomic electron tomography utilizes iterative algorithms combined with high-resolution tomographic tilt to resolve the atomic structure of materials without assuming crystallinity.[196] This technique has previously been used successfully to quantitatively determine many details of atomic scale structuring of various materials.[197-199] It is possible to apply the atomic electron tomography technique to the metal chloride salts treated by the glass machine to quantitatively define extent of crystallinity. This will be accomplished through analysis of the short- and medium-range order as determined by the experiment.

Short-range ordering characterizes the local atomic arrangement by identifying the nearest neighbor atoms around each central atom to form a Voronoi polyhedron.[200] The identification of the most abundant Voronoi polyhedron and associated geometries will result in quantitative confirmation of extent of crystallization for two reasons. First, the crystal structure of solid metal chloride salts relevant to molten salt research is generally well known. Comparison of the atomic electron tomography measured local structures with literature crystal structures will determine the quantity of local clusters that match the arrangement of the crystalline solid. Secondly, the measurements will provide the extent of geometric ordering within the glass machine treated product. A high degree of geometric disordering is observed in in bulk metallic glass material and will also be observed in a metal chloride glass.[201] Furthermore, the atomic electron tomography technique can also quantify medium-range structural organization which is defined as nanometer-scale structural details beyond the nearest neighbor.[202] Through determination of large scale arrangement, the measurements will provide details of crystal growth within the amorphous matrix of this work.

Once the presence of amorphous character is quantitatively determined through the atomic electron tomography technique, then the glass machine can be used to create many types of materials of interest for molten salt research. For example, nanoparticles suspended in molten metal chloride solutions are of interest for heat transfer applications as outlined in more detail in the next chapter. Crystallization of the metal chloride matrix upon cooling necessitates maintaining

salt in the molten state at high temperatures to perform analytical experiments to quantify the colloid's structure in solution. By utilizing the glass machine in this work, the colloid can be frozen in the amorphous state allowing measurements to be made at room temperature. The solution structure can also be quantified at room temperatures to understand solvent-solvent interactions within the salt matrix. The same could be said for solvent-solute interactions including fissile material, fission products, and corrosion products. This technique will likely prove to be especially useful in quantifying the solvent-solute interactions for fissile materials. Many user facilities require exhaustive containment with many redundancies to measure fissile materials at elevated temperatures due to radioactivity and associated volatilization concerns. Some disallow heating of radioactive materials regardless of containment. Supercooling the chloride salts containing radioactive materials will allow room temperature measurements that will have a substantial impact in moving forward the collective understanding of molten chloride salts.

6.7 Conclusion

In this chapter, a novel glass forming machine was designed to freeze 45.6% KCl – 54.4% $ZnCl_2$, 51.5% KCl – 48.5% $ZnCl_2$, 70.0% KCl – 30.0% $ZnCl_2$ and 68.0% KCl – 32.0% $MgCl_2$ in an amorphous state. The crux of the design enabled mixtures to be cooled from 700 ^oC to -196 ^oC. The results of the X-ray diffraction and Raman spectroscopy demonstrated a change in crystallinity when the measurements of treated samples were compared to untreated samples from the same original batch. Comparing the results of X-ray diffraction results of this work to the literature values revealed reduces detected KCl crystalline features by 60%, 80%, and 85% for 45.6% KCl – 54.4% $ZnCl_2$, 51.5% KCl – 49.5% $ZnCl_2$, and 70.0% KCl – 30.0% $ZnCl_2$ samples, respectively. Treatment reduces detected $ZnCl_2$ crystalline features by 0%, 75%, and 62% for 45.6% KCl – 54.4% $ZnCl_2$, 51.5% KCl – 49.5% $ZnCl_2$, and 70.0% KCl – 30.0% $ZnCl_2$ samples, respectively. Treatment reduces detected K_2ZnCl_4 crystalline features by 17%, 75%, and 76% for 45.6% KCl – 54.4% $ZnCl_2$, 51.5% KCl – 49.5% $ZnCl_2$, and 70.0% KCl – 30.0% $ZnCl_2$ samples, respectively. The 68.0% KCl – 32.0% $MgCl_2$ sample had a total reduction of crystalline character of 66%, 33%, 75%, 16%, and 40% for crystalline KCl, $MgCl_2$, $KMgCl_3$, K_2MgCl_4, and $K_3Mg_2Cl_7$, respectively. All measured Raman spectra for KCl – $ZnCl_2$ containing samples demonstrated a reduction in the lower energy peak associated with bridging Cl^- anions. Measured Raman spectra for KCl – $MgCl_2$

containing samples demonstrated a reduction in number of detected species present when compared to previous literature measurements.

The results of the X-ray and Raman spectroscopy measurements of the glass machine treated salt demonstrate a reduction in crystalline features when compared to the untreated sample. These results demonstrate that the glass machine treatment successfully alters the crystal structure of $KCl - ZnCl_2$ and $KCl - MgCl_2$ material. The reduction of detected crystalline features confirms successful completion of the research objective. Vitrification of molten metal chlorides is completed successfully through treatment with the glass machine and subsequent confirmation via X-ray diffraction and Raman spectroscopy analysis. Further investigation is required to assess the degree of remaining polycrystalline structures within the treated salt matrix. This can be accomplished by completing measurements of the treated salt utilizing atomic electron microscopy to map the chemical structure of the solid on the atomic scale as outlined in section 6.6. The success of freezing amorphous metal chloride salts will enable increased ability of analytical measurements to understand chemical structure. Room temperature measurements will allow more variation in the type of analytical measurements that can be utilized for chloride salts.

Chapter 7. Molten Chloride Ferrofluid

7.1 State of the Field

Chloride salts have the advantage of some of the lowest production costs of all molten salt mixtures being considered for high-temperature thermal energy storage and heat transfer. The large disadvantage of chloride salts for this application is their relatively low specific heat capacity compared to other molten salt mixtures. Mohan et al. compared the cost of various metal-chlorides, -fluorides, -carbonates, and -hydroxide salts that have previously been considered for as candidates for application.[203] Additionally, the same author compared the costs of the production of candidate salts to their melting point. The results of the findings of Mohan et al. comparing the molten salt candidate's price/heat capacity and price/melting temperature are reproduced in Figure 7.1.1 and Figure 7.1.2, respectively.

Increasing the specific heat capacity is directly proportional to efficiency of the heat transfer fluid in application. Therefore, increasing the specific heat capacity of the lower cost chloride salts will greatly benefit their potential for applications. It has already been shown that the addition of nanoparticles creates a molten salt nanofluid that has increased specific heat capacity.[204] It is believed the increase of specific heat capacity is due to the formation of a new phase that has a semi-ordered structure and this more dense phase significantly enhances the molten salt's thermal properties.[205] It has been shown in lower temperature nanofluids that interact with an external magnetic field, or ferrofluids, addition of the magnetic nanoparticles affects the thermal and physical properties of the solution. Additionally, the extent of alteration of solution's physical properties is dependent on the properties of the external magnetic field, covered in more detail in section 7.1.2. There is no information available in the literature regarding molten metal chloride ferrofluid in any capacity. Therefore, the work presented in this chapter advances the state of the field by creating and evaluating a molten metal chloride ferrofluid for the first time. Formation of the ferrofluid is evaluated in the chloride salts being considered for application with the lowest specific heat capacity shown in Figure 7.1.1. These two salts are also the lowest melting mixture (228^{o} KCl – $ZnCl_2$) and the highest melting mixture (456^{o} KCl – $MgCl_2$) of chloride-based salts being considered for application (Figure 7.1.2). Proof of colloidal, chemical, and magnetic stability of the solution indicates the possibility of external magnetic field induced control of heat capacity and transfer properties in molten chloride salts.

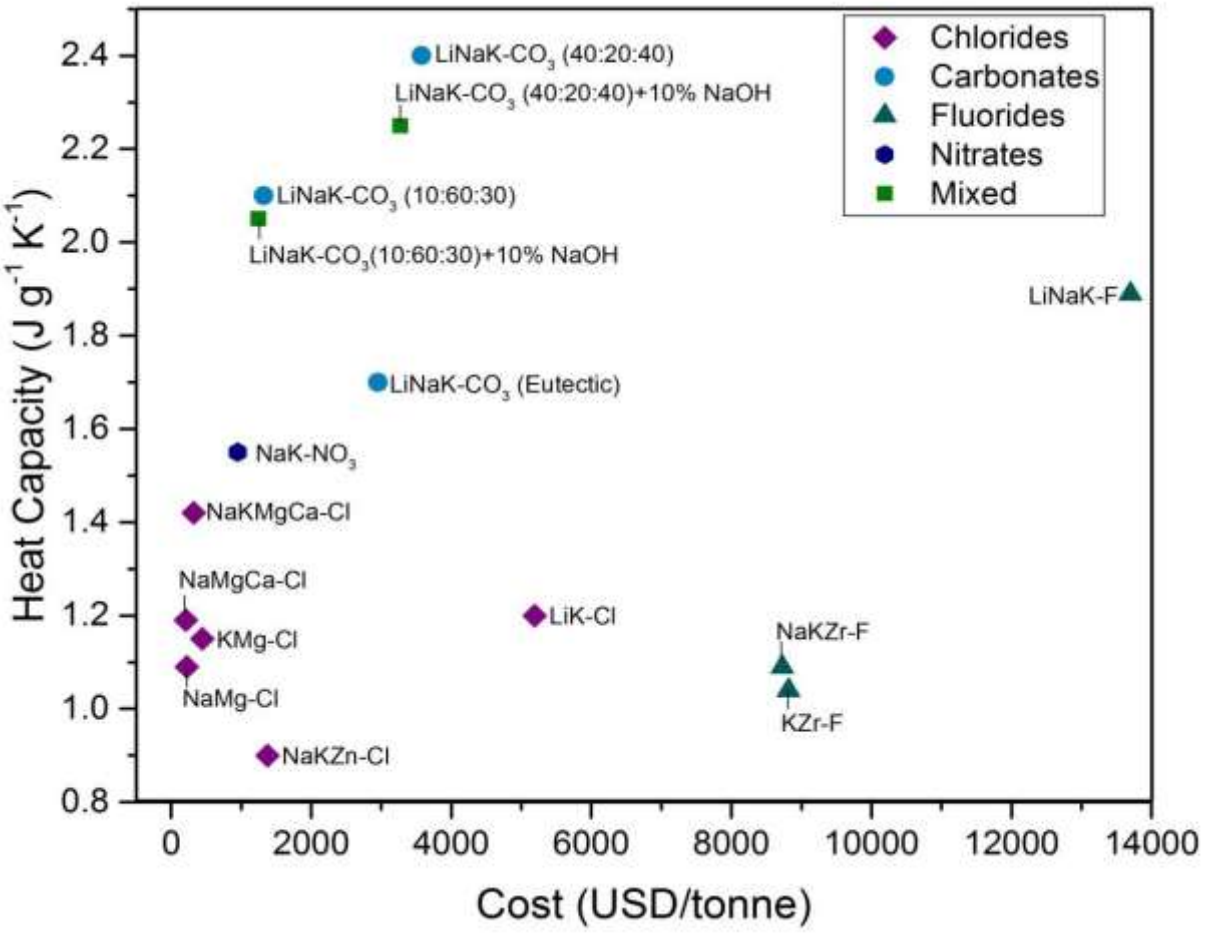

Figure 7.1.1. Summary of cost per unit mass versus heat capacity. Reprinted from *development of high-temperature sensible thermal energy storage systems for advanced concentrating solar power generation.*[203]

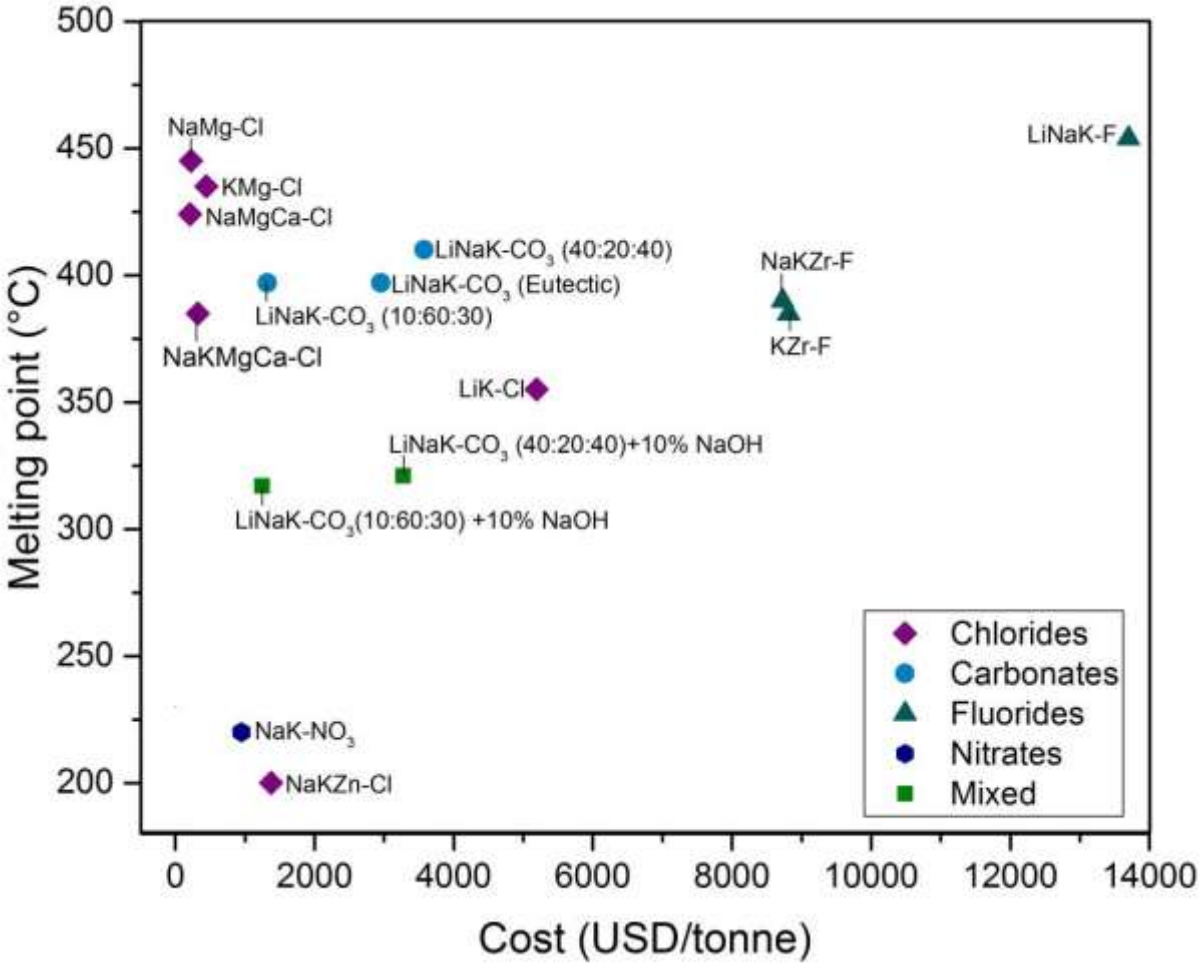

Figure 7.1.2. Summary of cost per unit mass versus melting temperature. Reprinted from *development of high-temperature sensible thermal energy storage systems for advanced concentrating solar power generation.*[203]

7.2 Introduction

A nanofluid is a colloidally stable suspension containing nanometer size particles that are inseparable from the bulk of the solution.[61] A specific subset of nanofluids involves the formation of a suspension containing magnetic nanoparticles called ferrofluid. In ferrofluid systems, the bulk solution assumes the magnetic properties of the suspended magnetic nanoparticles.[206] Ferrofluid is a relatively new class of materials, first produced by NASA in the 1960's for application in rotating shaft seals.[207] The liquid solution containing a small amount (typically 1.0% - 10.0% particles by weight) of nanometer size particles that form a colloidally stable suspension.[208] Since inception, there has been vast amounts of research done related to these magnetic solutions. The solutions have found application throughout many different industrial sectors. More recently, they have been examined for use in heat transfer applications related to small electronic devices.[209] Most of the research done toward ferrofluids has been carried out at the micro-scale although the scaling of these findings to industrial applications is believed to be possible.[210]

Molten salt is a high temperature fluid that has unique properties such as low vapor pressure, moderate viscosity, high boiling point, and little structural effect from high energy radiation.[211] Due to peculiar properties of molten salt it has been shown to be an ideal fluid for use in nuclear reactor systems.[212] Currently, implementation of molten chloride salt reactors as the most recent Generation IV design has become a large focus of the Department of Energy research consortium.[213-215] Much of the focus of this research has been into atomic level structure and speciation within different salt matrices of interest. This effort has been driven in hopes of optimizing systems for full scale implementation to replace current nuclear energy systems. One of the largest physical property drawdowns of molten salt is a characteristic low specific heat capacity (C_p). If colloidal stability can be achieved while also retaining magnetic properties of the solution, then the resulting implications for next generation HTF could be immense. It has been shown previously that the addition of non-magnetic nanoparticles to molten chloride media can increase the specific heat capacity of the fluid.[63] In addition to measurements of Cp when particles have been added, molten salt matrices have demonstrated colloidal stability with a myriad of various types of particles.[62] The physical parameters through which colloidal stability is governed give rise to interesting physical implications of using these materials in molten salts at ultra-high temperatures.

Ferrofluid has become a well-examined area of academic research in recent years.[216] Even so, little to no research effort has been given to the study of ultra-high temperature ferrofluids. This is due to the relatively low value of T_C related to most classes of magnetic materials. One place where materials that contain a characteristically high T_C values can find application is within molten salt media. No academic research has been focused on the possibility of dispersing magnetic nanoparticles in chloride based molten salts to form a molten chloride ferrofluid. This work represents the first-time investigation into the properties of molten chloride ferrofluid. Accomplished through synthesis of ferrofluid and subsequent examination of solution's magnetic susceptibility utilizing a novel experimental apparatus. For ferrofluid to maintain its magnetic properties, the hottest temperature of a heat exchanger must not exceed the Curie temperature (T_c) of the nanoparticles. Upon reaching T_c magnetic materials undergo a phase transition, permanently losing magnetic properties. As ferromagnetic material approaches T_c, there is a non-permanent loss of magnetism, which varies depending on the type of material. A visualization of a materials magnetic properties relative to increasing temperature can be seen in Figure 7.2.1.

It has been shown extensively that the addition of magnetic nanoparticles to solutions can dramatically affect the specific heat capacity (C_p) of the entire solution.[66-76] The increased C_p of the solutions examined during previous experiments was variable depending on the magnitude of magnetic field exposed to the solution.[217-219] In addition to the variability of C_p, previous literature also determined that the solution viscosity could be varied according to magnetic field parameters.[220, 221] The application for heat transfer fluid (HTF) that contains magnetic properties may not be limited to small electronic devices. If similar control over physical properties of the ferrofluid solution demonstrated in other liquids is true for molten salt ferrofluid, then this would be advantageous for application as a heat transfer fluid. This potential impact on application motivated this work to determine the ability of molten chloride solutions to form a ferrofluid. For ferrofluid to maintain its magnetic properties, the hottest temperature of a heat exchanger must not exceed the Curie temperature (T_c) of the nanoparticles. Upon reaching T_c magnetic material undergoes a phase transition, permanently losing magnetic properties.[222] As ferromagnetic material approaches Tc, there is a non-permanent loss of magnetism. The temperature and magnitude that reduction of magnetism occurs varies depending on the material's composition.

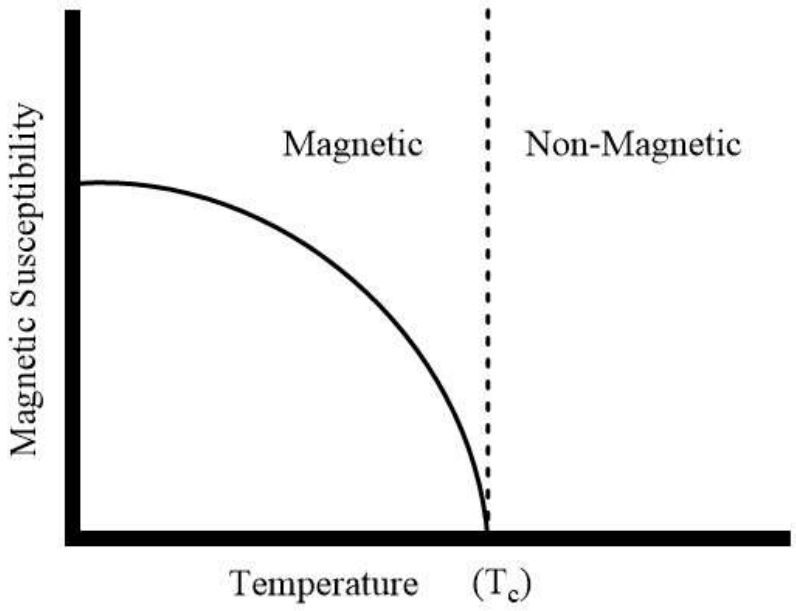

Figure 7.2.1. Depiction of material's magnetic field decreases with increasing temperature approaching the Curie Temperature.

In an externally applied magnetic field the critical values needed for solution stability have been derived.[223] These equations allow for the calculation of maximum particle diameter allowed for colloidal stability (d) as it relates to gravity (d_G), applied magnetic field (d_{AMF}) and particle-particle interaction (d_P). Equations for d_G, d_{AMF}, and dp are shown in Equations 7.2.1, 7.2.2, and 7.2.3, respectively.

$$d_G < \left(\frac{6K_BT}{\pi(\rho_p - \rho_{bf})gh}\right)^{\frac{1}{3}} \tag{7.2.1}$$

$$d_{AMF} < \left(\frac{6K_BT}{\pi\mu_0 M_{s,p} H_{Max}}\right)^{\frac{1}{3}} \tag{7.2.2}$$

$$d_P < \left(\frac{144K_BT}{\pi\mu_0 M_{s,p}^2}\right)^{\frac{1}{3}} \tag{7.2.3}$$

Such that Boltzmann constant (K_B), magnetic permeability of vacuum (μ_0), nominal gravity (g), saturation magnetization of nanoparticle $(M_{s,p})$, maximum magnetic field intensity (H_{Max}), density of nanoparticles (ρ_p), density of base fluid (ρ_{bf}), fluid height (h), and solution temperature (T).

It is important to note the implications of the above equations. In nearly all ferrofluids that have thus far been studied, the solution in which the particles are suspended is composed of either water or some organic solvent.[224] It can be shown in the above equations that the diameter of the particles can only be increased by increasing the temperature of the base fluid. Meaning in application that the magnitude of the magnetic field that can be imparted by the ferrofluid is limited by solution temperature. The working temperature in molten salt reactors is magnitudes above that of water or any organic liquid. If these equations hold true at the ultra-high temperature of molten

salt reactors, then the magnetic force available will be much larger than what has been studied previously. This presents a unique opportunity to examine a new class of magnetic ultra-high temperature heat transfer fluids with application beyond nuclear reactors.

This work examines the formation of stable colloids in molten chloride matrices. This is achieved using four particles of different materials and sizes. The particles used were iron oxide Fe_2O_3, carbon coated iron, carbon coated cobalt, and cobalt iron oxide with diameters of 8 nm, 25 nm, 30 nm, and 50 nm, respectively. For simplification, the particle types are abbreviated as IO, CCI, CCCo, and CIO. Each of these particles were then dispersed into two types of chloride media, all added in eutectic ratios including $KMgCl_3$ and $ZnKCl_3$. After initial experiments, the best suited material was determined to be cobalt nanoparticles and various sizes of cobalt particles were used. Only the particles consisting of IO, CCI, CCCo, and CIO were utilized for theoretical calculations to determine preliminary feasibility of forming a colloidally stable solution (Equations 7.2.1 – 7.2.3).

If it is true that d_{AMF}, d_G, and d_P from equations 7.2.1-7.2.3 can only be increased through change in temperature, then high temperature molten chloride salt media would be the ideal candidate. To approximate the efficacy of this, the following values of constants were used to solve for d_{AMF}, d_G, and d_P: K_B is 1.3806×10^{-23} $J\cdot K^{-1}$, 1.2566×10^{-6} H/m^{-1} μ_0, nominal gravity (g) is 9.81 $m\cdot s^{-2}$, magnet specific H_{max} is $5.28x10^5$ $A\cdot m^{-1}$, density of nanoparticles ρ_p is 5.24 $g\cdot cm^{-1}$, 7.87 $g\cdot cm^{-1}$, 1.14 $g\cdot cm^{-1}$, and 5.23 $g\cdot cm^{-1}$ for IO, CCI, CCCo, and CIO, respectively. Density of base fluid ρ_{bf} is 2.2, 2.8, and 2.6 for $KMgCl_3$, $ZnKCl_3$, and $AlNaKCl_5$, respectively. Values of $M_{s,p}$ for IO, CCI, CCCo, and CIO $8.8x10^4$, $2.18x10^5$, $1.63x10^5$, and $7.5x10^4$, respectively.[225] Using the values specified above and the experimental temperatures used during this work the particle sizes needed for maintenance of colloidal stability can be calculated.

The results of calculating d_g as shown in Table 7.2.1 – 7.2.3, confirm the ability for the particles to maintain colloidal stability at increased temperatures. The theoretical calculations for d_p show the increase in size of particle that can be used to form the colloid is substantial as the temperature increases. Due to the increased activity within the solution, the temperature increases. The elevated Brownian motion of the particles at 800°C allows for a smaller statistical likelihood of agglomeration if no other physical characteristics are accounted for.

Table 7.2.1. Maximum theoretical particle size in nanometers for colloidal stability condition as related to gravity (d_g) for iron oxide (IO, 8 nm), carbon coated iron (CCI, 25 nm), carbon coated cobalt (CCCo, 50 nm), and cobalt iron oxide (CIO, 30 nm) in $KMgCl_3$ and $KZnCl_3$.

Salt Matrix	*Particles*	d_G *25°C*	d_G *200°C*	d_G *400°C*	d_G *600°C*	d_G *800°C*
$KMgCl_3$	IO	133	155	174	190	204
	CCI	164	191	215	234	251
	CCCo	173	201	226	247	264
	CIO	133	155	174	190	203
$ZnKCl_3$	IO	123	144	162	177	189
	CCI	158	184	207	225	241
	CCCo	167	195	219	239	256
	CIO	123	144	162	176	189

Table 7.2.2. Maximum theoretical particle size in nanometers for colloidal stability condition as related to applied magnetic field (d_{AMF}) for iron oxide (IO, 8 nm), carbon coated iron (CCI, 25 nm), carbon coated cobalt (CCCo, 50 nm), and cobalt iron oxide (CIO, 30 nm).

Particles	d_{AMF} *25°C*	d_{AMF} *200°C*	d_{AMF} *400°C*	d_{AMF} *600°C*	d_{AMF} *800°C*
IO	5	6	7	7	8
CCI	4	4	5	5	6
CCCo	4	5	5	6	6
CIO	5	6	7	8	8

Table 7.2.3. Maximum theoretical particle size in nanometers for colloidal stability condition as related to particle-particle interactions (d_p) for iron oxide (IO, 8 nm), carbon coated iron (CCI, 25 nm), carbon coated cobalt (CCCo, 50 nm), and cobalt iron oxide (CIO, 30 nm).

Particles	d_P *25°C*	d_P *200°C*	d_P *400°C*	d_P *600°C*	d_P *800°C*
IO	27	31	35	38	41
CCI	15	17	19	21	22
CCCo	18	21	23	26	27
CIO	30	35	39	43	46

Accounting for more physical properties of the solution forces limits the size of particles that can be maintained as a stable colloid. It can be seen in Table 7.2.2 that the applied magnetic field severely limits particle size relative to the force of gravity alone. This is reasonable considering the strength of magnet used for these calculations. As the strength of the magnetic field that is felt by particles increases, the particles are more likely to overcome the colloid stability and be attracted toward the magnet. The particle sizes can be increased by moving the magnet farther from the solution or using particles that have a smaller magnetic susceptibility. Lastly, when the magnetic particles are in the presence of a magnetic field, there are particle-particle interactions which can cause agglomeration and result in loss of colloid stability. Using Equation 7.2.3 this factor can be calculated and is shown in Table 7.2.3. According to the results in Tables 7.2.1-7.2.3, the strength of the magnetic field is the limiting factor for particle size.

The agglomeration from particle interaction demonstrates a particle limit larger than from the interaction between the magnetic field and particles alone. Although the theoretical limits calculated show varying limits to particle size, a clear trend it established. As the temperature increases, so does the size of particles that will remain stable in the solution. Given the high operating temperature of molten salt heat transfer fluids in both nuclear reactors and concentrated solar systems, a molten chloride ferrofluid has the potential to be the model application of this technology.

During literature review of this topic, it was found that there are no available experiments examining the physical properties of a molten chloride solution containing magnetic nanoparticles. In fact, the available literature examining the characteristics of any composition ferrofluid at temperatures exceeding 400 ^{o}C is nearly negligible. There are two factors that can help to explain the lack of available research data. The first is the Curie temperature degradation of the particle's magnetism as it approaches T_c, as demonstrated previously in Figure 7.2.1. Most common magnets have a T_c value within ±100 ^{o}C of 400 ^{o}C and the associated loss in magnetism makes their use at higher temperatures impractical. Only a handful of materials will maintain magnetism above this temperature resulting in few candidates for application. Of the high Tc materials available, their retaining magnetism is affected by the second potential reason for lack of published research. This is the relationship between the particle's magnetic strength and the size of the nanoparticle. It has been demonstrated that the magnetic strength of the particle decreases with decreasing particle

size.[226] Considering the smaller particle diameter increases the colloidal stability, as demonstrated in Tables 7.2.1 – 7.2.3, the magnetism decreasing with size could be seen as prohibitive for the functioning of these materials.

Examining the efficacy of molten chloride salts and magnetic nanoparticles for potential ultra-high temperature ferrofluid matrices would require three experimental determinations. First, verification of particle dispersion in the molten salt would need to be verified over the temperature range. The second determination needed is that the particles must remain stable while dispersed in the salt in the molten state. For use in real world applications the particles must also remain stable in the solidified salt matrix. The third determination that would prove the viability of material is that magnetism of the particles is retained over the whole temperature range.

This work examines the experimental determinations needed to prove the efficacy of molten chloride ferrofluid. Particle dispersion is examined qualitatively via visual confirmation of the Tyndall effect. The particles are then melted under dynamic vacuum until a stable pressure is maintained to demonstrate absence of reaction produced gaseous products. After this, the solution is sealed in a quartz ampule and examined for magnetic susceptibility over temperature range utilizing a novel experimental apparatus. Continued magnetic field susceptibility at the highest temperature demonstrates the magnetic particles retain magnetism. The retaining of magnetic interaction throughout heating also further verifies the chemical stability of the particles in the molten salt at high temperature. The agglomeration from particle interaction demonstrates a particle limit larger than from the interaction between the magnetic field and particles alone. Although the theoretical limits calculated show varying limits to particle size, a clear trend it established. As the temperature increases, so does the size of particles that will remain stable in the solution. Solving Equations 7.2.1 – 7.2.3 for the maximum particle diameter to maintain colloidal stability using four different sizes and compositions of nanoparticles can provide insight into the feasibility of forming a stable colloid as shown in Tables 7.2.1 – 7.2.3. The results reveal the limiting factor for maintenance of stability is strength of the external magnetic field as shown in Table 7.2.2. Additionally, the theoretical limits of size of stable particles increases as temperature increases which is an advantageous physical characteristic for this work.

7.3 Experimental Methods

Materials.

Three types of magnetic nanoparticles were used as purchased from Sigma-Aldrich (>99%, trace metal basis) and used for subsequent ferrofluid formation. The particles used were iron oxide (Fe_2O_3), carbon coated iron NP, carbon coated cobalt NP, and cobalt iron oxide NP with average particle sizes of 8 nm, 25 nm, 30 nm, and 50 nm, respectively. The salt NaCl was used as purchased from Sigma-Aldrich (>99.999%, trace metal basis) while $MgCl_2$ was purchased from Sigma-Aldrich (99.9%) and further purified via fractional distillation prior to use. $ZnCl_2$ was purchased from Sigma-Aldrich (99.9%) and further purified via fractional distillation prior to use. For the magnetic interaction experiments a 2" x 2" NdFeB magnet (1.48 Tesla) was purchased from K&J Magnetics, Inc.

Ferrofluid Synthesis.

To form molten ferrofluid solutions, eutectic mixture of NaCl – $MgCl_2$ and KCl – $ZnCl_2$ were first fused. This was accomplished by adding appropriate amounts of each component to a quartz test tube inside an inert atmosphere dry box. The tubes were then fitted with compression fittings attached to a vacuum valve. Each was taken out of the dry box and evacuated to $1x10^{-3}$ Torr. Each mixture was heated under dynamic vacuum at 850^{o}C for 15 minutes or until the solution was visibly homogenous. The salt cooled to ambient temperatures under dynamic vacuum and was returned to the inert atmosphere dry box.

The newly formed eutectic ratios of salts were transferred to fused silica test tubes (10 mm x 12 mm I.D. x O.D.) containing various amounts of NP required to form nanofluids used for subsequent experimentation. Each tube containing salt and particles was then attached to a vacuum valve and removed from the dry box. After this, the tube was evacuated to $1x10^{-3}$ Torr and flame sealed using an oxygen-natural gas torch.

Colloidal Stability.

Each ampule of salt-NP mixture was heated to 50°C above the eutectic melting point of the specific salt for a duration of 12 hours. During this time, the mixtures were agitated by using a shaker plate set to 100 RPM. At the conclusion of mixing time the mixtures were cooled to room temperature and visually inspected for homogeneity. All mixtures had visually equivalent NP dispersion as shown in Figure 7.3.1. In addition, a laser was shown through the tubes to observe the Tyndall Effect. All solutions demonstrated a high degree of scattering as the laser propagated through the salt, qualitatively confirming the presence of NP polydispersity. Higher concentration samples became opaque, also shown in Figure 7.3.1.

Magnetic Susceptibility.

Magnetic susceptibility experiments began by placing the sealed ampule containing the chloride salt with magnetic nanoparticles on the holder placed on the balance at room temperature. This measurement provides the mass of the sample with no magnetic interaction as shown in Equation 7.3.1.

$$F_{min} = m * g = 0\%\ magnetic\ susceptability \tag{7.3.1}$$

Where F_{min} is the weight of the ampule containing salt and magnetic nanoparticles with no magnetic interaction. The m term is nominal mass and g is the acceleration due to gravity with no external interaction. After this, the magnet was placed above the salt at room temperature to obtain the value for weight of ampule during full interaction with external magnetic field. The apparent mass change of the salt was taken with the magnet located 5.0 cm from the surface of the salt solution. This measurement provided the total magnetic interaction due to external magnetic field as demonstrated in equation 7.3.2.

$$F_{max} = m_{magnet} * g = 100\%\ magnetic\ susceptability \tag{7.3.2}$$

It was noticed that the permanent magnet was hot to the touch after initial experiments. To ensure the magnetic susceptibility was due to particles an air-cooling system was added for results on pages 163-165. This was replaced by a water-cooling system for all results after page 165. Potentially explaining why the increase in susceptibility was not observed in early experiments.

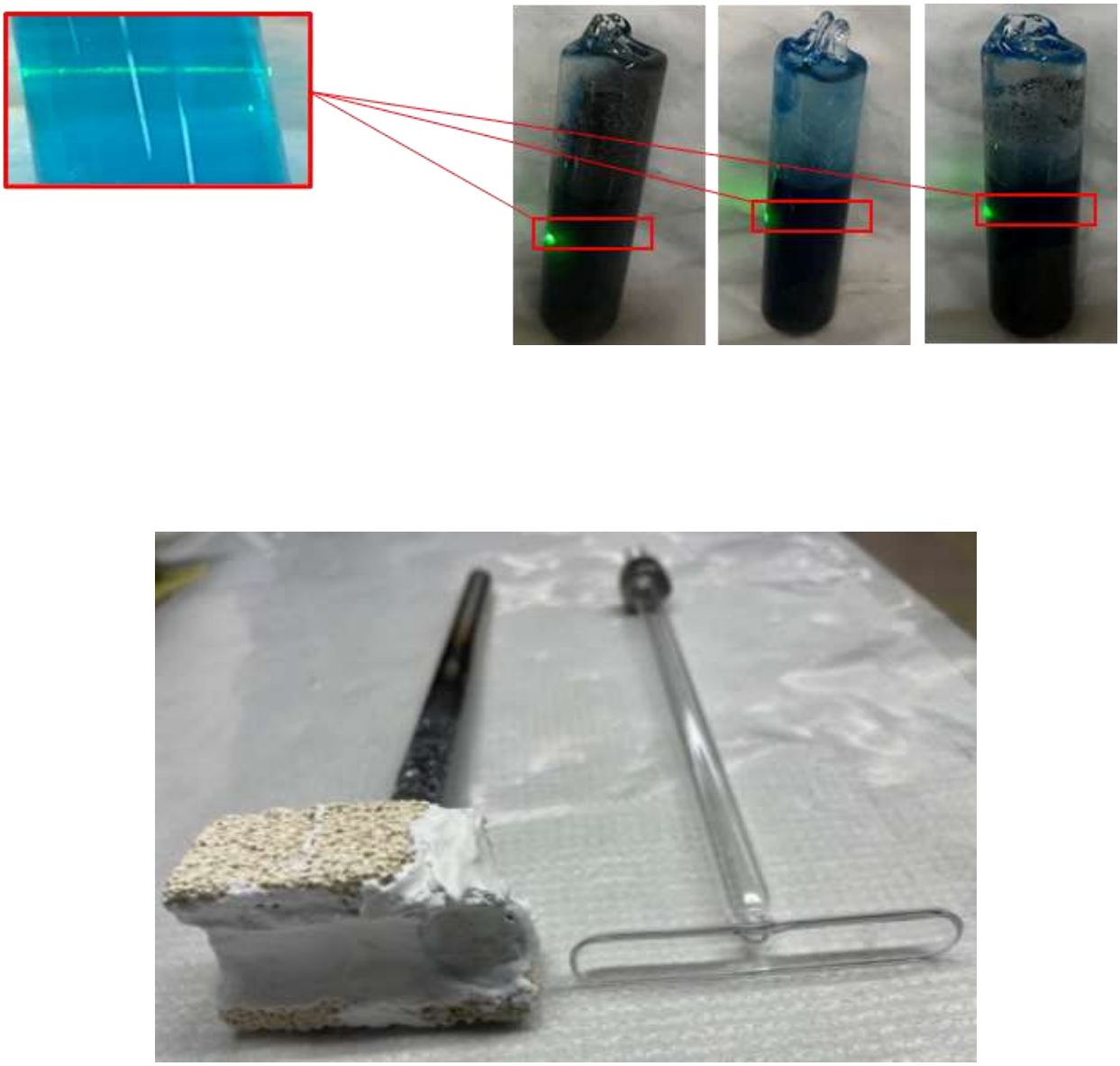

Figure 7.3.1. Evidence of colloidal stability in molten ferrofluid of $MgCl_2$-NaCl eutectic containing cobalt nanoparticles (top images). Sample holders used for experiments (bottom image)– Left holder stainless steel tube used for experimental results shown in Figures 7.4.1 – 7.4.6, right holder fused silica tubing used for experimental results shown in Figures 7.4.7 – 7.4.10.

Where F_{max} is the value of measured weight of the sample containing ampule for 100% interaction with external magnetic field. The m_{magnet} term is the change is perceived mass due to interaction with magnetic field and g is acceleration due to gravity. A schematic depiction of the magnet test apparatus is shown in Figure 7.3.2. The results of each of these measurements were used for subsequent calculations. In addition to mass loss experiments, the magnet was used to further examine the extent of colloidal stability. This was accomplished by maintaining the salt solutions above the melting temperature of the salt while the magnet was kept at 5.0 cm. The time required for the magnetic force to cause agglomeration of particles on the wall of the tube closest to the magnet was recorded for each sample. The physical implications of this can be manifested as mass loss of the sample relative to no magnetic field. This will occur if the attractive force of the magnetic field is opposite that of the force of gravity. This can be translated to the total mass of salt that is affected by the pull of the nanoparticles and therefore an approximate magnetic susceptibility of the particles at each temperature.

A generalized example of the interpretation of the results of an experiment utilizing the apparatus depicted in Figure 7.3.2 is as follows. A hypothetical fused silica tube is flame sealed under vacuum such that the ampule containment, salt, and nanoparticles weigh exactly 1.0 gram. Therefore, when the ampule is placed on the balance with no external magnetic field, the balance should read 1.0 grams. Thus, when the balance reads that the ampule, salt, and nanoparticles have a mass of 1.0 grams, there is 0% interaction with an external magnetic field (Equation 7.3.1). Conversely, when an external magnetic field is placed above the ampule, salt, and nanoparticles at room temperature, this is 100% magnetic interaction (Equation 7.3.2). In the hypothetical example, if the magnet is placed above the ampule, salt, and nanoparticles at room temperature and the balance reads a mass 0.5 grams, then a perceived mass change of 0.5 grams is the full force of the external magnetic field. All other factors remaining constant other than increased temperature should cause a change in the measured mass to increase. Once the material has reached T_c the mass measured on the balance should again read 1.0 grams due to total loss of magnetic susceptibility of the particles. For 50% of the magnetic susceptibility the balance would read 0.75 grams because this is half-way between full susceptibility and no susceptibility. Additionally, if the measured mass is less than 0.5 grams at elevated temperatures, then the magnetic susceptibility of the ampule, salt, and nanoparticles is greater than at room temperature.

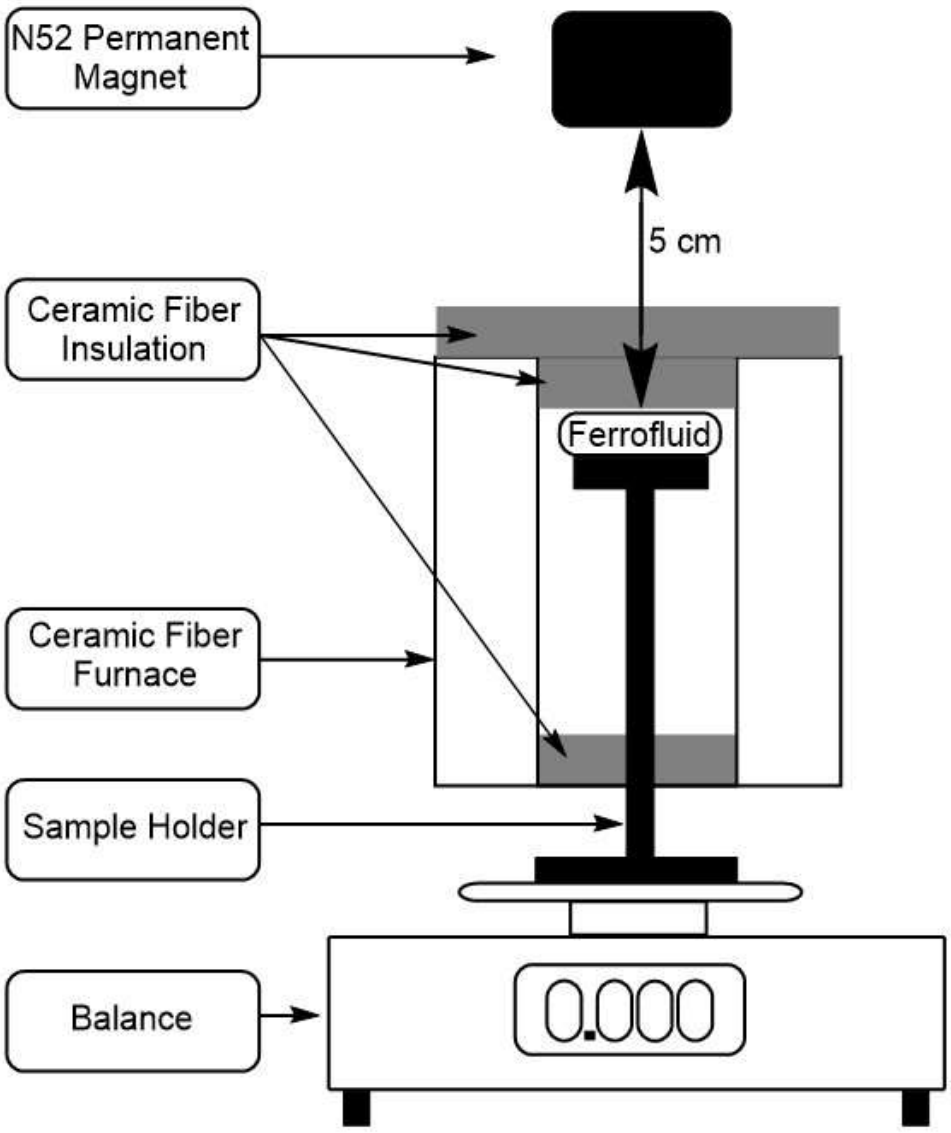

Figure 7.3.2. Schematic depiction of the mass loss experiment.

7.4 Results and Discussion

These experiments represent the first-time formation of a ferrofluid able to maintain magnetic susceptibility over such a broad temperature range. For the initial experiments, four nanoparticle compositions were chosen due to the high T_c of the bulk materials: T_c(Fe) = 770 ^oC, T_c(Co) = 1130 ^oC, T_c($FeOFe_2O_3$) = 675 ^oC, T_c($CoFe_2O_4$) = 515 ^oC.[227-230] The compositions included 8 nm iron (II,III) oxide, 30 nm carbon coated iron, 30 nm cobalt iron oxide, and 50 nm carbon coated cobalt. Each of the mixtures were added to the NaCl-$MgCl_2$ eutectic, mixed, and experimentally tested for magnetic susceptibility as a function of temperature. The results of each experiment are shown in Figure 7.4.1. The results of the first set of measurements confirm the efficacy of the methodology. As expected, the magnetism of the particles in the molten salt decreased inversely to temperature. Full loss of the magnetic interaction is demonstrated at the approximate Curie temperature of the bulk material. Surprisingly, the carbon coated cobalt nanoparticles experienced no loss in magnetism through the duration of the temperature range.

After the initial examination of particles in Figure 7.4.1, more cobalt particles of varying sizes were purchased from commercial suppliers. It was decided to focus on examination of cobalt based molten ferrofluid due to its characteristically high Curie temperature. The results shown in Figure 7.4.2 from the magnetic susceptibility experiments reveal a peculiar trend. This is that there is an apparent increase in the magnitude of magnetic field interaction with the ferrofluid as temperature increases. Interestingly, the increase of perceived strength of magnetic interaction (m_{magnet}) appears to be dependent on the concentration of particles in solution instead of the particle size.

Two different sample holders were utilized to position the ferrofluid ampule inside the furnace as shown in Figure 7.3.1. The stainless-steel tubing was used for the experimental results shown in Figures 7.4.1 – 7.4.6 and is believed to be the source of the fluctuations of magnetic susceptibility measured below the melting point. The error can be attributed to interaction of the stainless steel with the magnet, repeated oxidation of the stainless steel from heating cycles, and decomposition of the holder over time. To remedy the error, a custom designed silica holder was made and utilized for experiments shown in subsequent figures. After changing to the silica holder, the changes in measured magnetic susceptibility prior to the melting point of the salt mixture become negligible.

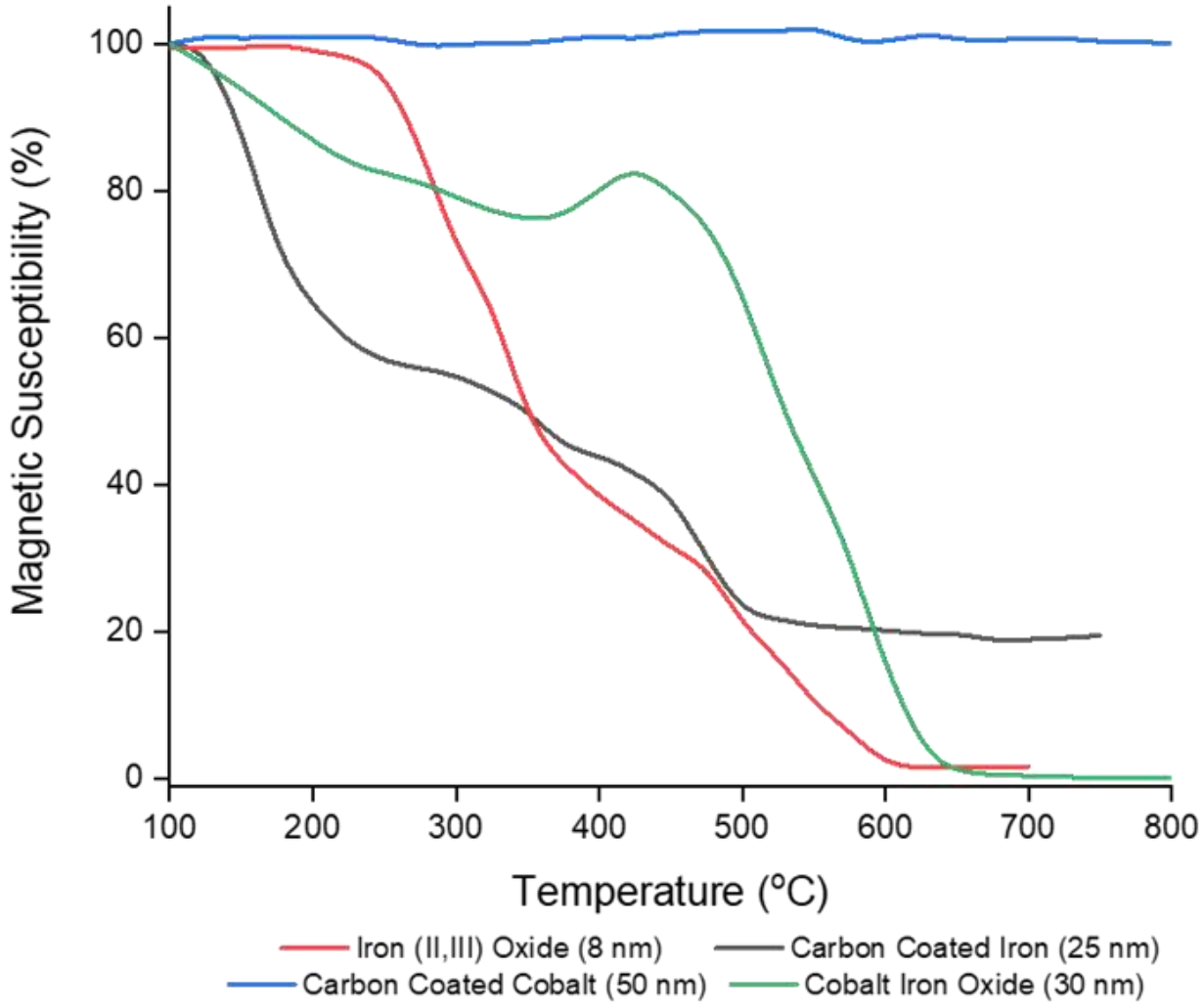

Figure 7.4.1. Results of magnetic susceptibility measurements of samples containing 1.0% weight of 50 nm carbon coated cobalt, 8 nm iron(II,III) oxide, 25 nm carbon coated iron, and 30 nm cobalt iron oxide in the 57% NaCl: 43% $MgCl_2$ mixture.

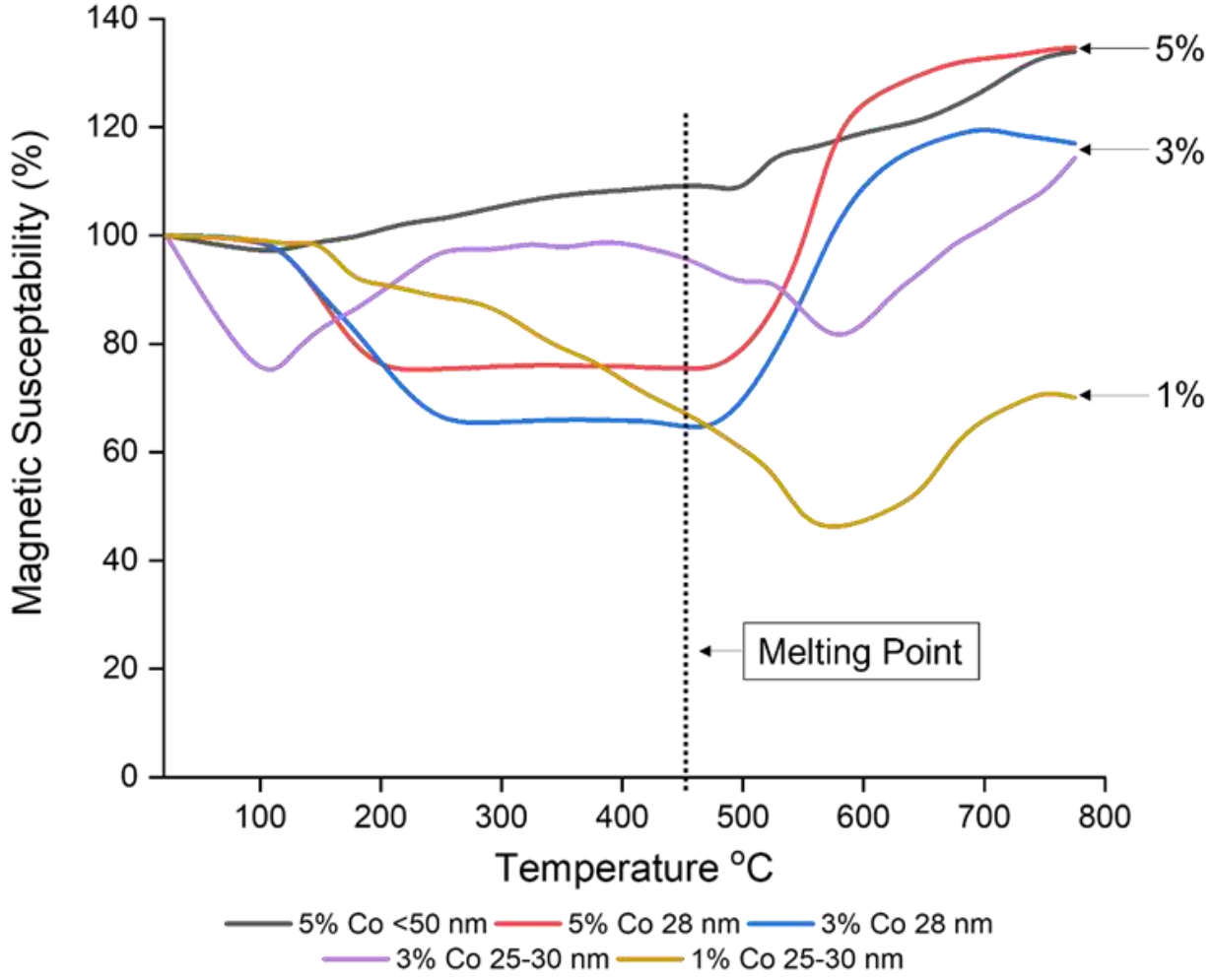

Figure 7.4.2. Results of gravimetric magnetic susceptibility experiment for 5.0 weight(%) carbon coated cobalt particles (<50 nm), 5.0 weight(%) cobalt particles (28 nm), 3.0 weight(%) cobalt particles (28 nm), 3.0 weight(%) cobalt particles (25-30 nm), and 1.0 weight(%) cobalt particles (25-30 nm) in NaCl – $MgCl_2$ eutectic mixture.

The peculiar results obtained in Figure 7.4.2 raised questions about the nature of the perceived increase in magnetic susceptibility observed above the melting point. The experimental apparatus was examined for potential error introduced to the measurements. This included further insulating the furnace and raising the furnace, sample, and magnet to a higher level further above the balance. In addition to this, the magnetic susceptibility experiment was carried out with a sample containing the base $MgCl_2$:NaCl eutectic salt with no nanoparticles, an empty sealed quartz ampule, the sample holder with no ampule, and finally the furnace was heated over the temperature range without the sample holder with negligible change in baseline mass observed. Furthermore, the temperature of the permanent magnet above the furnace was monitored for temperature change over the heating range. During this assessment, no increase in perceived magnetic susceptibility was observed originating from the experimental apparatus. After this, the 25-30 nm cobalt particles were analyzed for magnetic susceptibility utilizing a concentration range of 0.10 – 2.8 wt%. The results are shown in Figure 7.4.3.

The results of the magnetic susceptibility experiments utilizing varying particle concentrations shown in Figure 7.4.3 confirmed the magnetic susceptibility increases as a function of particle concentration. This observation below the melting point is not unreasonable considering the more magnetic material present results in more material interacting with the magnetic field. The more curious observation occurs above the melting point of the $MgCl_2$:NaCl eutectic mixture. Above the melting point, the solution experiences a marked increase in susceptibility to the magnetic field or a perceived increase in magnetism. The magnitude of increase in the ferrofluid's magnetism above the melting point also appears to be dependent on particle concentration due to the difference in increased magnetic susceptibility above the melting point.

As demonstrated in the top plot of Figure 7.4.4, all concentrations appear to have an increase magnetic susceptibility at 750^{o}C as opposed to 400^{o}C. Furthermore, the perceived increase in magnetic susceptibility of the 2.8 wt% sample is nearly four times that of the 0.10 wt% sample. The slope of the linear line of best fit of magnetic susceptibility as a function of nanoparticle mass percent demonstrates the extent of difference between concentrations at the same temperature. On the bottom plot shown in Figure 7.4.4, the slope of susceptibility as a function of concentration for each experimentally measured temperature is plotted.

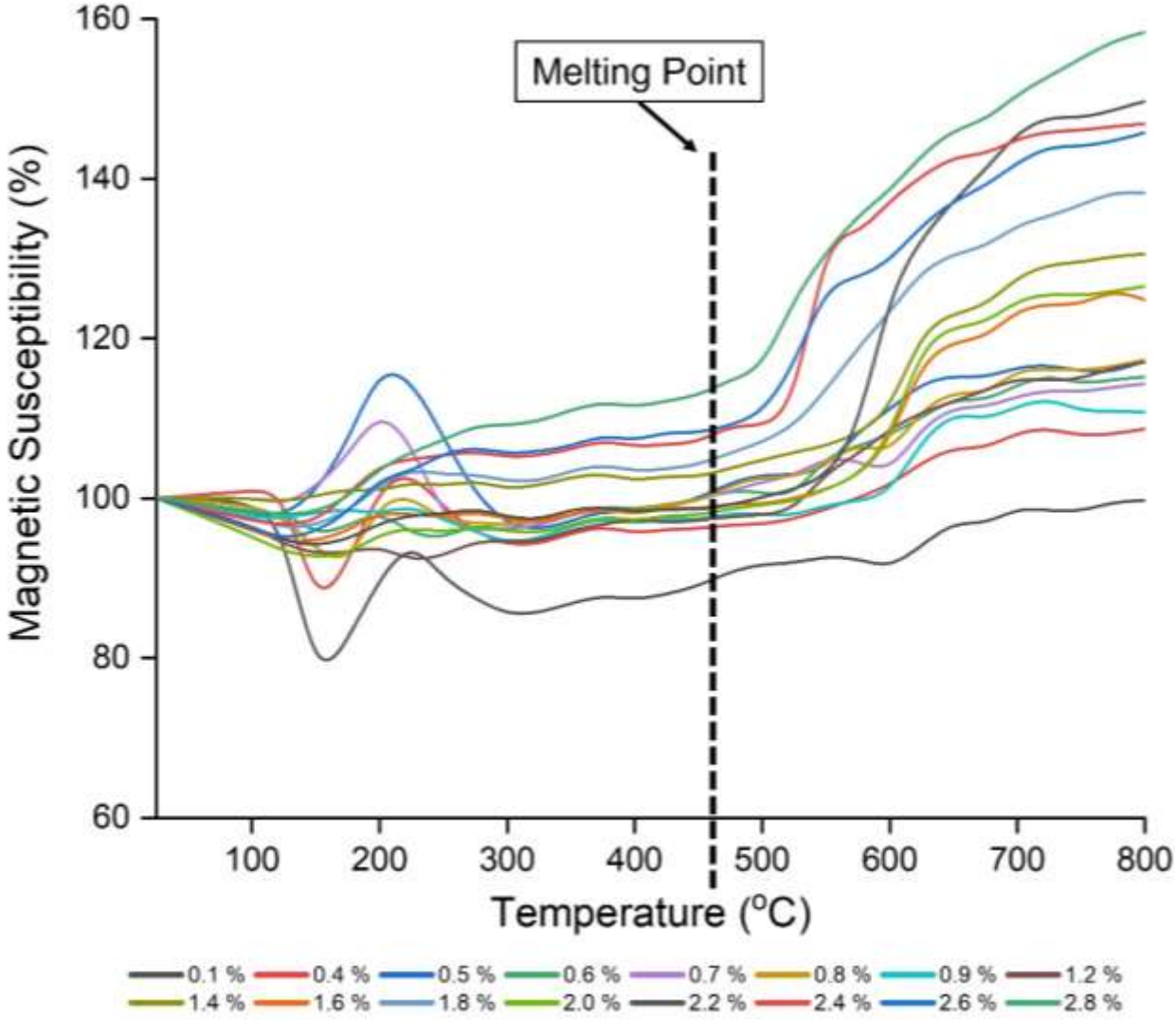

Figure 7.4.3. Magnetic susceptibility experiments of 25-30 nm cobalt nanoparticles in NaCl:$MgCl_2$ eutectic mixture.

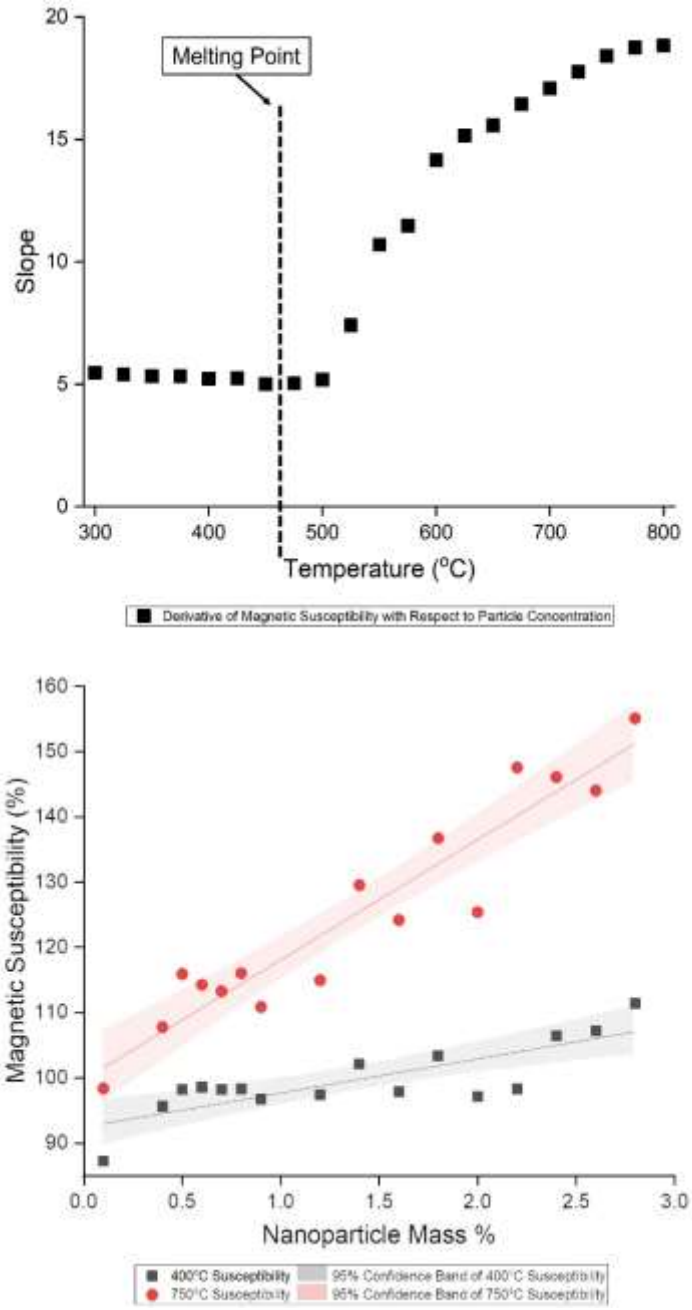

Figure 7.4.4. Magnetic susceptibility experiments of 25-30 nm cobalt nanoparticles in NaCl:$MgCl_2$ eutectic mixture for various particle concentrations at 400°C and 750°C (bottom). Slope of linear regression fitting of magnetic susceptibility vs. particle concentrations between 300°C and 800°C (top).

The results of plotting the slope at each temperature point reveal that higher concentration particles increase in magnetism at a faster rate than lower concentration only after melting. Prior to the melting point there is a difference in measured magnetic susceptibility between different particle concentrations. Albeit, prior to the melting point, the difference in magnetic susceptibility between different particle concentrations remains the same. Above the melting point the slope increases drastically as the measured magnetism of the samples with high particle concentrations become more magnetically susceptible faster than then lower concentrations as temperature increases. Another peculiar result is the difference between the measured magnetism of the samples continues to widen as the temperature continues to increase for all particle concentrations.

To examine the dependence of the perceived increase of magnetic susceptibility on the melting point of the mixture, the solution matrix was changed from 57% NaCl: 43% $MgCl_2$ eutectic ratio to 45% KCl: 55% $ZnCl_2$ eutectic ratio. This change lowered the solution melting temperature from 456 ^oC to 228 ^oC. The same particles that were used in the measurements for Figure 7.4.1 were measured for magnetic susceptibility in the lower melting 45:55 KCl:$ZnCl_2$ mixture. The results of the experiment showed that after melting, the same increase in total measured magnetism was still observed for all samples. The difference in the melting point and different cationic composition in the molten salt seemed to not hinder the increase in magnetic susceptibility from occurring above the melting point. The results of the magnetic susceptibility measurements of the 45:55 KCl:$ZnCl_2$ mixture can be seen in Figure 7.4.5. The decrease in measured magnetic susceptibility is likely due to error introduced by the first sample holder shown in Figure 7.3.1.

Magnetic susceptibility of solutions containing 1.0% weight of 50 nm carbon coated cobalt, 8 nm iron(II,III) oxide, 25 nm carbon coated iron, and 30 nm cobalt iron oxide 57% NaCl: 43% $MgCl_2$ solution to the same particles in a 45% KCl: 55% $ZnCl_2$ solution is shown in Figure 7.4.6. The results demonstrate a clear increase in magnetic susceptibility in the 45% KCl: 55% $ZnCl_2$ solution compared to the iron oxide 57% NaCl: 43% $MgCl_2$ solution. The increase is more visible due to the phase transition of the salt occurring at a temperature well below the particle T_c. Furthermore, the samples containing the 45% KCl: 55% $ZnCl_2$ solution demonstrated an increased temperature range of magnetic susceptibility compared to the 57% NaCl: 43% $MgCl_2$ solution as shown in Figure 7.4.6.

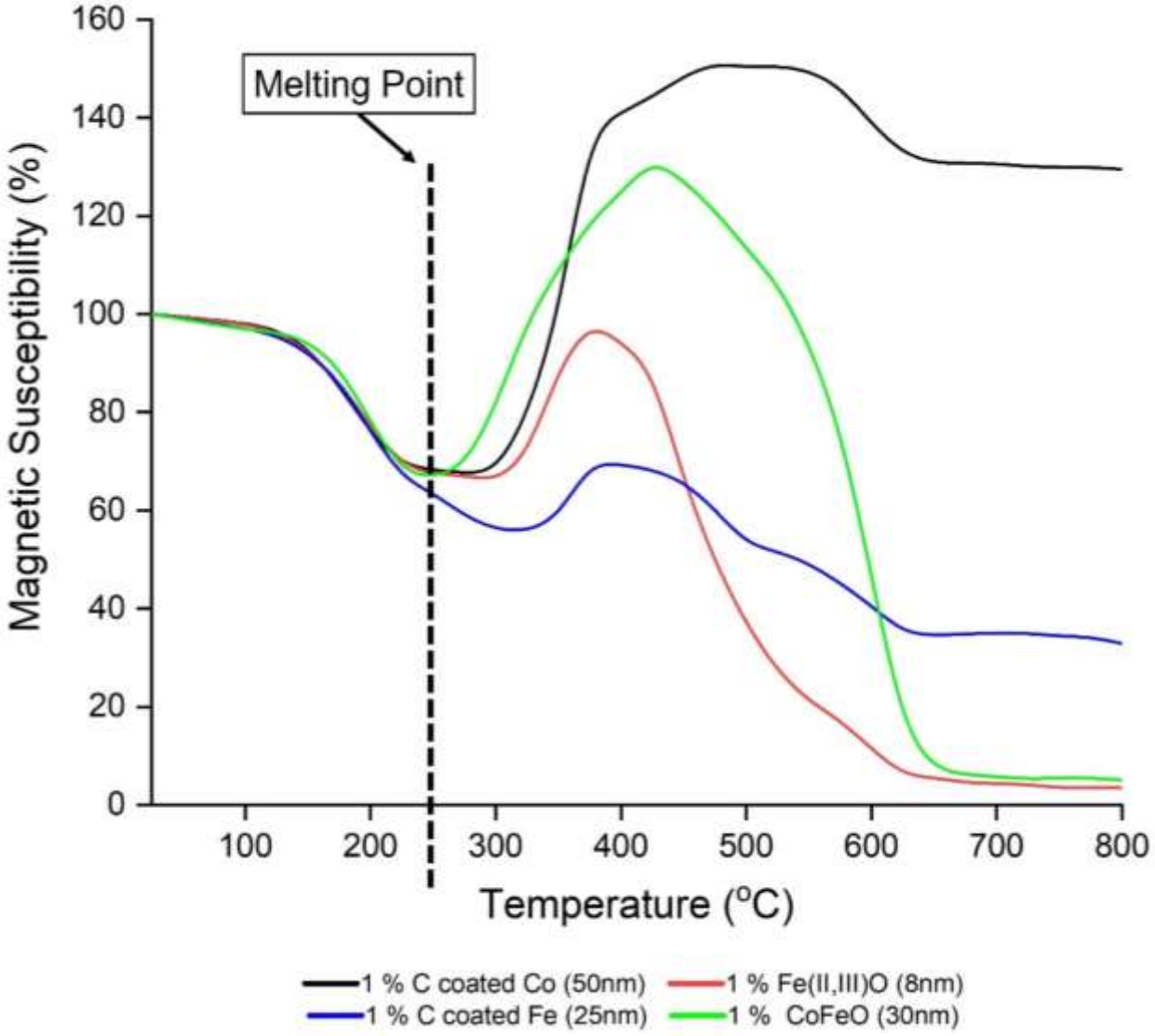

Figure 7.4.5: Results of magnetic susceptibility measurements of samples containing 1.0% weight of 50 nm carbon coated cobalt, 8 nm iron(II,III) oxide, 25 nm carbon coated iron, and 30 nm cobalt iron oxide in the 45% KCl: 55% $ZnCl_2$ mixture.

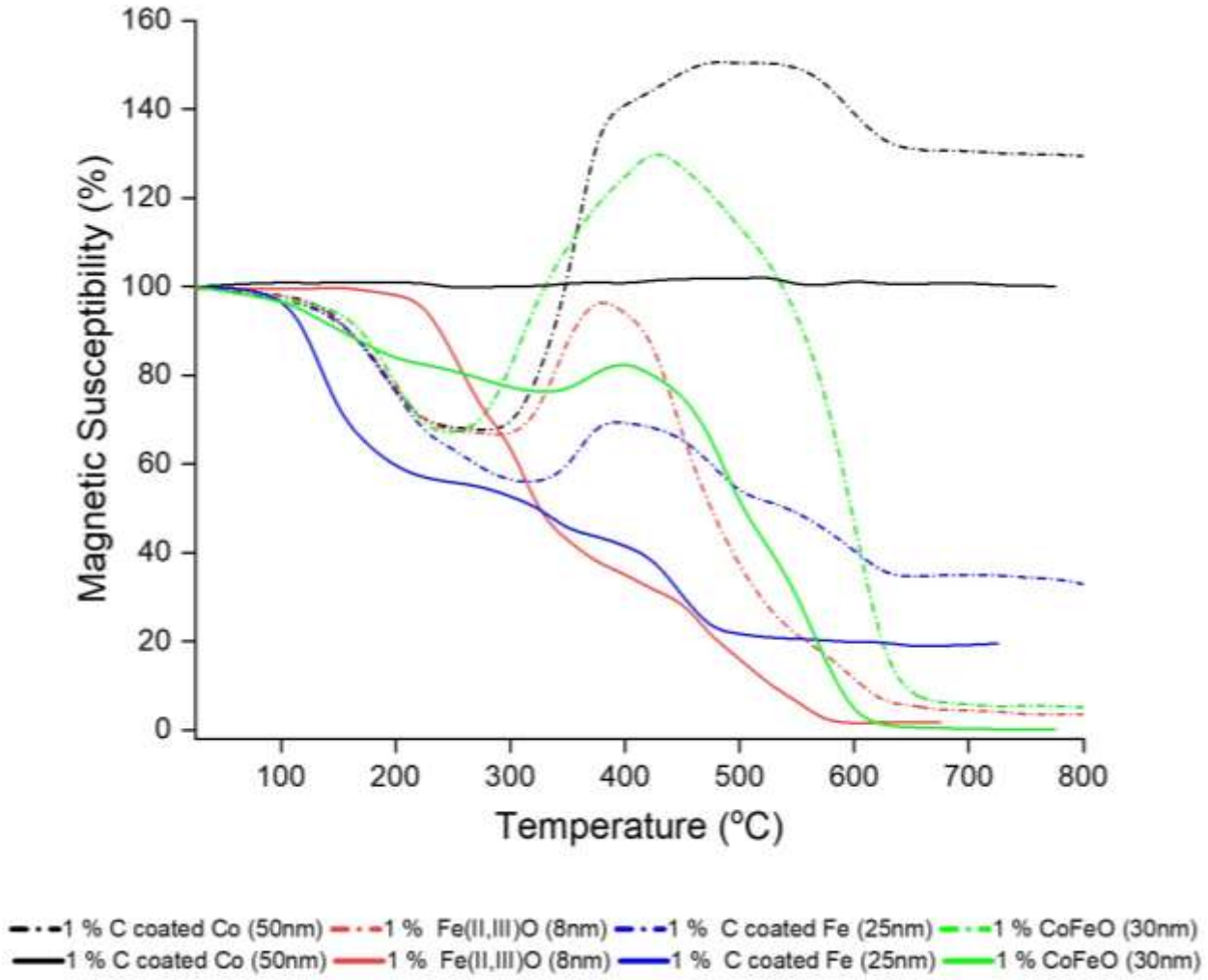

Figure 7.4.6: Results of magnetic susceptibility measurements of samples containing 1.0% weight of 50 nm carbon coated cobalt, 8 nm iron(II,III) oxide, 25 nm carbon coated iron, and 30 nm cobalt iron oxide. Solid lines represent the 57% NaCl: 43% $MgCl_2$ composition and dashed lines represent the 45% KCl: 55% $ZnCl_2$ composition.

It should be noted that there is a decrease in perceived magnetic susceptibility at temperatures well below the melting point of the solution in many of the measurements represented in Figures 7.4.1-7.4.6. This error is likely attributed to the loss of surface absorbed water present on the surface of the ampule containing the ferrofluid or the sample holding arm up to 200 ^{o}C. This is most evident in Figure 7.4.5 where all samples lose the same mass at approximately the same rate between room temperature and 200 ^{o}C. In addition to water, other errors can be attributed to dust and insulation debris from placing the sample. There is also the possibility that the stainless-steel tubing and attached fire brick holder maintained some magnetic susceptibility additionally, oxidation and high temperature binder degradations at high temperatures also increased measurement error.

To combat these sources of error, the sample holder attached to the balance was changed to a custom fused silica holder attached to the balance shown previously in Figure 7.3.1. The remaining measurements (Figures 7.4.7 – 7.4.10) were completed utilizing the new silica sample holder. The alteration of the sample holder resulted in less error compared to the earlier measurements as verified by measurements of 1.0% weight of 50 nm carbon coated cobalt nanoparticles, 28 nm cobalt nanoparticles, and 20 nm cobalt nanoparticles in the 45% KCl: 55% $ZnCl_2$ mixtures shown in Figure 7.4.7 . Magnetic susceptibility measurements were carried out on samples containing 28 nm cobalt nanoparticles at weight percent of 0.5%, 1.0%, 2.0%, and 3.0% in the 45% KCl: 55% $ZnCl_2$ mixture. The results shown in Figure 7.4.8 demonstrate a substantial increase in the perceived magnetic susceptibility of the particles with little to no error before melting. Additional measurements were completed on samples containing 20 nm cobalt nanoparticles at weight percent of 0.5%, 1.0%, 2.0%, and 3.0% in the 57% NaCl: 43% $MgCl_2$ mixture. These results, shown in Figure 7.4.9, again demonstrate a marked change in perceived magnetic susceptibility above the melting point of the mixture. Interestingly, the area of differing magnetic susceptibility covers a larger temperature range in Figure 7.4.8 but increases much more gradually after melting than in Figure 7.4.9. The measurements of Figures 7.4.8 and 7.4.9 are overlayed in Figure 7.4.10, further demonstrating the distinct change in magnetic susceptibility after melting in samples with different particles sizes and different cations. The overlay shown in Figure 7.4.10 also confirms that the magnetic susceptibility of particles measured in all plots begins to plateau above 700 ± 50 ^{o}C.

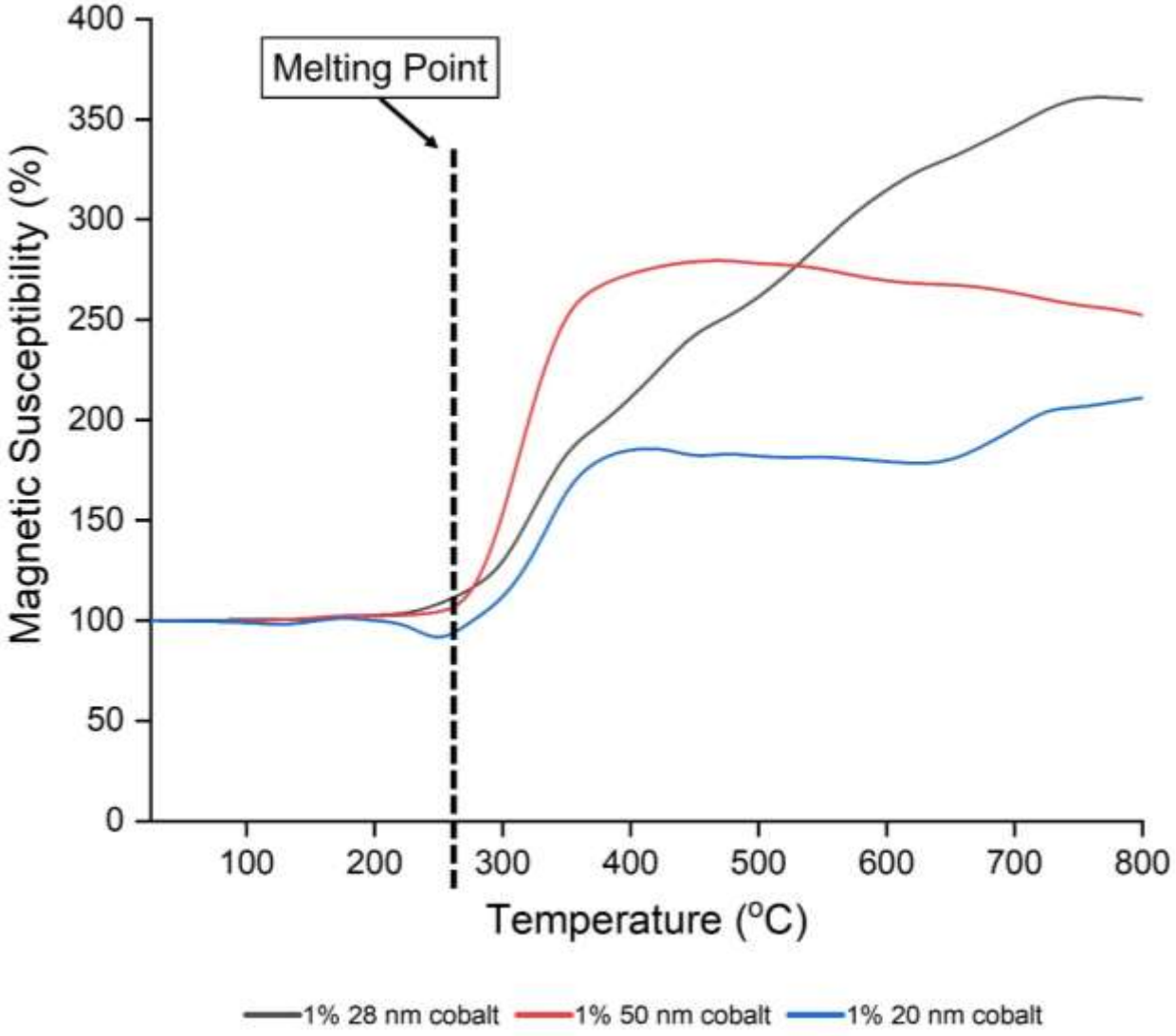

Figure 7.4.7: Results of magnetic susceptibility measurements of samples containing 1.0% weight of 50 nm carbon coated cobalt nanoparticles, 28 nm cobalt nanoparticles, and 20 nm cobalt nanoparticles in the 45% KCl: 55% $ZnCl_2$ mixture.

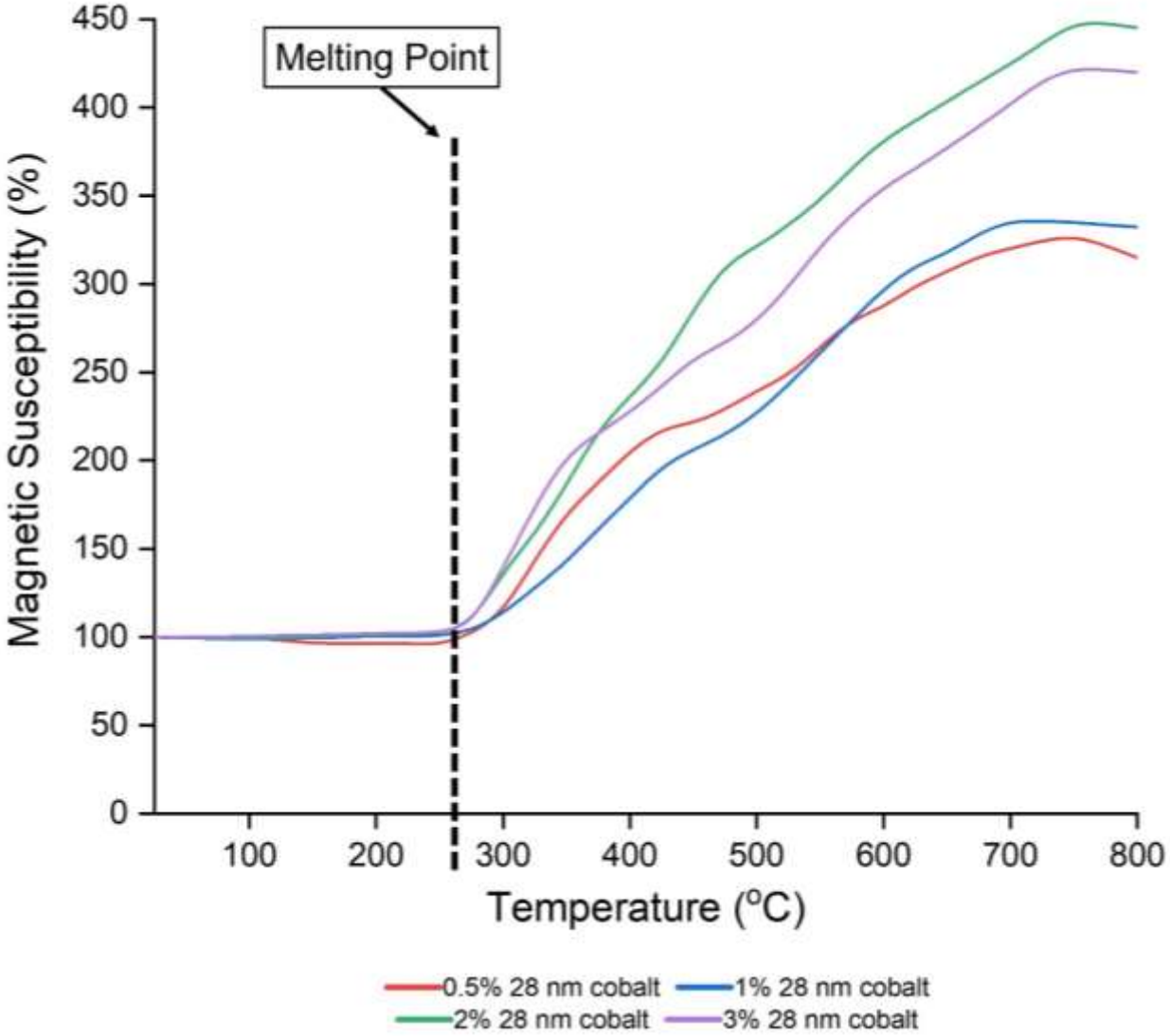

Figure 7.4.8: Results of magnetic susceptibility measurements of samples containing 28 nm cobalt nanoparticles at weight percent of 0.5%, 1.0%, 2.0%, and 3.0% in the 45% KCl: 55% $ZnCl_2$ mixture.

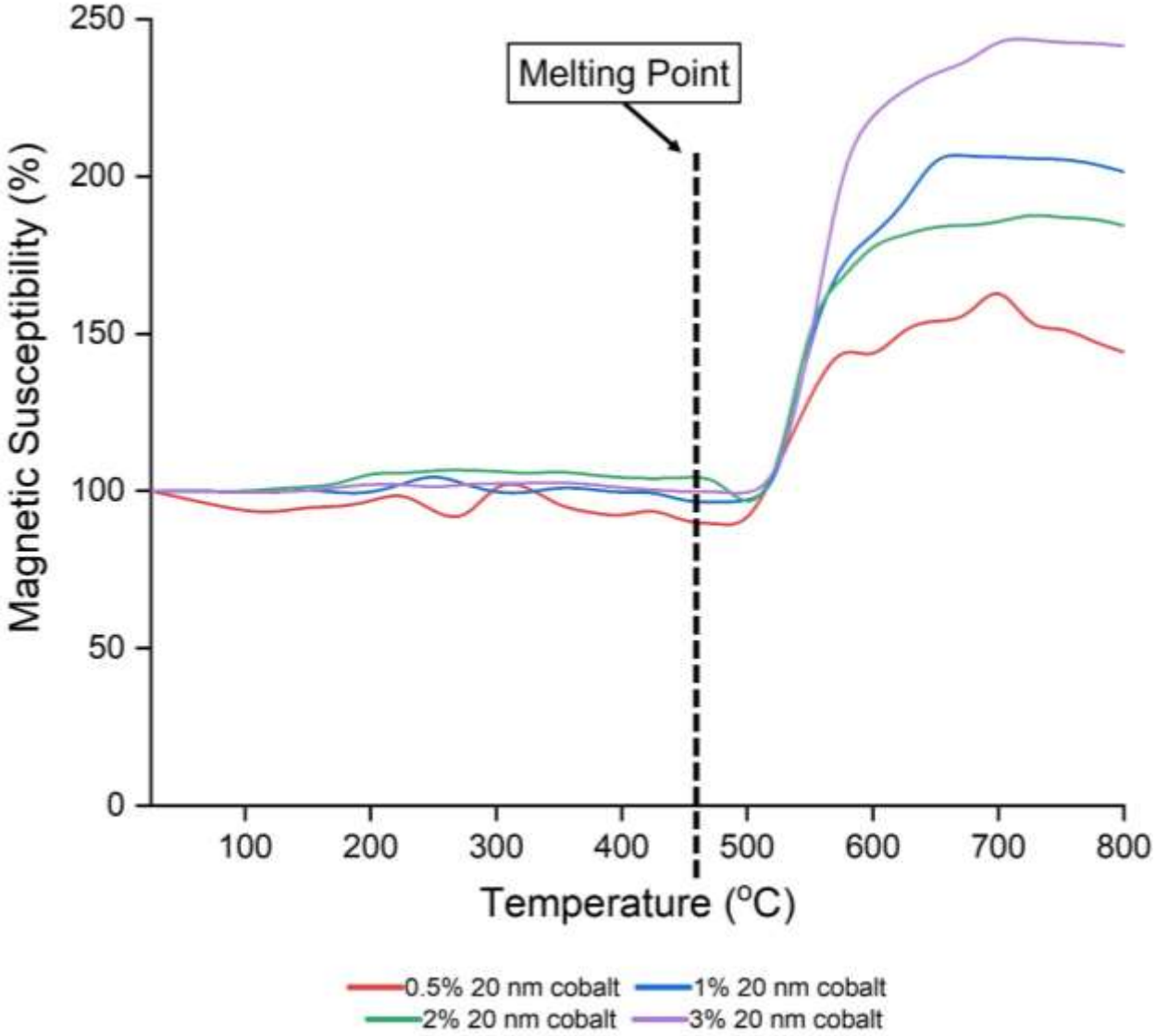

Figure 7.4.9: Results of magnetic susceptibility measurements of samples containing 20 nm cobalt nanoparticles at weight percent of 0.5%, 1.0%, 2.0%, and 3.0% in the 57% NaCl: 43% $MgCl_2$ mixture.

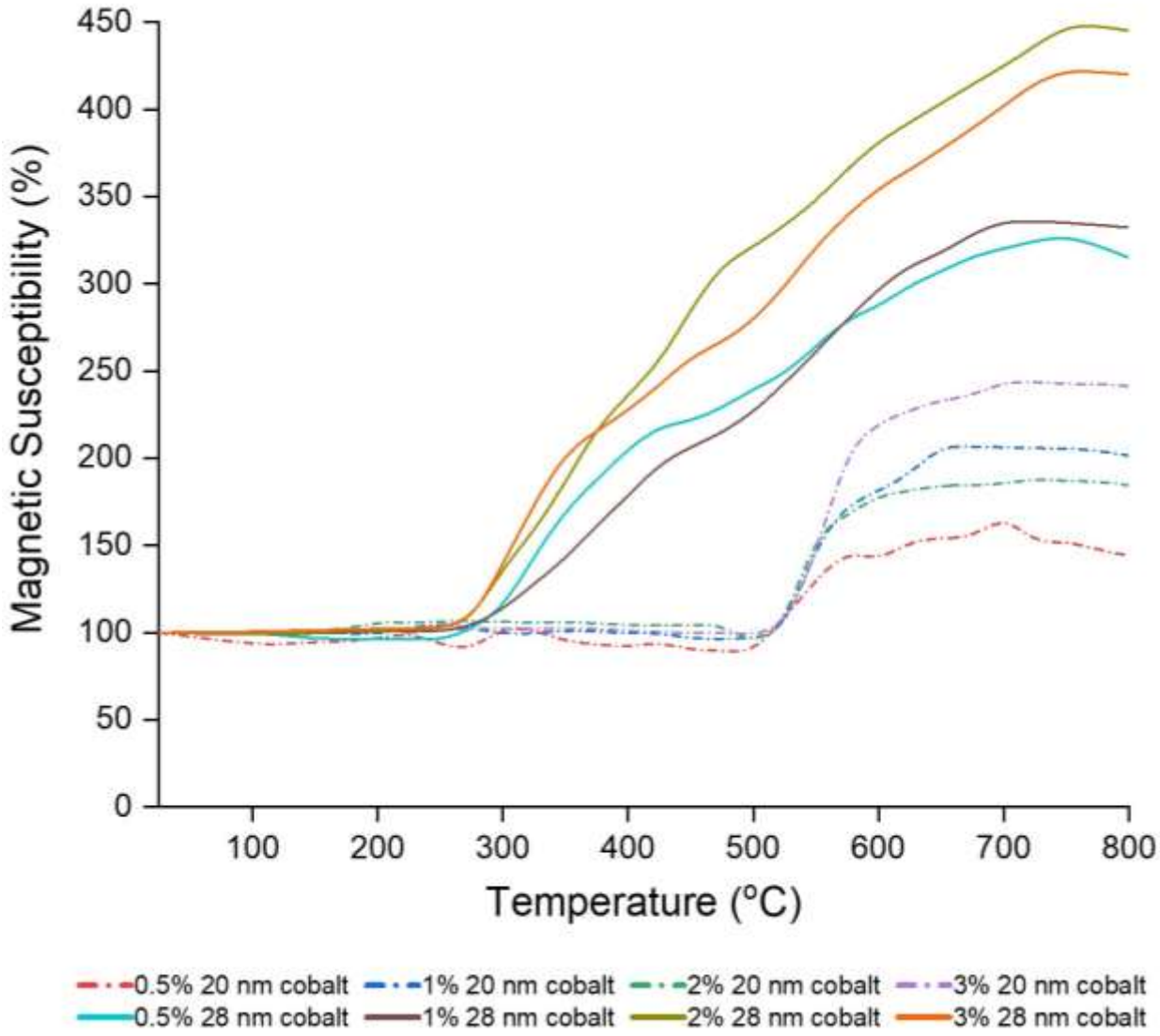

Figure 7.4.10: Results of magnetic susceptibility measurements of containing 20 nm cobalt nanoparticles at weight percent of 0.5%, 1.0%, 2.0%, and 3.0% in the 57% NaCl: 43% $MgCl_2$ mixture (dashed lines) and 28 nm cobalt nanoparticles at weight percent of 0.5%, 1.0%, 2.0%, and 3.0% in the 45% KCl: 55% $ZnCl_2$ mixture (solid lines).

The results of measurements demonstrate a reproducible increase in magnetic interaction of the solutions as temperature increases. These results reveal trends in measured magnetism inverse to the normal expectations for the effect of increasing temperature on magnetic material. This peculiar result is the consequence of the presence of the Hopkinson effect in the molten ferrofluid.[231] The results of the measurements coincide well with the results of other literature related to the measurements of the Hopkinson effect on hard and soft magnetic materials.[232-240] This effect is the experimentally measured increase of magnetic susceptibility, χ, with increasing temperature until reaching an χ maximum before T_c. There are differing explanations for the origin of the Hopkinson effect but are mostly related to changes wall domain motion. This physical implication of this has demonstrated that it is a superparamagnetic relaxation of a system of single domain interacting magnetic nanoparticles that are randomly oriented.[241]

When the particle diameter is small enough, energy fluctuations can overcome the particle's anisotropy forces and spontaneously reverse the direction of particles magnetization, M_s.[242] The physical result of this is that, in terms of magnetism, the particles do not behave as single domain magnets, but rather behave like a system of paramagnetic atoms.[243] The consequence of this is an absence of interactions between the nanoparticles and the existence of the atomic magnetic moment instead of the nanoparticle magnetic moment.[226] When this occurs, the system of nanoparticles is referred to as superparamagnetic due to their superparamagnetic behavior in the presence of an external magnetic field.[244] Therefore, the magnetization for a superparamagnetic system of nanoparticles can be described by the atomic theory of paramagnetism by Langevin.[243] The magnetism of superparamagnetic nanoparticles is described by Equations 7.4.1.

$$M_{SPM}(H,T) = nm_{m,NP}L(H,T) \tag{7.4.1}$$

Where $M_{SPM}(H,T)$ represents the magnetization of a superparamagnetic nanoparticle system as a function of magnetic field. The concentration of nanoparticles in the system is represented by n and the magnetic moment of the nanoparticles in the system is represented by $m_{m,NP}$. Equation 7.4.1 demonstrates dependence of the total magnetism of superparamagnetic nanoparticles is directly proportional to the particle concentration. This relation agrees well with the results of this work, as shown in Figure 7.4.3 and 7.4.4, providing supporting evidence for the existence of superparamagnetism in this system. The Langevin function is represented by $L(H,T)$ and is a

simplification of the Brillouin function describing magnetic moments becoming continuously aligned in a magnetic field.[245] The classical limit of the of the Langevin function can be calculated as shown in Equation 7.4.2.

$$L(x) = \coth(x) - \frac{1}{x} \tag{7.4.2}$$

Where x can be any integer value such that that the Langevin function, L(x), approaches 1 as $x \rightarrow \infty$ and approaches -1 as $x \rightarrow -\infty$. For nanoparticles to exhibit superparamagnetic behavior in an external magnetic field, two requirements must be met.[226] The first requirement is the experimentally measured magnetization curves recorded at different temperatures must be without hysteresis and follow the Langevin function. The second requirement is the magnetization curves in the $M/M_{sat} = f(H/T)$ must overlap. Equation 7.4.2 is plotted in Figure 7.4.11 for x values 0.01 – 10.0. A comparison between the plotted general Langevin function in Figure 7.4.11 to the results of experiments in solution state, shown in Figure 7.4.3 – Figure 7.4.10, shows good agreement, indicating the results of this work do follow the Langevin Function. Therefore, the particles meet the first requirement for the determination of superparamagnetic behavior. The second requirement for superparamagnetic behavior will require further investigation, but if met, will quantitatively prove the presence of superparamagnetism. Determination of M/M_{sat} can be measured by analyzing the change in flux density as a function strength of external magnetic field beginning with M_{sat}.[246]

Once the experimental apparatus was optimized, every particle size and composition examined in this work demonstrated some degree of superparamagnetic character. The material being superparamagnetic is dependent on the salt being in the molten state prior to the T_c of the nanoparticle's material due to gravimetric magnetic susceptibility results only following the Langevin function after melting. According to the trends in the results the total magnitude of alteration in magnetic susceptibility seems loosely dependent on particle concentration instead of particle size. Additionally, the magnitude of overall change seems to be influenced by solution composition that will require further research to understand the influence of solution-particle interaction and the viability of this material for application. While the preliminary results of this work indicate superparamagnetic character it is possible that susceptibility increase is due to the particles being removed from solution and pulled closer to the permanent magnet. The increase could also be explained by particle solubilization, or it could be a function of the magnetic nanoparticle colloid that has been described previously.[247]

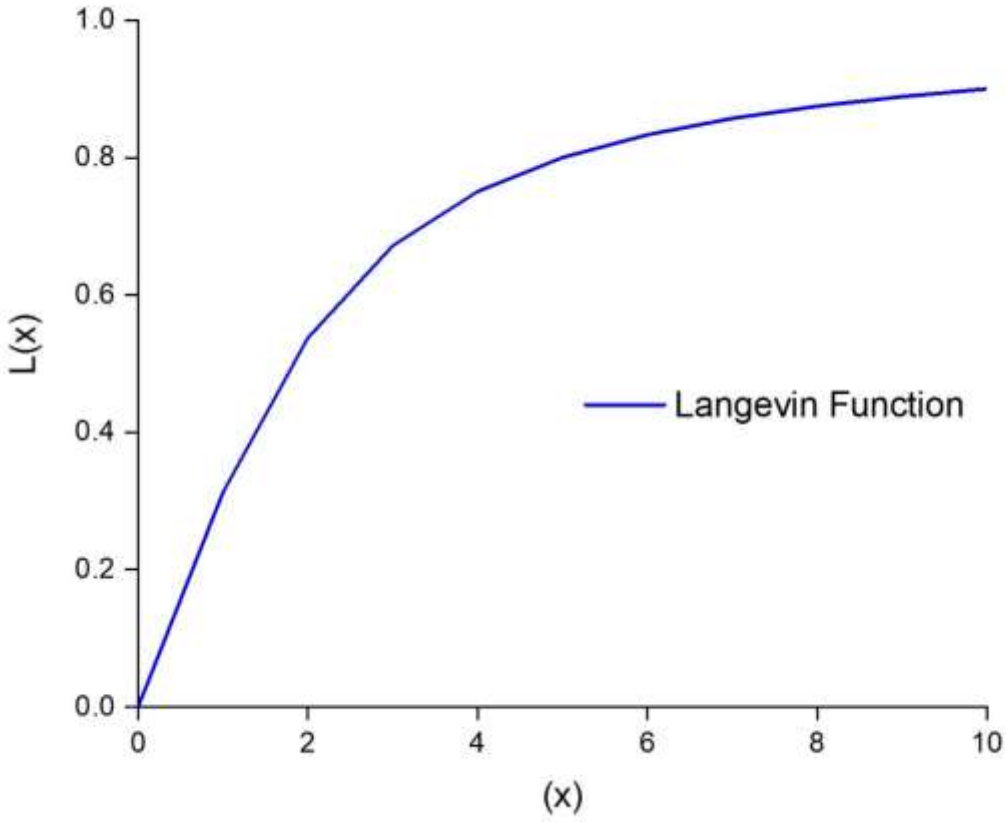

Figure 7.4.11. A Plot of the Langevin function from 0.01 – 10 from Equation 7.4.2 that is used to indicate superparamagnetic character as shown in Equation 7.4.1.

7.4 Impact of Research Progression

The central impact of this work is the creation of a novel material that was synthesized and studied for the first time. The experimental results of this research demonstrated the efficacy of the creation of the molten chloride ferrofluid. The material demonstrated suspension of various sizes and compositions of magnetic nanoparticles for the duration of experiments in this work and therefore contains some degree of colloidal stability. An experimental apparatus and methodology unique to this work demonstrated that particles maintained magnetic susceptibility at elevated temperatures. Of the types of particles tested, cobalt was found to have the largest temperature range of magnetic susceptibility. Additionally, maintaining magnetic susceptibility for the duration of the temperature range infers that the particles contained some degree of chemical inertness to the molten salt matrix to retain ferromagnetism. Lastly, the surprising increase in magnetic susceptibility at elevated temperatures above the melting point of the material represents the first time the Hopkinson Effect has been observed in any solution at the temperatures tested.

The impact of the developments of this work could be very advantageous in applications utilizing molten chloride salts as heat transfer fluids. The temperature range of magnetic susceptibility found in this work confirms that this material would maintain magnetism in a range relevant to both concentrated solar power and nuclear reactor applications. Both applications require pumping of molten salt through the system and currently use internal mechanical pumping mechanisms.[248, 249] If the molten salt heat transfer fluid's matrix is made magnetic then external magnetic fields could be utilized to pump fluid through the system without an internal pumping mechanism. Pumping of ferrofluid via thermomagnetic pumps with no moving parts has already been demonstrated and is finding application in microfluidics.[250-252] In addition to the potential improvement to pumping systems, the ability to tune thermophysical properties of ferrofluids using external magnetic fields can be advantageous to heat transfer fluid applications. Augmentation of various ferrofluid's viscosity, effective heat capacity, and thermal conductivity have been demonstrated in lower temperature systems.[253, 254] Introducing the ability to alter the heat transfer rate in nuclear reactor and concentrated solar power systems only by using an external magnetic field could have a broad impact on advancement of control, efficiency, and size of the systems.

7.5 Future Directions

The results of this work provide evidence to help answer the question of whether it is possible to create a high temperature ferrofluid that utilizes molten chloride salts as the base fluid. The three research objectives outlined in section 1.4.3 were achieved. Visual light scattering confirmed continued suspension of particles within the solution demonstrating some degree of colloidal stability of the particles. The suspended particles demonstrated a degree of chemical stability to the matrix by maintaining their magnetic susceptibility prior to the material's Curie temperature during experiments. The final research objective of determining of particles retain magnetism at elevated temperatures was also achieved by magnetic susceptibility measurements. After optimization of methodology all cobalt particles examined demonstrated no loss of magnetic susceptibility. The achievement of all research objectives in this work were in a qualitative manner demonstrating proof of concept of molten chloride ferrofluids.

To fully understand the physical properties of molten chloride ferrofluids the three outlined research objectives must be examined with more quantitative methodologies. The visual confirmation of the Tyndall Effect present in the ferrofluids during this work cannot provide any information other than confirmation of particle suspension. The next step for this research objective would be to quantify the extent of colloidal stability and details of particle suspension. There are several analytical techniques that have been applied to understand physical details of colloids that form ferrofluids. Transmission electron microscopy has been applied to magnetic nanoparticle colloids previously demonstrating the ability to provide size and structural information.[255] This technique could be applied to this work if the ferrofluid can be vitrified with the glass machine outlined in Chapter 6 due to crystallization. Thermomagnetic measurements have been applied to superparamagnetic nanoparticles by using the zero-field magnetic moment to indirectly provide size information of the particles.[256] Acoustic spectrometry can provide particle size and distribution information based on scattering and absorption of acoustic energy pulses through the sample.[257] Optical signals while the particles are undergoing Brownian motion can provide size and diffusion information in dark-field microscopy.[258] Dark-field microscopy can also provide visual information of particle flocculation, which could provide useful stability information related to molten chloride ferrofluids.[259] Transmission electron microscopy can also be used to probe the degradation of particles before and after suspension in molten salt.

While other techniques can provide further information, the most widely used analytical technique for further insight into the physical details of the magnetic colloids is dynamic light scattering or photon correlation spectroscopy.[260] A technique that has been previously applied to ferrofluids successfully.[261] This technique operates via scattering of incident light beams by suspended particles resulting in changes in direction and intensity of incident light that is subsequently detected.[262] The Brownian motion of particles results in variations of scattering over time and can yield the particle's diffusion coefficient.[263] The diffusion coefficient in conjunction with the Stokes-Einstein equation could then be used to determine the hydrodynamic radius of the particles.[264] Information that could be useful for quantification of both colloidal details and insight into potential particle degradation over extended periods. Dynamic light scattering has also been utilized to quantify total colloidal stability of magnetic nanoparticle colloids.[265] This technique can also provide the kinetics of particle aggregation.[266, 267] Analysis of molten chloride ferrofluid utilizing dynamic light scattering is the next logical step in fully understanding colloidal stability needed to guide future research.

While the result of this work infers that the particles contain some degree of chemical stability in the solution due to presence of continued magnetic susceptibility. The only definitive conclusion that can be drawn from this result is that the particles are not degraded by the solution to the point of magnetism loss. The next step in research would be to quantitatively evaluate the particle-solution interaction at the particle surface. The results of the dynamic light scattering experiments can provide some quantitative insight into change of particle hydrodynamic radius over time revealing degradation kinetics. Two techniques can be applied in a complimentary manner to paint the full picture of particle-solution interaction. The first measurements would require full field x-ray imaging via the hard x-ray transmission microscope located at Brookhaven National Laboratory's National Synchrotron Light Source II. This technique would allow in-situ three dimensional spatial measurements with a resolution of 30 nm and field of view of approximately 40 μm.[268] This technique can reveal real time particle-solution interactions while the solution is molten demonstrating degradation kinetics and mechanisms. Furthermore, small angle neutron scattering can complement the quantitative understanding of chemical stability. This experimental technique utilizes elastic neutron scattering at small angles of $\leq 10^{o}$ to probe structural features at a length scale between 0.6 – 100 nm.[269] This is a robust technique that has reliably

provided structural information and particle surface characteristics in lower temperature colloids and has been successfully applied to ferrofluids.[270-272]

The final research objective that was completed during this work determined that magnetic nanoparticles of the sizes and identities measured will maintain some degree of susceptibility to an external magnetic field at increased temperatures. The non-cobalt particles maintained magnetic susceptibility approximately matching the literature value for the Curie Temperature of the bulk material. To quantitatively understand the impact of the magnitude of an external magnetic field, the experimental measurements mentioned previously in this section would require measurements in magnetic fields of varying strengths. These measurements would provide a robust analysis of precise details of the extent of magnetic susceptibility by analyzing particle orientation as a function of magnetic field strength and temperature. To validate the measurements obtained by the magnetic susceptibility experimental apparatus used during this work, measurements utilizing superconducting quantum interference device relaxometry can be applied. This technique detects particles by first magnetizing the particles with a pulse of a DC magnetic field. This is followed by detection of decaying particle magnetization in a zero field.[273] The results of these measurements are the dependence of the particles on an external magnetic field and can therefore demonstrate magnetic susceptibility as a function of temperature.[274] This would allow for quantification of extent of magnetic interaction and would provide further proof of the Hopkinson Effect present in the molten chloride ferrofluid systems.

7.6 Conclusion

Nanoparticles can be introduced to various molten salt matrices and can form a colloidally stable solution or a nanofluid. This work demonstrated that magnetic particles could remain suspended in a solution and interact with an external magnetic field up to 800 ^{o}C creating the first molten chloride ferrofluid. With the interest in molten salt being used for industrial HTF applications these findings create a unique opportunity to advance engineering controls in all aspects. Each of the three original research objectives for this work were met. The Tyndall Effect was visually observed in all solutions containing magnetic nanoparticles. The absence of immediate phase separation confirms a degree of colloidal stability in the solutions. Measuring the

molten ferrofluid's magnetic susceptibility in an external magnetic field as a function of temperature fulfilled the two remaining research objectives. The gravimetric magnetic susceptibility experiment confirmed solutions containing magnetic nanoparticles maintained a degree of magnetism at increased temperature to their literature Curie Temperature value or 800 ^{o}C. The chemical stability of the particles is inferred due to the continued magnetism of the particles in the molten state at elevated temperatures. Had the particles been fully digested through reacting with the solution matrix, then the magnetic susceptibility would have been impacted. Additionally, the flame sealed silica ampules that were used to contain ferrofluid during experiments were a closed system. The absence of over pressurization and subsequent rupturing of ampules during experiments infers reactions between the salt and particles did not evolve gaseous products. Now that research objectives have been met showing efficacy of molten chloride ferrofluid, studies on influence of external magnetic field's effect on solution specific heat capacity can begin. If the molten chloride ferrofluid's heat capacity can be increased with an external magnetic field the result could lay the framework through which novel designs of heat transfer systems in Generation IV reactor systems can be established. Potentially allowing for microscopic control of all aspects of solutions within the reactor. Based on established literature characteristics of this fluid and the confirmation of this work that it can be extended to molten salt systems to tune viscosity, heat capacity, and flow rates. Even opening the door to using magneto pumping mechanisms as opposed to classical pumps to reduce material exposed to the potentially corrosive salt media.

In addition to the research objectives, this work resulted in peculiar findings of an increase in magnetic susceptibility after the melting point of the salt and continuing to increase until the Curie Temperature. Review of the literature determined this surprising finding is the result of the Hopkinson Effect indicating the particles become superparamagnetic above the salt's melting temperature. This conclusion is based on the results of previous literature and data similarity to the Langevin function. Superparamagnetic character has not previously been observed in a molten chloride salt solution or any solution at temperatures >400 ^{o}C. Further studies are warranted to understand the increase of magnetic susceptibility and can be accomplished through the more quantitative approaches to the three research objectives outlined in the previous section. Implications of quantitative confirmation of presence of superparamagnetic characteristics has the potential to greatly impact the field of high-temperature heat transfer fluids.

References

1. Pauling, L., The nature of the chemical bond. Application of results obtained from the quantum mechanics and from a theory of paramagnetic susceptibility to the structure of molecules. *Journal of the American Chemical Society* **1931,** *53* (4), 1367-1400.

2. Wilkes, J. S., A short history of ionic liquids—from molten salts to neoteric solvents. *Green Chemistry* **2002,** *4* (2), 73-80.

3. Ma, Z.; Yu, J.; Dai, S., Preparation of Inorganic Materials Using Ionic Liquids. *Advanced Materials* **2010,** *22* (2), 261-285.

4. Lantelme, F.; Groult, H., *Molten salts chemistry: from lab to applications*. Newnes: 2013.

5. White, S., Halides. In *Molten salt techniques. Vol. 1*, 1983.

6. Mamantov, G.; Marassi, R., *Molten salt chemistry: An introduction and selected applications*. Springer Science & Business Media: 2012; Vol. 202.

7. Hsu, Y.-T.; Escue, R.; Tidwell Jr, T., The stabilities of complex ions in molten salts. *Journal of Electroanalytical Chemistry and Interfacial Electrochemistry* **1967,** *15*, 245-267.

8. Shimoji, M., Interaction in molten salt mixtures. *Discussions of the Faraday Society* **1961,** *32*, 128-137.

9. Taube, M. *Fast reactors using molten chloride salts as fuel*; INFCE (Switzerland): 1978.

10. Briant, R. C.; Weinberg, A. M., Molten fluorides as power reactor fuels. *Nuclear science and engineering* **1957,** *2* (6), 797-803.

11. McPherson, H. *Molten Salts for Civilian Power*; Oak Ridge National Lab., Tenn.: 1957.

12. Bettis, E.; Cottrell, W.; Mann, E.; Meem, J.; Whitman, G., The aircraft reactor experiment—operation. *Nuclear Science and Engineering* **1957,** *2* (6), 841-853.

13. Rosenthal, M.; Kasten, P.; Briggs, R., Molten-salt reactors—history, status, and potential. *Nuclear Applications and Technology* **1970,** *8* (2), 107-117.

14. Haubenreich, P. N.; Engel, J., Experience with the molten-salt reactor experiment. *Nuclear Applications and technology* **1970,** *8* (2), 118-136.

15. Taube, M., Plutonium Fused Salts for Fast Breeder Reactor. *Nukleonika (Poland)* **1961,** *6*.

16. MacPherson, H., The molten salt reactor adventure. *Nuclear Science and engineering* **1985,** *90* (4), 374-380.

17. Goodman, C.; Greenstadt, J. L.; Kiehn, R. M.; Klein, A.; Mills, M. M.; Tralli, N. *Nuclear problems of non-aqueous fluid-fuel reactors*; Massachusetts Inst. of Tech., Cambridge, MA. Nuclear Engineering Project (US): 1952.

18. Bulmer, J., *Fused salt fast breeder: reactor design and feasibility study*. United States Atomic Energy Commission, Technical Information Service Extension: 1957; Vol. 56.

19. Alexander, L. In *Molten-salt fast reactors*, Proc. Conf. Breeding, Economics and Safety in Large Fast Power Reactors, 1963; p 553.

20. White, R., Depleted uranium, state crime and the politics of knowing. *Theoretical Criminology* **2008,** *12* (1), 31-54.

21. Dunn, R. I.; Hearps, P. J.; Wright, M. N., Molten-salt power towers: newly commercial concentrating solar storage. *Proceedings of the IEEE* **2011,** *100* (2), 504-515.

22. Kearney, D.; Kelly, B.; Herrmann, U.; Cable, R.; Pacheco, J.; Mahoney, R.; Price, H.; Blake, D.; Nava, P.; Potrovitza, N., Engineering aspects of a molten salt heat transfer fluid in a trough solar field. *Energy* **2004,** *29* (5-6), 861-870.

23. Kerestes, R. J.; Reed, G. F.; Sparacino, A. R. In *Economic analysis of grid level energy storage for the application of load leveling*, 2012 IEEE Power and Energy Society General Meeting, IEEE: 2012; pp 1-9.

24. Qiao, Z.; Guo, Q.; Sun, H.; Pan, Z.; Liu, Y.; Xiong, W., An interval gas flow analysis in natural gas and electricity coupled networks considering the uncertainty of wind power. *Applied energy* **2017,** *201*, 343-353.

25. Gordon, J. M.; Fasquelle, T.; Nadal, E.; Vossier, A., Providing large-scale electricity demand with photovoltaics and molten-salt storage. *Renewable and Sustainable Energy Reviews* **2021,** *135*, 110261.

26. Zhang, H.; Baeyens, J.; Caceres, G.; Degreve, J.; Lv, Y., Thermal energy storage: Recent developments and practical aspects. *Progress in Energy and Combustion Science* **2016,** *53*, 1-40.

27. Vignarooban, K.; Xu, X.; Wang, K.; Molina, E.; Li, P.; Gervasio, D.; Kannan, A. M., Vapor pressure and corrosivity of ternary metal-chloride molten-salt based heat transfer fluids for use in concentrating solar power systems. *Applied Energy* **2015,** *159*, 206-213.

28. Zhang, H.; Baeyens, J.; Degrève, J.; Cacères, G., Concentrated solar power plants: Review and design methodology. *Renewable and sustainable energy reviews* **2013,** *22*, 466-481.

29. González-Roubaud, E.; Pérez-Osorio, D.; Prieto, C., Review of commercial thermal energy storage in concentrated solar power plants: Steam vs. molten salts. *Renewable and sustainable energy reviews* **2017,** *80*, 133-148.

30. Desideri, U.; Campana, P. E., Analysis and comparison between a concentrating solar and a photovoltaic power plant. *Applied energy* **2014,** *113*, 422-433.

31. Williams, D. F.; Toth, L. M.; Clarno, K. T., *Assessment of Candidate Molten Salt Coolants for the Advanced High Temperature Reactor (AHTR)*. United States. Department of Energy: 2006.

32. Sabharwall, P.; Clark, D.; Glazoff, M.; Zheng, G.; Sridharan, K.; Anderson, M., Advanced heat exchanger development for molten salts. *Nuclear Engineering and Design* **2014,** *280*, 42-56.

33. Sood, D.; Iyer, P.; Prasad, R.; Vaidya, V.; Roy, K.; Venugopal, V.; Singh, Z.; Ramaniah, M., Plutonium trifluoride as a fuel for molten salt reactors-solubility studies. *Nuclear technology* **1975,** *27* (3), 411-415.

34. Le Brun, C., Molten salts and nuclear energy production. *Journal of nuclear materials* **2007,** *360* (1), 1-5.

35. Roper, R.; Harkema, M.; Sabharwall, P.; Riddle, C.; Chisholm, B.; Day, B.; Marotta, P., Molten salt for advanced energy applications: A review. *Annals of Nuclear Energy* **2022,** *169*, 108924.

36. Gat, U.; Dodds, H. *The source term and waste optimization of molten salt reactors with processing*; Oak Ridge National Lab., TN (United States): 1993.

37. Gehin, J. C.; Powers, J. J., Liquid fuel molten salt reactors for thorium utilization. *Nuclear Technology* **2016,** *194* (2), 152-161.

38. Janz, G. J.; Tomkins, R. *Physical properties data compilations relevant to energy storage. IV. Molten salts: data on additional single and multi-component salt systems*; National Standard Reference Data System: 1981.

39. Elsheikh, B. M., Safety assessment of molten salt reactors in comparison with light water reactors. *journal of radiation research and applied sciences* **2013,** *6* (2), 63-70.

40. Mohan, G.; Venkataraman, M.; Gomez-Vidal, J.; Coventry, J., Thermo-economic analysis of high-temperature sensible thermal storage with different ternary eutectic alkali and alkaline earth metal chlorides. *Solar Energy* **2018,** *176*, 350-357.

41. Brockner, W.; Toerklep, K.; Oeye, H. A., Viscosity of molten alkali chlorides. *Journal of Chemical and Engineering Data* **1981,** *26* (3), 250-253.

42. Kleppa, O., Thermodynamics of molten salt mixtures. In *Molten Salt Chemistry*, Springer: 1987; pp 79-122.

43. Pasamehmetoglu, K. O., *Transient critical heat flux*. University of Central Florida: 1986.

44. Li, Y.; Xu, X.; Wang, X.; Li, P.; Hao, Q.; Xiao, B., Survey and evaluation of equations for thermophysical properties of binary/ternary eutectic salts from NaCl, KCl, MgCl2, CaCl2, ZnCl2 for heat transfer and thermal storage fluids in CSP. *Solar Energy* **2017,** *152*, 57-79.

45. Joskow, P. L., Capacity payments in imperfect electricity markets: Need and design. *Utilities Policy* **2008,** *16* (3), 159-170.

46. Nuttall, W. J., *Nuclear renaissance: technologies and policies for the future of nuclear power*. CRC Press: 2022.

47. Cooper, M., Small modular reactors and the future of nuclear power in the United States. *Energy Research & Social Science* **2014,** *3*, 161-177.

48. Mayes, R. T.; Kurley III, J. M.; Halstenberg, P. W.; McAlister, A.; Sulejmanovic, D.; Raiman, S. S.; Dai, S.; Pint, B. A. *Purification of Chloride Salts for Concentrated Solar Applications*; Oak Ridge National Lab.(ORNL), Oak Ridge, TN (United States): 2018.

49. Kurley, J. M.; Halstenberg, P. W.; McAlister, A.; Raiman, S.; Dai, S.; Mayes, R. T., Enabling chloride salts for thermal energy storage: implications of salt purity. *RSC Adv.* **2019,** *9* (44), 25602-25608.

50. Macedo, P.; Napolitano, A., Inadequacies of viscosity theories for B2O3. *The Journal of Chemical Physics* **1968,** *49* (4), 1887-1895.

51. Xu, D.; Duan, G.; Johnson, W. L.; Garland, C., Formation and properties of new Ni-based amorphous alloys with critical casting thickness up to 5 mm. *Acta Materialia* **2004,** *52* (12), 3493-3497.

52. Harms, N.; Rodriguez, P., Safeguards at light-water reactors: Current practices, future directions. *IAEA Bulletin* **1996,** *38* (4), 16-19.

53. Zhao, Y. *Molten Chloride Thermophysical Properties, Chemical Optimization, and Purification*; National Renewable Energy Lab.(NREL), Golden, CO (United States): 2020.

54. Redkin, A.; Korzun, I.; Yaroslavtseva, T.; Reznitskikh, O.; Zaikov, Y., Isobaric heat capacity of molten halide eutectics. *J. Therm. Anal. Calorim.* **2017,** *128* (1), 621-626.

55. Xu, X. K.; Dehghani, G.; Ning, J. X.; Li, P. W., Basic properties of eutectic chloride salts NaCl-KCl-ZnCl2 and NaCl-KCl-MgCl2 as HTFs and thermal storage media measured using simultaneous DSC-TGA. *Sol. Energy* **2018,** *162*, 431-441.

56. Qiao, G.; Lasfargues, M.; Alexiadis, A.; Ding, Y. L., Simulation and experimental study of the specific heat capacity of molten salt based nanofluids. *Appl. Therm. Eng.* **2017,** *111*, 1517-1522.

57. Ho, M. X.; Pan, C., Optimal concentration of alumina nanoparticles in molten Hitec salt to maximize its specific heat capacity. *Int. J. Heat Mass Transf.* **2014,** *70*, 174-184.

58. Jo, B.; Banerjee, D., Enhanced specific heat capacity of molten salt-based nanomaterials: Effects of nanoparticle dispersion and solvent material. *Acta Mater.* **2014,** *75*, 80-91.

59. Lai, C. C.; Chang, W. C.; Hu, W. L.; Wang, Z. M. M.; Lu, M. C.; Chueh, Y. L., A solar-thermal energy harvesting scheme: enhanced heat capacity of molten HITEC salt mixed with Sn/SiOx core-shell nanoparticles. *Nanoscale* **2014,** *6* (9), 4555-4559.

60. Shin, D.; Banerjee, D., Specific heat of nanofluids synthesized by dispersing alumina nanoparticles in alkali salt eutectic. *Int. J. Heat Mass Transf.* **2014,** *74*, 210-214.

61. Wang, X. Q.; Mujumdar, A. S., Heat transfer characteristics of nanofluids: a review. *Int. J. Therm. Sci.* **2007,** *46* (1), 1-19.

62. Zhang, H.; Dasbiswas, K.; Ludwig, N. B.; Han, G.; Lee, B.; Vaikuntanathan, S.; Talapin, D. V., Stable colloids in molten inorganic salts. *Nature* **2017,** *542* (7641), 328-+.

63. Chieruzzi, M.; Cerritelli, G. F.; Miliozzi, A.; Kenny, J. M., Effect of nanoparticles on heat capacity of nanofluids based on molten salts as PCM for thermal energy storage. *Nanoscale Res. Lett.* **2013,** *8*, 9.

64. Yuan, F.; Li, M. J.; Qiu, Y.; Ma, Z.; Li, M. J., Specific heat capacity improvement of molten salt for solar energy applications using charged single-walled carbon nanotubes. *Appl. Energy* **2019,** *250*, 1481-1490.

65. Raj, K.; Moskowitz, B.; Casciari, R., Advances in ferrofluid technology. *Journal of magnetism and magnetic materials* **1995,** *149* (1-2), 174-180.

66. Philip, J.; Shima, P. D.; Raj, B., Evidence for enhanced thermal conduction through percolating structures in nanofluids. *Nanotechnology* **2008,** *19* (30), 305706.

67. Gul, A.; Khan, I.; Shafie, S.; Khalid, A.; Khan, A., Heat Transfer in MHD Mixed Convection Flow of a Ferrofluid along a Vertical Channel. *PLoS One* **2015,** *10* (11), e0141213-e0141213.

68. Singh, A. K.; Raykar, V. S., Experimental Investigation of Thermal Conductivity and Effusivity of Ferrite Based Nanofluids under Magnetic Field. *ISRN Nanotechnology* **2013,** *2013*, 479763.

69. Xie, H.; Yu, W.; Li, Y.; Chen, L., Discussion on the thermal conductivity enhancement of nanofluids. *Nanoscale Res Lett* **2011,** *6* (1), 124-124.

70. Philip, J.; P Damodaran, S.; Raj, B., Enhancement of thermal conductivity in magnetite based nanofluid due to chainlike structures. *Applied Physics Letters* **2007,** *91*, 203108-203108.

71. Hong, T.-K.; Yang, I. H.-S.; Choi, C., Study of the Enhanced Thermal Conductivity of Fe Nanofluids. *Journal of Applied Physics* **2005,** *97*, 064311-064311.

72. Hong, k.; Hong, T.-K.; Yang, I. H.-S., Thermal conductivity of Fe nanofluids depending on the cluster size of nanoparticles. *Applied Physics Letters* **2006,** *88*, 031901-031901.

73. Holotescu, S.; Stoian, F. D., Evaluation of the effective thermal conductivity of composite polymers by considering the filler size distribution law. *Journal of Zhejiang University-SCIENCE A* **2009,** *10*, 704-709.

74. Krichler, M.; Odenbach, S., Thermal conductivity measurements on ferrofluids with special reference to measuring arrangement. *Journal of Magnetism and Magnetic Materials* **2013,** *326*, 85-90.

75. Nkurikiyimfura, I.; Wang, Y.; Pan, Z.; Hu, D., *Thermal conductivity enhancement of magnetic nanofluid in magnetic field*. 2011; Vol. 2.

76. P Damodaran, S.; Philip, J.; Raj, B., Magnetically controllable nanofluid with tunable thermal conductivity and viscosity. *Applied Physics Letters* **2009,** *95*, 133112-133112.

77. Lovering, D. G.; Gale, R. J., *Molten salt techniques. Volume 3*. Plenum Press,New York, NY: United States, 1987; p Medium: X; Size: Pages: 349 2008-02-07 Plenum Press, 233 Spring Street, New York, NY 10013.

78. Schlenk, W.; Thal, A., Über Metallketyle, eine große Klasse von Verbindungen mit dreiwertigem Kohlenstoff II. *Berichte der deutschen chemischen Gesellschaft* **1913,** *46* (3), 2840-2854.

79. Xi, J.; Jiang, H.; Liu, C.; Morgan, D.; Szlufarska, I., Corrosion of Si, C, and SiC in molten salt. *Corrosion Science* **2019,** *146*, 1-9.

80. Smith, L., Control of corrosion in oil and gas production tubing. *British Corrosion Journal* **1999,** *34* (4), 247-253.

81. Janz, G. J., *Molten salts handbook*. Elsevier: 2013.

82. Janz, G. J.; Allen, C. B.; Bansal, N.; Murphy, R.; Tomkins, R., Physical properties data compilations relevant to energy storage, 2. Molten salts: Data on single and multi-component salt systems. *Nasa Sti/recon Technical Report N* **1979,** *80*, 10643.

83. Wen, H.; Zhang, X.; Xia, R.; Yang, Z.; Wu, Y., Thermal Decomposition Properties of Epoxy Resin in SF_6/N_2 Mixture. *Materials (Basel)* **2018,** *12* (1).

84. Zehnder, C.; Bruns, S.; Peltzer, J.-N.; Durst, K.; Korte-Kerzel, S.; Möncke, D., Influence of cooling rate on cracking and plastic deformation during impact and indentation of borosilicate glasses. *Frontiers in Materials* **2017,** *4*, 5.

85. De Bakker, J.; Peacey, J.; Davis, B., Thermal decomposition studies on magnesium hydroxychlorides. *Canadian Metallurgical Quarterly* **2012,** *51* (4), 419-423.

86. Kashani-Nejad, S.; Ng, K.-W.; Harris, R., MgOHCl thermal decomposition kinetics. *Metallurgical and Materials Transactions B* **2005,** *36* (1), 153-157.

87. Martin, R.; West, J., Solubility of magnesium oxide in molten salts. *Journal of Inorganic and Nuclear Chemistry* **1962,** *24* (1), 105-111.

88. Ishitsuka, T.; Nose, K., Stability of protective oxide films in waste incineration environment - solubility measurement of oxides in molten chlorides. *Corrosion Sci.* **2002,** *44* (2), 247-263.

89. Ruh, A.; Spiegel, M., Thermodynamic and kinetic consideration on the corrosion of Fe, Ni and Cr beneath a molten KCl-ZnCl2 mixture. *Corrosion Sci.* **2006,** *48* (3), 679-695.

90. Wang, S. L.; Zhang, F. S.; Liu, X.; Zhang, L. J., CaO solubility and activity coefficient in molten salts CaCl2-x (x=0, NaCl, KCl, SrCl2, BaCl2 and LiCl). *Thermochim. Acta* **2008,** *470* (1-2), 105-107.

91. Cherginets, V. L.; Khailova, E. G., ON THE SOLUBILITIES OF BIVALENT-METAL OXIDES IN MOLTEN ALKALINE CHLORIDES. *Electrochim. Acta* **1994,** *39* (6), 823-829.

92. Cherginets, V. L., On studies of oxide solubilities in melts based on alkaline halides. *Electrochim. Acta* **1997,** *42* (23-24), 3619-3627.

93. W., G. J., A Method of Geometrical Representation of the Thermodynamic Properties of Substances by Means of Surface. *Transactions of the Connecticut Academy of Arts and Sciences* **1873,** *2*, 382-404.

94. Earnshaw, N. N. G. a. A., *Chemistry of the Elements*. 1997; p 1600.

95. Hildenbrand, R. H. L. a. D. L., High-Temperature Vaportization Behavior of Oxides II. Oxides of Be, Mg, Ca, Sr, Ba, B, Al, Ga, Ti, Si, Ge, Sn, Pb, Zn, Cd, and Hg. *Journal of Physical Chemistry Reference Data* **1986,** *16* (3), 419-433.

96. Young, S.; Fortey, E. C., Fractional distillation as a method of quantitative analysis. *Journal of the Chemical Society* **1902,** *81*, 752-768.

97. Naumann, A.; Muller, W., Distillation method for the determination of hydrolysis. *Journal Fur Praktische Chemie-Leipzig* **1906,** *74* (5), 218-221.

98. Baes Jr, C. *The chemistry and thermodynamics of molten salt reactor fluoride solutions*; Oak Ridge National Lab., Tenn.: 1965.

99. DeVan, J.; Evans III, R. *Corrosion behavior of reactor materials in fluoride salt mixtures*; Oak Ridge National Lab., Tenn.: 1962.

100. Shaffer, J. H. *PREPARATION AND HANDLING OF SALT MIXTURES FOR THE MOLTEN SALT REACTOR EXPERIMENT*; Oak Ridge National Lab., Tenn.: 1971.

101. Maltsev, D.; Halstenberg, P. W.; Mahurin, S. M.; Dai, S., Promising Method of Sm–Co Magnet Reprocessing in Alkali Chloride Melts. *Industrial & Engineering Chemistry Research* **2022,** *61* (44), 16577-16583.

102. Fray, D. J., Emerging molten salt technologies for metals production. *JOM* **2001,** *53* (10), 27-31.

103. Dobbins, M. S.; Burnet, G., Carbochlorination of dispersed oxides in a molten salt reactor. *AIChE Journal* **1988,** *34* (7), 1086-1093.

104. Dai, S.; Begun, G.; Young, J.; Mamantov, G., Application of chemometric methods in Raman spectroscopic studies of molten salt system containing MgCl2-KCl: Experimental evidence for existence of Mg2Cl dimer and its Raman spectrum. *Journal of Raman Spectroscopy* **1995,** *26* (10), 929-932.

105. Shchukarev, S. A., CONCERNING BASICITY AND ACIDITY OF OXIDES OF THE HEAVIER METALS OF THE PERIODIC SYSTEM. *Zhurnal Obshchei Khimii* **1958,** *28* (4), 845-859.

106. Zinchenko, V. F.; Timukhin, E. V.; Pavlinchuk, S. A.; Nechiporenko, A. V.; Sadkovskaya, L. V., Basicity-acidity and solubility of metal fluorides and oxides in salt melts. *Russ. J. Electrochem.* **2012,** *48* (10), 995-999.

107. Jeong, N. C.; Lee, J. S.; Tae, E. L.; Lee, Y. J.; Yoon, K. B., Acidity Scale for Metal Oxides and Sanderson's Electronegativities of Lanthanide Elements. *Angew. Chem.-Int. Edit.* **2008,** *47* (52), 10128-10132.

108. Podder, J.; Gao, S.; Evitts, R.; Besant, R.; Matthews, D., Synthesis of carnallite crystal from KCl-MgCl2 solutions and its characterization. *International Journal of Materials Research (formerly Zeitschrift fuer Metallkunde)* **2013,** *105*.

109. Zhang, Z.; Lu, X.; Wang, T.; Yan, Y.; Pan, F., The dehydration of MgCl2· 6H2O in MgCl2· 6H2O–KCl–NH4Cl system. *Journal of Analytical and Applied Pyrolysis* **2014,** *110*, 248-253.

110. Dias, E. T.; Gill, S. K.; Liu, Y.; Halstenberg, P.; Dai, S.; Huang, J.; Mausz, J.; Gakhar, R.; Phillips, W. C.; Mahurin, S.; Pimblott, S. M.; Wishart, J. F.; Frenkel, A. I., Radiation-Assisted Formation of Metal Nanoparticles in Molten Salts. *The Journal of Physical Chemistry Letters* **2021,** *12* (1), 157-164.

111. Thapaliya, B. P.; Luo, H.; Halstenberg, P.; Meyer, H. M.; Dunlap, J. R.; Dai, S., Low-Cost Transformation of Biomass-Derived Carbon to High-Performing Nano-graphite via Low-Temperature Electrochemical Graphitization. *ACS Applied Materials & Interfaces* **2021,** *13* (3), 4393-4401.

112. Ronne, A.; He, L.; Dolzhnikov, D.; Xie, Y.; Ge, M.; Halstenberg, P.; Wang, Y.; Manard, B. T.; Xiao, X.; Lee, W.-K., Revealing 3D morphological and chemical evolution mechanisms of metals in molten salt by multimodal microscopy. *ACS applied materials & interfaces* **2020,** *12* (15), 17321-17333.

113. Liu, X.; Ronne, A.; Yu, L.-C.; Liu, Y.; Ge, M.; Lin, C.-H.; Layne, B.; Halstenberg, P.; Maltsev, D. S.; Ivanov, A. S., Formation of three-dimensional bicontinuous structures via molten salt dealloying studied in real-time by in situ synchrotron X-ray nano-tomography. *Nature communications* **2021,** *12* (1), 1-12.

114. Sure, J.; Gill, S. k.; Wang, Y.; Bawane, K. K.; He, L.; Halstenberg, P.; Dai, S.; Mahurin, S. M.; Wishart, J. F.; Sasaki, K., Electrochemical noise studies on localized corrosion of Ni and Ni-20Cr in molten ZnCl2. *Electrochimica Acta* **2022,** *431*, 141126.

115. Bawane, K.; Manganaris, P.; Wang, Y.; Sure, J.; Ronne, A.; Halstenberg, P.; Dai, S.; Gill, S. K.; Sasaki, K.; Chen-Wiegart, Y.-c. K.; Gakhar, R.; Mahurin, S.; Pimblott, S. M.; Wishart, J. F.; He, L., Determining oxidation states of transition metals in molten salt corrosion using electron energy loss spectroscopy. *Scripta Materialia* **2021,** *197*, 113790.

116. Browning, J. F.; Seo, J.; Wenzel, J. F.; Veith, G. M.; Doucet, M.; Ivanov, A. S.; Halstenberg, P.; Lynn, G.; Dai, S., A high temperature cell for investigating interfacial structure on the molecular scale in molten salt/alloy systems. *Review of Scientific Instruments* **2021,** *92* (12), 123903.

117. Wu, F.; Roy, S.; Ivanov, A. S.; Gill, S. K.; Topsakal, M.; Dooryhee, E.; Abeykoon, M.; Kwon, G.; Gallington, L. C.; Halstenberg, P.; Layne, B.; Ishii, Y.; Mahurin, S. M.; Dai, S.; Bryantsev, V. S.; Margulis, C. J., Elucidating Ionic Correlations Beyond Simple Charge Alternation in Molten MgCl2–KCl Mixtures. *The Journal of Physical Chemistry Letters* **2019,** *10* (24), 7603-7610.

118. Wu, F.; Sharma, S.; Roy, S.; Halstenberg, P.; Gallington, L. C.; Mahurin, S. M.; Dai, S.; Bryantsev, V. S.; Ivanov, A. S.; Margulis, C. J., Temperature Dependence of Short and Intermediate Range Order in Molten MgCl2 and Its Mixture with KCl. *The Journal of Physical Chemistry B* **2020,** *124* (14), 2892-2899.

119. Roy, S.; Brehm, M.; Sharma, S.; Wu, F.; Maltsev, D. S.; Halstenberg, P.; Gallington, L. C.; Mahurin, S. M.; Dai, S.; Ivanov, A. S.; Margulis, C. J.; Bryantsev, V. S., Unraveling Local Structure of Molten Salts via X-ray Scattering, Raman Spectroscopy, and Ab Initio Molecular Dynamics. *The Journal of Physical Chemistry B* **2021,** *125* (22), 5971-5982.

120. Roy, S.; Sharma, S.; Karunaratne, W. V.; Wu, F.; Gakhar, R.; Maltsev, D. S.; Halstenberg, P.; Abeykoon, M.; Gill, S. K.; Zhang, Y.; Mahurin, S. M.; Dai, S.; Bryantsev, V. S.; Margulis, C. J.; Ivanov, A. S., X-ray scattering reveals ion clustering of dilute chromium species in molten chloride medium. *Chemical Science* **2021,** *12* (23), 8026-8035.

121. Roy, S.; Wu, F.; Wang, H.; Ivanov, A. S.; Sharma, S.; Halstenberg, P.; Gill, S. K.; Milinda Abeykoon, A. M.; Kwon, G.; Topsakal, M.; Layne, B.; Sasaki, K.; Zhang, Y.; Mahurin, S. M.; Dai, S.; Margulis, C. J.; Maginn, E. J.; Bryantsev, V. S., Structure and dynamics of the molten alkali-chloride salts from an X-ray, simulation, and rate theory perspective. *Physical Chemistry Chemical Physics* **2020,** *22* (40), 22900-22917.

122. Gill, S. K.; Huang, J.; Mausz, J.; Gakhar, R.; Roy, S.; Vila, F.; Topsakal, M.; Phillips, W. C.; Layne, B.; Mahurin, S.; Halstenberg, P.; Dai, S.; Wishart, J. F.; Bryantsev, V. S.; Frenkel, A. I., Connections between the Speciation and Solubility of Ni(II) and Co(II) in Molten ZnCl2. *The Journal of Physical Chemistry B* **2020,** *124* (7), 1253-1258.

123. Vutukuru, R.; Pegallapati, A. S.; Maddali, R., Suitability of various heat transfer fluids for high temperature solar thermal systems. *Applied Thermal Engineering* **2019,** *159*, 113973.

124. Cordaro, J. G.; Rubin, N. C.; Bradshaw, R. W., Multicomponent Molten Salt Mixtures Based on Nitrate/Nitrite Anions. *Journal of Solar Energy Engineering* **2011,** *133* (1).

125. Gimenez, P.; Fereres, S., Effect of heating rates and composition on the thermal decomposition of nitrate based molten salts. *Energy Procedia* **2015,** *69*, 654-662.

126. Xu, X.; Wang, X.; Li, P.; Li, Y.; Hao, Q.; Xiao, B.; Elsentriecy, H.; Gervasio, D., Experimental Test of Properties of KCl–MgCl2 Eutectic Molten Salt for Heat Transfer and Thermal Storage Fluid in Concentrated Solar Power Systems. *Journal of Solar Energy Engineering* **2018,** *140* (5).

127. Wu, F.; Roy, S.; Ivanov, A. S.; Gill, S. K.; Topsakal, M.; Dooryhee, E.; Abeykoon, M.; Kwon, G.; Gallington, L. C.; Halstenberg, P.; Layne, B.; Ishii, Y.; Mahurin, S. M.; Dai, S.; Bryantsev, V. S.; Margulis, C. J., Elucidating Ionic Correlations Beyond Simple Charge Alternation in Molten MgCl2-KCI Mixtures. *J. Phys. Chem. Lett.* **2019,** *10* (24), 7603-7610.

128. Anderson, N.; Sabharwall, P., Molten salt mixture properties (KF-ZrF4 and KCl-MgCl2) for use in RELAP5-3D for high-temperature reactor application. *Nuclear technology* **2012,** *178* (3), 335-340.

129. Motkuri, R. K.; Vemuri, R. S.; Barpaga, D.; Schaef, H.; Loring, J. S.; Martin, P. F.; Lao, D. B.; Nune, S. K.; McGrail, B. P., An Efficient, Solvent-Free Process for Synthesizing Anhydrous MgCl2. *ACS Sustainable Chemistry & Engineering* **2018,** *6* (1), 1048-1054.

130. Kipouros, G. J.; Sadoway, D. R., A thermochemical analysis of the production of anhydrous MgCl2. *Journal of Light Metals* **2001,** *1* (2), 111-117.

131. Fernández, A. G.; Lasanta, M. I.; Pérez, F. J., Molten Salt Corrosion of Stainless Steels and Low-Cr Steel in CSP Plants. *Oxidation of Metals* **2012,** *78* (5), 329-348.

132. Chen, H.-z.; Li, B.-r.; Wen, B.; Ye, Q.; Zhang, N.-q., Corrosion resistance of iron-chromium-aluminium steel in eutectic molten salts under thermal cycling conditions. *Corrosion Science* **2020,** *173*, 108798.

133. Ding, W.; Gomez-Vidal, J.; Bonk, A.; Bauer, T., Molten chloride salts for next generation CSP plants: electrolytical salt purification for reducing corrosive impurity level. *Solar Energy Materials and Solar Cells* **2019,** *199*, 8-15.

134. Goods, S. H.; Bradshaw, R. W., Corrosion of stainless steels and carbon steel by molten mixtures of commercial nitrate salts. *Journal of Materials Engineering and Performance* **2004,** *13* (1), 78-87.

135. Wu, Y.-L.; Huang, X.-F.; Yang, M.-D.; Zou, S.-P.; Dang, J.; Hu, H.-S., Study on the mechanisms and kinetics of complex's thermal decomposition getting anhydrous magnesium chloride. *Journal of Analytical and Applied Pyrolysis* **2008,** *81* (1), 133-135.

136. Do, J.-L.; Friščić, T., Mechanochemistry: A Force of Synthesis. *ACS Central Science* **2017,** *3* (1), 13-19.

137. Chen, D.; Zhao, J.; Zhang, P.; Dai, S., Mechanochemical synthesis of metal–organic frameworks. *Polyhedron* **2019,** *162*, 59-64.

138. Bao, J.; Chen, H.; Yang, S.; Zhang, P., Mechanochemical redox-based synthesis of highly porous CoxMn1-xOy catalysts for total oxidation. *Chinese Journal of Catalysis* **2020,** *41* (12), 1846-1854.

139. Nie, S.; Yang, S.; Zhang, P., Solvent-free synthesis of mesoporous platinum-aluminum oxide via mechanochemistry: Toward selective hydrogenation of nitrobenzene to aniline. *Chemical Engineering Science* **2020,** *220*, 115619.

140. Koby, R. F.; Doerr, A. M.; Rightmire, N. R.; Schley, N. D.; Brennessel, W. W.; Long, B. K.; Hanusa, T. P., Mechanochemical Formation, Solution Rearrangements, and Catalytic Behavior of a Polymorphic Ca/K Allyl Complex. *Chemistry–A European Journal* **2021,** *27* (31), 8195-8202.

141. Ardila-Fierro, K. J.; Pich, A.; Spehr, M.; Hernández, J. G.; Bolm, C., Synthesis of acylglycerol derivatives by mechanochemistry. *Beilstein Journal of Organic Chemistry* **2019,** *15*, 811-817.

142. Chen, Z.; Zhu, X.; Yang, J.; Mercer, J. A. M.; Burns, N. Z.; Martinez, T. J.; Xia, Y., The cascade unzipping of ladderane reveals dynamic effects in mechanochemistry. *Nature Chemistry* **2020,** *12* (3), 302-309.

143. Bolm, C.; Hernández, J. G., Mechanochemistry of Gaseous Reactants. *Angewandte Chemie International Edition* **2019,** *58* (11), 3285-3299.

144. Zhao, Y.; Klammer, N.; Vidal, J., Purification strategy and effect of impurities on corrosivity of dehydrated carnallite for thermal solar applications. *RSC advances* **2019,** *9* (71), 41664-41671.

145. Emons, H.-H., Mechanism and kinetics of formation and decomposition of carnallitic double salts. *Journal of Thermal Analysis and Calorimetry* **1988,** *33* (1), 113-120.

146. Emons, H. H., Mechanism and kinetics of formation and decomposition of carnallitic double salts. *Journal of thermal analysis* **1988,** *33* (1), 113-120.

147. Top, S.; Yildirim, M., Preparation of synthetic carnallite and amorphous silica from chromite beneficiation plant tailings. *Gospodarka Surowcami Mineralnymi* **2017,** *33*, 5-24.

148. Schlemper, E.; Sen Gupta, P.; Zoltai, T., Refinement of the structure of carnallite, Mg (H2O) 6KCl3. *American Mineralogist* **1985,** *70* (11-12), 1309-1313.

149. Young, J.; Mamantov, G. *In-line sensors for electrolytic magnesium cells*; Oak Ridge National Lab., TN (USA): 1990.

150. Zhang, Z.; Lu, X.; Wang, T.; Yan, Y.; Chen, S., Synthesis and electrolysis of K3NaMgCl6. *Industrial & Engineering Chemistry Research* **2015,** *54* (5), 1433-1438.

151. Kiani, H.; Sun, D.-W., Water crystallization and its importance to freezing of foods: A review. *Trends in Food Science & Technology* **2011,** *22* (8), 407-426.

152. Handle, P. H.; Loerting, T.; Sciortino, F., Supercooled and glassy water: Metastable liquid (s), amorphous solid (s), and a no-man's land. *Proceedings of the National Academy of Sciences* **2017,** *114* (51), 13336-13344.

153. Gallo, P.; Amann-Winkel, K.; Angell, C. A.; Anisimov, M. A.; Caupin, F.; Chakravarty, C.; Lascaris, E.; Loerting, T.; Panagiotopoulos, A. Z.; Russo, J.; Sellberg, J. A.; Stanley, H. E.; Tanaka, H.; Vega, C.; Xu, L.; Pettersson, L. G. M., Water: A Tale of Two Liquids. *Chemical Reviews* **2016,** *116* (13), 7463-7500.

154. Burton, E.; Oliver, W., X-ray diffraction patterns of ice. *Nature* **1935,** *135* (3413), 505-506.

155. Mayer, E., New method for vitrifying water and other liquids by rapid cooling of their aerosols. *Journal of applied physics* **1985,** *58* (2), 663-667.

156. Nilsson, A.; Pettersson, L. G., The structural origin of anomalous properties of liquid water. *Nature communications* **2015,** *6* (1), 1-11.

157. Warren, B.; Biscob, J., Fourier analysis of x-ray patterns of soda-silica glass. *Journal of the American Ceramic Society* **1938,** *21* (7), 259-265.

158. Chen, N.; Martin, L.; Luzguine-Luzgin, D. V.; Inoue, A., Role of alloying additions in glass formation and properties of bulk metallic glasses. *Materials* **2010,** *3* (12), 5320-5339.

159. Lovering, D. G., *Molten salt technology*. Plenum Press,New York, NY: United States, 1982; p Medium: X; Size: Pages: 533 2008-02-12 Plenum Publishing Corp., New York, N.Y.

160. Turnbull, D., Formation of crystal nuclei in liquid metals. *Journal of Applied Physics* **1950,** *21* (10), 1022-1028.

161. Turnbull, D.; Cohen, M. H., Free-volume model of the amorphous phase: glass transition. *The Journal of chemical physics* **1961,** *34* (1), 120-125.

162. Rawson, H., *Inorganic glass-forming systems*. Academic press: 1967; Vol. 2.

163. Janz, G. J.; Allen, C. B.; Bansal, N. P.; Murphy, R. M.; Tomkins, R. P. T. *Physical properties data compilations relevant to energy storage. II. Molten salts: data on single and multi-component salt systems*; United States, 1979; p Medium: X; Size: Pages: 442.

164. Maiti, H. S., Transparent and Machinable Glass-Ceramics. In *Handbook of Advanced Ceramics and Composites: Defense, Security, Aerospace and Energy Applications*, Mahajan, Y.; Roy, J., Eds. Springer International Publishing: Cham, 2019; pp 1-33.

165. Sehgal, J.; Ito, S., Brittleness of glass. *Journal of Non-Crystalline Solids* **1999,** *253* (1), 126-132.

166. Bale, C. W.; Chartrand, P.; Degterov, S.; Eriksson, G.; Hack, K.; Mahfoud, R.; Melancon, J.; Pelton, A. D.; Petersen, S., FactSage thermochemical software and databases. *Calphad-computer Coupling of Phase Diagrams and Thermochemistry* **2002,** *26*, 189-228.

167. Mulcahy, M.; Heymann, E., On the Nature of Molten Salts and their Mixtures. *The Journal of Physical Chemistry* **1943,** *47* (7), 485-496.

168. Agarwal, M.; Garg, S.; Asokan, K.; Kanjilal, D.; Kumar, P., Facile synthesis of KCl: Sm 3+ nanophosphor as a new OSL dosimetric material achieved through charge transfer between the defect states. *RSC advances* **2017,** *7* (23), 13836-13845.

169. Thushara, K.; Mathew, R.; Ajithkumar, T.; Rajamohanan, P.; Bhaduri, S.; Gopinath, C. S., MgCl2· 4 (CH3) 2CHOH: A new molecular adduct and super active polymerization catalyst support. *The Journal of Physical Chemistry C* **2009,** *113* (20), 8556-8559.

170. Trivedi, M. K.; Sethi, K. K.; Panda, P.; Jana, S., A comprehensive physicochemical, thermal, and spectroscopic characterization of zinc (II) chloride using X-ray diffraction, particle size distribution, differential scanning calorimetry, thermogravimetric analysis/differential thermogravimetric analysis, ultraviolet-visible, and Fourier transform-infrared spectroscopy. *International Journal of Pharmaceutical Investigation* **2017,** *7* (1), 33.

171. Li, M.; Liu, Y.; Han, W.; Wang, S.; Zhang, M.; Yan, Y.; Shi, W., The electrochemical co-reduction of Mg-Al-Y alloys in the LiCl-NaCl-MgCl2-AlF3-YCl3 melts. *Metallurgical and Materials Transactions B* **2014,** *46*, 644-652.

172. Abualfadl, A.; Soltan, A. M.; Shaalan, N., Influence of cationic substitution on lattice constants and optical characterization in solution grown mixed crystals of potassium- ammonium zinc chloride. *Crystal Research and Technology - CRYST RES TECH* **2006,** *41*, 1013-1019.

173. Wang, D.; Hua, S.; Wu, L.; Liu, K.; Wang, H., Coupled thermodynamics and phase diagram analysis of gas-duct concretion formation in pyro-processing ironmaking and steelmaking dust. *Minerals* **2021,** *11* (10), 1125.

174. The Materials, P., Materials Data on KMgCl3 by Materials Project. United States, 2020.

175. Robelin, C.; Chartrand, P., Thermodynamic evaluation and optimization of the (NaCl+ KCl+ MgCl2+ CaCl2+ ZnCl2) system. *The Journal of Chemical Thermodynamics* **2011,** *43* (3), 377-391.

176. Madsen, I. C.; Scarlett, N. V.; Webster, N. A., Quantitative phase analysis. In *Uniting Electron Crystallography and Powder Diffraction*, Springer: 2012; pp 207-218.

177. Brooker, M.; Huang, C.-H., Raman spectroscopic studies of structural properties of solid and molten states of the magnesium chloride–alkali metal chloride system. *Canadian Journal of Chemistry* **1980,** *58* (2), 168-179.

178. Brooker, M., A Raman spectroscopic study of the structural aspects of K2MgCl4 and Cs2MgCl4 as solid single crystals and molten salts. *The Journal of Chemical Physics* **1975,** *63* (7), 3054-3061.

179. Morris, D.; Short, E.; Waters, D., Zinc chloride and zinc bromide complexes—III: Structures of species in solution. *Journal of Inorganic and Nuclear Chemistry* **1963,** *25* (8), 975-983.

180. Irish, D.; McCarroll, B.; Young, T., Raman study of zinc chloride solutions. *The Journal of Chemical Physics* **1963,** *39* (12), 3436-3444.

181. Kadono, K.; Kageyama, H.; Kamijo, N.; Tanaka, H., Structure of zinc halide-based glasses. *Journal of non-crystalline solids* **1992,** *140*, 98-102.

182. Itoh, M.; Sakai, K.; Nakamura, T., Raman spectral study of the molten zinc chloride-potassium chloride system. *Inorganic Chemistry* **1982,** *21* (9), 3552-3555.

183. Kalampounias, A.; Papatheodorou, G.; Yannopoulos, S., Light scattering from glass-forming molten salts. *Zeitschrift für Naturforschung A* **2002,** *57* (9-10), 65-70.

184. Maroni, V. A.; Hathaway, E. J.; Cairns, E. J., Structural studies of magnesium halide-potassium halide melts by Raman spectroscopy. *The Journal of Physical Chemistry* **1971,** *75* (1), 155-159.

185. Wang, W.-H.; Dong, C.; Shek, C., Bulk metallic glasses. *Materials Science and Engineering: R: Reports* **2004,** *44* (2-3), 45-89.

186. Hwang, J.; Melgarejo, Z.; Kalay, Y. E.; Kalay, I.; Kramer, M. J.; Stone, D.; Voyles, P., Nanoscale structure and structural relaxation in Zr 50 Cu 45 Al 5 bulk metallic glass. *Physical review letters* **2012,** *108* (19), 195505.

187. Tang, C.; Harrowell, P., Anomalously slow crystal growth of the glass-forming alloy CuZr. *Nature materials* **2013,** *12* (6), 507-511.

188. Sachdev, S.; Nelson, D. R., Order in metallic glasses and icosahedral crystals. *Physical Review B* **1985,** *32* (7), 4592.

189. Kelton, K.; Lee, G.; Gangopadhyay, A. K.; Hyers, R.; Rathz, T.; Rogers, J.; Robinson, M.; Robinson, D., First x-ray scattering studies on electrostatically levitated metallic liquids: Demonstrated influence of local icosahedral order on the nucleation barrier. *Physical Review Letters* **2003,** *90* (19), 195504.

190. Sheng, H.; Luo, W.; Alamgir, F.; Bai, J.; Ma, E., Atomic packing and short-to-medium-range order in metallic glasses. *Nature* **2006,** *439* (7075), 419-425.

191. Hirata, A.; Kang, L.; Fujita, T.; Klumov, B.; Matsue, K.; Kotani, M.; Yavari, A.; Chen, M., Geometric frustration of icosahedron in metallic glasses. *Science* **2013,** *341* (6144), 376-379.

192. Zhong, L.; Wang, J.; Sheng, H.; Zhang, Z.; Mao, S. X., Formation of monatomic metallic glasses through ultrafast liquid quenching. *Nature* **2014,** *512* (7513), 177-180.

193. Hirata, A.; Guan, P.; Fujita, T.; Hirotsu, Y.; Inoue, A.; Yavari, A. R.; Sakurai, T.; Chen, M., Direct observation of local atomic order in a metallic glass. *Nature materials* **2011,** *10* (1), 28-33.

194. Debenedetti, P. G.; Stillinger, F. H., Supercooled liquids and the glass transition. *Nature* **2001,** *410* (6825), 259-267.

195. Yang, Y.; Zhou, J.; Zhu, F.; Yuan, Y.; Chang, D. J.; Kim, D. S.; Pham, M.; Rana, A.; Tian, X.; Yao, Y., Determining the three-dimensional atomic structure of an amorphous solid. *Nature* **2021,** *592* (7852), 60-64.

196. Chen, C.-C.; Zhu, C.; White, E. R.; Chiu, C.-Y.; Scott, M.; Regan, B.; Marks, L. D.; Huang, Y.; Miao, J., Three-dimensional imaging of dislocations in a nanoparticle at atomic resolution. *Nature* **2013,** *496* (7443), 74-77.

197. Goris, B.; De Backer, A.; Van Aert, S.; Gómez-Graña, S.; Liz-Marzán, L. M.; Van Tendeloo, G.; Bals, S., Three-dimensional elemental mapping at the atomic scale in bimetallic nanocrystals. *Nano letters* **2013,** *13* (9), 4236-4241.

198. Xu, R.; Chen, C.-C.; Wu, L.; Scott, M.; Theis, W.; Ophus, C.; Bartels, M.; Yang, Y.; Ramezani-Dakhel, H.; Sawaya, M. R., Three-dimensional coordinates of individual atoms in materials revealed by electron tomography. *Nature materials* **2015,** *14* (11), 1099-1103.

199. Yang, Y.; Chen, C.-C.; Scott, M.; Ophus, C.; Xu, R.; Pryor, A.; Wu, L.; Sun, F.; Theis, W.; Zhou, J., Deciphering chemical order/disorder and material properties at the single-atom level. *Nature* **2017,** *542* (7639), 75-79.

200. Finney, J., Random packings and the structure of simple liquids. I. The geometry of random close packing. *Proceedings of the Royal Society of London. A. Mathematical and Physical Sciences* **1970,** *319* (1539), 479-493.

201. Cheng, Y.; Ma, E., Atomic-level structure and structure–property relationship in metallic glasses. *Progress in materials science* **2011,** *56* (4), 379-473.

202. Miracle, D. B., A structural model for metallic glasses. *Nature materials* **2004,** *3* (10), 697-702.

203. Mohan, G. Development of high-temperature sensible thermal energy storage systems for advanced concentrating solar power generation. The Australian National University (Australia), 2019.

204. Muñoz-Sánchez, B.; Nieto-Maestre, J.; Iparraguirre-Torres, I.; García-Romero, A.; Sala-Lizarraga, J. M., Molten salt-based nanofluids as efficient heat transfer and storage materials at high temperatures. An overview of the literature. *Renewable and Sustainable Energy Reviews* **2018,** *82*, 3924-3945.

205. Shin, D.; Banerjee, D., Enhanced specific heat capacity of nanomaterials synthesized by dispersing silica nanoparticles in eutectic mixtures. *Journal of Heat Transfer* **2013,** *135* (3).

206. Genc, S.; Derin, B., Synthesis and rheology of ferrofluids: a review. *Curr. Opin. Chem. Eng.* **2014,** *3*, 118-124.

207. Khairul, M. A.; Doroodchi, E.; Azizian, R.; Moghtaderi, B., Advanced applications of tunable ferrofluids in energy systems and energy harvesters: A critical review. *Energy Conv. Manag.* **2017,** *149*, 660-674.

208. Oehlsen, O.; Cervantes-Ramírez, S. I.; Cervantes-Avilés, P.; Medina-Velo, I. A., Approaches on Ferrofluid Synthesis and Applications: Current Status and Future Perspectives. *ACS omega* **2022,** *7* (4), 3134-3150.

209. Mehta, J. S.; Kumar, R.; Kumar, H.; Garg, H., Convective Heat Transfer Enhancement Using Ferrofluid: A Review. *J. Therm. Sci. Eng. Appl.* **2018,** *10* (2), 12.

210. Buschmann, M. H., Critical review of heat transfer experiments in ferrohydrodynamic pipe flow utilising ferronanofluids. *International Journal of Thermal Sciences* **2020,** *157*, 106426.

211. Weinberg, A. M., A REVIEW OF MOLTEN SALT REACTOR TECHNOLOGY . PREFACE . MOLTEN-SALT REACTORS. *Nuclear Applications and Technology* **1970,** *8* (2), 105-&.

212. Serp, J.; Allibert, M.; Benes, O.; Delpech, S.; Feynberg, O.; Ghetta, V.; Heuer, D.; Holcomb, D.; Ignatiev, V.; Kloosterman, J. L.; Luzzi, L.; Merle-Lucotte, E.; Uhlir, J.; Yoshioka, R.; Dai, Z. M., The molten salt reactor (MSR) in generation IV: Overview and perspectives. *Prog. Nucl. Energy* **2014,** *77*, 308-319.

213. Moir, R. W., Cost of electricity from molten salt reactors. *Nucl. Technol.* **2002,** *138* (1), 93-95.

214. Moir, R. W., Recommendations for a restart of molten salt reactor development. *Energy Conv. Manag.* **2008,** *49* (7), 1849-1858.

215. Holcomb, D. In *U.S. MSR Development Programs & Supportive Efforts*, GIF Molten Salt Reactor pSSC, Switzerland, January 23-25th; Paul Scherer Institute: Switzerland, 2017.

216. Felicia, L. J.; Vinod, S.; Philip, J., Recent Advances in Magnetorheology of Ferrofluids (Magnetic Nanofluids)-A Critical Review. *J. Nanofluids* **2016,** *5* (1), 1-22.

217. Engler, H.; Lange, A.; Borin, D.; Odenbach, S., Hindrance of thermomagnetic convection by the magnetoviscous effect. *Int. J. Heat Mass Transf.* **2013,** *60*, 499-504.

218. Lajvardi, M.; Moghimi-Rad, J.; Hadi, I.; Gavili, A.; Isfahani, T. D.; Zabihi, F.; Sabbaghzadeh, J., Experimental investigation for enhanced ferrofluid heat transfer under magnetic field effect. *Journal of Magnetism and Magnetic Materials* **2010,** *322* (21), 3508-3513.

219. Blums, E.; Mezulis, A.; Kronkalns, G., Magnetoconvective heat transfer from a cylinder under the influence of a nonuniform magnetic field. *J. Phys.-Condes. Matter* **2008,** *20* (20), 5.

220. Tsai, T. H.; Kuo, L. S.; Chen, P. H.; Yang, C. T., Effect of viscosity of base fluid on thermal conductivity of nanofluids. *Applied Physics Letters* **2008,** *93* (23), 3.

221. Tsai, T. H.; Kuo, L. S.; Chen, P. H.; Yang, C. T., Thermal Conductivity of Nanofluid with Magnetic Nanoparticles. In *Piers 2009 Beijing: Progess in Electromagnetics Research Symposium, Proceedings I and Ii*, Kong, J. A., Ed. Electromagnetics Acad: Cambridge, 2009; pp 1344-+.

222. Curie, P., *Propriétés magnétiques des corps a diverses températures*. Gauthier-Villars et fils: 1895.

223. Zanella, R., Thermomagnetic Convection in Ferrofluids : Finite Element Approximation and Application to Transformer Cooling. *Doctoral Thesis* **2018**.

224. Pamme, N., Magnetism and microfluidics. *Lab Chip* **2006,** *6* (1), 24-38.

225. Schwerdt, J.; Goya, G.; Calatayud, M. P.; Herenu, C.; Reggiani, P.; Goya, R., Magnetic Field-Assisted Gene Delivery: Achievements and Therapeutic Potential. *Current gene therapy* **2012,** *12*, 116-26.

226. Caizer, A. P. C., Nanoparticle Size Effect on Some Magnetic Properties. 2015; pp 475-519.

227. Buschow, K. J., *Encyclopedia of materials: science and technology*. Elsevier: 2001; Vol. 1.

228. ANDRE, G.; DUFFIN, W., SOLID STATE FROM SUPERCONDUCTORS TO SUPERALLOYS. University Press: 1989.

229. Kittel, C., Introduction to Solid State Physics, 6th edn., translated by Y. *Uno, N. Tsuya, A. Morita and J. Yamashita,(Maruzen, Tokyo, 1986) pp* **1986**, 124-129.

230. Ouaissa, S.; Benyoussef, A.; Abo, G. S.; Ouaissa, M.; Hafid, M., Magnetization study of cobalt ferrite by mean field approximation. *Physics Procedia* **2015,** *75*, 792-801.

231. Hopkinson, J., XIV. Magnetic and other physical properties of iron at a high temperature. *Philosophical Transactions of the Royal Society of London. (A.)* **1889,** *180*, 443-465.

232. Pfeiffer, H.; Schüppel, W., Temperature dependence of the magnetization in fine particle systems and the Hopkinson effect. Application to barium ferrite powders. *Journal of Magnetism and Magnetic Materials* **1994,** *130* (1), 92-98.

233. Gheiratmand, T.; Hosseini, H. R. M.; Davami, P.; Gjoka, M.; Song, M., The effect of mechanical milling on the soft magnetic properties of amorphous FINEMET alloy. *Journal of Magnetism and Magnetic Materials* **2015,** *381*, 322-327.

234. Manikandan, M.; Kumar, K. S.; Aparnadevi, N.; Venkateswaran, C., Hopkinson effect and temperature-dependent dielectric properties of single domain SrFe12O19 particles. *physica status solidi (a)* **2015,** *212* (10), 2179-2185.

235. Manikandan, M.; Venkateswaran, C., Effect of high energy milling on the synthesis temperature, magnetic and electrical properties of barium hexagonal ferrite. *Journal of Magnetism and Magnetic Materials* **2014,** *358-359*, 82-86.

236. Aronin, A. S.; Abrosimova, G. E.; Kiselev, A. P.; Zhukova, V.; Varga, R.; Zhukov, A., The effect of mechanical stress on Ni63.8Mn11.1Ga25.1 microwire crystalline structure and properties. *Intermetallics* **2013,** *43*, 60-64.

237. Zhukova, V.; Ipatov, M.; Talaat, A.; Zhukov, A., Hopkinson effect in Co-rich glass-coated microwires. *physica status solidi c* **2014,** *11* (5-6), 1130-1132.

238. Sláma, J.; Šoka, M.; Grusková, A.; Gonzalez, A.; Jančárik, V., Hopkinson Effect Study in Spinel and Hexagonal Ferrites. *Journal of Electrical Engineering* **2011,** *62* (4), 239-243.

239. Grusková, A.; Sláma, J.; Ušáková, M.; Šoka, M.; Dosoudil, R.; Degmová, J., Study of Magnetic and Structural Properties of Non-Stoichiometric NiZn Ferrites Prepared by Wet Method. *Acta Physica Polonica-Series A General Physics* **2010,** *118* (5), 780.

240. Ušák, E.; Šoka, M.; Ušáková, M.; Dobročka, E., Structural and Magnetic Properties of Nano-Sized NiZn Ferrites. *Acta Physica Polonica, A.* **2014,** *125* (6).

241. Sláma, J.; Ušáková, M.; Šoka, M.; Dosoudil, R.; Jančárik, V., Hopkinson Effect in Soft and Hard Magnetic Ferrites. *Acta Physica Polonica A* **2017,** *131*, 762-764.

242. Neel, L., Theorie du trainage magnetique des ferromagnetiques en grains fins avec applications aux terres cuites. *Ann. Geophys.* **1949,** *5*, 99-136.

243. Langevin, P., Magnetism and electron theory. *Ann. Chem. Phys.* **1905,** *5* (8), 70-127.

244. Bean, C. P.; Livingston, J. D., Superparamagnetism. *Journal of Applied Physics* **1959,** *30* (4), S120-S129.

245. Kittel, C.; McEuen, P.; McEuen, P., *Introduction to solid state physics*. Wiley New York: 1996; Vol. 8.

246. Shibataki, T.; Takahashi, Y.; Fujiwara, K., Investigation of measurement method of saturation magnetization of iron core material using electromagnet. *AIP Advances* **2018,** *8* (4), 047202.

247. Cheng, G.; Dennis, C. L.; Shull, R. D.; Walker, A. H., Influence of the colloidal environment on the magnetic behavior of cobalt nanoparticles. *Langmuir* **2007,** *23* (23), 11740-11746.

248. Barth, D. L.; Pacheco, J. E.; Kolb, W. J.; Rush, E. E., Development of a high-temperature, long-shafted, molten-salt pump for power tower applications. *J. Sol. Energy Eng.* **2002,** *124* (2), 170-175.

249. Robb, K. R.; Jain, P. K.; Hazelwood, T. J., High-Temperature Salt Pump Review and Guidelines—Phase I Report. *US Department of Energy (DOE) SciTech Connect* **2016**.

250. Pal, S.; Datta, A.; Sen, S.; Mukhopdhyay, A.; Bandopadhyay, K.; Ganguly, R., Characterization of a ferrofluid-based thermomagnetic pump for microfluidic applications. *Journal of Magnetism and Magnetic Materials* **2011,** *323* (21), 2701-2709.

251. Kole, M.; Khandekar, S., Engineering applications of ferrofluids: A review. *Journal of Magnetism and Magnetic Materials* **2021,** *537*, 168222.

252. Mao, L.; Koser, H., Ferrohydrodynamic pumping in spatially traveling sinusoidally time-varying magnetic fields. *Journal of magnetism and Magnetic materials* **2005,** *289*, 199-202.

253. Susan Mousavi, N. S.; Kumar, S., Effective heat capacity of ferrofluids – Analytical approach. *International Journal of Thermal Sciences* **2014,** *84*, 267-274.

254. Alsaady, M.; Fu, R.; Li, B.; Boukhanouf, R.; Yan, Y., Thermo-physical properties and thermo-magnetic convection of ferrofluid. *Applied Thermal Engineering* **2015,** *88*, 14-21.

255. Chatterjee, J.; Haik, Y.; Chen, C.-J., Size dependent magnetic properties of iron oxide nanoparticles. *Journal of Magnetism and Magnetic Materials* **2003,** *257* (1), 113-118.

256. DiPietro, R.; Johnson, H.; Bennett, S.; Nummy, T.; Lewis, L.; Heiman, D., Determining magnetic nanoparticle size distributions from thermomagnetic measurements. *Applied Physics Letters* **2010,** *96* (22), 222506.

257. Dukhin, A.; Goetz, P.; Fang, X.; Somasundaran, P., Monitoring nanoparticles in the presence of larger particles in liquids using acoustics and electron microscopy. *Journal of colloid and interface science* **2010,** *342* (1), 18-25.

258. Lim, J.; Yeap, S. P.; Che, H. X.; Low, S. C., Characterization of magnetic nanoparticle by dynamic light scattering. *Nanoscale research letters* **2013,** *8* (1), 1-14.

259. Jans, H.; Liu, X.; Austin, L.; Maes, G.; Huo, Q., Dynamic light scattering as a powerful tool for gold nanoparticle bioconjugation and biomolecular binding studies. *Analytical chemistry* **2009,** *81* (22), 9425-9432.

260. Goldburg, W. I., Dynamic light scattering. *American Journal of Physics* **1999,** *67* (12), 1152-1160.

261. Lim, J.; Yeap, S. P.; Che, H. X.; Low, S. C., Characterization of magnetic nanoparticle by dynamic light scattering. *Nanoscale Research Letters* **2013,** *8* (1), 381.

262. Hulst, H. C.; van de Hulst, H. C., *Light scattering by small particles*. Courier Corporation: 1981.

263. Hiemenz, P. C.; Rajagopalan, R., Principles of colloid and surface. *Chemistry* **1977,** *3*.

264. Berne, B. J.; Pecora, R., *Dynamic light scattering: with applications to chemistry, biology, and physics*. Courier Corporation: 2000.

265. Wiogo, H. T.; Lim, M.; Bulmus, V.; Yun, J.; Amal, R., Stabilization of magnetic iron oxide nanoparticles in biological media by fetal bovine serum (FBS). *Langmuir* **2011,** *27* (2), 843-850.

266. Yeap, S. P.; Ahmad, A. L.; Ooi, B. S.; Lim, J., Electrosteric stabilization and its role in cooperative magnetophoresis of colloidal magnetic nanoparticles. *Langmuir* **2012,** *28* (42), 14878-14891.

267. Andreu, J. S.; Camacho, J.; Faraudo, J., Aggregation of superparamagnetic colloids in magnetic fields: the quest for the equilibrium state. *Soft Matter* **2011,** *7* (6), 2336-2339.

268. Coburn, D. S.; Nazaretski, E.; Xu, W.; Ge, M.; Longo, C.; Xu, H.; Gofron, K.; Yin, Z.; Chen, H. H.; Hwu, Y.; Lee, W.-K., Design, characterization, and performance of a hard x-ray transmission microscope at the National Synchrotron Light Source II 18-ID beamline. *Review of Scientific Instruments* **2019,** *90* (5), 053701.

269. King, S. M., Small-angle neutron scattering. *Modern Techniques for Polymer Characterisation* **1999,** *12*.

270. Stieger, M.; Richtering, W.; Pedersen, J. S.; Lindner, P., Small-angle neutron scattering study of structural changes in temperature sensitive microgel colloids. *The Journal of Chemical Physics* **2004,** *120* (13), 6197-6206.

271. Avdeev, M.; Khokhryakov, A.; Tropin, T.; Andrievsky, G.; Klochkov, V.; Derevyanchenko, L.; Rosta, L.; Garamus, V.; Priezzhev, V.; Korobov, M., Structural features of molecular-colloidal solutions of C60 fullerenes in water by small-angle neutron scattering. *Langmuir* **2004,** *20* (11), 4363-4368.

272. Mühlbauer, S.; Honecker, D.; Périgo, É. A.; Bergner, F.; Disch, S.; Heinemann, A.; Erokhin, S.; Berkov, D.; Leighton, C.; Eskildsen, M. R.; Michels, A., Magnetic small-angle neutron scattering. *Reviews of Modern Physics* **2019,** *91* (1), 015004.

273. Adolphi, N. L.; Huber, D. L.; Jaetao, J. E.; Bryant, H. C.; Lovato, D. M.; Fegan, D. L.; Venturini, E. L.; Monson, T. C.; Tessier, T. E.; Hathaway, H. J.; Bergemann, C.; Larson, R. S.; Flynn, E. R., Characterization of magnetite nanoparticles for SQUID-relaxometry and magnetic needle biopsy. *J Magn Magn Mater* **2009,** *321* (10), 1459-1464.

274. Grob, D. T.; Wise, N.; Oduwole, O.; Sheard, S., Magnetic susceptibility characterisation of superparamagnetic microspheres. *Journal of Magnetism and Magnetic Materials* **2018,** *452*, 134-140.

VITA

Phillip Halstenberg grew up in Kannapolis, North Carolina. After graduating from A.L. Brown High School, he attended the University of North Carolina Wilmington receiving a Bachelor of Science degree in Chemistry. After undergraduate, Phillip worked on various research projects at Oak Ridge National Laboratory before entering graduate school. He obtained a degree from the University of Tennessee Knoxville as a Doctor of Philosophy in Analytical Chemistry. His research area during graduate school was molten chloride salts.